Controlling foam ageing in viscoelastic media

Chiara Guidolin

université
PARIS-SACLAY

Controlling foam ageing in viscoelastic media

Contrôle du vieillissement des mousses dans les milieux visco-élastiques

Thèse de doctorat de l'Université Paris-Saclay

École doctorale n° 564, Physique en Île-de-France (PIF)
Spécialité de doctorat: Physique
Graduate School: Physique. Référent: Faculté des sciences d'Orsay

Thèse préparée dans l'unité de recherche Laboratoire de Physique des Solides (Université Paris-Saclay, CNRS), sous la direction de Anniina SALONEN, maître de conférences, et la co-direction de Emmanuelle RIO, professeure.

Thèse soutenue à Paris-Saclay, le 11 mai 2022, par

Chiara GUIDOLIN

Composition du jury

Charles Baroud Professeur, École Polytechnique	Président
Guillaume Ovarlez Directeur de recherche, Université de Bordeaux	Rapporteur & Examinateur
Arnaud Saint-Jalmes Directeur de recherche, Université de Rennes 1	Rapporteur & Examinateur
Véronique Bosc Maître de conférences, AgroParisTech, Université Paris-Saclay	Examinatrice
Emanuela Del Gado Associate Professor, Georgetown University	Examinatrice
Christophe Raufaste Maître de conférences, Université Côte d'Azur	Examinateur
Anniina Salonen Maître de conférences, Université Paris-Saclay	Directrice de thèse
Emmanuelle Rio Professeure, Université Paris-Saclay	Co-directrice de thèse

Thèse de doctorat
NNT : 2022UPASP045

Acknowledgements

During these three years of PhD I had the chance to meet many people, whose support has proved essential for reaching this important milestone.

My first acknowledgements go to the members of the jury, for accepting to evaluate this work. Thank you to Arnaud Saint-Jalmes and Guillaume Ovarlez for carefully reviewing this thesis, which they probably expected to be slightly shorter. Thank you also to the president of the jury Charles Baroud, as well as to the examiners Christophe Raufaste, Véronique Bosc and Emanuela Del Gado, for all their stimulating questions during the defense.

I am immensely grateful to my PhD advisors, Anniina Salonen and Emmanuelle Rio, for giving me the opportunity to join the MMOI group already for my Master thesis, and for believing in me in a moment in which I needed it the most. Thank you for the patience in convincing me to continue with a PhD afterwards, as in the end this experience has allowed me to mature and overcome many of my own limits and fears, even though initially I was not so sure to move back to France for such a long period. I thank both of you for your precious guide, for your constant enthusiasm and optimism in sharing your points of view when I had the feeling that my projects were not going anywhere, as well as for your tireless attempts to rebuild some of my self-confidence throughout the PhD.

A word of thanks goes also to my thesis committee, for the stimulating discussions we had during our annual meetings. I would like to thank my scientific tutor François Graner, as his comments were a precious source of motivation for the advance of the overall thesis project. Thank you also to "mon parrain" Giuseppe Foffi, for his pieces of advice not only about science. I remember for example when we met at Orly airport after our flights were canceled for strikes, and your words convinced me to rent a car and drive all night to be sure to get home for Christmas.

The work presented in this thesis is the result of many fruitful collaborations. I start by thanking Benjamin Dollet, whom I had the pleasure to first meet in Leuven during my first conference and then to collaborate with on the aqueous 2D foams. Thank you for your precious help, as well as for your contagious enthusiasm and your kind words of encouragement during the writing of this manuscript. I continue by thanking Jonatan Mac Intyre and Antti Puisto, for all the discussions about foamed emulsions and for their help with the quantification of bubble rearrangements. Thank you also for the warm welcome in your group during my short stay in Helsinki. I would like to thank also Roberto Cerbino and Fabio Giavazzi for accepting to start the project on the coarsening dynamics very close to the end of my PhD. I am especially indebted to Fabio, for the huge patience he showed in teaching me how to perform DDM analysis starting from scratch. Thank you for always finding some time in your busy agenda to promptly clarify all my doubts, not only about DDM. I would like to say thank you to Dominique Langevin as well, for her kindness and

for all the interesting discussions about the one-step generation of aerated emulsions, after which I always felt enriched.

Then I would like to thank each single member of the MMOI group, for the friendly environment I had the pleasure to work in. Thank you for being my sort of "French family" during these years as expat. A very special thanks goes to our caring group leader, Frédéric Restagno. Thank you Fred for always being there "as a father" (even if we agree you are way too young to potentially be it): I will never forget how you physically brought some Wi-Fi at my place in the middle of the first lockdown. Thank you also for your gluten-free bakery experiments, and for all our funny discussions about French vs Italian food culture. A warm thanks goes also to Sandrine, our amazing engineer, for the positive vibes she brings in the lab and for being a reference point for any sort of issue. I also thank all the PhD students and post-docs, present and past, I met during my stay. Among them, a special thanks maybe goes to the ones I spent more time with. I begin by thanking Anna, for literally taking me out of my lonely routine. I glimpsed a wonderful person behind that shield, thank you for your friendship. Thank you also to my first office mate, Jonas, whom I did not expect to miss so much. Plus I really enjoyed sharing my first-conference experience with you in Leuven. Thank you to Marina, Marie, Manon, and Julian, for always being ready to answer all my questions and help me with any sort of daily issue. Marina, thank you for all the long chats in your office, for your cheerfulness and for your prompt help with all kinds of French paperwork. Marie, thank you for your contagious laughter and for your ability to cheer me up with just a few words. Manon, thank you for the dinners and the board game nights at your place. Julian, I really loved wandering aimlessly in Athens with you and I will definitely miss our neverending chats about the future. Thank you as well to all the other people in the group, even if not explicitly mentioned here, as I treasure so many nice little memories that I cannot gather all of them in a paragraph.

Getting to the end, I would like to thank of course my family, my mother and my brother, for the special bond that unites us and for they know what we went through before arriving to this point.

Last, but definitely not least, I owe the most special thanks to the person I have been sharing half of my life with, and who knows me the most. Thank you Tommaso for your crucial support and for the infinite forbearance it took for you to remain by my side.

université PARIS-SACLAY | ÉCOLE DOCTORALE Physique en Île-de-France (PIF)

Titre: Contrôle du vieillissement des mousses dans les milieux visco-élastiques
Mots clés: mousse, émulsion, mûrissement, viscoelasticité

Résumé: Les mousses sont des dispersions concentrées de bulles de gaz dans un milieu continu, largement rencontrées dans de nombreuses applications, de l'industrie alimentaire à la cosmétique, où la phase liquide de la mousse est souvent un fluide à rhéologie complexe. Néanmoins, ces systèmes sont par nature instables: leur structure peut être modifiée au cours du temps par différents mécanismes, dont la diffusion de gaz entre les bulles due à leur différence de pression. Même si ce mûrissement a été largement étudié dans les mousses aqueuses, sa dépendance aux propriétés mécaniques de la phase liquide et sa fraction volumique manquent encore d'une compréhension approfondie. Dans cette thèse, nous étudions expérimentalement comment l'augmentation de la fraction liquide influence le mûrissement de monocouches de bulles aqueuses confinées entre deux plaques en verre. La diminution progressive et la disparition éventuelle des films minces entre les bulles entraîne une réduction du taux de mûrissement au cours du temps, que nous comparons avec les modèles existants. Nous étudions ensuite l'effet d'une phase continue viscoélastique sur le mûrissement des mousses, en remplaçant la phase aqueuse par des émulsions concentrées d'huile dans l'eau. Nous montrons que l'augmentation de l'élasticité de l'émulsion se traduit par une hétérogénéité de croissance des bulles qui modifie profondément la structure de la mousse, avec l'apparition de motifs de bulles non relaxés. Cela entraîne un retard dans le rétrécissement et la disparition des petites bulles, ce qui réduit le taux de croissance des bulles. D'autres résultats sur la dynamique de mûrissement dans ces mousses d'émulsions montrent que le mouvement des bulles pendant le grossissement est également réduit lors de l'augmentation de l'élasticité de l'émulsion. Enfin, nous montrons comment des émulsions aérées peuvent être générées en une seule étape en mélangeant simultanément l'huile, l'air et la phase aqueuse, assurant une bonne séparation d'échelle entre les bulles de gaz et les gouttes d'huile. En outre, nous montrons comment une technique standard de diffusion de la lumière telle que la granulométrie par diffraction laser peut être utilisée pour une mesure rapide de la taille des bulles dans des doubles dispersions de fluides ayant un indice de réfraction différent. Nos résultats sur la séparation de phase des mousses d'émulsions fournissent de nouvelles informations sur leur mécanisme de déstabilisation qui peuvent aider à contrôler la stabilité de ces systèmes complexes pour la création de nouveaux matériaux à morphologie cellulaire atypique.

université PARIS-SACLAY | ÉCOLE DOCTORALE Physique en Île-de-France (PIF)

Title: Controlling foam ageing in viscoelastic media.
Keywords: foams, emulsions, coarsening, viscoelasticity

Abstract: Foams are concentrated dispersions of gas bubbles in a continuous medium which are widely encountered in many applications, from food industry to cosmetics, where their liquid phase is often a fluid with complex rheology. Nevertheless, such systems are intrinsically unstable, as their structure can be altered over time by a competition of different mechanisms, including pressure-driven gas diffusion between the bubbles. Even though this coarsening process has been widely studied in aqueous foams, its dependence on the mechanical properties of the liquid phase and its volume fraction still lacks a thorough understanding. In this thesis, we first experimentally probe how an increasing liquid fraction influences the coarsening process of aqueous bubble monolayers confined between two glass plates. The gradual decrease and eventual vanishing of the thin film area between adjacent bubbles results in a reduction of the global coarsening rate over time, which we compare with existing models. We then investigate the effect of a viscoelastic foam continuous phase on the coarsening process, by replacing the aqueous phase with concentrated oil-in-water emulsions. We show that an increase of the emulsion elasticity results in an heterogeneous bubble growth which deeply modifies the foam structure, with the appearance of unrelaxed bubble patterns. This leads to a delay in the shrinkage and disappearance of smaller bubbles which reduces the bubble growth rate. Further investigations on the coarsening dynamics in such systems show that the motion of the bubbles during coarsening is also reduced upon increase of emulsion elasticity. Finally, we show how aerated emulsions can be generated in a single step by simultaneously mixing the oil, gas and aqueous phases, ensuring a good scale separation between gas bubbles and oil drops. Moreover, we show how a standard light scattering technique such as laser diffraction granulometry can be used for a fast measure of the bubble size also in double dispersions of fluids having different refractive index. Our results on the phase separation of foamed emulsions provide new insights on their destabilising mechanism which can help controlling the stability of such complex systems for the design of new materials with atypical cellular morphology.

Contents

Introduction **1**

I State of the art **3**

1 Liquid interfaces **5**
1.1 Interfacial tension 5
1.2 Laplace law 6
1.3 Surface active molecules 8

2 Foams **11**
2.1 Definition and applications 11
2.2 Foam structure 13
2.2.1 Multiscale structure 13
2.2.2 Ideal foams and the laws of Plateau 14
2.3 Liquid volume fraction 15
2.3.1 The vanishing of the osmotic pressure 16
2.4 The role of surfactants 18
2.5 Foam ageing 19
2.5.1 Drainage 19
2.5.2 Coalescence 20
2.5.3 Coarsening 21

3 2D and quasi-2D foams **23**
3.1 Ideal 2D foams 23
3.2 Quasi-2D foams 24
3.2.1 Configurations and 3D structure 24
3.2.2 Liquid fraction definitions 25
3.3 From dry to wet: the decoration lemma and beyond 26
3.3.1 The decoration lemma 26
3.3.2 The rigidity loss transition in 2D 27
3.3.3 Film disappearance in quasi-2D foams 28

4 Foam coarsening **31**
4.1 The dry limit 31
4.1.1 2D foams 31
4.1.2 3D foams 33

4.2 The influence of the physical chemistry . . . 34
4.3 The wet limit . . . 34
4.4 Self-similar growth regime . . . 35
4.5 Bubble rearrangements . . . 37
4.6 From dry to wet . . . 39
4.6.1 2D foams . . . 39
4.6.2 Quasi-2D foams . . . 40
4.6.3 3D foams . . . 41

5 Foamed emulsions **43**
5.1 Yield-stress fluids . . . 43
5.2 Concentrated emulsions . . . 44
5.2.1 Analogies with foams . . . 45
5.2.2 Mechanical properties . . . 45
5.2.3 Emulsion stability . . . 47
5.3 Aerated emulsions . . . 47
5.3.1 Influence of oil droplets on foam stability . . . 48
5.3.2 Rheology of aerated dense emulsions . . . 50
5.4 Foam coarsening in viscoelastic media . . . 52

Contextualisation of the experimental work **55**

II Experimental work **57**

6 Quasi-2D aqueous foams **59**
6.1 Introduction . . . 59
6.2 Experimental approach . . . 61
6.2.1 Foaming solutions . . . 61
6.2.2 Foam generation . . . 61
6.2.3 From 3D to quasi-2D foams . . . 62
6.2.4 Image treatment . . . 63
6.3 Results . . . 65
6.3.1 Self-similar growth regime . . . 65
6.3.2 Coarsening at constant liquid fraction . . . 72
6.3.3 Towards the vanishing of the thin films . . . 78
6.4 Conclusions . . . 85

7 Quasi-2D foamed emulsions **87**
7.1 Introduction . . . 87
7.2 Experimental approach . . . 89
7.2.1 Emulsion generation . . . 89
7.2.2 Emulsion rheology . . . 89
7.2.3 Foam generation . . . 90
7.2.4 Imaging . . . 93
7.3 Results . . . 95
7.3.1 Emulsion properties . . . 95
7.3.2 Mean bubble size evolution . . . 99

7.3.3 Bubble size distributions . . . 101
7.3.4 Coarsening mechanism . . . 104
7.3.5 Bubble pattern . . . 113
7.3.6 Effect of the liquid fraction . . . 116
7.3.7 Effect of confinement . . . 119
7.4 Conclusions . . . 121

8 Coarsening dynamics in foamed emulsions 123
8.1 Introduction . . . 123
8.2 Experimental approach . . . 125
8.2.1 Sample preparation and imaging . . . 125
8.2.2 Real space image treatment . . . 125
8.2.3 Correlation maps . . . 125
8.2.4 Differential Dynamic Microscopy . . . 127
8.3 Results . . . 131
8.3.1 3D foamed emulsions . . . 131
8.3.2 3D/2D transition . . . 140
8.3.3 Coarsening dynamics in quasi-2D foams . . . 143
8.4 Conclusions . . . 150

9 One-step generation of aerated emulsions 151
9.1 Introduction . . . 151
9.2 Experimental approach . . . 153
9.2.1 Materials . . . 153
9.2.2 Sample generation . . . 153
9.2.3 Laser diffraction granulometry . . . 154
9.2.4 Optical microscopy . . . 158
9.2.5 Surface tension measurements . . . 160
9.3 Results . . . 162
9.3.1 Bubbly and foamed emulsions . . . 162
9.3.2 Comparison with microscopy . . . 163
9.3.3 Bubble and drop size . . . 167
9.3.4 Detected volume fractions . . . 170
9.3.5 Limit on the bubble size . . . 173
9.4 Conclusions . . . 177

General conclusions 179

Appendices 183

A Résumé de la thèse 185

Bibliography 201

Introduction

From the head on a pint of beer to the shampoo lather under the shower, or from the whipped cream on top of a slice of cake to the cake itself, every one encounters several examples of foams in daily life. All these materials share a specific cellular structure that sees gas bubbles dispersed in a continuous medium, and that lends them their distinctive properties for which they find such a large use both in industry and in our houses.

Their stability and mechanical properties mainly depend on the size and density of these gas pockets, but a crucial role can also be played by the nature of the continuous medium. Indeed, the matrix among the bubbles can be liquid, but also solid or even a composite material characterised by a complex rheology.

While solid foams, which have as many applications as their liquid counterparts, are clearly static systems, liquid foams are intrinsically unstable. When their continuous phase is liquid, indeed, these ephemeral systems undergo an interplay of different mechanisms which tend to modify their structure over time and eventually lead to an irreversible foam damage.

Even though a lot of work has been done in the last decades to understand the stability of aqueous foams, what happens when the continuous phase is a complex fluid is a more recent question which still lacks a total understanding. Nevertheless, studying how to control the foam stability in more complex systems can be useful for example in the storage of many airy food products, as well as in the design of new solid cellular materials with a well-controlled internal structure.

In the present thesis, we will first address how an increasing amount of liquid affects the pressure-driven phase separation of single layers of bubbles, in which gravitational drainage and coalescence can be neglected.

We will then investigate what happens when we change the rheology of the fluid between the bubbles, to shed a light on the link between its mechanical properties and the coarsening of these bubble monolayers. To this end, we shall use concentrated emulsions as the continuous phase of our foams. These systems, which are in turn made of tiny oil droplets dispersed in an aqueous continuous phase, are indeed able to exhibit a viscoelastic behaviour if the drop volume fraction is sufficiently high. We shall thus play with the emulsion droplet fraction to vary the mechanical properties of the foam continuous phase and characterise the hallmarks of coarsening in foamed emulsions at different levels of emulsion viscoelasticity. In doing that, a special focus will be kept on the structural evolution of these systems, to understand the link between the latter and the overall bubble growth, but we shall then also probe how the bubble movements during coarsening are affected by a change of emulsion elasticity. Finally, we shall probe a new way for generating and characterising these double dispersions of gas bubbles and oil droplets, overstepping the need of prepare aerated emulsions in two separate steps.

The thesis is divided in two parts. The first part encloses the basic theoretical concepts about interfaces and foams, followed by a review of the most relevant literature concerning foam coarsening in aqueous and complex media. The aim of this part is to highlight the main open questions and provide all the necessary information for understanding the main goals and results of the experimental work, which is the object of the second part.

This second part is structured into four chapters presenting the main results of this work, divided by single but highly interconnected projects. In each chapter we shall first introduce the addressed questions and explain the experimental approach used to reach our goals, with in-depth explanations of the experimental techniques when needed. For each project we then present and discuss the main experimental results obtained, raising also new interesting questions and perspectives for future studies on these systems.

Part I

State of the art

1 Liquid interfaces

An interface is the boundary between two spatial regions occupied by different matter or by matter in a different state. We call liquid interface the one that forms whenever a liquid comes in contact with another immiscible fluid. Such interfaces however do not form spontaneously: supplying energy is necessary for their creation. In this chapter we introduce some basic physical concepts about the behaviour of such interfaces, which are essential for the understanding of the next chapters.

1.1 Interfacial tension

In all fluids there are some kind of attractive interactions between molecules. If attraction is stronger than thermal agitation, then the molecules switch from a gaseous state to a condensed, yet still disordered, state of matter called liquid [20].

Whenever a liquid comes into contact with a gas or another immiscible liquid, an interface is created between the two fluids. While a molecule in the liquid bulk feels the attractive interaction with all its neighbours, the liquid molecules wandering to the interface lose half of their cohesive interactions, as half of their neighbours are replaced by molecules of the second fluid, as sketched in figure 1.1.

In fact, if the cohesion energy per molecule is U in the bulk, a molecule sitting at the interface will be lacking roughly $U/2$, and it is thereby in an unfavourable situation. Thus, liquids tend to adjust their shape in order to minimise their exposed area, that is the reason why for instance single bubbles or drops are perfectly spherical.

At a molecular level, the interfacial tension γ reflects this energy loss per unit of interface area A. If we call l the molecular size, the area covered by a molecule at the interface will be roughly l^2 and therefore one can write:

$$\gamma = \frac{\Delta U}{A} \simeq \frac{U}{2l^2} \tag{1.1}$$

This simple relation predicts values of γ which are very close to the real surface tensions of many liquids [73].

Although the physical origin of the interfacial tension can be explained at a molecular level, γ is a macroscopic parameter defined only at a macroscopic scale. Indeed, γ can be related to the work δW necessary to increase the interfacial area by a small quantity $\mathrm{d}A$. Since this work will be proportional to the number of molecules that must be carried from the bulk to the interface, and thus to $\mathrm{d}A$, one can write [20]:

$$\delta W = \gamma \mathrm{d}A \tag{1.2}$$

The variation of the fluid total free energy F that follows this increase of surface area is $\mathrm{d}F = \gamma\,\mathrm{d}A - P\,\mathrm{d}V - S\,\mathrm{d}T$, where P is the pressure, V is the total volume, T the temperature and S is the entropy [73]. Thus, at constant temperature and volume, one can write:

$$\gamma = \left(\frac{\partial F}{\partial A}\right)_{T,V,n} \tag{1.3}$$

where n is the number of molecules. We can see that dimensionally γ is indeed an energy per unit area $[\gamma] = EL^{-2}$, thus measured in $\mathrm{J/m^2}$. But γ being the work done per unit area to create a surface, it can also be viewed as the force exerted on the line limiting the area under creation counted per unit length. Therefore $[\gamma] = FL^{-1}$, which justifies the name tension, and is commonly measured in N/m [20].

Traditionally, γ is called *surface* tension when referring to a liquid in contact with a gas (typically air), while the more general term *interfacial* tension is reserved for interfaces between two immiscible liquids. All observations in this section are however general and hold in both cases.

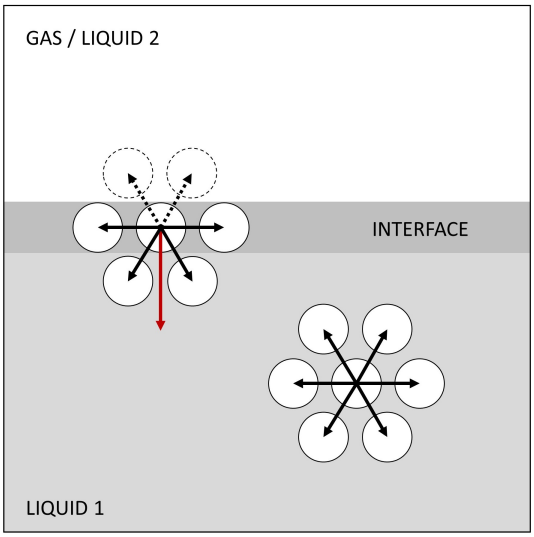

Figure 1.1 – **Illustration of interfacial tension at molecular level.** The molecules sitting on the interface lose part of their interactions resulting in a net force towards the bulk which is at the origin of the interfacial tension.

1.2 Laplace law

In the previous section we have seen that liquids tend to minimise their surface area. As a consequence, if an interface is not flat, the surface tension provokes orthogonal forces which, at equilibrium, must be counterbalanced by the pressures on each side [9]. There must be therefore a relationship that links the pressures, the tension and the shape of an interface.

Let us consider a curved interface Σ of tension γ that separates two domains A and B, like the one shown in figure 1.2. In any arbitrary interfacial point P, the interface will be locally characterised by its principal curvature radii R_1 and R_2, conventionally counted positive if the centre of curvature is in A and negative otherwise.

The Young-Laplace law states that the pressure difference ΔP existing between the two sides of the interface is related to its tension γ and to its mean curvature H as follows:

$$\Delta P = P_A - P_B = \gamma H = \gamma\left(\frac{1}{R_1} + \frac{1}{R_2}\right) \tag{1.4}$$

and shows that interfacial tension tends to make the interface flatter, offsetting the pressure difference which tends to bend the interface.

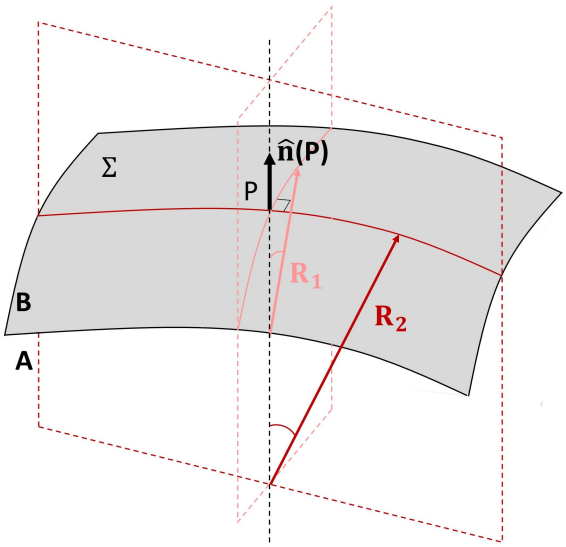

Figure 1.2 – **Curved interface separating two domains A and B.** The pressure difference between the two sides, $P_A - P_B$, is proportional to the interfacial tension γ and to its mean curvature, given by $H = 1/R_1 + 1/R_2$.

Single bubbles or drops

Surface tension is hence at the origin of the overpressure existing inside drops and bubbles.

Let us consider a soap bubble of radius R suspended in air, as in figure 1.3 (a). The gas inside the bubble is confined by a liquid film of negligible thickness $h \ll R$ with tension 2γ as two gas/liquid interfaces are present. The bubble will not shrink to decrease its surface area to zero because the tension in its two surfaces is countered by an excess pressure, namely the pressure difference between the interior of the bubble and its surroundings, $\Delta P = P_{\text{int}} - P_{\text{ext}}$.

For a spherical interface $R_1 = R_2 = R$ in each point, thus equation (1.4) gives the pressure difference existing between the inside and the outside of the bubble, which is:

$$\Delta P = P_{\text{int}} - P_{\text{ext}} = \frac{4\gamma}{R} \tag{1.5}$$

Likewise, the same reasoning holds for single bubbles and drops surrounded by a liquid, with interfacial tension γ as only one interface is now present: the pressure difference in this case will be $\Delta P = 2\gamma/R$.

Since the overpressure is inversely proportional to the radius R, large bubbles or drops will have a lower inner pressure than small ones. When bubbles or drops of different size

coexist inside a dispersion, as sketched in figure 1.3 (b), the pressure difference between them drives the diffusion of dispersed material from smaller objects to larger ones and is thus at the origin of the destabilising mechanism of such dispersions called coarsening process. Coarsening is the key topic of the present thesis and will be discussed in detail for bubble dispersions in chapter §4.

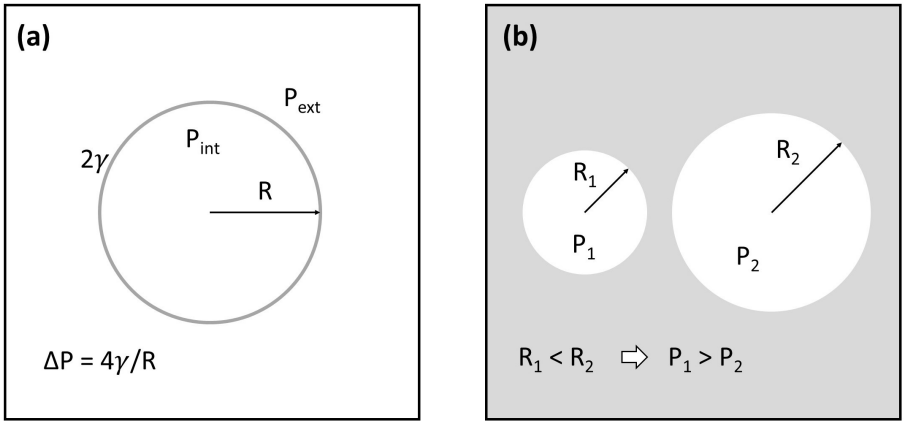

Figure 1.3 – **Excess pressure of single bubbles and drops.** (a) The tension 2γ on a bubble film in air is counteracted by a pressure difference $\Delta P = 4\gamma/R$ between interior and exterior. (b) The inverse proportionality between overpressure and radius results in a pressure difference between bubbles or drops of different size, which is at the origin of the material transfer from smaller objects to larger ones.

1.3 Surface active molecules

Ideal liquid interfaces are smooth and chemically homogeneous, and their interfacial tension γ depends on their chemical composition as well as on the temperature: it decreases as the temperature rises. Although γ is a trait of the two fluids in contact, in real life interfaces can be easily contaminated with impurities which lower the interfacial tension.

Sometimes it might be desirable to reduce the interfacial tension. In particular, γ can be significantly lowered by adding special objects of different nature, like detergent molecules, proteins, polymers or even solid particles. Among them, a special category of molecules called surfactants usually present a polar hydrophilic head group linked to a hydrophobic, but lyophilic, carbon chain. These molecules are thus said to be *amphiphilic* (or occasionally *amphiphobic*), where the Greek etymology reflects their indecision about what they like (or hate). Their two halves being hydrophobic and hydrophilic, such undecided molecules can get the best of both phases by adsorbing at interfaces [126].

In fact, when such molecules are dissolved in a liquid they tend to adsorb from the bulk solution to the interfaces, with their heads lodging in water and their tails outstretched in air or in oil.

There exist different kinds of surfactants, depending on their chemical features [73]. When the polar head group is an ion, either negative or positive, the surfactant is called anionic or cationic respectively. Sodium Dodecyl Sulfate (SDS), widely employed in many hygiene products like toothpaste or shampoo, is an example of anionic surfactant bearing

a sulfate group at the end of a 12-carbon chain tail, as illustrated in figure 1.4 (a). It will be the main surfactant used in the experimental part of the present thesis.

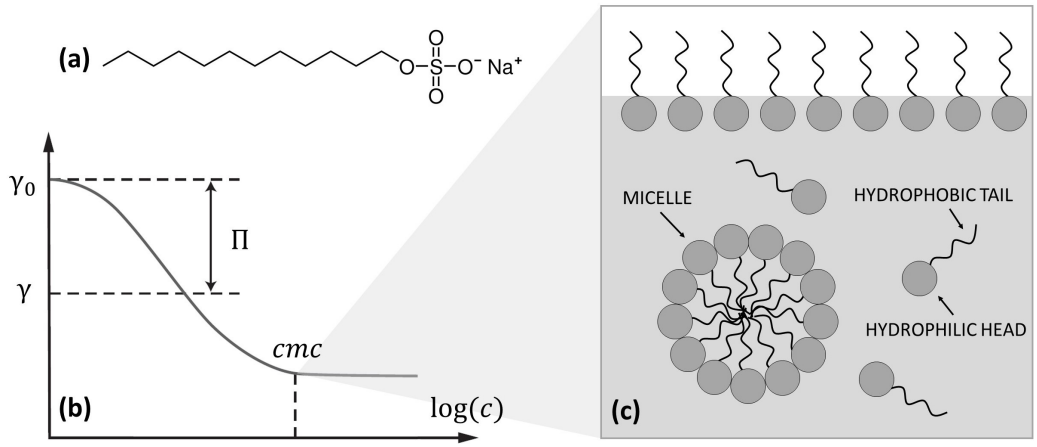

Figure 1.4 – **Effect of surfactants on the interface.** (a) Molecular structure of SDS. (b) The gradual addition of surfactant results in a decrease of the interfacial tension γ, which becomes constant when the critical micellar concentration is reached. (c) Above the cmc, a further addition of surfactant results in the aggregation of surfactant molecules in order to hide their hydrophobic part inside the micelles.

Surfactant adsorption lowers the interfacial tension γ, whose value will depend on the surfactant concentration. As we increase the bulk concentration c, γ will decrease to a value lower than the bare surface tension γ_0, and their difference is called surface pressure $\Pi = \gamma_0 - \gamma$. In figure 1.4 (b) we can see how the surface tension γ monotonically decreases with the addition of dissolved surfactants, until it reaches a constant plateau. Indeed, the increase of surfactant concentration gradually leads to the formation of a monolayer of such molecules covering the whole surface. Above a critical value, a further increase of surfactant concentration will no longer affect the surface tension value, which remains constant. The concentration at which this happens is called critical micellar concentration (cmc) and its value depends on the surfactant. Above the cmc, no more surfactants can be placed at the interface, thus the surfactant molecules in the bulk begin to gather forming clusters, the micelles, within which the hydrophobic part can be hidden, as depicted in figure 1.4 (c).

2 Foams

We saw in the previous chapter the main features of liquid interfaces. In this chapter we shall introduce foam systems, which are special liquid architectures characterised by an extremely high specific surface area. Since foams are widely encountered in many fields, we start by giving a short overview of their main applications. We will then describe in detail the peculiar multiscale structure that confers them such a vast range of properties, and see how this is actually governed by a group of simple rules coming from the minimisation of surface area. After that, we shall discuss the role of the amount of liquid inside the foam and how this impacts the overall structure. Finally, we will briefly explain the three mechanisms which can alter the foam structure over time, making liquid foams only meta-stable systems.

2.1 Definition and applications

Foams are dense dispersions of gas bubbles in a continuous medium, which is liquid at first thought, but which can also be solid or even a complex fluid itself. Beyond the nature of the material forming their continuous phase, on a very basic level foams can be described by the amount of dispersed gas and by the size of the bubbles, which is typically taken as the radius of a sphere of equivalent volume. Their cellular structure lends them unique physical properties which make these systems ubiquitous. Figure 2.1 shows just a few examples of different foam applications.

In everyday life, liquid foams are found in beverages, as well as in household and personal care products, where their appeal is often largely psychological. However, while foaming of detergents, like shampoo or washing-up liquid, certainly helps pleasing the customer sensorial perception, the elasticity of shaving foam is what enables the product to cling to vertical surfaces like the face skin until the razor blade removes it [126].

On a larger scale, liquid foams are also employed in fire-fighting for extinguishing burning liquids, like petrol, and suppressing their reignition [109]. In fact, the low density of foam makes it float on top of the combustible, whereas simple water would just agitate the liquid and help spreading the fire. Many industrial processes also use liquid foams as chemical carriers whenever a product must be spread upon large areas, such as textile dyeing but also nuclear decontamination: this allows reducing both the amount of water needed and the volume of waste to process afterwards [109].

Several complex fluid foams can be encountered in the kitchen when sipping a cappuccino, beating a cake batter, or whipping cream or egg whites to make a chocolate mousse. In food industry, edible foams are indeed common not only for their pleasant mouth feel, but also because their high interfacial area facilitates the aroma molecular transfer to the consumer tongue [109]. Thus foams can be exploited as effective flavor enhancers, as they allow to reduce salt or sugar content in dietary products.

Without moving too far, when taking a cake or a bread loaf out of the oven we meet a first example of solid foam. Solid foams are as important and widespread as their liquid counterparts as, being made mostly of air, they combine lightness with other desirable properties like compressibility or low thermal conductivity [109]. Solid foams are formed by solidification of a liquid precursor, from which they inherit their morphology. Typical examples include cellular building materials, like aerated concrete, or polymer foams, which can be found in vehicles, as well as in home furniture or in packaging.

The final properties will clearly depend on the nature of the starting material, but a crucial role is primarily played by the foam structure. If the solid product retains the bubble faces of its liquid parent, the solid foam is called *closed-cell*. Typically rigid, such structures are found for example in insulation materials [31]. However, one could prefer to solidify only the framework of liquid channels, obtaining a so-called *open-cell* foam. Such structures are usually soft and found for example in seat cushions, but also in sponges where the open-cell structure is what enhances their ability to soak up liquids.

While foams are clearly static once solidified, as long as they are liquid they can destabilise through different physical processes which modify their internal structure over time. In fact, liquid foams are only metastable systems and their desired lifetime strongly depends on the final application, this is why a thorough understanding of liquid foam stability is crucial. The rest of the chapter will thus focus on liquid foams, addressing in more detail the main structural and stability properties of these original systems.

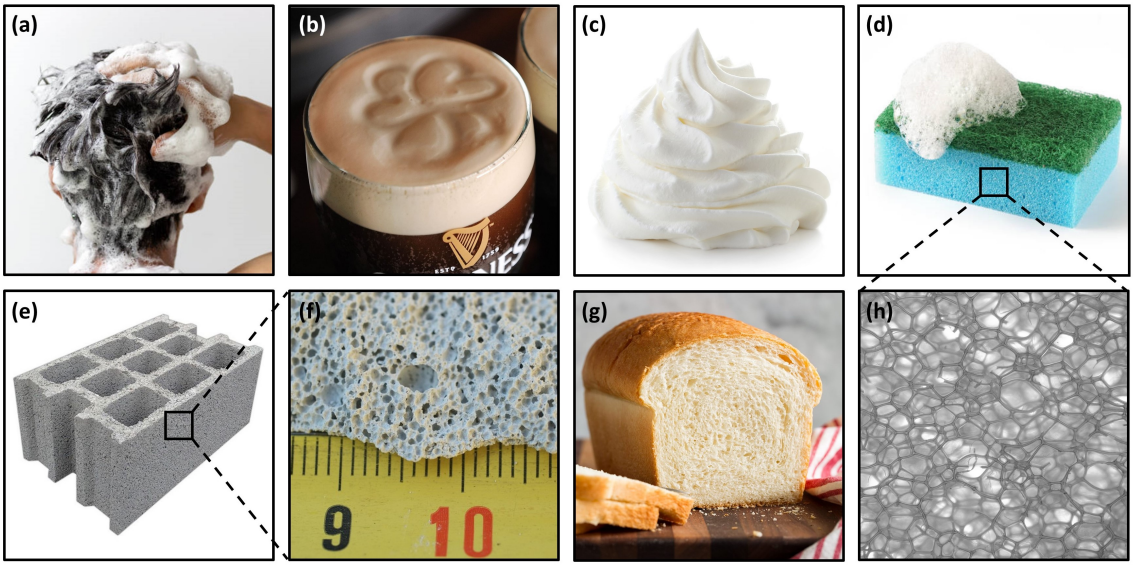

Figure 2.1 – **Foam applications.** Liquid foams can be found in hygiene products (a), beverages (b), food (c) or household detergents (d). Whipped cream (c) is a typical example of foam whose continuous phase is a complex fluid. The sponge in (d) is itself an example of solid polymer foam with open-cell structure, as observed under the microscope (h). Other examples of solid foams include building materials like aerated concrete blocks (e) with their cellular structure highlighted in (f), but also the bread crumb (g).

2.2 Foam structure

Foam systems present unique properties thanks to their characteristic multiscale structure. The bubble packing inside a foam is not completely disordered, as the minimisation of the surface area gives a set of rules which govern the structural properties of a foam at equilibrium. This is the focus of this section.

2.2.1 Multiscale structure

The structure of a foam at equilibrium can be described at different length scales, ranging from macroscopic to molecular, as shown in figure 2.2.

At a macroscopic scale, liquid foams appear as soft solid materials, which can be considered homogeneous. However, their turbidity comes from the light scattered at the inner interfaces which gives them their typical white appearance.

In fact, such materials are not homogeneous, as a closer look unveils its characteristic cellular structure made of soft gas units tightly packed together, the bubbles, whose typical size ranges from tens of microns to several millimeters.

At the microscopic scale, one can also distinguish how the liquid is distributed among such bubbles. The foam skeleton can be thought of as a network of thin liquid films that separate neighbouring bubbles, with a thickness generally from tens to hundreds of nanometers. Whenever three of these thin films intersect, they form liquid-carrying channels called *Plateau borders*, which have a triangle-shaped cross section with concave sides. Such channels act as collectors of liquid coming from the films, thus contain most of the foam mass. Four of these Plateau borders then meet in a junction called vertex or node.

Finally, jumping down to the nanometric scale one can recognise the structure of the liquid interfaces, revealing the presence of adsorbed surface-active molecules. Such objects are necessary to provide stability to the thin liquid films and thus prevent the overall foam to quickly collapse, as it will be explained in section §2.4.

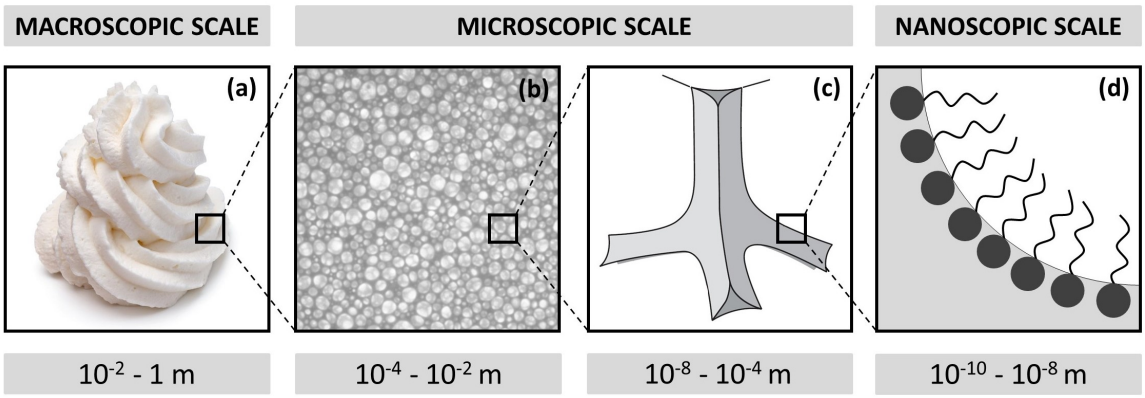

Figure 2.2 – **Multiscale structure of a foam.** At the observer scale foams appear as soft homogeneous solids (a). At the microscopic scale one can recognise the gas bubbles (b) and the network of liquid channels among them (c). At the molecular scale one can observe the presence of stabilisers adsorbed at the interfaces (d).

2.2.2 Ideal foams and the laws of Plateau

Being an architecture of liquid interfaces, the structure of a liquid foam at equilibrium is governed by the minimisation of its total interfacial area. As long as a foam is in good approximation ideal, its structure is determined by simple geometric rules at the scale of a few bubbles: the laws of Plateau.

But when can a real foam be considered ideal? First and foremost, it has to be very dry, namely its liquid content must be only a negligible part of the foam total volume. In such a case, a foam can be seen as a partition of space into many cells without overlaps or gaps, where the thin films between adjacent bubbles are assumed to have zero thickness and film tension 2γ.

But in order to be considered ideal, a dry foam has to satisfy further requirements. First, the foam has to be at mechanical equilibrium, and second, the gas inside each bubble is considered as incompressible. Under these assumptions, the foam structure is dictated by the so-called laws of Plateau.

Let us consider two adjacent bubbles i and j separated by a face Σ with principal radii of curvature R_1 and R_2 counted as positive if the centre of curvature is in bubble i. The ideal film between the two bubbles satisfies the Laplace law, as seen in §1.2, thus its mean curvature $H = 1/R_1 + 1/R_2$ is independent of the point of the surface and satisfies the following relation:

$$P_i - P_j = 2\gamma H \tag{2.1}$$

which represents the first Plateau's law. According to equation (2.1) foam films are thus surfaces of constant mean curvature H determined by the law of Laplace.

The second Plateau's law concerns how three films meet along an edge. Let us consider for instance two bubbles having the same volume touching each other, as sketched in figure 2.3 (a).

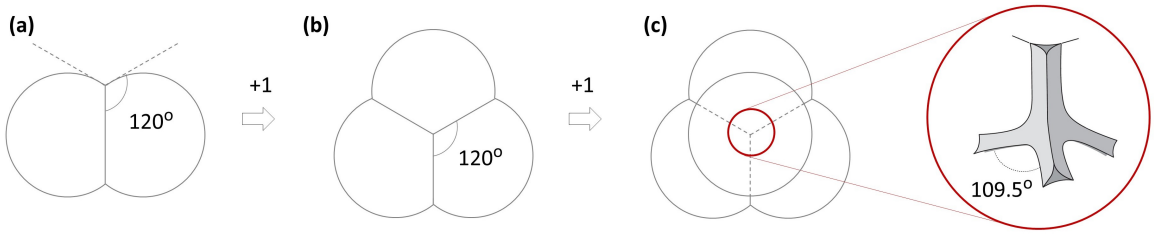

Figure 2.3 – **Second and third law of Plateau.** (a) The angle between the film shared by two touching bubbles and the tangent to each curved film must be 120°. (b) If we add a third bubble, the angle between the three films meeting at the central edge must be equal to 120°. (c) If we add a fourth bubble, the four edges meet at the vertex at an angle 109.5° as it is the only configuration that ensures an angle of 120° between each couple of films.

To reduce the energy of the system the two bubbles will share part of their interface, creating a flat circular film between them. When a third bubble is added, it minimises the surface area of the system by sharing a film with each of the first two bubbles. If the system is at equilibrium, the vectorial forces of surface tension exerted by each of the three films must cancel out, and this happens only if the angle between each pair of adjacent films is

120°, as in figure 2.3 (b). The second Plateau's law thus states that the angle at which three films meet along the edge is 120°.

If we now add a fourth bubble to the system, it will once again share part of its interface with the three bubbles: at the centre there will be now four edges connected at a vertex, as shown in figure 2.3 (c). The only configuration that allows angles of 120° between each couple of films has a tetrahedral symmetry, thus the third law of Plateau states that no more than four edges meet at a vertex with an angle equal to $\cos^{-1}(-1/3) = 109.47°$.

Finally, foams are not suspended in air but usually deposited on a solid surface. It is thus necessary to add to these laws a condition for contact with a solid wall: at equilibrium, the angle between a solid wall and a film in an ideal foam is 90°.

2.3 Liquid volume fraction

At a macroscopic level the external aspect and macroscopic properties of a foam may be totally characterised by the size of its bubbles, let us say their radius R, and by the amount of liquid between them, namely its liquid volume fraction, defined as:

$$\varepsilon = \frac{V_{\text{liq}}}{V_{\text{foam}}} \tag{2.2}$$

that is the ratio between the volume of liquid inside the foam, V_{liq}, and the total foam volume $V_{\text{foam}} = V_{\text{liq}} + V_{\text{gas}}$.

When considering the liquid fraction, one puts the focus on the relative amount of continuous phase inside the foam, and thus on its mass. However, depending on the specific application, sometimes one might prefer to highlight the relative volume of dispersed phase, in this case the gas, and thereby use the gas fraction φ:

$$\varphi = \frac{V_{\text{gas}}}{V_{\text{foam}}} = 1 - \varepsilon \tag{2.3}$$

which is the complementary fraction of ε, as their sum must be equal to 1.

In addition, for instance in food industry, it is quite common to work in terms of overrun, defined as:

$$\text{overrun} = \frac{V_{\text{foam}} - V_{\text{liq}}}{V_{\text{liq}}} = \frac{V_{\text{gas}}}{V_{\text{liq}}} = \frac{\varphi}{\varepsilon} \tag{2.4}$$

which is always expressed as a percentage and basically quantifies the relative increase of volume after foaming a given amount of liquid. Relation (2.4) also shows how the overrun is related to the gas and liquid fraction, being the ratio between the two.

Along the present thesis, we will mainly think in terms of foam liquid fraction, except for chapter §9 where we will use the gas fraction for reasons that will be clarified. Moreover, we will always express the volume fractions as percentages for the sake of simplicity.

Despite the user discreption in the choice of one parameter rather than another, what has physical relevance is the structural change of the foam as the amount of liquid between the bubbles is gradually increased. In fact, both mechanical behaviour and stability strongly depend on the foam wetness, and thus change with the liquid fraction.

When the amount of liquid is negligible (ε typically a few percents), the foam is said to be *dry* and the bubbles, tightly packed together, have polyhedral shapes. But, as shown in figure 2.4, as we gradually increase the liquid fraction, the liquid channels between the

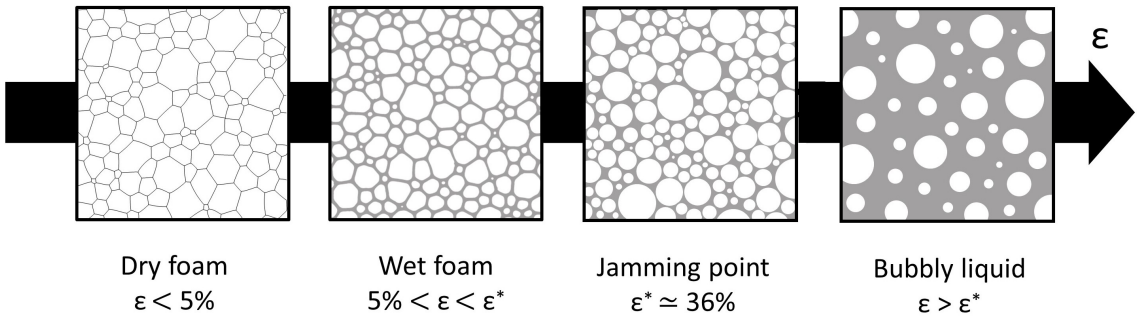

Figure 2.4 – **Influence of the liquid fraction.** In dry foams the amount of liquid is negligible and bubbles have polyhedral shapes. As we wet the foam we gradually reduce the area of shared interfaces between the bubbles, until the contact is lost at the critical liquid fraction ε^* corresponding to random close packing. Above ε^* we no longer have a foam but a bubbly liquid in which spherical bubbles are far away from each other.

bubbles start to thicken and the polyhedrons change their shape into squashed spheres. This is what is called a *wet* foam. As soon as ε reaches a critical value ε^*, the contact between the bubbles is lost and, since they no longer touch each other, they become perfectly spherical. Since above ε^* the bubbles are not jammed, this case is not referred to as a foam but is more properly called a *bubbly liquid*.

While the transition between dry and wet foam is not univocally defined, the transition from wet foam to bubbly liquid occurs at a precise value of liquid fraction ε^*, close to 36% for monodisperse bubbles, which has a well-defined physical explanation behind. It might be more intuitive to reason in terms of gas fraction: the critical value $\varphi^* \simeq 64\%$ geometrically corresponds to the random close packing of monodisperse hard spheres in a given volume. The critical liquid fraction ε^* will then mirror the empty space inside such disordered sphere packing.

Since the value 64% refers to perfectly monodisperse spheres, it slightly increases when accounting for a certain polydispersity, especially if the size distribution is bimodal as smaller spheres tend to fill up the empty space between larger ones [33].

But in general, the critical liquid fraction is the value at which the bubbles in the foam assume a spherical shape and physically corresponds to the vanishing of the so-called foam osmotic pressure.

2.3.1 The vanishing of the osmotic pressure

Let us consider a closed container with a semi-permeable membrane separating a volume V of foam from a reservoir of its solution, as sketched in figure 2.5. The membrane is permeable for the liquid in the foam, but impermeable for the gas bubbles. In order to obtain a gas fraction $\varphi > \varphi^*$ a force must be applied to the membrane, extracting some liquid out of the foam. The corresponding force per unit area exerted by the gas phase on the membrane is called osmotic pressure, in analogy to the usual osmotic pressure in the context of solutions as if the foam was a "solution" of bubbles [9]. However the physical origin behind this pressure is different. While in solutions the osmotic pressure is due to the entropy of the solute, in foams it arises because a wet foam has a lower surface energy than a dry foam [9].

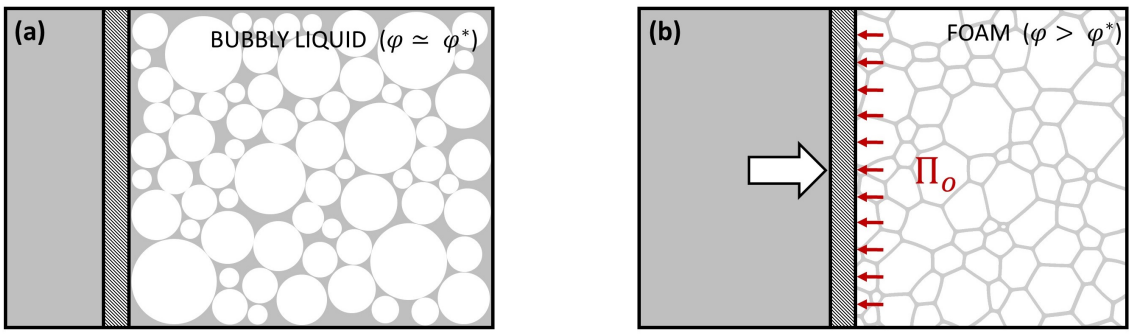

Figure 2.5 – **Osmotic pressure of foams.** One must apply a force to the semi-permeable membrane and overcome the osmotic pressure in order to extract liquid from a bubble dispersion (a) and make a foam increasing the total interfacial area (b)

Indeed, if we neglect gravity, so that φ can be considered homogeneous inside the foam, and the gas compressibility, the work required to extract a volume of liquid $\mathrm{d}V_{\mathrm{liq}}$ from the foam is determined by the change in the interfacial energy:

$$-\Pi_o \, \mathrm{d}V_{\mathrm{liq}} = \gamma d\Sigma \tag{2.5}$$

where Σ is the total area of interfaces. The variation in $\mathrm{d}V_{\mathrm{liq}}$ alters the foam gas fraction according to:

$$\frac{\mathrm{d}\varphi}{\mathrm{d}V_{\mathrm{liq}}} = \frac{\mathrm{d}}{\mathrm{d}V_{\mathrm{liq}}}\left(\frac{V_{\mathrm{gas}}}{V_{\mathrm{gas}}+V_{\mathrm{liq}}}\right) = -\frac{V_{\mathrm{gas}}}{(V_{\mathrm{gas}}+V_{\mathrm{liq}})^2} \tag{2.6}$$

thus we can write:

$$\mathrm{d}V_{\mathrm{liq}} = -\frac{\mathrm{d}\varphi}{V_{\mathrm{gas}}}(V_{\mathrm{gas}}+V_{\mathrm{liq}})^2 = -\frac{\mathrm{d}\varphi}{\varphi^2}V_{\mathrm{gas}} \tag{2.7}$$

Then, inserting this relation into equation (2.5) yields:

$$\Pi_o = \gamma\varphi^2 \frac{\mathrm{d}(\Sigma/V_{\mathrm{gas}})}{\mathrm{d}\varphi} \tag{2.8}$$

where Σ/V_{gas} is the surface area per unit volume of gas in the foam. If we write the total surface energy E of the foam as $E = \gamma\Sigma$, equation (2.8) can be written as:

$$\Pi_o = -\left(\frac{\partial E}{\partial V}\right)_{V_{\mathrm{gas}}} \tag{2.9}$$

At the gas volume fraction φ^*, corresponding to close packing, the bubbles are spherical, thus the surface energy density is minimum, and consequently the osmotic pressure vanishes: $\Pi_o(\varphi^*) = 0$. By contrast, Π_o increases as the foam gets drier and diverges to infinity as $\varphi \to 1$. Indeed, as φ is increased above φ^*, the bubbles deform and their surface area is larger than for spheres of equivalent volume. Thus, the foam prefers to suck liquid from the reservoir, in order to inflate the Plateau borders and make the bubbles rounder.

2.4 The role of surfactants

Foams do not form spontaneously, as dispersing gas in a liquid means creating new interfaces which requires energy. However, even if some energy is supplied to the system, for example by shaking, it is evident that not all liquids foam in the same way. Their foamability, namely their capacity to produce a foam, strongly depends on the liquid nature.

Being the energy cost for creating interfaces proportional to the surface tension, one might think that low surface tension values should improve the liquid foamability. However, a low surface tension alone does not ensure this, as freshly created interfaces need to be stabilised to avoid immediate bubble rupture.

Neighbouring bubbles within a foam are separated by liquid films having two gas/liquid interfaces each. If such interfaces are bare, the foam will be highly unstable: Laplace pressure gradients will draw the liquid from the film into the adjoining Plateau borders, thus the film starts thinning until it eventually breaks.

If we want the foam to last, molecules like surfactants must adsorb to the interfaces so that both sides of the liquid film will be covered by a monolayer of amphiphilic molecules which repel each other. Once the film reaches thicknesses of a few tens of nanometers, Van der Waals attractive forces are compensated by electrostatic repulsion if surfactants carry an electric charge, while at smaller thicknesses only short-range forces like steric repulsion dominate. The repulsive force can be thought of as an effective pressure inside the film, the *disjoining pressure*, which compensates for the Van der Waals attraction, leading to an enhanced stability of the film against thinning and subsequent rupture.

The adsorption dynamics also plays a fundamental role as new bubbles need to be covered with surfactants as quickly as possible, so if the adsorption is too slow, the foamability of the solution will still be poor [9].

Once the foam is formed and films have reached their equilibrium thickness, its stability against sudden rupture is enhanced if the thin films are elastic. In fact, when the liquid film is suddenly stretched, for example because of a bubble rearrangement, its surface increases and the expanded portion of the film will have a lower surface concentration of surfactants. This causes a local rise in surface tension which opposes to further expansions and produces an immediate contraction of the surface. Since the surface is coupled by viscous forces to the underlying liquid layers, this surface contraction induces a liquid flow from the low-tension to the high-tension region. This transport of liquid due to surface tension gradients is called Marangoni effect: it re-thickens the thin films and provides a resisting force to counteract film thinning and possible rupture. This effect only exists until the surfactant adsorption equilibrium is re-established in the film. If this adsorption occurs too fast, it can suppress the Marangoni effect, resulting in a reduced film stability.

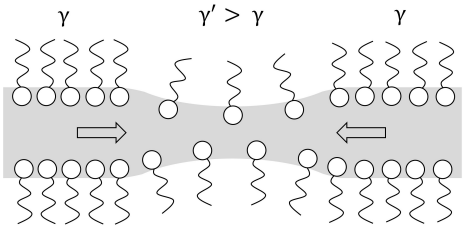

Figure 2.6 – **Marangoni effect.** Surface tension gradients arising after sudden film expansion induce a bulk liquid flow which fattens up the film and counteracts its thinning.

2.5 Foam ageing

In section §2.1 we have seen several applications of solid foams, which are obtained by solidifying a liquid foam precursor. As long as their continuous phase is liquid, foam systems are intrinsically unstable: a competition between different mechanisms can alter their structure over time and eventually lead to an irreversible foam damage. Indeed, liquid foams can undergo gravitational drainage, bubble coalescence and coarsening. The physics that lies behind each of these processes is very different, as they affect the foam structure at different length and time scales. However, a strong correlation exists between them and studying such mechanisms and their interplay is crucial for understanding and controlling foam stability. In the next subsections we shall briefly discuss the underlying mechanisms at the origin of these destabilising processes.

2.5.1 Drainage

The first mechanism that undermines foam stability is caused by gravity and strongly limits the lifetime of a liquid foam. Because of their density difference, the liquid and the gas phase of the foam tend to separate: so-called gravitational drainage makes the liquid flow downwards through the interstitial space among the bubbles. This way the liquid between the bubbles is gradually removed, resulting in a drier foam on top and a wetter foam on the bottom. A typical example of drainage effect is shown in figure 2.7.

Furthermore, gravity will cause the overall structure to rearrange, with bigger bubbles rising and smaller ones remaining at the bottom, leading to an actual bubble size sorting within the sample. However, this effect is partially limited by the yield stress of the foam: the bubble size has to be larger than a critical value in order for the buoyancy force to overcome the yield stress and make the bubble rise through the foam [126].

In dry foams, most of the liquid is contained inside the channels at which three thin films meet, thus liquid drainage occurs essentially through the network of Plateau borders and nodes [99]. Such gravity-driven liquid flow is typically counteracted by the osmotic pressure, which opposes to liquid removal between bubbles as seen in section §2.3. Indeed, the liquid can also flow because of capillary effects: in the dry part of the foam, the curvature of the Plateau borders is higher than in the wetter part, thus the Laplace pressure difference induces a capillary suction that tends to bring liquid from wet to dry regions, smoothing out the vertical liquid fraction gradients.

This also explains why drainage does not make all the liquid leak out of a foam. A draining foam sitting on a liquid bath will eventually reach a final equilibrium state where drainage halts. This happens when the hydrostatic pressure is perfectly counterbalanced by capillarity [80].

The liquid flow is also hindered by the viscous processes taking place within the channels and nodes. These depend on the interfacial rheology of the foam liquid phase, thus the physical chemistry of the foam components matters. However, its effect remains small compared to the one obtainable by changing the physical parameters: the liquid flow velocity is more affected by a variation of the bubble size or the liquid fraction than of the surface shear viscosity [99]. The viscous damping is in fact more efficient when the size of the Plateau borders and nodes are smaller, which means that, for a given liquid fraction, drainage is slower if the foam is made of smaller bubbles.

Since drainage quickly changes the spatial liquid distribution inside the foam, it is easy to conceive why such process can be a strong limitation to applications and experimental studies of foams: an uneven liquid distribution translates into an heterogeneity of mechanical properties as well as stability against the other two destabilising mechanisms, which are film rupture and foam ripening. A smart way to experimentally mitigate gravity effects is the so-called forced drainage, where the foam is constantly wet from the top with a controlled amount of foaming solution in order to keep the liquid fraction constant and homogeneous inside the sample [63].

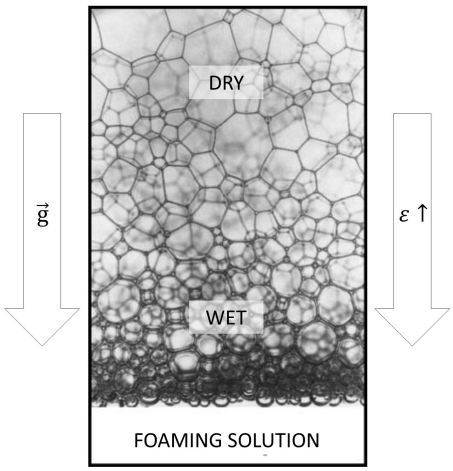

Figure 2.7 – **Gravitational drainage.** Gravity gradually removes the liquid between the bubbles, making the foam drier on top and wetter at the bottom. The bubbles on the bottom are smaller than the ones on the top because of the buoyancy of larger bubbles combined with a faster ageing where the foam is drier. Picture adapted from [99]

2.5.2 Coalescence

When the thin liquid film separating two adjacent bubbles suddenly breaks, the two bubbles are said to coalesce as they merge into a single larger one. As such events typically occur in avalanches, the ultimate result of coalescence is a sudden reduction of the total number of bubbles inside the sample. If the foam is in direct contact with the environment, then coalescence also leads to a loss of gas from the breakup of boundary bubbles, so that the total dispersed volume decreases until the foam completely disappears.

The importance in understanding the mechanisms at play that trigger this phenomenon is thus evident, as it can rapidly lead to a complete foam destruction.

Nevertheless, despite several hypothesis having been developed to explain its origin [95, 72], this process is still poorly understood: its extreme rapidity and its coupling to other mechanisms like gravitational drainage, diffusive bubble growth or evaporation, make coalescence really hard to investigate experimentally.

Coalescence can be induced by mechanical solicitations but also by thermodynamic fluctuations, which make it a stochastic process. Intuitively, large bubbles would seem more fragile than smaller ones, suggesting a film rupture probability simply proportional to its surface area.

However, experiments performed in draining aqueous foams pointed out a dramatic increase of the coalescence rate as soon as the liquid fraction decreases below a critical value, depending on the surfactant type and its concentration, but not on the bubble size [10]. They suggested that the initiation of such avalanches could be attributed to the film dilatation occurring during bubble rearrangements: when the liquid fraction becomes too low, the relative increase of interfacial area is too fast to be readily stabilised by surfactants [10].

Other studies suggested the existence of a critical capillary pressure at which film rupture is induced [95]. However, recent experiments in bubble monolayers in which capillary pressure and bubble size could be independently varied have shown that the probability of coalescence events is proportional to the film area, thus showing that the parameter controlling coalescence is the bubble size rather than the capillary pressure [35].

2.5.3 Coarsening

Gravitational drainage and bubble coalescence are not the only mechanisms which can damage the foam: even when those are negligible, a third process can modify the foam structure in the long run.

As any gas is partially soluble in any liquid, the foam liquid phase does not act as a total barrier to the gas inside the bubbles. The Laplace pressure difference existing between bubbles of different size makes the gas diffuse from smaller bubbles to larger ones. Small bubbles will then lose their gas to the neighbours, so they will shrink until they disappear, leading to a decrease of the total number of bubbles over time and to an increase of the average size of the bubbles left. The final effect could thus resemble the one of coalescence, even though the physical process is completely different.

Since the gas has to diffuse through the foam liquid phase, the coarsening rate is strongly affected by the physical chemistry of the foam components [6], but a crucial role is played in the first place by the foam liquid fraction. In fact, if the foam is dry, the gas will diffuse through the thin films separating adjacent bubbles, and in this case it has been shown that bubble topology plays a fundamental role in deciding which bubbles grow or shrink [120]. The presence of such thin films makes the coarsening faster than in bubbly liquids, where the gas diffusion between non-touching bubbles is mediated by the bulk liquid phase which acts as a gas reservoir. While this mechanism is well understood for the two limits of very dry foams and bubbly liquids, how the coarsening rate changes with an increasing liquid fraction in moderately wet foams is still an open question, although experimental data exist [64, 89].

Because of its dependency on the liquid fraction, it is easy to imagine how the coarsening process is strongly correlated with drainage. Indeed, since drainage modifies the vertical distribution of the liquid fraction, the coarsening rate will not be homogeneous inside the foam sample: if they do not burst first, the drier bubbles on top will coarsen faster than the wetter ones on the bottom.

This pressure-driven coarsening process has been widely studied in aqueous foams and froths, both theoretically and experimentally. Since this mechanism is the main focus of this work, an in-depth review of its features in aqueous foams will be the subject of chapter §4. On the other hand, how foam coarsening is affected when the aqueous phase is replaced with a complex fluid still lacks a thorough understanding, and the current state of the art will be discussed in chapter §5.

3 2D and quasi-2D foams

In the previous chapter we saw how three-dimensional foams are hard to study experimentally mainly because of gravitational drainage, which rapidly makes the liquid fraction uneven inside the foam sample. Moreover, the light backscattering from the inner interfaces gives foams their typical turbidity, so that measuring the bubble size by imaging the foam surface can be a hard task. In this chapter we shall introduce a special kind of foams which strongly simplify their investigation and which have thereby been for many years the traditional framework for studying the physics of such systems: two-dimensional foams. We shall distinguish between purely two-dimensional foams, typically considered in simulations, and the real-world case of bubble monolayers called quasi-2D foams. We shall present the main features of their structure and the influence of an increasing liquid fraction in both cases.

3.1 Ideal 2D foams

A purely 2D dry foam is a partition of a plane into polygonal cells of area A representing the bubbles. As in three dimensions, the bubble pattern is not disordered, as its structure is dictated by the minimisation of energy.

We start by considering an ideal foam, namely a very dry foam which is at mechanical equilibrium and for which the energy is proportional to the amount of interfaces. Since we have only two dimensions, we can define the line tension λ as the equivalent of the surface tension γ in 3D, so that the total energy can be written as $E = \lambda L_{\text{int}}$, where L_{int} is the total length of interfaces, namely the total bubble perimeter.

An adaptation of Plateau's laws in two dimensions then state that the thin films between bubbles are represented by lines of zero thickness and constant curvature, having a line tension 2λ, which meet in three at bubble vertices at angles of 120°.

Concerning the topology of these patterns, the number of polygons N, sides S and vertices V are linked by the following Euler's relation $N - S + V = 2$. This equation, combined with the laws of Plateau, leads to the conclusion that for an infinite ideal 2D foam the average number of sides n per polygon is six. However, in a foam having a large but finite number of bubbles N, border effects result into an actual value of $\langle n \rangle$ slightly lower than six, as a correction of the order of $1/N$ must be subtracted. This rule does not fix the number of sides of each single bubble, but only its average, which means that if there are bubbles with 5 sides or less, there must be also some with 7 sides or more. But clearly, if the foam is perfectly monodisperse, the bubble pattern will have a ordered honeycomb structure. One can define the topological charge of a bubble as the quantity $q_t = 6 - n$ to describe its difference from a hexagon. The average of q_t over the entire foam is zero, or very small for a large number of bubbles as it is of the order of $1/N$.

If the amount of liquid in the foam starts to be no longer negligible, we can define the liquid fraction of a 2D foam as the ratio between the area occupied by the liquid and the total foam area, namely $\varepsilon_{2D} = A_{liq}/A_{foam}$. The liquid will accumulate at the Plateau borders at each bubble vertices, which will then become small concave triangles. A gradual increase of ε_{2D} will evidently affect the foam structure, as discussed later in section §3.3.

3.2 Quasi-2D foams

Purely 2D foams are only ideal systems, as real foams always have a thickness larger than zero. However, the closest experimental counterpart to 2D foams is provided by the so-called quasi-two-dimensional foams, consisting of a single layer of bubbles. Quasi-2D foams have been for many years the standard system for experimental foam studies, from coarsening [47] to coalescence [35] to rheology [78]. Indeed, in contrast to 3D foams, they offer the advantage of not being significantly affected by gravitational drainage, and the possibility to observe each single bubble, which strongly simplifies the experimental characterisation of foam behaviour. As long as these quasi-2D foams are rather dry, their behaviour is well described by the one of the corresponding 2D foam given by the cross-section through a horizontal cut in the middle of the bubble monolayer.

3.2.1 Configurations and 3D structure

If the foam is not too polydisperse it is possible for the bubbles to be arranged in a single layer. These quasi-2D foams can be experimentally realised in three different configurations, as depicted in figure 3.1. One can obtain a bubble monolayer by sandwiching a foam between two parallel rigid plates with a spacing smaller than the bubble size. This plate-plate configuration is called Hele-Shaw cell [9] and is the most common experimental configuration as it allows the best control (and definition) of the foam liquid fraction.

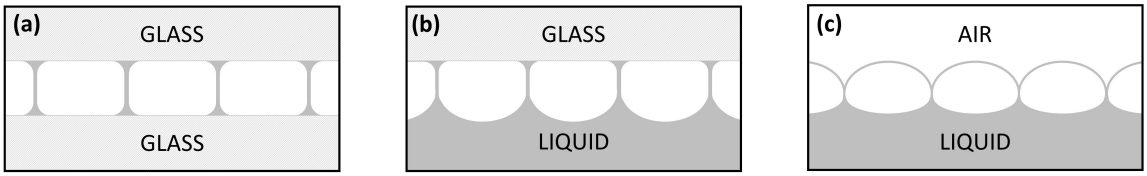

Figure 3.1 – **Quasi-2D foam configurations.** (a) Hele-Shaw cell: a bubble monolayer sandwiched between two parallel plates. (b) Plate-liquid configuration: bubbles floating upon a liquid but pressed down by a top rigid plate. (c) Bubble raft: bubbles floating upon a liquid and directly in contact with air.

Nevertheless, one could observe a quasi-2D foam in a plate-liquid configuration, namely a layer of bubbles floating upon their foaming solution with a horizontal rigid plate pressed on them. There is now a meniscus at the bottom of the foam, the height of which is determined by the balance between surface tension and gravity.

Finally, if we further open this configuration by removing the top plate and leaving the bubbles directly in contact with air, we obtain what is typically called a bubble raft. In the latter two configurations one cannot define a liquid fraction but can only give some effective measure of the liquid content, because of the presence of liquid reservoir beneath

the bubbles. The liquid distribution in each case has been numerically studied with Surface Evolver simulations for arrays of hexagonal bubbles [18].

Let us focus on the plate-plate configuration, which is the one that will be used in the experiments of chapters §6 and §7. When viewed from the top, a dry quasi-2D foam highly resembles its purely 2D counterpart: bubbles have a polygonal shape, whose sides correspond to films and vertices to vertical Plateau borders. In fact, due to their non-zero thickness, such systems have a three-dimensional structure, as it can be seen from figure 3.2 (a). In this configuration, Plateau borders are formed at the three-fold junctions between vertical films but also where these films meet the plates. We can thus distinguish the vertical internal Plateau borders, which vertically span the gap between the plates at each bubble vertex, from the surface external Plateau borders, which spread out horizontally on the top and bottom glass plates, as shown in figure 3.2 (b). Thus what one sees from the top are not the thin vertical films but the corresponding top surface Plateau borders. Moreover, surface Plateau borders are not the only contact between the foam liquid and the glass plate: each bubble wets both top and bottom glass surfaces with horizontal pseudo-films.

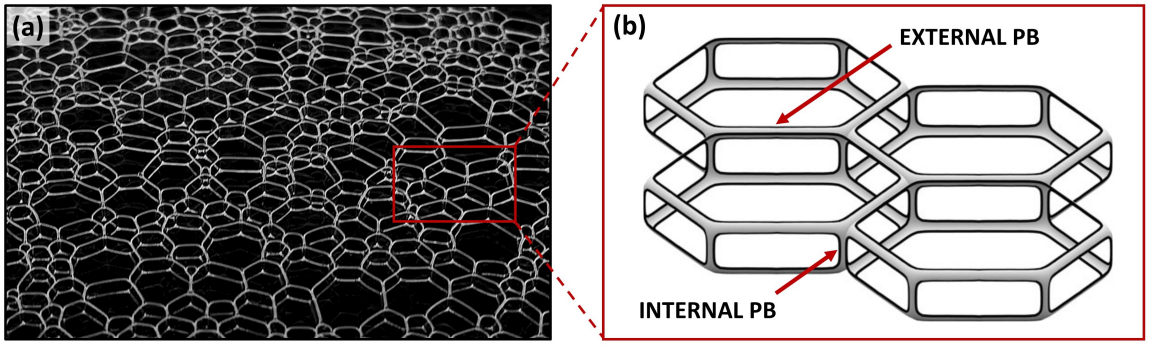

Figure 3.2 – **Quasi-2D foam structure.** (a) Perspective view of a bubble monolayer in a plate-plate configuration. One can distinguish the three-dimensional structure due to their non-zero thickness. (b) Internal and external Plateau borders. Picture taken from [42].

3.2.2 Liquid fraction definitions

Unlike the case of three-dimensional foams, there is no univocal definition of liquid fraction in quasi-2D systems. One could take the area fraction of liquid in a horizontal cut through the bubble monolayer, as it is the closest to the liquid fraction ε_{2D} defined for an ideal 2D foam in section §3.1 and typically used in simulations [37]. However, this is not easy to measure experimentally.

By contrast, the surface liquid fraction ε_s, namely the portion of the glass surface wetted by the external Plateau borders, is usually considered in experiments as it is easily measurable from the foam pictures [38, 70]. Since the imaging of the foam surface depends on the illumination, for an accurate measure of ε_s one should use a prism to collect the light reflected from the foam surface at an angle of 45°. Indeed, this way only the light reflected from the flat film wetting the glass surface is collected by the camera, whereas the light reflected by curved interfaces is not detected, and this ensures that the real size of the surface Plateau borders is not underestimated [36].

However, in a closed glass-glass configuration, one can also define the liquid fraction

similarly to the one of 3D foams as the volume fraction of liquid inside the cell $\varepsilon = V_{\text{liq}}/V_{\text{foam}}$. A relation that links the surface liquid fraction ε_s to the volume liquid fraction ε has been proposed for monodisperse quasi-2D foams made of hexagonal bubbles [18], while how ε_s is linked to ε in 3D foams has been proven both theoretically and experimentally [36].

We highlight that these three definitions would coincide only if bubbles were right prisms or cylinders, which is not the case of real quasi-2D foams because of the presence of Plateau borders, as seen in section §3.2.1. Typically $\varepsilon_{2\text{D}} < \varepsilon < \varepsilon_s$.

Particular attention must therefore be paid to which of such definitions authors refer to when assuming a *constant* liquid fraction in the literature.

3.3 From dry to wet: the decoration lemma and beyond

In this section, we shall give a "static" description of how the structure of purely-2D and quasi-2D foam systems change as we increase their wetness, with a special attention to the definition of the liquid fraction in each case.

3.3.1 The decoration lemma

As long as real quasi-2D foams are dry, they are expected to be well-described by their ideal 2D counterpart, both in structure and in behaviour. However, first experiments on the coarsening of dry quasi-2D foams [47] pointed out a structural difference which was apparently breaking one of the laws of Plateau: the angle between the films at the vertices was observed to be different from 120° and the average internal angle of bubbles was found to be varying with their number of sides [48, 108].

The origin of this discrepancy between theory and experiments was soon explained by introducing the so-called *decoration lemma* [123, 5].

The lemma states that the lines which adjoin a triangular Plateau border, which we recall are circular arcs, may be continued with the same curvature to meet at a single point, and they do so at angles of 120° [5]. An immediate consequence of this lemma is that, to account for a non-negligible liquid fraction, an ideal foam structure can be simply decorated with Plateau borders by inserting an appropriate 3-sided border on top of each of its vertices, as depicted in figure 3.3. The lemma is proven to be valid only if there is no overlap between Plateau borders on adjacent vertices, thus if only triangular Plateau borders are present, and cannot be generalised to the case of Plateau borders with more than three sides.

The discrepancies observed in [48, 108] thus arose from the experimental measure of the angles as the ones between the tangents at the points where films meet the Plateau border, thereby missing that part of the angle which results from extending the bubble edges to meet at a point at the centre of the border [5].

The importance of this lemma will be evident when talking about the asymptotic self-similar regime of coarsening 2D foams in section §4.4, as it has been experimentally shown that, as long as this lemma holds, the geometrical and topological features of a quasi-2D bubble pattern in its scaling state are independent of the liquid fraction [97].

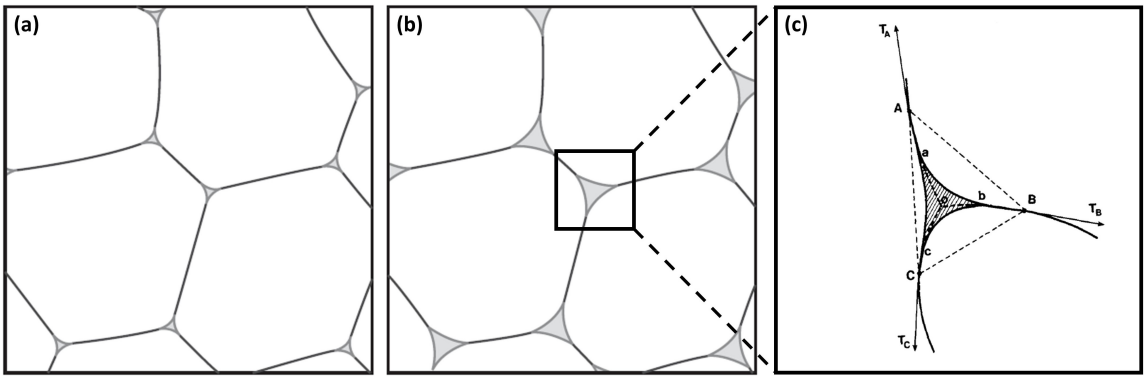

Figure 3.3 – **Decoration lemma.** (a,b) When the liquid fraction increases, the structure of the foam remains the same as the ideal one just decorated with triangular Plateau borders at each bubble vertex. Pictures adapted from [9]. (c) The films join at the centre of the 3-sided Plateau border at angles of 120° if they are prolonged with the same curvature, while the angles between the tangents at points A, B and C clearly differ from 120°. Picture adapted from [5].

3.3.2 The rigidity loss transition in 2D

At negligible liquid fraction, $\varepsilon_{2\mathrm{D}} \simeq 0$, we saw that 2D foams are arrays of polygonal bubbles, as shown in figure 3.4 (a), and then as we increase $\varepsilon_{2\mathrm{D}}$, the liquid starts accumulating at the bubble vertices, namely the 2D Plateau borders, assuming the shape of concave triangles. A further increase of $\varepsilon_{2\mathrm{D}}$ will then cause some of these triangular vertices to merge, leading to the appearance of n-sided Plateau borders with $n > 3$: where this occurs, as in figure 3.4 (b,c), the contact between the adjacent bubbles is lost. If we keep adding liquid, the bubbles gradually lose their polygonal shape and start resembling squashed circles, and once a critical value $\varepsilon^*_{2\mathrm{D}}$ is reached, the contact between all bubbles is lost. At this point the bubbles become perfectly circular, and we have the 2D equivalent of a bubbly liquid. It has been shown that this transition occurs at the critical value $\varepsilon^*_{2\mathrm{D}} \simeq 16\%$ [4], which corresponds to the empty space left among a random close packing of hard disks [2, 122]. This value holds for both monodisperse and rather polydisperse systems as long as the size ratio between the largest and the smallest disk remains below 6.46: at larger ratios the smaller objects can fit within the cavity left between three larger ones and the critical value $\varepsilon^*_{2\mathrm{D}}$ can be lower [2].

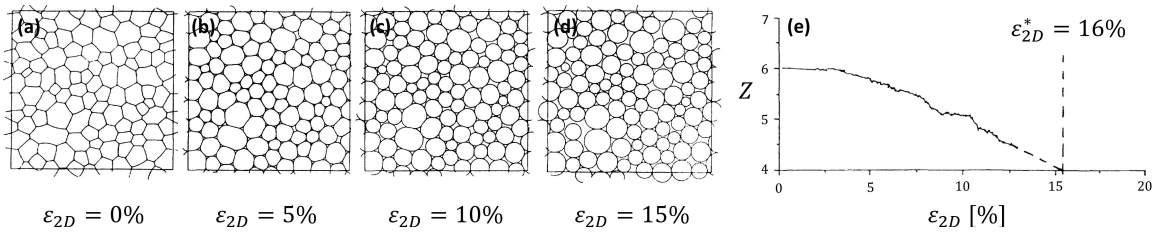

Figure 3.4 – **Rigidity loss transition of 2D foams.** (a-d) 2D foam structure at different liquid fractions $\varepsilon_{2\mathrm{D}}$: note the appearance of many-sided Plateau borders already at $\varepsilon_{2\mathrm{D}}$=5%. (e) Decrease of the mean bubble coordination number Z from 6 to 4 with increasing $\varepsilon_{2\mathrm{D}}$. Pictures adapted from [4].

After the appearance of many-sided Plateau borders, it becomes meaningless to consider the number of neighbours of a bubble and one should rather talk about its coordination number Z. The coordination number accounts only for the neighbours which actually touch the bubble, namely it is the bubble number of real contacts. As shown in figure 3.4 (e), the mean coordination number remains equal to six as long as ε_{2D} is sufficiently low so that all Plateau borders are triangular, but then, as we further increase ε_{2D}, Z gradually drops down to the value 4 at ε^*_{2D} [4], which is once again in perfect analogy with the mean coordination number of random hard disks [2, 122]. They also show that ε^*_{2D} corresponds to the vanishing of the foam yield stress, thus to its rigidity loss transition.

3.3.3 Film disappearance in quasi-2D foams

The transition from dry to wet quasi-2D foams needs to account for their 3D structure and thus deserves a separate description. Let us consider a monodisperse bubble monolayer confined within two parallel plates with a fixed spacing d. If the foam is rather dry, the surface Plateau borders will be so thin to be negligible and the bubbles will resemble an array of hexagonal floor tiles, whose cross section is sketched in figure 3.5 (a).

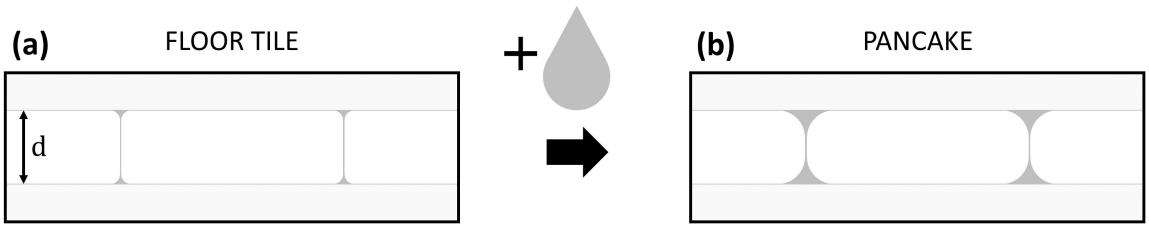

Figure 3.5 – **Floor tile and pancake configurations.** An increase of the foam liquid fraction in a closed Hele-Shaw cell thickens the Plateau borders and makes the bubbles change from a floor-tile (a) to a pancake (b) shape.

If we now imagine to gradually add some liquid to the same foam, namely to increase its volume liquid fraction ε without changing the gap d, both surface and vertical Plateau borders will inflate and the bubbles start assuming a pancake shape, like the one shown in figure 3.5 (b). Let us call r_{PB} the radius of curvature of the surface Plateau borders. Since the separation d between the plates is fixed, the surface Plateau borders can grow up to a maximum value of r_{PB} corresponding to half the spacing between the plates, namely $r^{max}_{PB} = d/2$. When this happens, the height of the thin films between adjacent bubbles will be equal to zero, thus the bubble contact is lost as the film area vanishes.

The liquid distribution between monodisperse bubbles in a closed Hele-Shaw cell has been numerically studied with Surface Evolver simulations in different conditions by varying the system parameters such as the liquid fraction, the bubble size and the plate separation [18].

It has been shown that the area A_v of the vertical thin films that separate adjacent bubbles depends on the liquid fraction ε and on the ratio between the gap d and the bubble size L taken as the length of the hexagonal bubble edge, as sketched in figure 3.6.

More precisely, from figure 3.6, we can see that the film area A_v shrinks with increasing liquid fraction ε at fixed d/L, until it vanishes at a critical value ε^* that marks the rigidity loss transition. While this is rather intuitive, it is worth highlighting that ε^* depends on the ratio d/L, as shown in the inset. Indeed, A_v is also found to decrease with decreasing

d/L at a given ε. This means that, for a fixed liquid fraction and a fixed plate separation, an increase of the bubble size gradually reduces the vertical film area, and there exist a critical bubble size at which A_v eventually vanishes.

Since these simulations were carried out on monodisperse bubble patterns, the disappearance of vertical films occurs simultaneously for each bubble. This is not the case if the foam is rather polydisperse: as either the liquid fraction ε or the average bubble size $\langle L \rangle$ are increased at a fixed gap d, only part of the bubbles will lose the films, depending on their size, so such a transition will be less sharp.

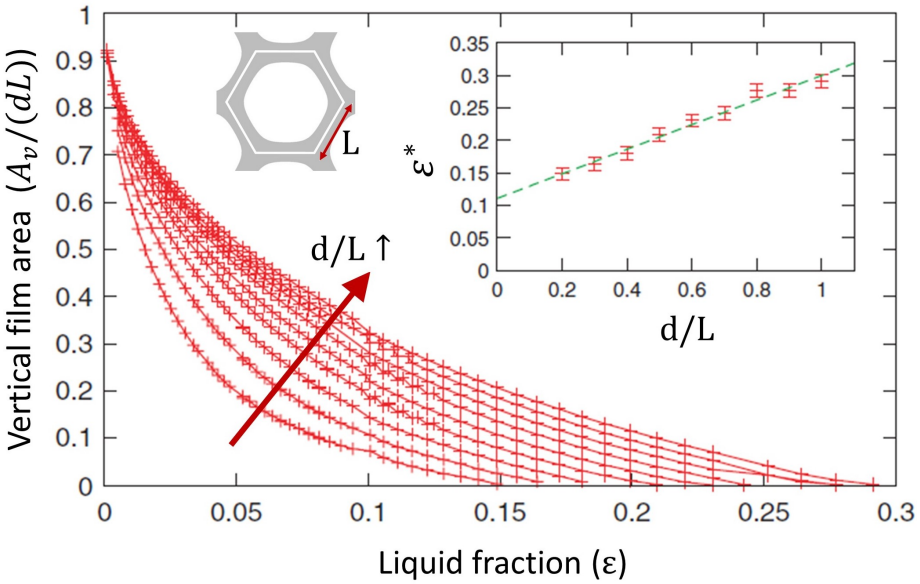

Figure 3.6 – **Vertical film disappearance in a closed quasi-2D foam.** The area of vertical films A_v in a closed Hele-Shaw cell depends on the liquid fraction ε and on the ratio between the gap and the bubble size d/L. The critical liquid fraction ε^* at which the films vanish also depends on the ratio d/L. Picture adapted from [18].

4 Foam coarsening

In section §2.5.3 we anticipated that liquid bubble dispersions can undergo a pressure-driven ripening mechanism through which they evolve towards thermodynamic equilibrium, corresponding to a complete phase separation. By this process, which will be the object of our experimental investigations, small higher-pressure bubbles shrink as they lose their gas to larger lower-pressure ones, whereas the latter grow, resulting in an increase of the average bubble size over time. In this chapter we shall first describe this coarsening process in the two extreme cases of dry foams and bubbly liquids, and see how in both cases the system asymptotically tends towards a self-similar regime in which the average bubble size grows in time as a power law. We will explain how foam coarsening induces bubble rearrangements and their importance for reaching the scaling state. We will finally see how coarsening of moderately wet foams still lacks a full characterisation by reviewing the current state of the art and highlighting the main questions which are still unanswered. Along the chapter we shall mainly focus on 2D and quasi-2D systems, making a parallel to 3D foams whenever possible.

4.1 The dry limit

4.1.1 2D foams

It has been shown that the coarsening of ideal 2D foams, in which adjacent bubbles are separated by soap films of zero thickness, is governed by the topology of the bubble pattern, namely whether a bubble shrinks or grows is determined only by its number of neighbours [120] and not at all by its size or shape.

Let us consider a single bubble i in contact with n neighbouring bubbles j, and let us define its geometrical charge as the quantity:

$$q = \sum_{j=1}^{n} k_{ij} l_{ij} \tag{4.1}$$

where k_{ij} is the curvature of the edge ij, taken as positive if the centre of curvature is towards the bubble i, and l_{ij} is its length. The dimensionless quantity q basically represents the angle at which it is necessary to curve the sides so that they all meet at an angle of 120° at each vertex, and it is proportional to the topological charge $q_t = 6 - n$ defined in §3.1, according to the relation:

$$q = \sum_{j=1}^{n} k_{ij} l_{ij} = \frac{\pi}{3}(6 - n) = \frac{\pi}{3} q_t \tag{4.2}$$

This equation describes the link between the number of sides of a bubble and its shape, as it fixes the sign of the edge curvature depending on the sign of the term $6 - n$. Indeed, as shown in figure 4.1, bubbles with less than six sides have a positive geometric charge, consequently they have convex sides on average. By contrast, bubbles with more than six sides have a negative geometric charge, so their sides are concave. Finally, if all the bubble edges are flat, then it must be hexagonal, while the reverse statement is not true as hexagonal bubbles can have both convex and concave sides, as long as the sum of the single terms $k_{ij}l_{ij}$ is zero [9].

We saw in section §1.2 that, according to the law of Laplace, the pressure difference existing between the two sides of an edge ij is proportional to its curvature k_{ij}, which is constant along the edge as stated by the first Plateau's law. Thus, a fundamental equation due to Von Neumann links the internal bubble pressure to its shape and to its number of neighbours as follows [120]:

$$\sum_{j=1}^{n} \frac{e}{2\lambda}(P_i - P_j)l_{ij} = \sum_{j=1}^{n} k_{ij}l_{ij} = \frac{\pi}{3}(6 - n) = q \tag{4.3}$$

where e is the thickness of the 2D foam and λ is the line tension. Therefore, bubbles with positive geometric charge, namely with $n < 6$, will have a higher pressure than the average of their neighbours, while bubbles with more than six sides will have a lower pressure than their neighbours. This implies that if the gas can diffuse through the thin liquid films, it will go from bubbles with less sides to neighbouring bubbles having a larger number of sides.

Indeed, if the gas diffuses from the bubble i to a neighbouring bubble j only through the film ij, the gas flux will be proportional to $l_{ij}(P_i - P_j)$, that is the product of the driving force (the pressure difference) and the size of the region of gas exchange (the length of the film). If this flux is positive, the amount of gas contained in the bubble i will decrease over time, and so will its area. The global variation of the bubble area A_i will thereby be proportional to the sum of the gas fluxes through all its n edges, namely we can write:

$$\frac{\mathrm{d}A_i}{\mathrm{d}t} = -\kappa \sum_{j=1}^{n} l_{ij}(P_i - P_j) \tag{4.4}$$

where the constant of proportionality κ describes the gas permeability of the thin liquid films and it is the same for each of them. By combining this relation with equation (4.3) we then obtain the famous Von Neumann's law, which relates the evolution of the bubble i to its topology as follows:

$$\frac{\mathrm{d}A_i}{\mathrm{d}t} = -D_{\mathrm{eff}}\, q = \frac{\pi}{3} D_{\mathrm{eff}}(n - 6) \tag{4.5}$$

where the positive term D_{eff}, called *effective diffusion coefficient*, encloses all the physico-chemical properties of the foam. Equation (4.5) implies that bubbles with less than six sides will lose their gas to adjacent bubbles having more than six sides.

It has been shown that this law, together with the assumption of time-independent statistical foam properties, results in a linear growth also of the mean bubble area for an ideal 2D foam $\langle A \rangle \sim t$ [87], and thus the mean radius is expected to grow in time as $\langle R \rangle \sim t^{1/2}$.

Equation (4.5) has been experimentally proved to hold only for very dry quasi-2D foams,

where the excess of liquid was allowed to drain [107]. When the liquid fraction is not negligible, the presence of Plateau borders makes this law no longer valid locally, but still holding on average, which means that we can even observe single five-sided bubbles growing or seven-sided bubbles shrinking depending on their actual shape [97, 14].

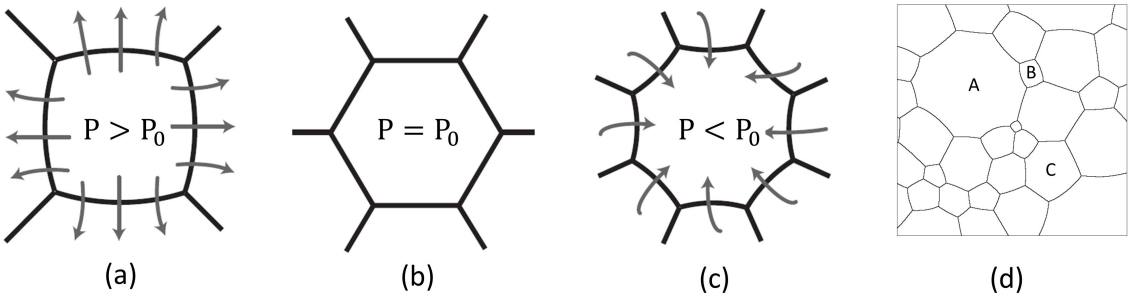

Figure 4.1 – **Link between bubble shape and pressure.** (a) An example of 4-sided bubble having convex sides. Its pressure will be higher than the average pressure of its neighbours P_0 and thus it will shrink. (b) A bubble with all its edges flat must have six sides and its pressure will be equal to P_0. (c) An example of growing 8-sided bubble having concave sides and thus pressure lower than P_0. Pictures adapted from [9]. (d) Bubbles in a foam. While bubbles A and B have all sides with the same curvature sign, bubble C exhibits both convex and concave sides but its geometrical charge q is zero as it has $n = 6$. Indeed, n-sided bubbles can have both concave and convex sides, as it can be seen in the picture, but their global geometrical charge will be positive or negative depending only on their number of sides.

4.1.2 3D foams

While in ideal 2D foams Von Neumann relationship states that the bubble growth rate is an exact function of its number of sides, this result cannot be generalised exactly as it is in three dimensions. However, the flux of gas across a film will still be proportional to the pressure difference between its two sides and the global bubble volume variation will be given by the sum of the gas fluxes trough each of its facets. A law describing the mean volume variation of bubbles with n facets in the dry limit was proposed by Mullins [88, 86]:

$$\frac{\mathrm{d}V_n}{\mathrm{d}t} = -D_{\mathrm{eff}} V_n^{1/3} G(n) \tag{4.6}$$

where the effective diffusion coefficient D_{eff} is the same as in 2D and $G(n)$ is an average geometric charge of all the bubbles with n facets in the foam, which is not a simple linear function of n [61]. It has been mathematically proven that bubbles with more than 13 facets grow, whereas bubbles with $n < 13$ gradually shrink [86]. Since large bubbles have statistically more facets than small ones, in a foam the largest bubbles will grow and the smallest ones will shrink and eventually perish, leading to a reduction of the total number of bubbles and a consequent increase of the average volume of the bubbles left.

Equation (4.6) holds under the assumption of statistical self-similarity, for which successive configurations developed by the coarsening foam are geometrically and topologically similar [88], as explained in more detail in section §4.4. After a certain time that depends

on the initial foam configuration, coarsening foams reach an asymptotic regime in which this is true and in which the mean bubble radius $\langle R \rangle$ grows in time according to:

$$\langle R(t) \rangle^2 = \langle R(t_0) \rangle^2 + K(t - t_0) \tag{4.7}$$

where the parameter K depends not only on D_{eff} but also on the bubble size distribution. From equation (4.7) we can see that in the dry limit the average bubble size grows as $\langle R(t) \rangle \sim t^{1/2}$.

4.2 The influence of the physical chemistry

The chemical composition of the gas and liquid phases of the foam plays a fundamental role in its ripening [6], as it directly affects the coarsening rate through the effective diffusion coefficient D_{eff}. This coefficient, which appears in equations (4.5) and (4.6), is the same in 2D and in 3D and includes all the physico-chemical properties of the foam.

Indeed, D_{eff} is proportional to the rate of gas diffusion D_f but it is also related to several other parameters as follows:

$$D_{\text{eff}} = \frac{2\, D_f\, He\, \gamma\, V_m}{h}\, a(\varepsilon) \tag{4.8}$$

where He is the Henry coefficient, which reflects the solubility of the gas in the liquid phase, V_m is the molar volume of the gas at ambient temperature and pressure, γ is the surface tension of the foaming solution and h is the actual film thickness.

From equation (4.8) we can see that D_{eff} is proportional to the quantity $\kappa = D_f He/h$ which is what is called film permeability, and quantifies how easily the gas can diffuse through the thin film between two adjacent bubbles.

Moreover, we can see that surfactants can affect the coarsening rate mainly through the surface tension γ and the film thickness h, the latter being determined by the disjoining pressure [9].

The term $a(\varepsilon)$ appearing in equation (4.8) is a dimensionless geometric parameter which quantifies in which proportion the bubble is covered by thin films rather than Plateau borders, and clearly depends on the foam liquid fraction [9]. Indeed, it is mainly through the film surface that gas diffuses from bubble to bubble, since diffusion across Plateau borders is much slower as they are several orders of magnitude thicker. However, while in rather dry foams the contribution of gas diffusion through the Plateau borders can be reasonably neglected [97], this is no longer true in moderately wet foams where the bulk contribution must be taken into account [104], as we shall see in section §4.6.

4.3 The wet limit

We now consider the coarsening process in the opposite limit of a bubbly liquid, namely a dilute dispersion of well-separated spherical bubbles, like the one sketched in figure 4.2.

Since the bubbles no longer touch each other, the gas diffusion has to be mediated by the bulk liquid around them, that acts as a gas reservoir in which small bubbles supply gas and large bubbles remove it. This process is often called Ostwald or Lifshitz–Slyozov–Wagner ripening, and it has been described for dispersions in the limit of ε approaching 100% [77, 121].

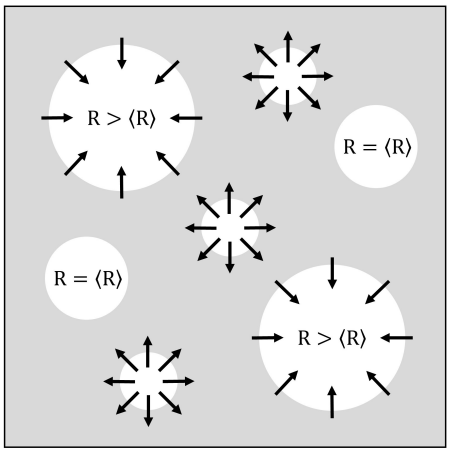

Figure 4.2 – **Ostwald ripening.** In bubbly liquids, bubbles smaller than the average size $\langle R \rangle$ supply their gas to the liquid and shrink, while bubbles larger than $\langle R \rangle$ remove it from the liquid and grow. The black arrows represent the gas flux.

It has been shown that in this dilute regime, the radius of a single bubble evolves in time according to:

$$\frac{\mathrm{d}R}{\mathrm{d}t} = \frac{1}{4\pi R^2}\frac{\mathrm{d}V}{\mathrm{d}t} = \frac{He D_f P_0 V_m}{R}\left(s - \frac{2\gamma}{P_0 R}\right) \tag{4.9}$$

where He is the Henry constant, D_f is the gas diffusion coefficient, P_0 is the reference pressure, V_m is the gas molar volume and $s = (c_\infty - c_0)/c_0$ is the saturation parameter. Thus for every bubble having $s > 0$ there exists a critical radius $R_s = 2\gamma/sP_0$ at which a gas bubble is in equilibrium with the solution, namely $\mathrm{d}R/\mathrm{d}t = 0$. By contrast, if $R > R_s$ the bubble takes gas from the liquid and thus grows over time, whereas it shrinks if $R < R_s$. It has been shown that this critical value R_s corresponds to the average bubble size $\langle R \rangle \equiv R_s$ [77, 121], so that the previous equation can be rewritten as:

$$\frac{\mathrm{d}R}{\mathrm{d}t} = \frac{K}{R}\left(\frac{1}{\langle R \rangle} - \frac{1}{R}\right) \tag{4.10}$$

where $K = 2\gamma He D_f V_m$. Large bubbles will thus grow at the expense of small ones, leading to a gradual increase of the average bubble size in the system. It has been shown that the average bubble size growth will asymptotically tend to the following expression [77, 121]:

$$\langle R(t) \rangle = \left(\frac{4}{9}Kt\right)^{1/3} \sim t^{1/3} \tag{4.11}$$

which holds both in 2D and 3D but only for very dilute systems, in which interactions between bubbles are negligible.

4.4 Self-similar growth regime

In both two and three dimensions, bubble dispersions in the dry and wet limits are expected to eventually reach a scaling state, in which the average bubble size $\langle R \rangle$ grows in time as

a power law $\langle R \rangle \sim t^{\beta}$, with an exponent β depending on how the gas diffuses between the bubbles, and thus on the liquid fraction. In the dry limit, we saw that the gas diffusion occurring through the thin films between neighbouring bubbles results in an exponent $\beta = 1/2$. By contrast, in the wet limit where gas diffusion has to be mediated by the bulk liquid phase, a constant volume growth rate is expected, resulting in $\beta = 1/3$ for the average radius evolution over time.

The foam in its scaling state is self-similar, meaning that by definition all the dimensionless statistical distributions become time invariant. If one length, like the bubble size R, is magnified by a factor λ, all lengths in the foam structure must increase by the same factor. Self-similarity does not involve only geometrical features, but also the topology of the bubble lattice: the distribution of the bubble number of neighbours must be steady. Topological constraints are not limited to single bubbles, but they extend to their neighbours, for example in 2D the number of sides of a bubble is correlated to the number of sides of its neighbours [46]. Moreover, there exist also a correlation between geometry and topology both in 3D [9] and in 2D: in the latter case at any time the average radius of n-sided bubbles in a self-similar 2D foam is experimentally observed to be linearly dependent on n, contrary to the linear correlation between n and the average area $\langle A_n \rangle$ predicted by Lewis' law [46]. In very simple words, all these conditions imply that if we take a picture of the foam at two different time instants within this self-similar regime, its structure looks alike if the scale is not specified. This is visually shown in figure 4.3 for the case of a 2D foam.

The time needed for a foam to reach this scaling state strongly depends on its initial configuration. Polydisperse foams will reach this regime sooner than initially monodisperse ordered foams, as in the latter coarsening slowly starts from defects in the bubble lattice [47]. The achievement of the self-similar growth regime (SSGR) is traditionally checked by looking at the time evolution of the moments of both topological and normalised geometrical distributions. If only one of these parameters is observed to vary over time, it is enough to claim that the SSGR is not attained, provided that it is a physical variation and not an artifact due for example to lack of statistics.

While imagining self-similarity of ideal foams is quite easy both in 3D and in 2D, things get more complicated once we consider real foam systems, which have a finite size and often a non-negligible foam liquid fraction.

Indeed, while for an infinite sample the coarsening process has no end and we can speak of its asymptotic behaviour, in a real finite foam the process will eventually stop once complete phase separation is attained. However, finite size effects can be reasonably neglected as long as the foam container is much larger than the typical bubble size, and if this condition remains true for a time long enough to have a wide range of bubble sizes in which to probe this scaling state. In such a case, a coarsening 3D foam can eventually reach a self-similar growth regime [117], at constant liquid fraction ε, and there is experimental evidence of the existence of such scaling state in rather dry foams [30].

In the real case of quasi-2D foams, self-similarity is clearly meant only on a horizontal plane crossing the bubble array at the middle of their height: their confinement within a fixed gap makes them not self-similar in three dimensions. The existence of this scaling state has been experimentally proved in dry quasi-2D foams [47, 108, 107]. However, we shall see in section §4.6.1 that as soon as the liquid fraction is not negligible their 3D structure complicates the foam evolution.

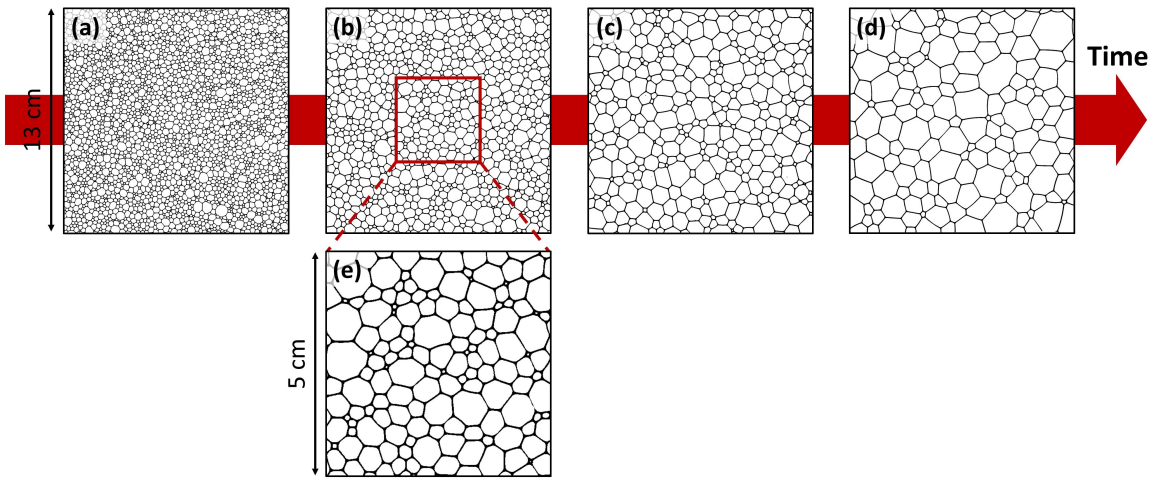

Figure 4.3 – **Self-similar growth regime.** (a-d) Time evolution of a quasi-2D foam in its scaling state: the average bubble size grows over time because of coarsening. By comparing the enlargement (e) and the photo (d) we can see how the foam structure at two different instants looks alike if we do not specify the frame scale.

4.5 Bubble rearrangements

The coarsening process continuously alters the stress configuration of the foam: when small bubbles shrink, local stresses arise between the surrounding bubbles which eventually result in bubble rearrangements. We talk about bubble rearrangement whenever two bubbles which were in contact separate or a new contact is established between two bubbles that were initially apart.

In a very dry foam there is a strong correlation between two such topological events occurring simultaneously and involving the same four bubbles [125]: this is what is commonly called a T1 event. Figure 4.4 shows an example of T1 event between red and grey bubbles: the two adjacent red bubbles are shrinking, as their number of sides n is lower than six. The contact between the two red bubbles is suddenly lost, while the grey bubbles come into contact. The initially 4-sided red bubble becomes 3-sided and keeps shrinking until it completely disappears: this is what is called a T2 event. T2 events can also occur while the bubble has still 4 or 5 sides [49]. These bubble rearrangements are fundamental for the coarsening foam to forget its initial configuration and attain its scaling state. Indeed, the SSGR is reached only once the distribution of side numbers is stationary, which means that the T2 processes which destroy the low-n tail of this distribution need to be compensated by bubble rearrangements all over the foam.

We remark that when a foam is rather wet, bubble rearrangements occur in arbitrary time sequences, it is thereby not appropriate to call them T1s even if the same four bubbles are involved [54]. This is why henceforth we shall talk about bubble rearrangements in general, independently of their duration.

3D bubbles in a quasi-2D foam

Before disappearing, shrinking bubbles undergo a Rayleigh-Plateau instability which makes them detach from the bottom plate. It is important to discriminate such 3D bubbles as

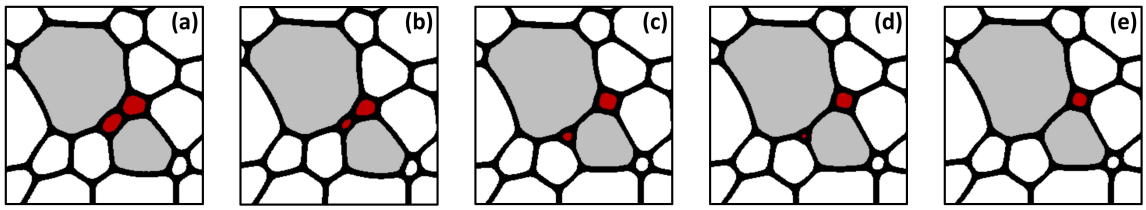

Figure 4.4 – **Bubble rearrangements.** (a) The two red bubbles are in contact with each other. (b) Having a number of sides equal to 4 and 5 respectively, they are gradually shrinking. (c) The contact between the two red bubbles is lost, while the two grey bubbles start touching each other: if this neighbour switch happens suddenly, as in a very dry foam, this is called a T1 event. The two red bubbles have now decreased their number of sides. (d) The 3-sided bubble keeps shrinking until it disappears (e): this is called a T2 event.

they have a different surface to volume ratio available for gas transfer compared to 2D ones.

To better understand this transition, let us first consider a single bubble of volume V sandwiched between two parallel plates separated by a distance d. For small d, the bubble will touch both plates and will assume an approximately cylindrical shape. If we now imagine to gradually increase the distance d, the bubble will first distort into a wine-bottle shape, and then detach from one of the boundaries once a critical value $d^* = \sqrt[3]{V\pi}$ is reached.

However, a bubble inside a dry quasi-2D foam is not isolated, but will be surrounded by a certain number of neighbours n. Only gas cells with less than six sides are subject to this wine-bottle instability as, according to Von Neumann's law, those are the ones that shrink as the foam coarsens. Thus, we expect each of these shrinking bubbles to finally undergo this instability before vanishing completely.

It has been shown that a foam cell of volume V having $n < 6$ sides, should undergo this Rayleigh-Plateau instability at a value of transverse thickness d_n^* given approximately by [19]:

$$d_n^* = d^* \sqrt{\frac{6}{6-n}} = \sqrt[3]{V\pi} \sqrt{\frac{6}{6-n}} \tag{4.12}$$

In a quasi-2D coarsening foam, however, the distance d is fixed and it is the volume V of the bubble that decreases over time. Thus, we can simply invert equation (4.12) and find that a n-sided vanishing bubble is expected to become unstable when it reaches a critical volume V_n^* equal to:

$$V_n^* = \frac{1}{\pi} \left(d \sqrt{\frac{6-n}{6}} \right)^3 \tag{4.13}$$

If we consider that in a dry quasi-2D foam the bubble volume V is in first approximation given by $V = A \cdot d$, the corresponding critical area is $A_n^* = V_n^*/d$. This critical area holds only for ideally dry quasi-2D foams, it is clearly larger at higher liquid fractions, as the thicker surface Plateau borders can merge when sufficiently close, meaning that in moderately wet foams small shrinking bubbles can detach from the bottom plate at larger sizes.

4.6 From dry to wet

Foam coarsening at intermediate liquid fractions still lacks a thorough and unified theoretical description. In this situation one needs to account for the gas diffusion through both the thin films and the bulk continuous phase: quantifying the two relative contributions is not trivial, as the foam structure, as well as its variation over time, must be considered. The coarsening description clearly varies as we switch from 2D to quasi-2D and 3D systems. In this section we shall review the state of the art for this dry/wet transition for the three different cases.

4.6.1 2D foams

In sections §3.3.1 and §3.3.2 we saw how the structure of a purely-2D foam is modified by an increasing liquid fraction. We now want to see how this structural change affects foam coarsening. For 2D foams at constant liquid fraction ε_{2D}, an equation for individual bubble growth rates has been proposed as the weighted sum of the area variation caused by the gas diffusion through the thin films and through the Plateau borders [37]:

$$\dot{A}^i = W_{\text{dry}} \dot{A}^i_{\text{dry}} + W_{\text{wet}} \dot{A}^i_{\text{wet}} \tag{4.14}$$

where the terms $\dot{A}_{\text{dry}}$ and $\dot{A}_{\text{wet}}$ are the growth laws predicted in the two extreme dry and wet limits, and their weights W_{dry} and W_{wet} account for the proportion of bubble perimeter made of thin films or wetted by Plateau borders.

These simulations, based on a bidimensional Potts model, showed that a self-similar growth regime is observed at any investigated liquid fraction ε_{2D} ranging from 0% to 90%, with the total number of bubbles decreasing over time as a power law $N \sim t^{-2\beta}$, where the exponent β interpolates between 1/2 and 1/3 as $\beta \simeq 1/2 - \varepsilon_{2D}^{0.2}/6$.

More recent simulations [65], based on a model originally developed for understanding foam rheology [27, 28], have studied the coarsening of wet 2D foams by considering the bubbles as soft disks. In this study, the rate of each bubble volume variation is also taken as a sum of two different terms:

$$\dot{V}^i = \dot{V}^i_{\text{tf}} + \dot{V}^i_{\text{cp}} \tag{4.15}$$

The first term $\dot{V}^i_{\text{tf}}$ represents the gas exchange through the thin film between two neighbouring bubbles, and it is thereby proportional to the thin film area, the difference in the bubble pressures and the film permeability. From this first term one can recover the Von Neumann's law expected for the dry limit.

The second term $\dot{V}^i_{\text{cp}}$ models the contribution of gas diffusion through the bulk continuous phase, similarly to what was done in older simulations [41] but in a more refined way, where the relative strength of diffusion through Plateau borders versus thin films is encoded in a dimensionless prefactor depending on the liquid fraction, which is varied between samples but kept constant for each simulation. The results showed that the mean bubble size grows as a power law for each investigated liquid fraction between 5% and 18%, with exponents ranging from 0.45 to 0.30 respectively [65].

Both models presented in this section cannot be applied to real quasi-2D foams, as they do not account for the presence of surface Plateau borders, which play a crucial role in moderately wet coarsening foams. Furthermore, in both cases the liquid fraction which is

kept constant is ε_{2D}: even though in the second model ε is volumetric, the bubbles are soft disks, so we have $\varepsilon = \varepsilon_{2D}$, which is not true in a quasi-2D foam.

4.6.2 Quasi-2D foams

The 3D structure of real quasi-2D foams strongly influences the coarsening process if the amount of liquid in the foam is not negligible. Indeed, first experiments on coarsening quasi-2D foams pointed out anomalous sublinear growth of the average bubble area over time [47, 48, 108]. These discrepancies were ascribed to the thickening of the surface Plateau borders when the foam coarsens at a constant volume liquid fraction, which gradually reduces the proportion of film area available for gas transfer. The linearity of the bubble area growth has then been recovered by draining the excess liquid as the foam coarsens, thus keeping the Plateau border size, and so the height of the thin films, constant [107].

Since then, most of the coarsening experiments in quasi-2D foams have thus been carried out at constant capillary pressure, by keeping the foam in contact with a reservoir of its own foaming solution [97, 14].

The influence of the Plateau borders on the area growth rate has been initially studied by comparing experimental data with a *border-blocking* model [97] which considers the Plateau borders as completely screening the gas diffusion, so that the gas diffuses between adjacent bubbles only through the portion of thin films. While this approximation of neglecting the diffusion through the bulk liquid phase works well for rather dry foams, it clearly fails at high liquid fractions close to unjamming. Indeed, it predicts an unphysical arrest of coarsening as soon as the film height vanishes, while in reality gas can diffuse through the Plateau borders, and thus coarsening still continues but more slowly.

A detailed *border-crossing* model that accounts also for the diffusion through the Plateau borders has been proposed later [104]: Von Neumann's law is basically modified by introducing geometrical factors accounting for the presence of both surface and vertical Plateau borders where the gas diffusion is slower, but not zero.

However, both kinds of models account for experimental observations that, if the amount of liquid is not negligible, the area growth rate of single bubbles no longer depends only on their number of sides but also on their shape through a circularity parameter [97, 104, 14].

A prediction for the average bubble growth rate has been proposed for quasi-2D foams both at constant capillary pressure and constant liquid fraction [104], the latter holding only in the regime of liquid fractions within the validity of the decoration lemma, where thin films are still present and no bubble contacts are lost. Therefore, it does not describe the bubble area growth rate when the foam is close to the jamming transition.

We highlight that, as seen in section §3.3.3, for a given volume liquid fraction the height of the thin films depends on the confinement [18]. Thus, for a sealed cell, as the foam coarsens the Plateau borders will fatten up [42] until their size eventually reaches half of the gap, at which point the thin film area vanishes. At the same time, vertical Plateau borders also increase their size and eventually merge into many-sided ones. Thus, at a given cell gap and constant liquid fraction, we could start from a foam configuration within the limits of the decoration lemma and end up in a configuration in which it no longer holds. In the long run, since coarsening does not stop until complete phase separation is reached, the bubbles can eventually unjam. How the bubble size evolves in this case is thereby still an open question.

4.6.3 3D foams

The study of coarsening at intermediate foam wetness requires a homogeneous liquid distribution inside the foam, which we saw in section §2.5.1 to be experimentally limited by gravitational drainage. In fact, over the time scales needed for the foam to coarsen and reach its scaling state, drainage is almost never negligible and its effect becomes more important as the liquid fractions ε approach the critical value ε^*.

Even though a full theoretical description of the dry/wet transition is still missing, experimental data on 3D foams exist in the literature. To overcome gravitational drainage, wet foams at liquid fractions ranging from 8% to 60% have been studied under magnetic levitation [64]. In this study, it has been found that the exponent of the average bubble growth undergoes a narrow but gradual transition from 1/2 to 1/3 at liquid fractions between 25% and 35%. By contrast, recent experimental data obtained from foam coarsening experiments performed in micro-gravity show that a sharp transition occurs at a higher liquid fraction, around 40% [89], whose interpretation is however still an ongoing discussion.

5 Foamed emulsions

In many applications, the foam liquid phase is often a complex fluid characterised by a non-Newtonian rheological behaviour, such as a polymer gel or a composite material, like a paste or an emulsion. Understanding the stability of these kinds of foams is crucial for instance in the design of solid cellular materials, to ensure that their structure does not change before complete solidification so that the final product will have the desired morphology. In this chapter we shall first briefly recall the peculiar rheological properties of so-called yield-stress fluids. We shall then introduce emulsion systems, highlighting the strong similarities between these concentrated liquid dispersions and foams. We will then see how we can make a foam out of an emulsion and we shall review the stability and mechanical properties of these complex three-phase systems, that will be the main focus of the experimental part of the present thesis.

5.1 Yield-stress fluids

The general aim of rheology is to establish constitutive relations between applied force and deformation in materials, mainly liquids, to describe their behaviour [79].

Let us consider a small element of a certain material, like the one drawn in figure 5.1. When a tangential force F is applied on the top surface Σ, the element will start deforming. We call *shear stress* τ the force per unit area exerted on the cube, namely $\tau = F/\Sigma$, whereas we call *shear strain* the subsequent deformation Γ undergone by the element, described as the adimensional ratio $\Gamma = d/h$.

If the material is solid and the applied stress is low enough so that the deformation is small, Hooke's law states that the latter is simply proportional to the stress, thus:

$$\tau = G\Gamma \tag{5.1}$$

where the constant of proportionality G is the elastic modulus of the material [79].

By contrast, if the material is liquid, its behaviour can be described by Newton's law, which states that the shear stress is proportional to the rate of deformation, namely the *strain rate* $\dot{\Gamma} = \mathrm{d}\Gamma/\mathrm{d}t$, according to:

$$\tau = \eta\dot{\Gamma} \tag{5.2}$$

where the constant η is now the Newtonian viscosity, meaning that the higher the fluid viscosity, the slower the deformation [79].

While many real materials obey these two ideal laws, many others, such as mayonnaise, polymer gels, and paints, lie between the ideal elastic solid and the ideal viscous fluid. For instance, a wide range of materials flow only if the applied stress is above a certain threshold

value, τ_y, which is called *yield stress*. As long as the applied stress τ is below the yield stress τ_y the fluid behaves as an elastic solid, while as soon as τ exceeds τ_y the material loses its rigidity and starts flowing as a viscous liquid. The flow behaviour of yield-stress fluids can thus be described with the more general empirical Herschel–Bulkley relation [60]:

$$\tau = \tau_y + K\dot{\Gamma}^n \tag{5.3}$$

where both the prefactor K and the exponent n are material dependent.

In general, however, these kinds of materials do not perfectly store the elastic energy but exhibit some viscous loss even in the limit of small deformations. Thus their linear viscoelastic behaviour can be described by generalising the elastic modulus into a complex frequency-dependent shear modulus G^*, that can be written as $G^*(\omega) = G'(\omega) + iG''(\omega)$. The real part G' is related to the storage of elastic energy and is thus called storage modulus, while the imaginary part G'' is called loss modulus as it describes the viscous dissipation. Three main examples of yield-stress fluids are of essential interest for the present work, which are foams, concentrated emulsions, and a combination of these two.

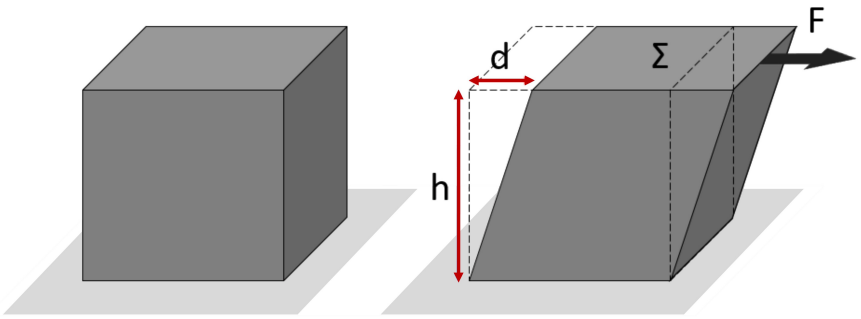

Figure 5.1 – **Shear strain and shear stress.** When applying a shear stress $\tau = F/\Sigma$ to a small volume of material, the latter will deform and its deformation can be described in terms of the adimensional shear strain $\Gamma = d/h$.

5.2 Concentrated emulsions

In its simplest form, an emulsion is a mixture of two immiscible liquids, typically water and oil, one of which is dispersed into the other in the form of microscopic droplets covered by a layer of surface-active molecules. These liquid dispersions can be found in a wide range of products, not only in food [83] but also in cosmetics and pharmaceutics, where for example their two-phase composition is exploited to simultaneously disperse components soluble only in water or in oil in the same product.

Depending on which one is the dispersed phase, we can find oil-in-water (O/W) or water-in-oil (W/O) emulsions, although more complex structures like oil-in-water-in-oil (O/W/O) or water-in-oil-in-water (W/O/W) can also be found. When mixing oil and water, the final emulsion type can be predicted by the Bancroft rule, which states that the resulting emulsion is the one for which the surfactant is soluble in the continuous phase [73]. Hereafter we shall focus on the case of interest of O/W emulsions, even though the following considerations equally apply to W/O emulsions after adapting the notation.

5.2.1 Analogies with foams

Similarly to all dispersions, emulsions are mainly characterised by the size of the oil droplets, let us say their radius r, and by the volume fraction of dispersed oil ϕ, which is defined as:

$$\phi = \frac{V_{\text{oil}}}{V_{\text{emulsion}}} \tag{5.4}$$

In complete analogy to bubble dispersions, the emulsion structure and properties strongly change as we vary the oil volume fraction ϕ. Indeed, since liquid drops are deformable, emulsions can span droplet volume fractions from zero to almost one. As sketched in figure 5.2, as we increase the oil fraction ϕ we switch from a dilute emulsion regime, where drops are spherical and do not touch each other, to concentrated emulsions where the drops are tightly packed together, assuming the shape of polyhedrons separated by a network of thin aqueous films and channels, exactly like foams. Concentrated emulsions are typically referred to as *creams* in food industry and in cosmetics, or sometimes also as *high internal phase emulsions* (HIPE) [73]. The transition between the two regimes occurs at a critical value ϕ^* around 64%, corresponding to the random close packing of monodisperse hard spheres, which clearly varies with drop polydispersity and order [33]. Once again, the jamming transition physically mirrors the vanishing of the emulsion osmotic pressure and marks the onset of a solid-like response in these systems, as we will see in §5.2.2

Concentrated emulsions, with oil fractions above close packing, can thus be thought of as "biliquid foams". What is usually different is the typical size of the dispersed phase which is in general smaller for oil drops than for bubbles, even though particle-stabilised emulsions with millimetric drops can be found in the literature [74].

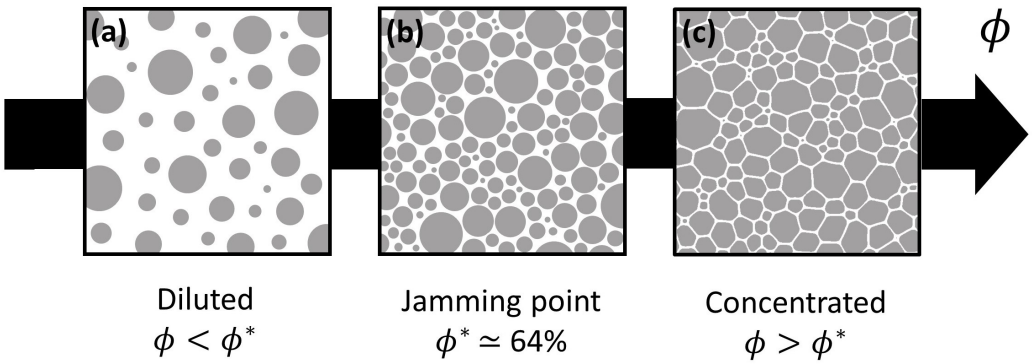

Figure 5.2 – **Diluted and concentrated emulsion.** At low drop volume fractions the oil droplets are spherical and do not touch each other (a). As soon as we exceed the random close packing threshold ϕ^* (b) the drops start touching each other and deform, so that concentrated emulsions look like biliquid foams (c).

5.2.2 Mechanical properties

Emulsions exhibit different rheological properties, depending on their drop volume fraction ϕ. When diluted, nonadhesive emulsions generally show a Newtonian behaviour: their flow can be described as the one of a simple viscous liquid [74]. By contrast, concentrated emulsions are yield-stress fluids. In fact, they can behave as elastic solids when subjected

to small deformations, even though their components are liquid: their elasticity is precisely due to the deformability of the drops coming from their liquid nature.

Indeed, above the critical volume fraction ϕ^*, the emulsion drops can no longer pack without deforming, thus their shape is distorted and energy is stored at their interfaces. If we now apply a small stress to the emulsion, an additional droplet deformation occurs. The energy scale that controls this deformation is the droplet Laplace pressure γ/r, where γ is the interfacial tension and r is the radius of the undeformed droplet. The emulsion elasticity thus exists only when the repulsive droplets have been concentrated up to a sufficiently large volume fraction which permits the storage of interfacial energy. If the emulsion is compressed up to $\phi > \phi^*$, each droplet is pressed against its neighbours sharing facets, and the emulsion elasticity can be understood by considering each of these facets as a spring repelling the adjacent drop [71].

After the pioneering work done by Princen and Kiss on polydisperse emulsions [93], the elastic properties of monodisperse concentrated O/W emulsions have been systematically studied at different droplet radii [82]. It has been shown that the emulsion storage modulus G' monotonically increases with the oil fraction ϕ according to the relation:

$$G' \sim \phi(\phi - \phi^*)\frac{\gamma}{r} \tag{5.5}$$

where the scaling with ϕ indicates that the elasticity of these compressed droplets depends only on the packing geometry, while the scaling with the Laplace pressure γ/r confirms that their elasticity results from the storage of interfacial energy from droplet deformations [82].

To be accurate, one should account for the repulsive interaction between droplets by considering an effective oil volume fraction ϕ_{eff} which includes the thin films within the volume of the drops to focus only on the effects of the droplet packing. ϕ_{eff} depends on the film thickness h, as $\phi_{\text{eff}} \sim \phi(1 + 3h/2r)$, where h in turn depends on the oil fraction itself but can be assumed to vary linearly with ϕ [82] and is typically a few nanometers [106].

Concerning the plasticity of such systems, it has been shown that their yield stress τ_y also scales with the Laplace pressure γ/r and the drop packing fraction ϕ [81] as follows:

$$\tau_y \sim (\phi - \phi^*)^2\frac{\gamma}{r} \tag{5.6}$$

Emulsions yield because of the rearrangement of oil droplets. The evolution of droplet motions as the emulsions undergo the transition from the linear to the nonlinear regime has been investigated with diffusing-wave spectroscopy and results showed that yielding occurs when about 5% of the droplets rearrange [59].

This macroscopic description holds at length scales much larger than the drop size, namely when the emulsion can be considered as a homogeneous viscoelastic material. However, at smaller length scales finite size effects have been pointed out [53, 52]. When confined between a narrow micrometric gap, the flow of concentrated emulsions is different from the bulk: there is no unique relation between local shear stress and local shear rate, as the flow strongly depends on the confinement and on the wall surface roughness [53, 52]. The concept of fluidity, which quantifies the local rate of plastic rearrangements, as well as a new characteristic flow cooperativity length ζ, which quantifies the spatial spreading of these plastic events, have been introduced to describe the local flow behaviour at these levels of confinement [53, 52].

5.2.3 Emulsion stability

The emulsion lifetime may vary from minutes to years, depending on the nature of the stabiliser and of both phases, as well as on their volume ratio and on the size of the drops. Just like foams, an irreversible emulsion damage can result from the interplay between different mechanisms.

They can undergo gravitational drainage, as explained in section §2.5.1 for foams, which in the case of emulsions is typically called creaming or sedimentation, depending on whether the dispersed phase is lighter or heavier than the continuous one. Clearly, this gravity effect strongly depends on the drop volume fraction: at low ϕ the emulsion viscosity is quite low thus the process is very efficient: the larger drops quickly migrate and concentrate at the top or bottom of the sample. By contrast, in highly concentrated emulsions, the tight packing can hinder droplet rearrangements thus their size distribution can remain spatially homogeneous for a long period of time. Moreover, the process is in general slower than in foams because of the smaller density difference between the two phases, and the typically smaller size of the drops.

Drop coalescence, due to the rupture of the thin film between them, can also occur leading to a rapid formation of a free layer of the dispersed phase at the top or the bottom of the sample. In general, emulsions are observed to be less stable when the surfactant is dissolved in the dispersed phase, probably because of a lack of Marangoni film-thickening effect, as the large amount of molecules available inside the drops quickly suppresses possible surface tension gradients [72]. As in foams, coalescence in emulsions is however still poorly understood, but since the underlying mechanisms are in principle the same, a unified study of coalescence in such systems has been suggested [72].

Finally, the same pressure-driven coarsening process explained in section §2.5.3 can take place resulting in a diffusive transfer of the dispersed phase between drops of different radii. Once again, the rate of droplet growth clearly depends on the drop volume fraction ϕ. More precisely a constant volume rate is expected in the very dilute regime where diffusion occurs across the bulk continuous phase, while a constant surface rate is expected when ripening is controlled by the permeation through the thin films between adjacent drops, namely at ϕ approaching 100% [74]. In both cases, the coarsening rate is highly reduced if the solubility of the dispersed oil in water is very low.

5.3 Aerated emulsions

In the previous section we introduced emulsion systems. However, there are many applications like in food industry and cosmetics, in which such products are found with the addition of gas bubbles, in which case we talk about aerated emulsions. A well-known example is whipped cream, which is an aerated O/W emulsion stabilised by proteins and fat droplets.

Let us consider the common case of bubbles much larger than the typical drop size. Depending on the amount of incorporated gas, we can distinguish between *bubbly* and *foamed* emulsions, in complete analogy to what done in section §2.3 when talking about simple bubble dispersions, the only difference being that the liquid phase is now an emulsion, thus a dispersion itself.

For the sake of clarity, we report the adapted definitions of gas and liquid fractions, φ and ε, in these composite systems:

$$\varphi = \frac{V_{\text{gas}}}{V_{\text{gas}} + V_{\text{oil}} + V_{\text{water}}}; \qquad \varepsilon = \frac{V_{\text{oil}} + V_{\text{water}}}{V_{\text{gas}} + V_{\text{oil}} + V_{\text{water}}} \tag{5.7}$$

At low φ, or equivalently high ε, we have a bubbly emulsion with well-separated spherical bubbles completely surrounded by the emulsion matrix. By contrast, at gas fractions above the random close packing value φ^*, adjacent gas bubbles start to be tightly-packed and separated by thin films, so their sphericity is lost in favor of squashed spheres or even polyhedral shapes. We thus have a so-called foamed emulsion, where all droplets are basically expelled from the films into the foam Plateau borders. Similarly, as we vary the emulsion oil fraction ϕ, we modify the structure of the emulsion matrix between the bubbles: the graph in figure 5.3 illustrates all the possible combinations of bubbly/foamed diluted/concentrated emulsions as we vary the gas and oil fractions.

Figure 5.3 also shows an example of how a concentrated O/W foamed emulsion looks like under the microscope, together with a sketch which highlights its more complex multi-scale structure. Foams made of highly concentrated emulsions will be the system under study in chapters §7 and §8. To avoid a very unstable system, there should be no direct contact between the dispersed oil and gas phases: a so-called aqueous pseudo-emulsion film separates the oil droplets from the bubble, on whose stability depends the lifetime of the overall foamed emulsion, as discussed in the next section.

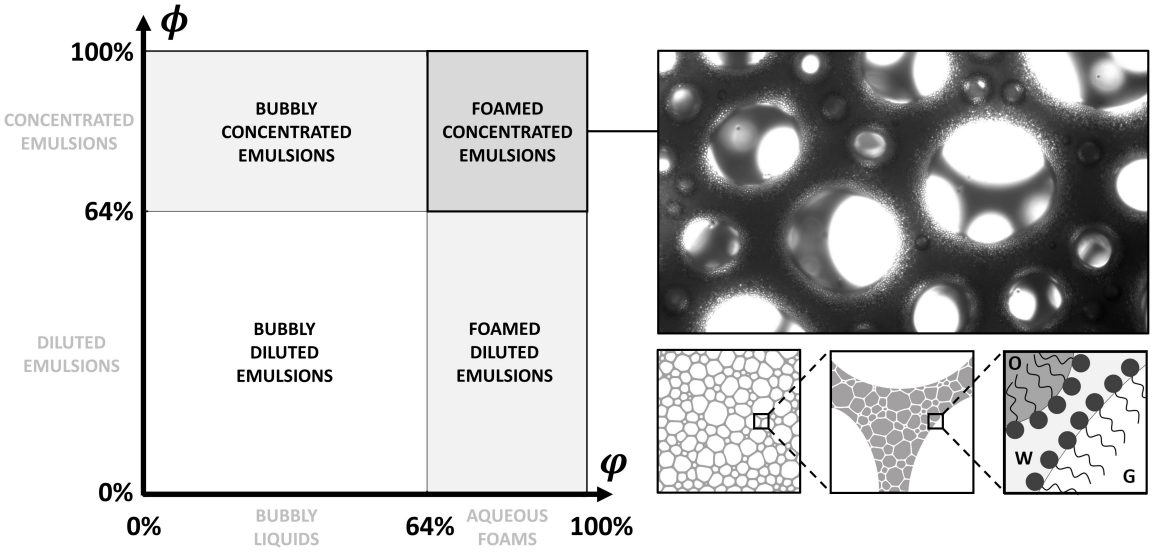

Figure 5.3 – **Aerated emulsions.** The diagram on the left shows the possible combinations for aerated emulsion structure depending on the gas fraction φ and on the emulsion oil fraction ϕ. On the top right, an example of a foamed emulsion as seen under the microscope: one can notice the emulsion inside the Plateau borders made of tiny oil drops tightly packed together. Its multi-scale structure is drawn below, highlighting the presence of the pseudo-emulsion film separating the oil drops from the gas phase stabilised by adsorbed surfactants.

5.3.1 Influence of oil droplets on foam stability

Oils are well-known to be potential effective antifoams. Oil-based antifoams are especially used in detergency where the presence of surfactants, often above the cmc, makes other

foam breakers inefficient: surfactant adsorption on hydrophobic particle surface for instance makes them hydrophilic and thus reduces their antifoam effect [22].

However, once emulsified, oil droplets inside the foam liquid phase can either stabilise or destabilise the overall foam, depending mainly on the stability of the aqueous pseudo-emulsion films separating the drops from the gas phase. In fact, if oil drops manage to enter and spread at the air/water interface they can induce film rupture through a so-called bridging mechanism and make the foam quickly collapse.

Film bridging by pre-emulsified oil drops depends on the so-called entry barrier, which describes their difficulty to pierce the air-water interface and strongly depends on the chemical nature of the oil phase [22].

However, this ability has been traditionally discussed in terms of entry, spreading and bridging coefficients, which are linked to the equilibrium interfacial tensions between the three phases. There is no direct relation between the magnitudes of these coefficients and the oil antifoam efficiency, their positive or negative values just help predicting the potential of an oil to act as antifoam.

The entry coefficient E is defined as:

$$E = \gamma_{gw} + \gamma_{ow} - \gamma_{og} \tag{5.8}$$

where the subscripts of γ refer to the interfacial tension between the gas (g), oil (o) and water (w) phases. If $E < 0$ the oil drop will be completely wetted by the aqueous phase, therefore oils with $E < 0$ are expected to be rather inactive as antifoam as their drops will tend to remain totally immersed inside the aqueous phase of the foam. By contrast, if $E > 0$ the oil drop can enter the air/water interface and form a lens. Hence, oil bridges can be formed when the oil has $E > 0$ and the entry barrier is not too high, thus $E > 0$ is a necessary (but not sufficient) condition for an effective antifoam performance.

Once the antifoam droplet manages to emerge at the interface it may be energetically favourable for it to spread out. This is determined by the spreading coefficient, which is defined as follows:

$$S = \gamma_{gw} - \gamma_{ow} - \gamma_{og} \tag{5.9}$$

A rather qualitative correlation between the spreading behavior of oils and their antifoam activity has also been pointed out, as it has been observed that most of (but no all) the oils with antifoam activity have $S > 0$ [22].

Finally, if we consider the so-called bridging coefficient B, defined as:

$$B = \gamma_{gw}^2 + \gamma_{ow}^2 - \gamma_{og}^2 \tag{5.10}$$

it can be proven that $B > 0$ implies $E > 0$, while the reverse statement is not true. Most importantly, positive values of B correspond to unstable bridges (and thus to foam film rupture) and vice versa. Thus the only requirement for having an active antifoam, with respect to the bridging mechanism, is that $B > 0$.

By contrast, when the pseudo-emulsion film is stable enough to prevent the entering of oil drops at the air/water interfaces, emulsified oil droplets can enhance foam stability by hindering its drainage: they can indeed accumulate within the Plateau borders, thus opposing to the water flow downwards [68]. It has been shown that the condition for solid particles to be captured inside the foam liquid channels depends on their confinement: only

if their size is larger than the size of the constriction within the Plateau borders they can be trapped, otherwise they are free to drain with the foam liquid phase [66]. Thus, in analogy, drops larger than these constrictions can be trapped and reduce drainage effects. Moreover, this stabilising effect has been observed to increase with increasing oil fraction inside the foam [68]. Indeed, if the emulsion is concentrated and thus has a yield stress, it can help delaying the buoyancy of bubbles induced by gravity [58, 7]. Moreover, bubble coarsening is also supposed to halt if the yield stress of the foam skeleton is larger than the bubble internal pressures [75, 7].

5.3.2 Rheology of aerated dense emulsions

Beyond their countless applications in daily life, aerated emulsions have also been used in the literature as model systems for studying the rheological properties of bubble dispersions in yield-stress fluids [69, 25, 50].

Let us consider an aerated concentrated emulsion. If the oil drops are much smaller than the gas bubbles, the scale separation between the two allows considering the emulsion as a continuous medium among the bubbles [53]. A medium which is viscoelastic, as seen in section §5.2.2.

The rheological behaviour of such composite systems has been experimentally studied both below [25] and above [50] the critical gas fraction φ^*, showing that it strongly depends on the bubble deformability under shear. If the applied stress is low enough, bubbles can behave like rigid spherical particles with a slip boundary condition as their surface tension acts to minimise their area by maintaining a spherical shape. Nonetheless, above a certain critical stress, surface tension is no longer sufficient to keep them spherical and they will thus deform. This has been observed to be also at the origin of the shear-dependent viscosity in suspensions of bubbles in simple viscous liquids [98].

It has been shown that the elastic and plastic behaviour of bubble dispersions in yield-stress fluids are governed by two different capillary numbers [69].

The role of bubble deformability in the elasticity of aerated dense emulsions can be described by introducing a so-called elasto-capillary number, defined as follows:

$$Ca_{\mathrm{el}} = \frac{G'(0)}{\gamma/R} \tag{5.11}$$

where $G'(0)$ is the storage modulus of the emulsion without bubbles, γ is the surface tension and R is the radius of the suspended bubbles [69]. This elasto-capillary number basically compares the matrix elasticity with the stiffness of the bubbles due to their surface tension. Rheological studies with gas fraction φ up to 50% have shown that the overall elastic response of the aerated emulsion is governed only by this elasto-capillary number Ca_{el} and the gas fraction φ itself [25].

Let us define the dimensionless elastic modulus $\hat{G}(\varphi, Ca_{\mathrm{el}})$ as the ratio between the storage modulus of the aerated material $G'(\varphi)$ and the one of the original emulsion $G'(0)$. If $Ca_{\mathrm{el}} \to \infty$ the surface tension forces are negligible and the bubbles can be considered as voids in the matrix, thus $\hat{G}(\varphi, Ca_{\mathrm{el}})$ will decrease with increasing φ, reflecting the weakening of the material with the addition of bubbles. By contrast, if $Ca_{\mathrm{el}} \to 0$ the bubbles are stiff and can be considered as rigid particles, thus their addition will strengthen the material and thereby $\hat{G}(\varphi, Ca_{\mathrm{el}})$ increases with φ.

Between these two limits $\hat{G}(\varphi, Ca_{\text{el}})$ exhibits little dependence on φ. In this regime the following relation for $\hat{G}(\varphi, Ca_{\text{el}})$ has been proposed [25]:

$$\hat{G}(\varphi, Ca_{\text{el}}) = 1 - \frac{\varphi(2Ca_{\text{el}} - 1)}{1 + \frac{6}{5}Ca_{\text{el}} + \frac{2}{5}\varphi(2Ca_{\text{el}} - 1)} \tag{5.12}$$

This study was later extended to gas fractions φ above close packing, showing that in this regime the final elastic modulus $G'(\varphi)$ is still governed by the same two parameters φ and Ca_{el} [50]. Moreover, they showed that $G'(\varphi)$ can be written as the sum of three terms as follows:

$$G'(\varphi) = G'_{\text{foam}} + G'_{\text{skeleton}} + \psi \tag{5.13}$$

where the first term G'_{foam} comes from the bubble packing, namely it corresponds to the elastic response of an aqueous foam having the same gas fraction, the second term G'_{skeleton} is linked to the elastic skeleton seen as a solid cellular material, and the third one ψ is a coupling term accounting for the mechanical interactions between the emulsion and the bubbles. One can thus re-write equation (5.13) as:

$$G'(\varphi) \simeq 1.6\frac{\gamma}{R}\varphi(\varphi - 0.64) + G'(0)(1-\varphi)^2 + 15(1-\varphi)^2(2\varphi - 1)G'(0)Ca_{el}^{-2/3} \tag{5.14}$$

where the form of the coupling term ψ is proposed analytically in the limit $Ca_{\text{el}} >> 1$ and $\varphi \to 1$. We highlight how, at high Ca_{el}, the presence of the elastic emulsion in the continuous phase of the foam makes the storage modulus of the foamed emulsion decrease as we increase the gas fraction, or equivalently its elasticity increases as we increase the foam liquid fraction, which is the opposite of what is expected for an aqueous foam [100].

Figure 5.4 shows how $\hat{G}(\varphi, Ca_{\text{el}}) = G'(\varphi)/G'(0)$ varies with φ at different Ca_{el} for both bubbly and foamed materials [50].

Concerning the plasticity of these aerated emulsions, one could define a plastic capillary number as the ratio between the emulsion yield stress τ_y and the bubble capillary pressure γ/R:

$$Ca_{\tau_y} = \frac{\tau_y}{\gamma/R} \tag{5.15}$$

It has been shown that for values of Ca_{τ_y} lower than 0.2 the yield stress of bubbly suspensions is found to be constant and very close to the one of the emulsion matrix τ_y [69]. However, at higher gas fractions in the foam regime, the overall yield stress increases with φ, with a φ transition value depending on the bubble to drop size ratio, suggesting that in this regime where drops are strongly confined inside the foam Plateau borders, the emulsion flow is harder to enforce due to its lack of disorder [69].

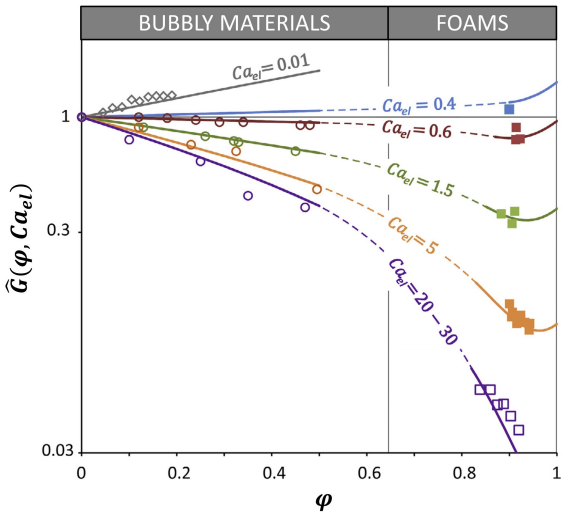

Figure 5.4 – **Aerated emulsion elasticity.** The normalised storage modulus of the aerated material $\hat{G}(\varphi, Ca_{\mathrm{el}}) = G'(\varphi)/G'(0)$ is governed by the gas fraction φ and the elasto-capillary number Ca_{el}. At high values of Ca_{el}, an increase of φ results in a weakening of the final aerated material, as opposed to what happens in aqueous foams. Picture adapted from [50].

5.4 Foam coarsening in viscoelastic media

In chapter §4 we saw that, apart from the dry/wet transition, the coarsening of aqueous foams is now rather well understood. By contrast, very little is currently known of what happens when the foam liquid phase is replaced by a complex fluid: how its mechanical properties impact on the coarsening process is still an open question which is of great interest for finding new ways of controlling foam ripening. The main part of the experimental investigation carried out in the present thesis will focus on the coarsening of foams having a viscoelastic continuous phase. In this section we thus review the most relevant theoretical and experimental studies dealing with hindering and arresting foam coarsening by exploiting the mechanical properties of the liquid phase or the foam itself.

One of the most common ways to reduce foam coarsening consists in adding a small fraction of insoluble gas molecules inside the bubbles: since only the fraction of soluble gas can be exchanged between adjacent bubbles, the build-up of an osmotic pressure due to different gas concentrations can counteract the Laplace pressure difference and thus hamper foam coarsening. This has been shown to lead to highly heterogeneous foam structures [124] which can in turn contribute to further hindering the coarsening process by acting as an elastic medium opposing to bubble growth. Indeed, a relevant theoretical study has shown that the late-stage foam morphology depends on the relative amount of soluble gas actually available for coarsening [127]. The trapped molecules of insoluble gas prevent small bubbles from totally disappearing, and if the volume fraction of soluble gas is very low the foam can reach a configuration like the one shown in figure 5.5 (a), with large bubbles surrounded by a sea of shrunken tiny ones. By contrast, if the excess of soluble gas is very high, the foam will end up assuming an heterogeneous structure like the one depicted in figure 5.5 (c), with chains of large bubbles decorated by groups of smaller bubbles at their vertices. At intermediate soluble gas fractions the foam will assume configurations between these two

limits, as shown in 5.5 (b) [127]. Particularly worth of note is that in the first scenario, the coarsening between larger bubbles requires a gas flux through the sea of smaller bubbles but also their rearrangements in order to let the large bubbles increasing their size. If the foam is dry, these regions of osmotically stabilised bubbles can behave as an elastic medium that counteracts the growth of well-separated large bubbles and thus elastically stabilise the entire foam against coarsening [127]. We shall see in chapter §7 that similar heterogeneous structures can also appear in foams made of viscoelastic media.

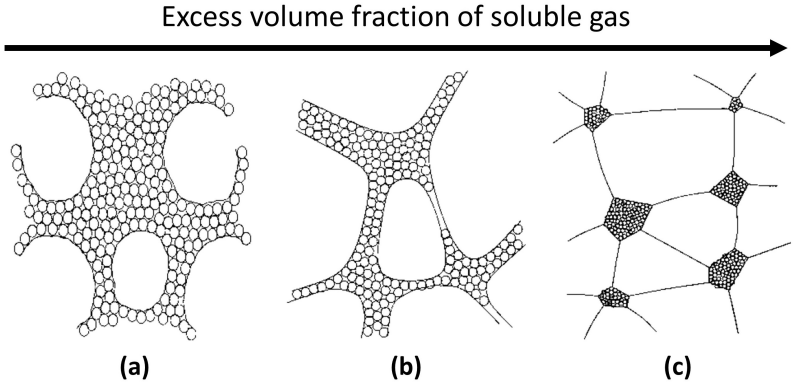

Figure 5.5 – **Effect of insoluble gas species.** As the relative amount of soluble gas changes from very low to very high, the foam can develop a structure in which large isolated bubbles are surrounded by a sea of small osmotically stabilised bubbles (a), to one in which chains of touching large bubbles are decorated by groups of shrunken bubbles at the vertices (c), with possible intermediate configurations between these two extremes (b). Picture adapted from [127].

Let us now consider the case of a complex fluid as the continuous phase of a bubble dispersion. It has been theoretically shown that the dissolution of a single bubble can be delayed when surrounded by an infinite sufficiently viscous medium, and even stopped if the latter has also a bulk elasticity [67], as shown in figure 5.6. Indeed, in saturated conditions and if interfacial viscoelasticity is sufficiently low to be neglected, it has been shown that a bubble of initial size R_0 immersed in an infinite elastic fluid stops shrinking when:

$$\frac{GR_0}{\gamma} = \frac{4r^3}{1 - 5r^4 + 4r^3} \tag{5.16}$$

where r is the dimensionless radius $r = R/R_0$ and γ is the surface tension [67]. One can see that for small values of r the term GR_0/γ grows as r^3, meaning that an increase of G by a factor 1000 would make the bubble shrink less by a factor 10. Equation (5.16) also shows that for a larger initial bubble size or a lower interfacial tension the bubble is stabilised at a higher r and thus shrinks less [67].

Even though foam coarsening can be in principle arrested if the bubble Laplace pressure is smaller than the yield stress of the continuous phase [75, 7], an arrest of coarsening precisely due to the continuous phase elasticity has not been experimentally shown yet.

In fact, a halt of coarsening has been experimentally observed, but only in monodisperse foams made of elastic polymer gels combined with weakly soluble gas species inside the bubbles, showing that the regime in which the foam is stable is set by a critical radius fixed by the ratio of the surface tension to the foam storage modulus [1]. However, since

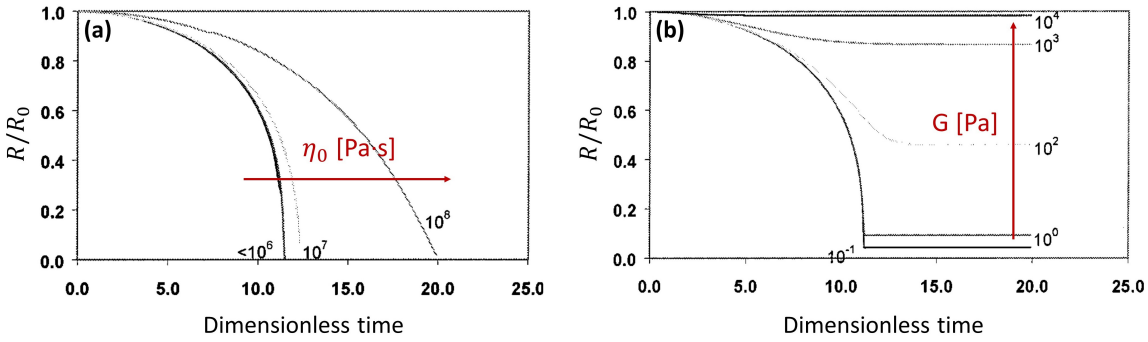

Figure 5.6 – **Effect of bulk viscoelasticity on single bubble dissolution.** (a) The bulk viscosity η_0 of the surrounding fluid can delay the disappearance of a single bubble of initial size R_0 but cannot stop it. (b) Only if the fluid has a bulk elastic modulus G the disappearance of the bubble can be halted at a critical bubble size increasing with G. Pictures adapted from [67].

the foams are initially monodisperse, the coarsening can initiate only from defects in the ordered bubble lattice. This means that the involved Laplace pressure differences between adjacent bubbles are really small, while the elastic modulus of the gelified continuous phase is extremely high being of the order of thousands of Pa. This way a tiny bubble size variation due to gas transfer can be seen as a perturbation to the foam equilibrium structure, which induces an elastic deformation of the surrounding matrix, and thus an elastic stress that tends to restore its initial unstrained volume [1]. Plus, this study focuses on whether an onset of coarsening occurs or not, without saying anything on the rate of coarsening in such complex foams, which still calls for experimental investigations. This is why, in chapters §7 and §8, we shall monitor the evolution of foamed concentrated emulsions, to probe how the viscoelasticity of the emulsion in the foam continuous phase affects the bubble growth rates and their displacements in the foam during coarsening.

Contextualisation of the experimental work

The aim of the first part was to give a general overview of the state of the art concerning the stability of foams in simple aqueous solutions but also in more complex media. Among the three different mechanisms which can destabilise these multi-scale systems, we focused on the pressure-driven coarsening process, which slowly makes the average bubble size grow over time because of gas diffusion from smaller bubbles to larger ones. In chapter §4 we saw that even though a robust theoretical explanation for this mechanism exists in the two limits of very dry and very wet bubble dispersions, what happens in the intermediate regime still lacks a unified description.

Foam coarsening has been studied for many years in quasi-2D foams made of monolayers of bubbles, in order to avoid the effects of gravitational drainage and, at the same time, strongly simplify the foam characterisation with image processing, as each bubble in the foam sample is visible and easily measurable.

In chapter §3 we saw that, as long as each of their vertical Plateau borders have a triangular section, quasi-2D foams share the same topological and geometrical features of their ideal 2D counterparts. Moreover, we saw that their ripening follows the rules established for ideal 2D foams only when they are really dry and the excess liquid is allowed to drain in a reservoir, or they behave as bubbly liquids if their liquid fraction is high enough to have well-separated bubbles. However, at intermediate liquid fractions, their three-dimensional structure plays a crucial role in their evolution, as the different liquid content sets the film area between adjacent bubbles. So far the effect of an increasing liquid fraction has been experimentally studied only for drained foams [97, 14], while previous experimental studies of coarsening in sealed Hele-Shaw cells just pointed out structural and evolution discrepancies with ideal behaviour due to the fattening of the Plateau borders, without however specifying or varying the actual foam liquid content [47, 48, 108]. Although a general model for the evolution of single bubbles accounting for different Plateau border size exists, to our knowledge there are no experiments showing how the mean bubble size grows in quasi-2D foams at different but constant liquid volume fractions.

For this reason, in chapter §6 we shall start by probing the coarsening of aqueous foams in sealed plate-plate quasi-2D configurations. We shall investigate how the gradual inflation of the Plateau borders affects the overall coarsening rate, starting from different initial liquid fractions. The results, which we shall compare with the existing models, will also be a useful reference for what we present next, when we shall move our attention to more complex foam systems.

In many foam applications the liquid phase is indeed not a simple aqueous solution, but can be a complex material itself, characterised by a non-Newtonian behaviour. Even

though foams made of complex fluids are ubiquitous, the conditions for their stability are still little understood. However, the mechanical properties of the fluid between the bubbles can play a fundamental role in the stabilisation of the global system. Indeed, we saw that a yield-stress fluid can delay the foam gravitational drainage, which in turn reduces bubble coalescence as the latter usually takes place at very low liquid fractions. Furthermore, the elasticity of the liquid medium can also hinder the foam ripening process. For example, we saw that a gelified elastic continuous phase can prevent the coarsening of monodisperse bubble packings [1], but how the presence of a viscoelastic medium among the bubbles impacts on the foam coarsening rate and structure is still an open question, that we shall address in chapter §7. In order to do that, we shall use concentrated O/W emulsions as the continuous phase of our foams. In fact, in chapter §5 we saw that if their droplet volume fraction is higher than close packing, such dense biliquid dispersions are yield-stress fluids, namely they can behave as elastic solids if the applied stress is lower than a threshold value. Moreover, their elasticity increases as we increase the internal phase volume fraction, which allows tuning their mechanical properties by simply varying the amount of dispersed oil. In chapter §7 we shall thereby probe the evolution of foamed dense emulsions, using the same quasi-2D plate-plate configuration as for the aqueous foams of chapter §6. We shall investigate the effect of an increasing emulsion viscoelasticity on their bubble growth, with a special focus on the foam structure and the interplay between the latter and the coarsening evolution. We shall also give preliminary insights on the influence of the liquid fraction and the level of confinement on the evolution of such systems.

After characterising the bubble growth in quasi-2D foamed emulsions, in chapter §8 we shall address the question of how the presence of a viscoelastic emulsion among the bubbles affects their motion during coarsening. As the foam coarsens, indeed, the bubble size variations can give rise to locally imbalanced stresses inside the foam which eventually cause the bubbles to rearrange. We shall then probe the coarsening dynamics in foamed emulsions, to see the effect of the emulsion viscoelasticity on the bubble mobility. We shall start from 3D systems, in which the emulsion yield stress allows delaying the gravitational drainage for a time depending on the dispersed oil fraction. To get insights on the bubble dynamics we shall exploit a tracking-free technique which looks at image correlations in the Fourier space. We shall then go back to quasi-2D systems to quantify the rate of bubble rearrangements in coarsening foamed emulsions.

Finally, we shall see how we can use well-established methods in a novel way to both generate and characterise aerated emulsions in a single step. Because of the potential antifoam activity of free oil discussed in section §5.3.1, these three phase systems are traditionally prepared in two different steps, consisting of either pre-emulsifying the oil and then aerating the emulsion, or in preparing an emulsion and a foam which are subsequently mixed. In chapter §9 we will investigate the outcome of a one-step generation of aerated emulsions in which the oil, the gas and the surfactant solution are simultaneously mixed all together. If foams are commonly turbid because of the light scattering at their inner interfaces, in aerated emulsions this turbidity is further enhanced by the presence of droplets among the bubbles. Estimating the bubble size in such systems when both drops and bubbles are in the micrometric regime is typically done with traditional microscopy techniques [39] which are however time consuming. We shall then see how, under certain conditions, we can take advantage of laser diffraction to assess not only the drop but also the bubble size in these composite systems in just a few seconds.

Part II

Experimental work

6 Quasi-2D aqueous foams

6.1 Introduction

In chapter §4 we saw that one of the mechanisms which can alter the structure of aqueous foams over time is a pressure-driven process that makes the gas diffuse from smaller bubbles to larger ones. We saw that, while in the limits of dry foams and dilute bubbly liquids the effects of coarsening are well understood theoretically, and verified experimentally, the ripening of foams at intermediate liquid fractions still lacks a unified theoretical description.

In this chapter, we shall probe the coarsening of aqueous foams at different liquid content in quasi-2D systems, made of a single layer of bubbles squeezed between two glass plates. We saw in section §4.1.1 that when such systems are ideal, their coarsening behaviour is well described by Von Neumann's law, which predicts the rate of size variation of a single bubble depending on its topology: whether the bubble shrinks or grows is dictated only by the number of its neighbours, while the rate magnitude also depends on the physical chemistry of the two foam phases.

As soon as we introduce some liquid in the foam, deviations from this law are observed. First experiments conducted in sealed Hele-Shaw cells, thus at constant liquid fraction, pointed out a sub-linear growth of the average area over time [47], ascribing this result to the gradual thickening of the Plateau borders. However, the exact value of the liquid fraction was not reported. Von Neumann's law was then recovered by leaving the foam in contact with a bath of its own solution so that the excess liquid was free to drain out as the foam coarsens [107]. This way, the size of the Plateau borders remains constant over time, being fixed by the balance between capillary and gravity forces, but the amount of liquid inside the foam is not constant: the volume liquid fraction decreases as the foam ripens. Experiments aiming to study the effects of an increasing foam wetness exist [97, 14], but they are performed in the latter experimental configuration: the rate of area growth is probed at different Plateau border sizes, thus changing the height ratio of thin films between adjacent bubbles. Theoretical models have been developed proposing a modified Von Neumann's law which accounts for the experimental observations: if the liquid fraction is not negligible, the growth rate of a single bubble also depends on its size and shape. While so-called *border-blocking* models [97], in which the gas diffusion through the Plateau borders is totally neglected, can well describe the behaviour of only slightly wet foams, a *border-crossing* model has been later proposed to account for the gas exchange through the bulk liquid phase [104], which can no longer be neglected in very wet foams where the height of the thin films is heavily reduced.

A version of this border-crossing model has been theoretically proposed also for the case of a constant liquid fraction, where the thin film area decreases over time [104]. However, all these models always assume that the decoration lemma holds for each bubble in the foam,

thus no contacts between the bubbles are lost, and so what happens at liquid fractions close to bubble unjamming is still an open question. Moreover, to our knowledge there are no experiments in the literature systematically testing the effect of an increasing, but constant over time, liquid volume fraction in such systems.

In this chapter, we thus experimentally probe the evolution of sealed quasi-2D aqueous foams that cannot drain their liquid over time, to study the effect of the Plateau border swelling on the global bubble growth rate. We shall start with already polydisperse foams in order to reduce the transient before the attainment of their self-similar growth regime (SSGR). Indeed, models rely on the assumption that foams are self-similar, thus comparison between experiments and theoretical predictions can be done only if the foams have reached their scaling state. After showing that our experimental approach allows reaching such SSGR quickly, by providing an in-depth characterisation of the foam structure, we will start from probing the evolution of moderately wet foams in which the thin films are still a considerable part of the lateral bubble surface. We shall then move our attention to even wetter foams, to see how the coarsening rate changes as we approach the thin film disappearance. In both cases, we shall compare our results with the existing models available in the literature. This work is done in collaboration with Benjamin Dollet (LiPhy, Université Grenoble-Alpes).

Beyond the investigation of the dry/wet foam transition itself, the experimental results reported in this chapter are an important reference for what we shall do in chapter §7, where the foam aqueous phase will be replaced with a viscoelastic fluid, but the coarsening process will be probed in the same configuration.

6.2 Experimental approach

6.2.1 Foaming solutions

Foam samples are generated by aerating two different aqueous solutions. The first one is a 10 vol% solution of Fairy®, that is a commercial brand of washing-up liquid, well known for creating very stable liquid interfaces. The ingredients are however not known, thus some of the samples are made with a more controlled solution of Sodium Dodecyl Sulphate (SDS, Sigma-Aldrich) at 30 g/L. This anionic surfactant has a molecular weight of 288.4 and a cmc of 8.2 mM, which corresponds to roughly 2.4 g/L. The concentration chosen is thus more than 10 times the cmc. In both cases the solutions are prepared with deionised water (Purelab®), where the absence of impurities is ensured by resistivity measurements (18.2 MΩ·cm for ultra pure water). In the case of SDS, the solution is freshly prepared and used within one day to avoid surfactant hydrolysis, by which it forms dodecanol, an alcohol that because of its high surface activity would compete with SDS at the interface.

6.2.2 Foam generation

Three-dimensional foams are generated with the double-syringe method [40]. As sketched in figure 6.1, this technique consists in partially filling a first syringe (60 mL, Codan Medical) with a given amount of foaming solution, and a second one with air, in proportions corresponding to the desired foam liquid fraction $\varepsilon = V_{\text{liq}}/(V_{\text{liq}} + V_{\text{gas}})$. The two syringes are then connected with a double female luer lock and the syringe plungers are manually pushed back and forth 30 times, at which point all gas is incorporated inside the foaming solution. The time at which we stop pushing is taken as the time $t_0 = 0$ s of the foam age. Although the exact foaming mechanism is not completely clear, the gas breakup occurs at the syringe inlets which, having an inner diameter of 2 mm, act as constrictions in the flow path [40].

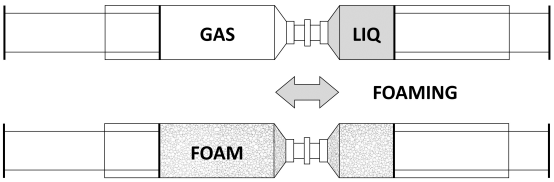

Figure 6.1 – **Double-syringe method.** Two syringes partly filled with air and foaming solution are connected, and foaming occurs by pushing both fluids repeatedly through the constriction given by the syringe inlets.

Given the possibility of choosing the volume of gas and liquid in advance, this foaming method intrinsically allows a good control of the foam liquid fraction. It has been shown that this technique ensures highly reproducible foam samples, with a bubble radius distribution peaked around 20 μm (in the presence of insoluble gas species) and a typical polydispersity of 40% which do not depend on the liquid fraction as long as the latter is in the foam regime [40]. Experiments in which syringes were pushed with a controlled velocity have reported no significant dependence of the final bubble size distribution on the pushing speed [40], which is why in this project we can safely push the syringes by hand. The final bubble

size is mainly affected by the physical chemistry of the foaming solution, more precisely it decreases upon increase of the solution viscosity [40].

We choose the double-syringe foaming method because it gives an initial bubble polydispersity very close to the value expected for a foam in its SSGR, with the exact purpose of shortening the duration of the foam transient state in our coarsening experiments.

6.2.3 From 3D to quasi-2D foams

The freshly-generated foam is carefully sandwiched between two glass plates (24 x 24 cm), separated by a rubber joint of thickness 1 mm or 2 mm which sets the cell gap d. The cell is then placed between two custom-made duraluminium frames which are tightly screwed together to keep the cell closed and the foam isolated from the environment. We highlight that in our experiments the foam cannot drain any liquid as it coarsens, which means that the liquid fraction, and not the Plateau border size, is kept constant over time. A scheme of the set-up is depicted in figure 6.2 (a).

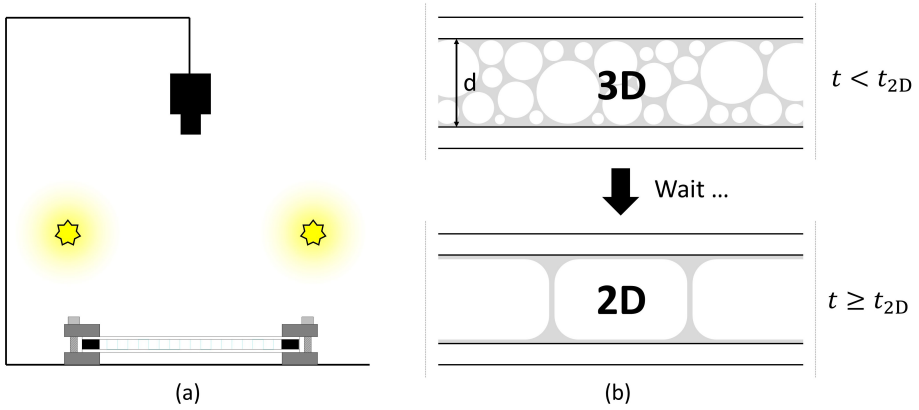

Figure 6.2 – **Experimental set-up.** (a) Sketch of the imaging set-up: the sealed Hele-Shaw cell is placed under a camera and illumination is provided from above by a square of LED lights. (b) Graphic illustration of the experimental approach: the initially 3D foam is let to coarsen until it becomes a monolayer of bubbles.

A square of LED lights provides rather uniform illumination from above without heating the sample. A camera (uEye, model UI-148xSE-C, resolution 2560x1920 pixels) equipped with a lens (Fujinon, 1:1.4/16mm HF16SA-1) is installed above the cell and pictures of the foam sample are taken at constant time intervals of 180 seconds at early coarsening stage, which are then extended to 1800 seconds at a later stage. For a second set of data a different camera is used (Basler acA3800-14um, resolution 3840x2748 pixels) with a lens (Tamron, 16mm F/1.4). All experiments are carried out at room temperature, namely at (20 ± 1)°C.

The foam obtained with the two syringes is clearly three dimensional, with a mean bubble size much smaller than the gap between the glass plates, thus the cell initially contains several layers of bubbles. Therefore, the foam is left to coarsen so that the bubbles grow over time until most of them become big enough to touch both the top and the bottom glass plates and the foam can be considered a bubble monolayer, as illustrated in figure 6.2 (b). The time t_{2D} that the foam takes before becoming in good approximation quasi-2D increases with the liquid fraction and is of the order of a few hours.

6.2.4 Image treatment

When viewed from above, rather dry 2D foams appear in photos as arrays of polygonal bubbles, outlined by a continuous network of curved boundaries corresponding to the surface Plateau borders. From these foam pictures we can obtain both geometrical and topological information by image analysis.

Image processing is performed with custom-made MATLAB scripts in different steps. The first step consists of cropping a region of interest where the illumination is homogeneous and adjusting the contrast. Images are then binarised and the so-called 2D foam skeleton is retrieved with a watershed algorithm. This skeleton outlines each bubble border with thin lines of thickness equal to 1 pixel. As long as the foam is dry enough so that bubble edges meet in three at each vertex, the skeleton appears as a lattice of polygonal cells corresponding to bubbles. Each edge lays in the middle of the surface Plateau border, thus pinpointing in good approximation the position of the thin film between adjacent bubbles. An example of contrast-adjusted foam picture with its skeleton overlaid is shown in figure 6.3 (a).

Foam skeletons are then processed with a MATLAB program, developed by Benjamin Dollet [35, 34] able to provide both geometrical and topological information on the bubble pattern, by measuring the area and the number of neighbours for each cell of the skeletonised picture. We remark that this measurement of the bubble size is based on the traditional approximation of negligible Plateau border size, as if the bubble was a prism of volume $A \cdot d$, while in fact part of this volume is occupied by the liquid of surface and vertical Plateau borders. The equivalent bubble radius is then calculated from the area as $R = \sqrt{A/\pi}$.

Since the foam samples are always polydisperse, at any time not all bubbles will be touching both glass surfaces. As explained in section §4.5 shrinking bubbles eventually reach a critical size at which they detach from the bottom plate and become three dimensional. Such tiny bubbles are not taken into account for the coarsening characterisation because their proportion of film area available for gas transfer is different. While most of them are lost during the image thresholding step, possible residual ones are discarded by putting a constant size threshold during the data treatment post image processing. Their contribution to the overall foam evolution is however negligible.

We remark that not only the surface Plateau borders but also the vertical triangular ones present at each bubble vertex become gradually thicker as the foam coarsens. At high liquid fractions, some of them eventually merge into liquid bridges so that the contact between some neighbouring bubbles is lost. Once this happens, these many-sided borders can be accidentally outlined as fake bubbles in the foam skeleton. An example of 4-sided Plateau border is shown in figure 6.3 (b).

In the foam samples discussed in this chapter, the number of such 4-sided Plateau borders is very low compared to the total number of bubbles (much less than 1%), so that even if some of them are occasionally counted as bubbles, the error on the mean bubble size is negligible. However, we remark that if the number of such many-sided vertical Plateau borders appearing in the foam skeleton became non-negligible, it would be necessary to discriminate between real bubbles and Plateau borders. One might think to put a simple threshold on the size to remove all the Plateau borders from the count of the areas, however these borders are thick and the risk is to lose also real small bubbles which are still 2D. An alternative and smart way to do that would be to consider the topology of these skeleton cells, as shown in figure 6.3 (c). If one observes only 3-sided and 4-sided Plateau borders, any

cell having a number of sides less than or equal to four will correspond to a Plateau border, whereas real bubble cells will all have more than four sides. In fact, each real bubble having n contacts will be decorated with n Plateau borders, which makes the measured number of sides of the bubble cell equal to $2n$. This way one could also retrieve the actual coordination number of each bubble. However, for this method to work properly it is necessary that *all* the foam Plateau borders are detected as polygonal cells on the picture, which is tricky around the tiny bubbles in our images. This is the reason why for our treatment we stick to the skeletonisation shown in figure 6.3 (a).

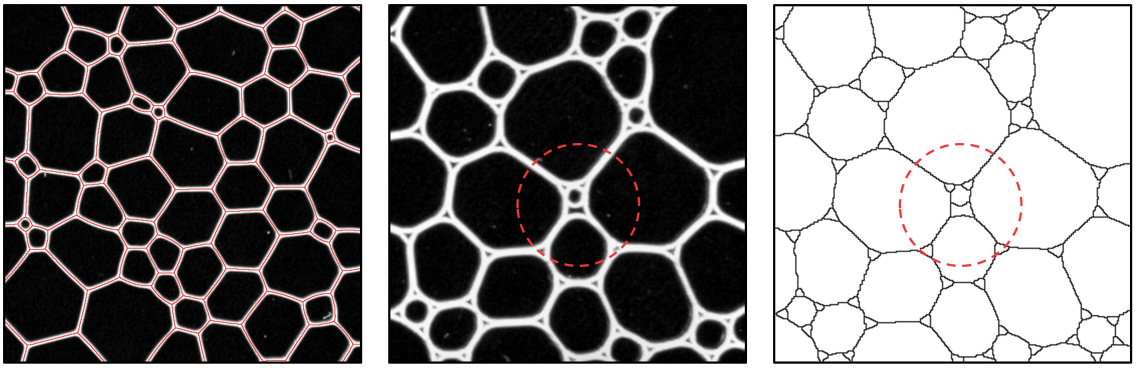

Figure 6.3 – **Image treatment.** (a) Example of overlay between the foam and its skeleton for a portion of sample made with Fairy solution at ε=10%. The edge size is 5 cm. (b) Example of 4-sided Plateau border appearing at late stage in the sample made with SDS solution at ε=15%. (c) Example of a different thresholding which would include the 3-sided and 4-sided Plateau borders in the skeleton. The discrimination between the two could be done on topological basis, as only cells having more than four sides represent real bubbles.

Surface liquid fraction

The assessment of the surface liquid fraction strongly depends on the sample illumination. As mentioned in section §3.2.2, in order to get the area actually wetted by the surface Plateau borders one should use a prism to collect only the light coming from the reflection on the surface thin pseudo-films. However, since in our samples the bubbles are millimetric and polydisperse, we should use a very large prism to cover a representative portion of the foam surface, as the Plateau border size is not homogeneous in the sample. Alternatively, one could imagine to scan the entire foam sample with a small prism in order to image enough bubbles. However, the precision gained from the correct imaging of the foam surface would be completely lost in border effects for each image. We thus measure the surface liquid fraction ε_s by cropping only the central portion of the foam pictures where the illumination is homogeneous, and then applying an automatic global threshold, so that we get ε_s as the ratio between the number of white pixels in the binarised picture and the total number of pixels in the cropped image. We shall use this method, even if it leads to a systematic underestimation of the real surface liquid fraction, as we shall be interested more in the variations of ε_s over time than in its actual value.

6.3 Results

To investigate the effect of a constant liquid fraction on quasi-2D foam coarsening, foams are generated at a given liquid fraction ε and then sandwiched between two glass plates, in order to monitor their coarsening evolution once they become bubble monolayers. Since foam self-similarity is a fundamental hypothesis behind every model we shall consider, before probing how the average bubble size evolves over time in our samples, we show how our experimental approach allows attaining the SSGR in a relatively short time.

6.3.1 Self-similar growth regime

As discussed in section §4.4, it is well known that aqueous foams which have had enough time to coarsen, eventually reach a SSGR in which by definition all the dimensionless statistical distributions become time-invariant. This means that the properties of both topological and normalised geometrical distributions must become stationary. The existence of such scaling state, which we recall is intended only in two dimensions, has been experimentally shown in quasi-2D soap froths [47, 107, 97].

In order to shorten the transient period before reaching this SSGR, we consider foams which are already polydisperse since their generation. The double-syringe technique generates foams with a polydispersity of roughly 40% [40], which is very close to the asymptotic value expected in 3D foams [117].

In this section, we shall characterise both geometrical and topological features of our quasi-2D foam samples. In order to have statistics high enough for this characterisation, we use a spacing of 1 mm between the plates which, combined with the large cell dimensions, translates into quasi-2D foams having a very high initial number of bubbles, of the order of 10^4.

To probe the consistency of both geometrical and topological distributions, we shall first plot their evolution over time for a qualitative visual assessment, and we will then check quantitatively the time invariance of the polydispersity and the distribution moments typically considered in the literature. We stop when the foam sample reaches a number of bubbles equal to 1000, corresponding to a time that we call $t_{N=1000}$, as the results afterwards might be affected by a lack of statistics.

For this characterisation, we consider three coarsening samples made with Fairy solution and having liquid fractions ε equal to 8%, 10% and 15% respectively, and a fourth sample stabilised by SDS having a liquid fraction of 15%.

Geometry

The first quantity that we measure from the skeletonised foam images is the area A of each single bubble in the pattern. We thus start by plotting in figure 6.4 the evolution of the distribution of bubble areas, normalised by their ensemble average value $\langle A \rangle$ at each time, for each sample. For a better visualisation the grey level of the curves is proportional to the foam age, they thus become darker over time.

As we can see from the graphs, the shape of the distribution shows no perceptible change over time, which moreover looks very similar between the different samples. To check that the distribution is stationary, one traditionally plots the time evolution of the parameter $\langle A^2 \rangle / \langle A \rangle^2$, which is reported in figure 6.5 for our samples.

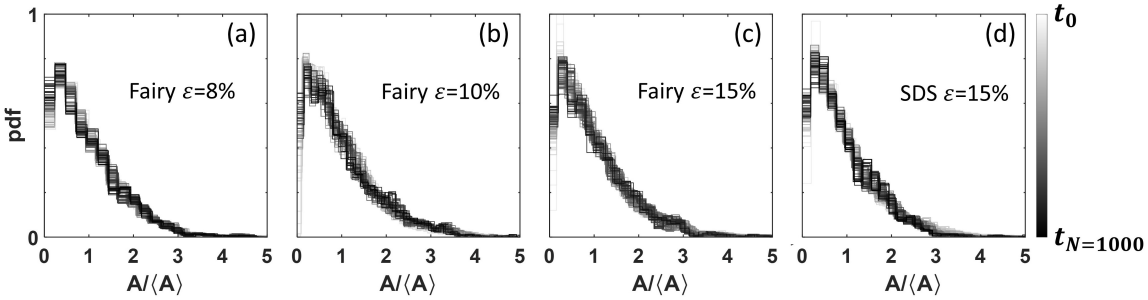

Figure 6.4 – **Normalised bubble area distribution.** Time evolution of the dimensionless $A/\langle A\rangle$ distribution for the samples at different liquid fractions. We can see that the shape of the area distribution is qualitatively similar in all the samples considered.

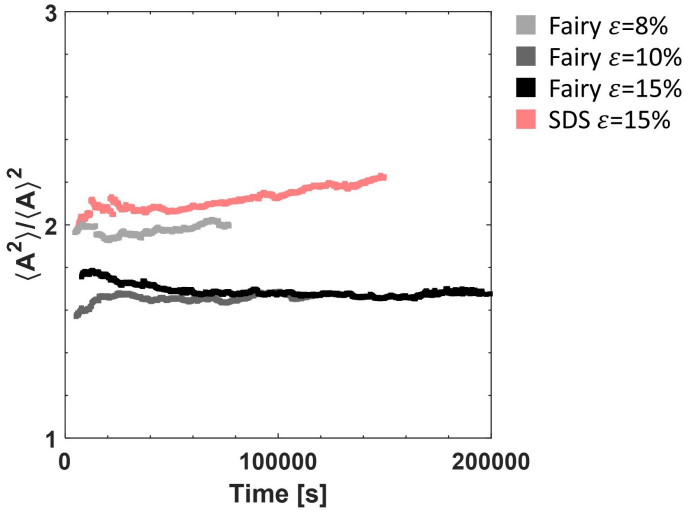

Figure 6.5 – **Time invariance of the dimensionless bubble area distributions.** Temporal evolution of the parameter $\langle A^2\rangle/\langle A\rangle^2$ for the different foam samples.

We can see that the two Fairy samples at ε =10% and 15% show values of $\langle A^2\rangle/\langle A\rangle^2$ which stabilise around 1.7, while the other two exhibit larger values around 2. Our results are in agreement with the ones in the literature, where a value of 1.72±0.25 has been reported [97]. However, the discrepancy between the two couples of samples is likely due to the presence of a few large bubbles created during the closure of the foam cell of the samples exhibiting a larger $\langle A^2\rangle/\langle A\rangle^2$, plus a few coalescence events occurring at early stage in the SDS sample as visible from the coarsening videos of the image aquisition. As shown in figure 6.6, these bubbles have a size much larger than the average, they thus affect the tail of the distributions resulting in a greater $\langle A^2\rangle/\langle A\rangle^2$.

The shape of the normalised area distributions is in good qualitative agreement with the one reported in the literature [46], which is shown in figure 6.7 (a). We remark that if the foam is not too wet, the area distribution in quasi-2D systems corresponds in first approximation to the distribution of bubble volumes, as the latter is simply given by $V = A{\cdot}d$, where d is the cell thickness which is constant. The area distribution is in fact observed to have a shape similar to the volume distribution expected in self-similar 3D foams [117]. Even though the experimental area distributions of coarsening quasi-2D foams have been

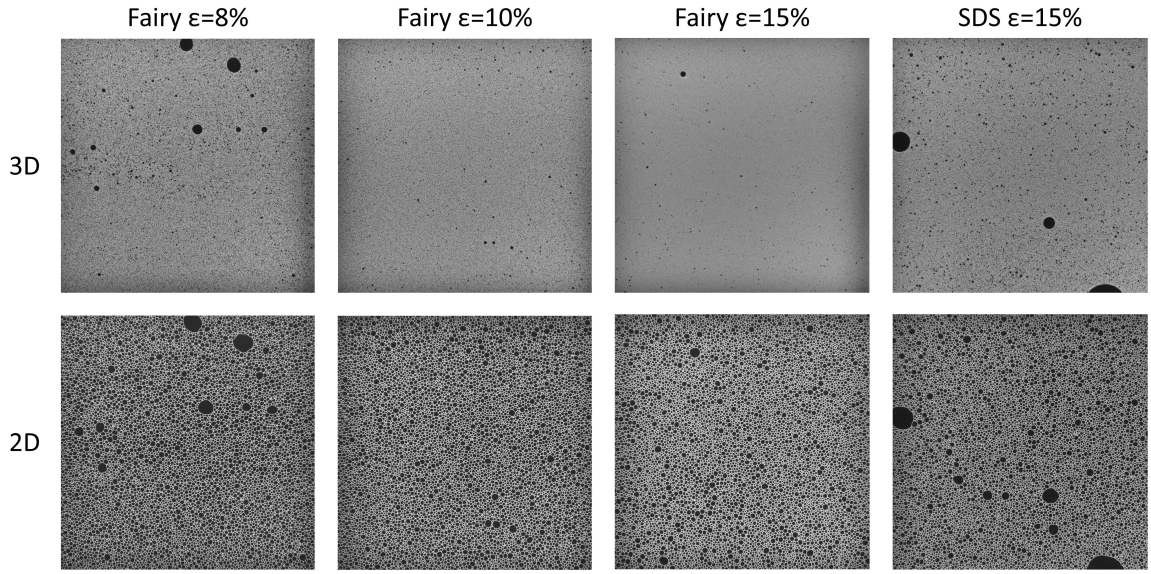

Figure 6.6 – **Extraneous large bubbles.** The top row shows the appearance of the different foam samples right after closing the cell, thus when the foam is still 3D. We can see that, while the samples Fairy ε=10% and ε=15% are highly homogeneous, the two samples Fairy ε=8% and SDS ε=15% present a few macroscopic bubbles generated while sandwiching the foam between the two glass plates. The difference between such large bubbles and the rest of the foam is still visible in the second row when the samples have just become quasi-2D. In the bottom frame of sample SDS ε=15% we can also recognise a few larger bubbles which are the result of some coalescence events, as they are not present on the top. The edge size of each frame is 15 cm.

found to be well described in the late stage by a log-normal distribution [21], a compressed exponential for the cumulative distribution function of the normalised areas has been more recently proposed [97], giving the following equations for the cumulative and differential probability distributions:

$$\text{cdf} = 1 - \exp\left\{ - \left[\Gamma\left(1 + \frac{1}{\alpha}\right) \frac{A}{\langle A \rangle} \right]^{\alpha} \right\} \tag{6.1}$$

$$\text{pdf} = \alpha \Gamma\left(1 + \frac{1}{\alpha}\right)^{\alpha} \left(\frac{A}{\langle A \rangle}\right)^{\alpha - 1} \exp\left\{ - \left[\Gamma\left(1 + \frac{1}{\alpha}\right) \frac{A}{\langle A \rangle} \right]^{\alpha} \right\} \tag{6.2}$$

where α is a fitting parameter found to be equal to 1.21 $\pm$ 0.05 [97]. We can thus quantitatively compare our results with this prediction. As an example, in figure 6.7 we plot in black the pdf (a) and the cdf (b) for the sample made with Fairy at ε = 10% at time t = 12 hours, with the corresponding curves given by equations (6.2) and (6.1) displayed in red. We can see that the agreement is remarkable, especially since we used exactly the same value for the fitting parameter α reported in [97], with no adjustment. The quality of the comparison can be better appreciated from the cdf, as the latter does not depend on the histogram binning, and we can see that the two curves perfectly overlap.

Let us now consider the distributions of the bubble radii, normalised by their average value $\langle R \rangle$, which are plotted in figure 6.8 for each sample.

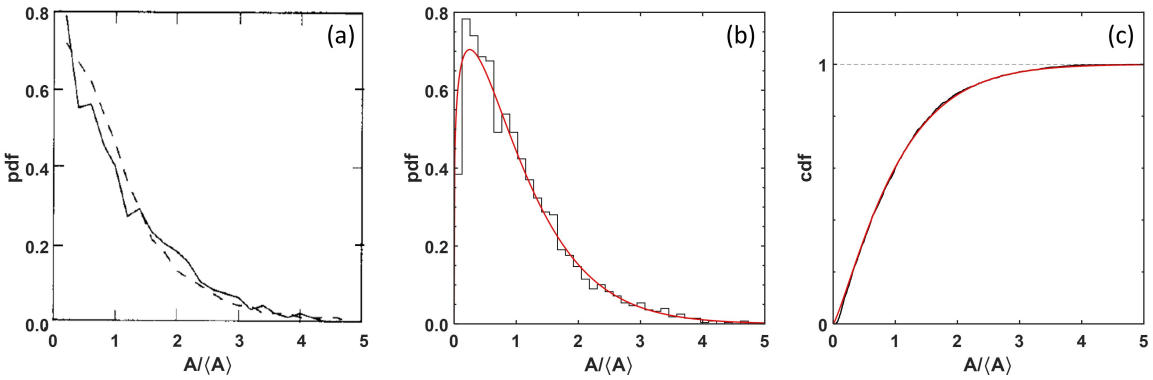

Figure 6.7 – **Comparison with the literature.** (a) Normalised area distribution obtained experimentally (solid line) and with Potts model simulations (dashed line). Picture adapted from [46]. (b-c) Probability and cumulative distribution functions of $A/\langle A\rangle$ for the sample Fairy at ε=10% after 12 hours (black lines) compared with equations (6.2) and (6.1) (red lines). The sample has still more than 2000 bubbles.

We can see that the normalised $R/\langle R\rangle$ distribution also becomes stationary over time in each sample. We can also notice that the tails due to the presence of extraneous large bubbles in the samples Fairy ε=8% and SDS ε=15% are now visible. To verify the time invariance of this distribution, its second central moment μ_2^R is traditionally considered in quasi-2D foams, defined as:

$$\mu_2^R = \left\langle \left(\frac{R}{\langle R\rangle} - 1 \right)^2 \right\rangle \tag{6.3}$$

which represents its variance and thus reflects the width of the distribution. However, one could similarly look at the bubble polydispersity, defined as:

$$p = \frac{\sqrt{\langle R^2\rangle - \langle R\rangle^2}}{\langle R\rangle} \tag{6.4}$$

The time evolution of both μ_2^R and p are shown in figure 6.9, where we can see that, after a slight and short initial increase, both parameters stabilise around a constant value for each sample. These values are very close to the ones found in the literature: the second moment μ_2^R has been reported to be around 0.16 for 2D foams [41], while the expected [117] and measured [6] polydispersity in self-similar 3D foams ranges between 0.45 and 0.5.

The consistency of the geometrical parameters discussed in this section is a necessary, but not sufficient, condition for claiming that the SSGR is attained. Indeed, we must ensure that the foam samples are also topologically self-similar.

Topology

As discussed in section §3.1, the average number of sides of a bubble $\langle n\rangle$ is expected to be equal to 6 for an infinite dry 2D foam. However, a slightly lower value is typically registered in real foams due to the finite size of the bubble pattern. The time evolution of $\langle n\rangle$ in our samples is reported in figure 6.10 (a), from which we can see that it stabilises around a value $\simeq 5.97$, consistently with previous results reported in the literature [46, 97].

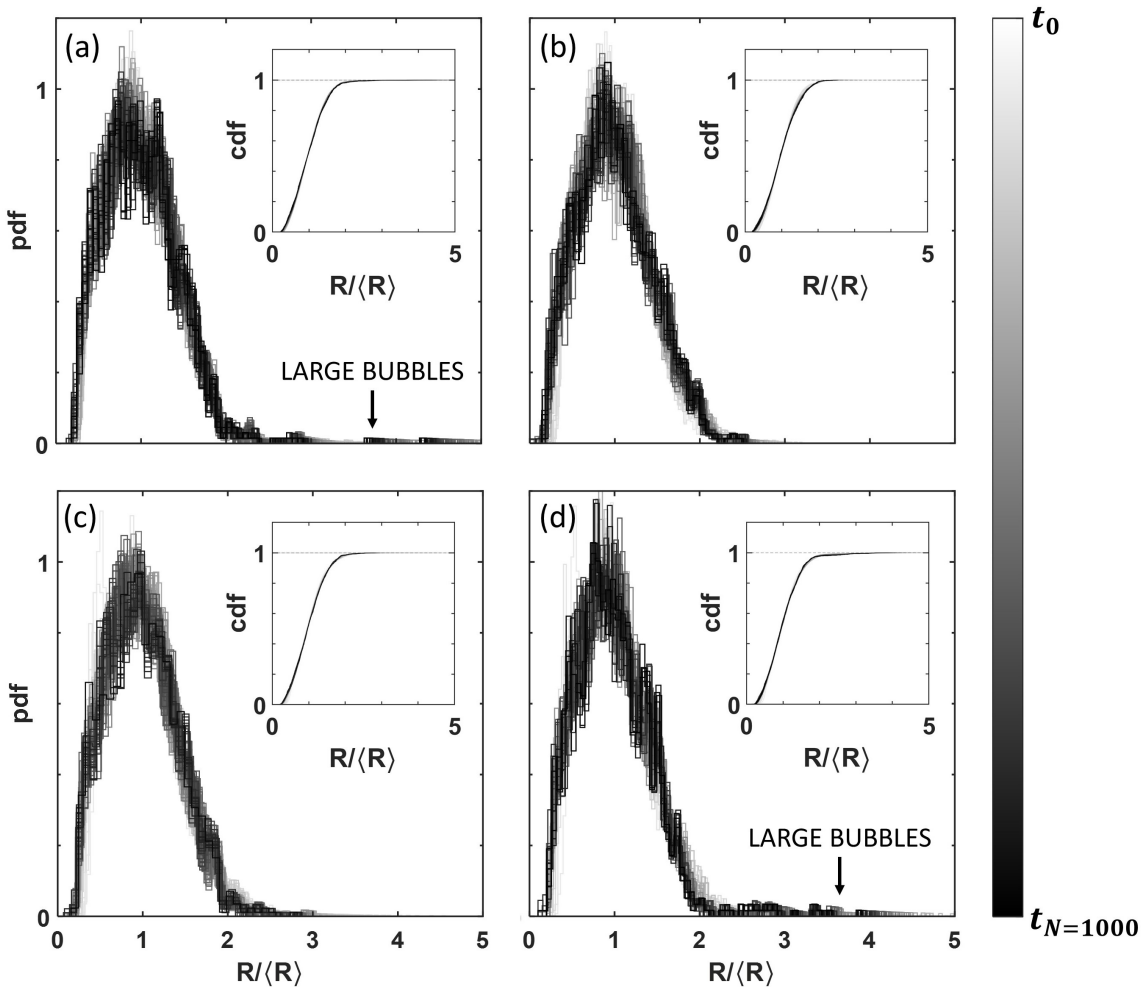

Figure 6.8 – **Normalised bubble radius distribution.** Time evolution of the dimensionless $R/\langle R\rangle$ distribution for the samples Fairy ε=8% (a), Fairy ε=10% (b), Fairy ε=15% (c), and SDS ε=15% (d). In (a) and (d) the presence of large bubbles is visible on the tail at large $R/\langle R\rangle$. The insets show the corresponding cumulative distributions.

As an example, we report in figure 6.10 (b) the time evolution of the n distribution for the Fairy sample at ε=10%. We can see that the distribution is centered around n=6 and its shape is consistent with literature results [46, 97]. The time invariance of such discrete distribution is usually checked by looking at its central moments of second, third and fourth order, where the k-th order moment is defined as:

$$\mu_k = \langle (n - \langle n \rangle)^k \rangle \tag{6.5}$$

We thus plot in figure 6.10 (c,d,e) the time evolution of the moments μ_2, μ_3, and μ_4 for each of our samples. We can see that the second moment of the distribution μ_2 stabilises around values between 1.6 and 2.2, thus consistent with the values 1.5±0.2 [46] and 2.1±0.2 [41] present in the literature.

Concerning the higher order moments, the results in the literature are usually noisy due to poor bubble statistics, with values of μ_3 roughly around 1.5 and μ_4 around 10 [46].

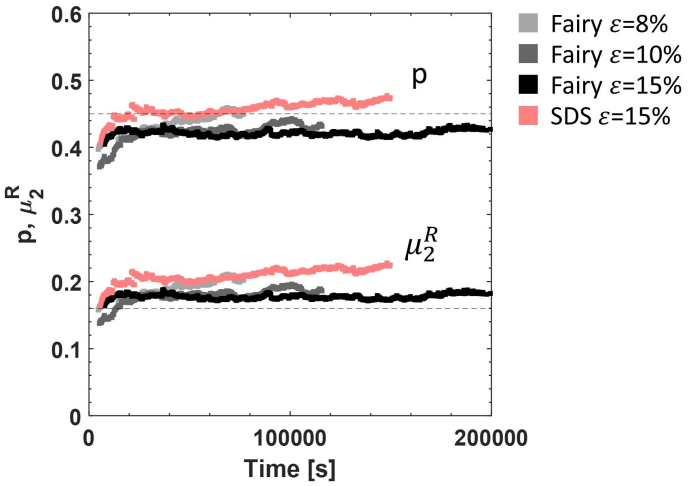

Figure 6.9 – **Width of the dimensionless radius distribution.** Polydispersity p and second moment μ_2^R of the distribution for the different samples. The dashed lines indicate the reference value of μ_2^R obtained from 2D foam simulations [41] and the polydispersity measured in 3D self-similar foams [6].

When comparing μ_3 and μ_4 in our foams, we can see that for the samples presenting the extraneous large bubbles the values are higher than the ones observed in the other two samples. These higher order moments are indeed more sensitive to data on the tails of the distribution, as the differences from the mean value $\langle n \rangle$ are raised to power 3 and 4 respectively. Indeed, if for instance we remove the few largest bubbles that are clearly not coming from the foam evolution for the two samples SDS ε=15% and Fairy ε=8%, we can see in figure 6.10 (f,g,h) that the moments jump back to lower values, closer to the ones observed in the other samples at the same or closer liquid fraction. We remark that even if the large bubbles are accidentally introduced during the cell closing, once they are there they contribute to the sample evolution. For this reason they are not discarded in the coarsening analysis.

Size-topology correlation

We now look at the correlation existing between geometry and topology, more precisely between the area of the bubbles and their number of sides. We first plot in figure 6.11 the evolution of the distributions of n-sided bubble areas A_n, normalised by the global average area $\langle A \rangle$, for the sample made with Fairy at $\varepsilon = 10\%$. Once again, we plot them with a grey scale proportional to the foam age. We can see that the shapes of these distributions are in good qualitative agreement with the ones found in the literature [46], which are reported in the same figure as insets for a direct visual comparison.

In figure 6.11 we also check the correlation between the number of sides n and the normalised average area $\langle A_n \rangle / \langle A \rangle$. We can see that the latter scales in good approximation with n^2, while the normalised average radius $\langle R_n \rangle / \langle R \rangle$ is observed to scale linearly with n for each sample, consistently with the literature [46, 97].

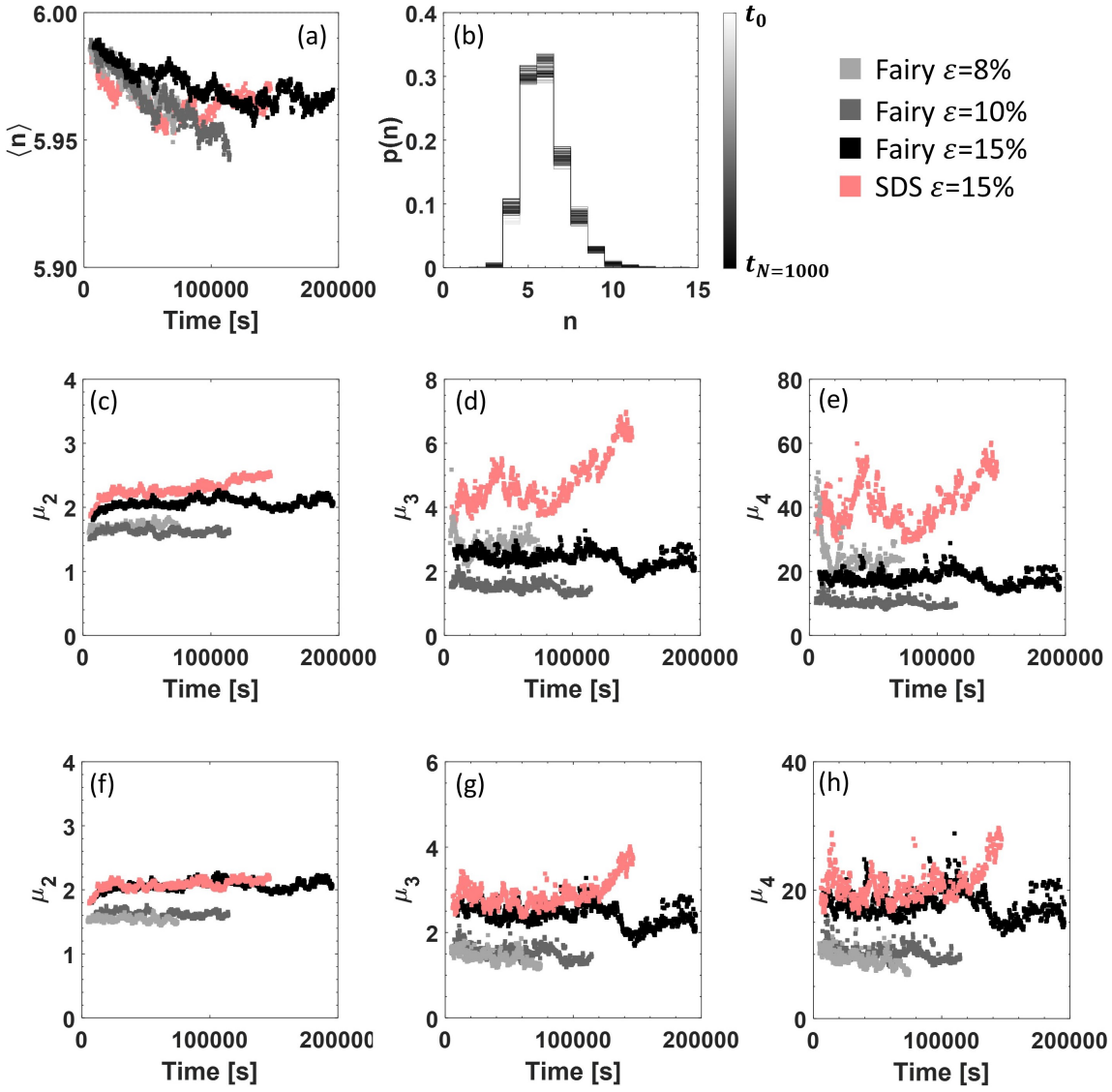

Figure 6.10 – **Bubble topology.** (a) Time evolution of the bubble average number of sides. (b) Example of evolution of the distribution of the number of sides for the sample made with Fairy at ε=10%. (c,d,e) Time evolution of the second, third and fourth central moments of the n distribution for the different samples. (f,g,h) The same moments recalculated after removing the extraneous large bubbles from the samples SDS ε=15% and Fairy ε=8%. We can see that their removal results in lower moment values, comparable to the ones registered in the samples having the same or closer liquid fraction but no accidental large bubbles. We can notice that slightly higher values are registered for wetter foams.

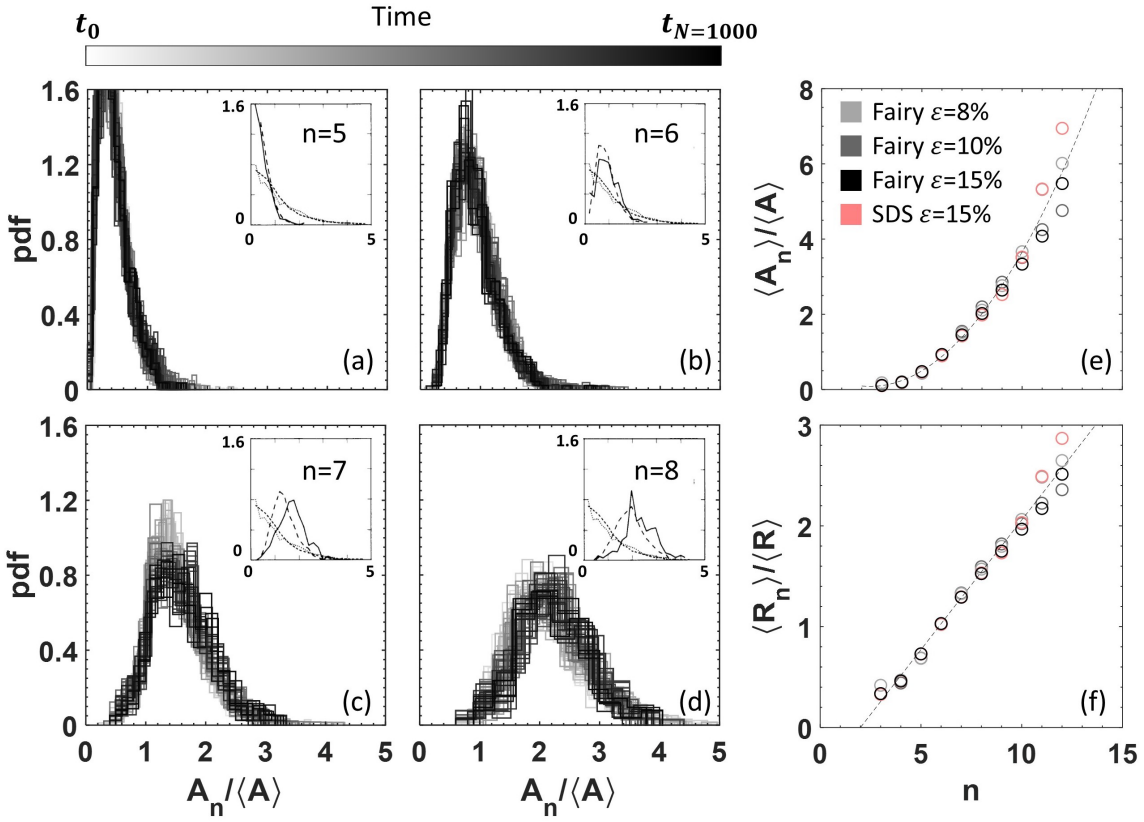

Figure 6.11 – **Size-topology correlation** (a,b,c,d) Evolution of the $A_n/\langle A\rangle$ distribution for different n. The insets show the asymptotic distribution of $A_n/\langle A\rangle$ reported in the literature for experimental foams (solid lines) and Potts model simulations (dashed lines), together with the global $A/\langle A\rangle$ distribution [46]. (e) $\langle A_n\rangle/\langle A\rangle$ versus n. The dashed line represents a quadratic fit. (f) Correlation between $\langle R_n\rangle/\langle R\rangle$ with n. The dashed line represents a linear fit.

6.3.2 Coarsening at constant liquid fraction

Now that we saw that our foam samples attain their SSGR within a couple of hours after becoming quasi-2D, we probe the coarsening evolution of a quasi-2D foam at constant liquid fraction, to see the effect of the Plateau border inflation over time.

We generate a foam with Fairy solution at a liquid fraction ε=10%, which is then enclosed within two glass plates with a spacing of 2 mm. The size of the gap and the liquid fraction are chosen in order to ensure the presence of thin films between adjacent bubbles. In figure 6.12 we report the time evolution of the average bubble area, together with the one of the total number of bubbles in the sample. The time considered here is the time elapsed after foam generation, thus t_0=0 marks the time at which we stop pushing the syringe plunger. From the graph of $\langle A(t)\rangle$ we can see that it seems to grow in good approximation linearly over time. However, when plotted in a logarithmic scale we can see that the mean bubble growth is actually sublinear, as observed also in previous experiments carried out in sealed Hele-Shaw cells [47]. The mean bubble area appears to grow in time as a power law with exponent close to the value 2/3 expected for bubbly liquids, even though neighbouring

bubbles share thin films. The reduced bubble growth rate compared to the one of a dry foam is the first clear hallmark of the presence of the Plateau borders, which increase their size over time.

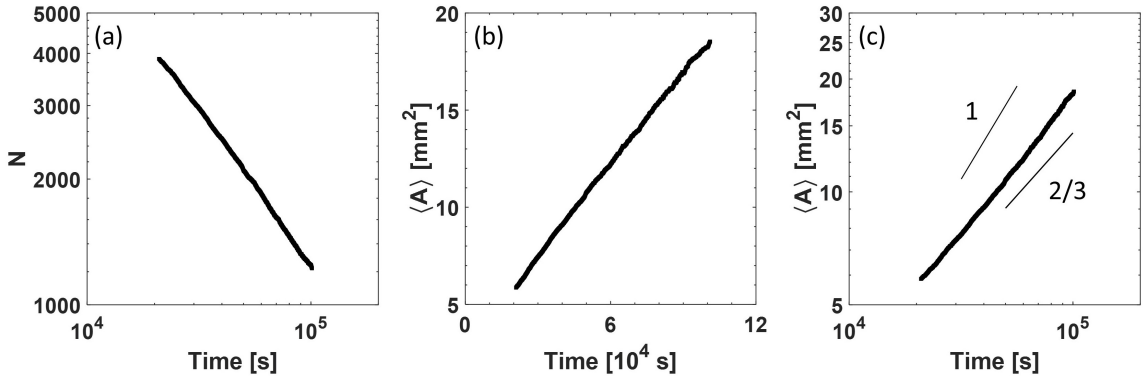

Figure 6.12 – **Coarsening evolution.** (a) Time evolution of the total number of bubbles in the sample. (b) Mean bubble area growth in linear scale. (c) Mean bubble area evolution in logarithmic scale, where we can see that the growth is clearly sublinear.

Single bubble evolution

The gradual swelling of the Plateau borders impacts also the evolution of single bubbles. To see this, we select different 4-sided bubbles at different foam ages and we follow their shrinkage over time. The area evolution measured for three of them is reported in figure 6.13 (a) as example, where we can see that the area of each bubble, after an initial linear decrease, starts deviating from linearity. This deviation from Von Neumann's law has been recently studied in wet foams at constant capillary pressure [14], showing that the bubble coarsening rate also depends on the bubble size and shape. It has been shown that the deviation of $\mathrm{d}A/\mathrm{d}t$ from linearity can be described by introducing a term linked to the bubble shape through a circularity parameter inside Von Neumann's law. In our experiments, the image resolution of the camera is exploited to have high bubble statistics, thus, as we shall better explain in section §7.3.5, the small size of the bubbles in our frames does not allow an accurate estimate of the bubble perimeter. The impossibility to accurately calculate shape parameters linked to the bubble perimeter, like the bubble circularity, prevents the comparison of the experimental evolution of single bubbles with the existing model prediction. However, we can calculate the rate $\mathrm{d}A/\mathrm{d}t$ for each bubble in its initial part where it is in good approximation linear. We can see in figure 6.13 (b) that the absolute value of the shrinking rate $\mathrm{d}A/\mathrm{d}t$, measured for single bubbles at different foam age, shows a global decrease over time, meaning that the bubbles shrink more slowly due to the gradual reduction of the film area during coarsening. The scatter in the data is due to the fact that the coarsening rate is highly influenced by the bubble shape, that here we are not considering.

Changing the gas phase

To show that the slowing down of coarsening is only due to the structural evolution of the quasi-2D foam, we repeat the same experiment by partially changing the foam physical

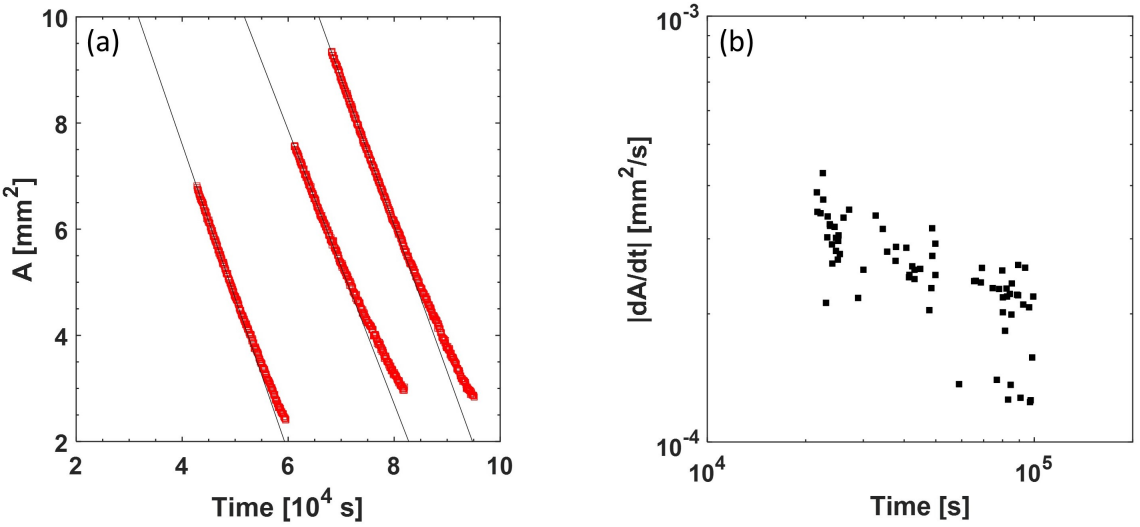

Figure 6.13 – **Single bubble evolution.** (a) Example of evolution of three single 4-sided bubbles, from which we can see the deviation from Von Neumann's linear prediction. (b) Absolute values of $\mathrm{d}A/\mathrm{d}t$ for several 4-sided bubbles at different foam age. Despite the scatter in the data, due to the neglect of the bubble shape, we can distinguish a global decreasing trend over time.

chemistry. For instance, we can think to speed up the coarsening by changing the foam gas phase, replacing air with a gas having a higher solubility in water. Air is in fact a mixture of different gases, including mainly nitrogen (78%), oxygen (20%), argon (1%) and other components present in minor quantities. The coarsening rate in foams made with gas mixtures is set by the slowest component, which in the case of air is nitrogen.

We can choose for example to generate a foam sample using only argon inside the bubbles. The solubility of argon in water is reflected by its Henry constant He which, as it can be seen from the values reported in table 6.1, is higher than the one of nitrogen. The film permeability, that we recall is defined as $\kappa{=}D_f He/l$, depends not only on the Henry constant but also on the gas diffusion coefficient D_f, as well as on the film thickness l. The diffusion coefficient D_f for argon and nitrogen in water at 25°C are also reported in table 6.1. Therefore, we can see that, for the same film thickness, the film permeability in a foam made with argon is roughly a factor 2.9 higher than the one for a foam made with air, which translates into a higher coarsening rate.

Gas	D_f [m^2/s]	He [mol kg^{-1} bar^{-1}]
Ar	$2.5 \cdot 10^{-9}$	0.0014
N_2	$2 \cdot 10^{-9}$	0.0006

Table 6.1 – **Film permeability.** Diffusion coefficient and Henry constant for argon and nitrogen in water at 25°C. Values taken from [76] and [102] respectively.

We thus generate a foam with Fairy solution at the same liquid fraction ε=10%, but using argon inside the double-syringe. The foam is then enclosed within two glass plates with the same gap of 2 mm, while constantly blowing argon on the cell under a fume

cupboard. Since argon is heavier than air, it remains low, so that the foam is not expected to enter in contact with air during the cell filling. Figure 6.14 reports the time evolution of the average bubble area and radius for the argon sample, compared with the corresponding curves of the sample made with air. We can see how once again the growth of the mean bubble area is sublinear and we get an average radius evolution resembling a power law $\langle R \rangle \sim t^{1/3}$. However, we can see that the curve of the sample made with argon starts at earlier time, meaning that it becomes 2D earlier than the sample made with air, reflecting a faster coarsening rate. To compare the difference in the coarsening rate, we can evaluate the gap between the two growth curves of the mean area at a given time, indicated in the graph as Δ. From the curves we obtain $\Delta \simeq 1.5$, thus a value smaller than the ratio between the two film permeabilities. This discrepancy could be due to some contamination of argon with air, either during the sample preparation or during the image acquisition. Indeed, even small traces of nitrogen could slow down the coarsening significantly.

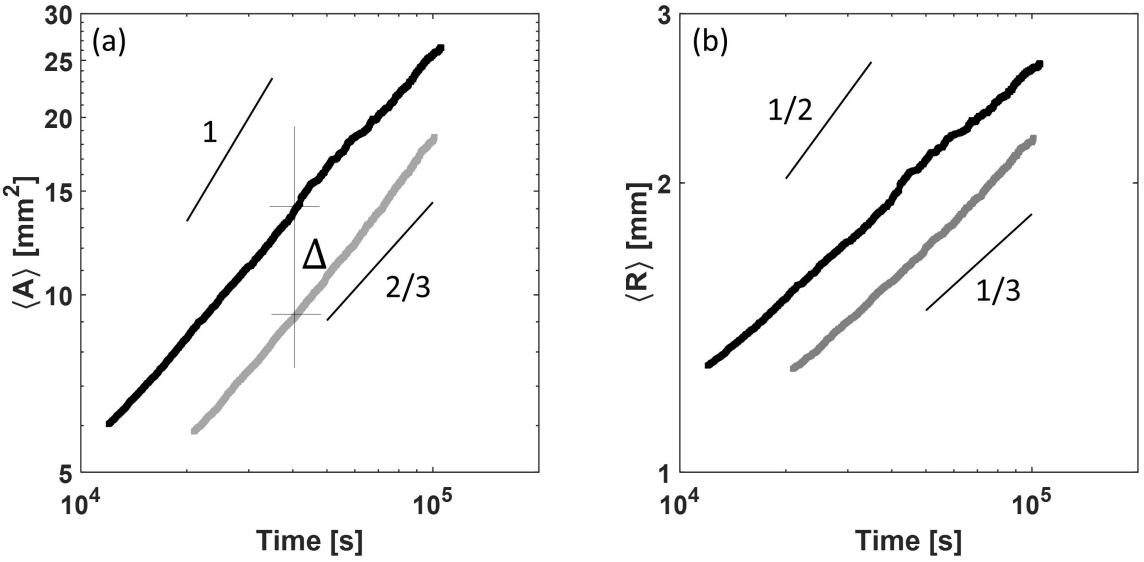

Figure 6.14 – **Foam coarsening with argon.** (a) Time evolution of the mean bubble area for the foam made with argon (black) and air (grey). (b) Time evolution of the mean bubble radius for the two samples.

Comparison with a border-blocking model

The gap of 2 mm used for these experiments ensures the presence of thin films for the entire duration of the image aquisition. However, we observed a sublinear growth of the mean bubble area, so that the average bubble radius appears to grow in time as a power law $\langle R \rangle \sim t^{1/3}$, as expected for bubbly liquids in which bubbles are well-separated from each other. This reduced coarsening rate can be ascribed to the Plateau border inflation. To check that, in this section we compare the observed evolution with a simplified border-blocking model, which accounts for the gradual reduction of the thin film area between adjacent bubbles but which neglects the gas diffusion through the Plateau borders.

Let us proceed by steps. It is well known that for an ideal (thus perfectly dry) 2D foam, Von Neumann's law holds both locally for single bubbles and on average, thus the mean

bubble area grows linearly over time, which means that we can write the following equation:

$$\frac{\mathrm{d}\langle A\rangle}{\mathrm{d}t} = \beta \tag{6.6}$$

where β is a positive constant. In our case, however, the foam is not ideally dry, as the liquid fraction ε is not negligible. Because of the presence of the surface Plateau borders the height of the thin films does not span the entire gap d between the plates: their reduced height can be written as $h = d - 2r_{\mathrm{PB}} < d$, where r_{PB} is the size of the surface Plateau borders.

If we neglect the presence of the vertical Plateau borders and the nodes, at each instant we can write the following scaling relation linking the liquid fraction, the average size of the Plateau borders and the mean size of the bubbles:

$$\varepsilon = \alpha\frac{r_{\mathrm{PB}}^2}{dR} = \alpha'\frac{r_{\mathrm{PB}}^2}{dA^{1/2}} \tag{6.7}$$

where α and α' are constants of proportionality enclosing the geometrical prefactors which account for the actual shape of the Plateau borders. According to this approximation, the vertical portion of thin films will be given by:

$$\frac{h}{d} = 1 - \frac{2r_{\mathrm{PB}}}{d} = 1 - 2\left(\frac{\varepsilon}{\alpha' d}\right)^{1/2} A^{1/4} \tag{6.8}$$

Since the foam is coarsening at a constant liquid fraction, equation (6.7) shows that as the foam coarsens, and thus the mean bubble area increases, the size of the Plateau borders r_{PB} also increases. This means that the foam evolution will be slower than the one predicted by Von Neumann's law, as the proportion of thin films h/d gradually decreases over time. If we assume that the gas transfer occurs only through the thin films (border-blocking assumption), we can thus rewrite equation (6.6) as follows:

$$\frac{\mathrm{d}\langle A\rangle}{\mathrm{d}t} = \beta\frac{h}{d} = \beta\left(1 - \frac{2r_{\mathrm{PB}}}{d}\right) = \beta\left[1 - 2\left(\frac{\varepsilon}{\alpha' d}\right)^{1/2} A^{1/4}\right] \tag{6.9}$$

where we corrected the ideal area growth rate β by the actual portion of film available for gas transfer. We remark however that equation (6.9) considers only the film reduction due to the surface Plateau borders, while it neglects the further area reduction due to the presence of the vertical ones at each bubble vertex. We can now think of introducing a critical bubble area A_c at which the two surface Plateau borders merge and thus the thin vertical films vanish. This happens when $r_{\mathrm{PB}} = d/2$, thus from equation (6.7) we obtain:

$$A_c = \frac{\alpha'^2 d^2}{16\varepsilon^2} \tag{6.10}$$

and introducing this relation in equation (6.9) we can write:

$$\frac{\mathrm{d}\langle A\rangle}{\mathrm{d}t} = \beta\left[1 - \left(\frac{A}{A_c}\right)^{1/4}\right] \tag{6.11}$$

As we can see from this relation, once the foam reaches the critical area A_c the coarsening rate goes to zero, thus leading to an unphysical arrest of coarsening due to the film disappearance. In the proximity of A_c one should thus replug the gas transfer through the

Plateau borders in order to describe the coarsening rate correctly. In the samples that we are considering in this section, the liquid fraction is ε=10% and the gap is d=2 mm, thus from (6.10) we obtain a critical area of roughly 58 mm^2 as the geometrical prefactor α' can be calculated to be approximately 1.52 for a rather dry foam [42]. From the mean area evolution showed in figure 6.14 (a) we see that the foam samples do not reach this critical area, we are thus far away from the film vanishing.

To simplify the notation, we can make equation (6.11) dimensionless by introducing a dimensionless time $\bar{t} = \beta t/A_c$ and a dimensionless area $\bar{A} = A/A_c$, so that it becomes:

$$\frac{\mathrm{d}\bar{A}}{\mathrm{d}t} = 1 - \bar{A}^{1/4} \tag{6.12}$$

We can solve this differential equation under the initial condition $\bar{A}(t = 0) = \bar{A}_0$, obtaining the following solution:

$$\bar{t} = \int_{\bar{A}_0}^{\bar{A}} \frac{\mathrm{d}\bar{A}}{1 - \bar{A}^{1/4}} = 4(\bar{A}_0^{1/4} - \bar{A}^{1/4}) + 2(\bar{A}_0^{1/2} - \bar{A}^{1/2}) + \frac{4}{3}(\bar{A}_0^{3/4} - \bar{A}^{3/4}) + 4\ln\frac{1 - \bar{A}_0^{1/4}}{1 - \bar{A}^{1/4}} \tag{6.13}$$

This gives an implicit relation $\bar{t}(\bar{A})$ that we can compare with our experimental results. From our experiments we estimate the value A_0 by fitting $A(t)$ with a power law function, and we consider β to be roughly $3.6{\cdot}10^{-4}$ mm^2/s, as the effective diffusion coefficient estimated in quasi-2D drained foams made of the same Fairy solution [56]. In figure 6.15 we compare the experimental curve $\bar{A}(\bar{t})$ with the one predicted by equation (6.13). We can see that, despite the strong assumptions, equation (6.13) predicts a sublinear evolution which is slower but very close to the experimental one. The neglect of gas transfer through the Plateau borders starts to be evident as the bubble area increases, causing a deviation of the prediction from the experimental curve.

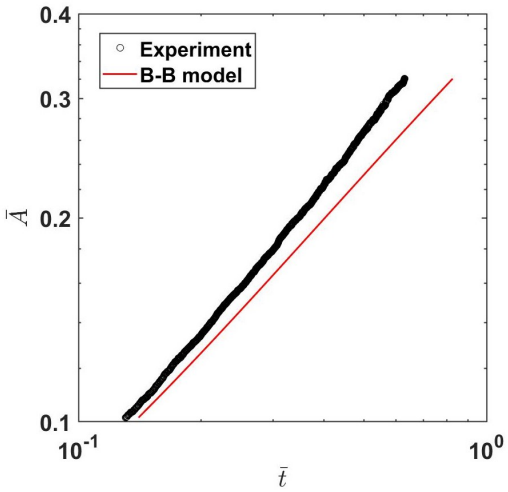

Figure 6.15 – **Comparison with border-blocking model.** Experimental (black circles) and predicted (red solid line) evolution. The simplified border-blocking model predicts an evolution slower than the experimental one, due to the strong assumption of no gas transfer through the Plateau borders.

6.3.3 Towards the vanishing of the thin films

In the previous section we saw that a border-blocking model is able to describe the slow mean bubble growth observed in our samples. However, this kind of model no longer works well if we consider foams in which Plateau borders start covering most of the lateral bubble surfaces. Moreover, it clearly fails when the thin film area vanishes, as it predicts an unphysical arrest of the coarsening process, which in reality continues with the gas transfer occurring through the bulk liquid phase.

We now want to probe what happens when the foams approach the critical point at which they are expected to lose the films between the bubbles. To do that, we consider the samples used for the characterisation of the SSGR in section §6.3.1. Indeed, according to equation (6.10), a reduction of the spacing between the plates reduces the critical bubble area at which we expect the height of the vertical thin films to vanish. The gap for those samples was 1 mm, namely half of the gap considered in the previous section, meaning that, for the same liquid fraction, we expect a critical area roughly four times smaller. Moreover, since for a given gap we expect to lose the films before at higher liquid fraction, we also vary the initial liquid fraction ε from 8% to 15%, to probe whether and how the coarsening evolution changes in proximity of the critical point.

Mean bubble growth at different liquid fractions

In figure 6.16 we report the time evolution of the total number of bubbles in the samples (a), of their average area (b) and of their average radius (c), the latter normalised by their initial values at instant t_{2D}, namely when the foams have just become in good approximation bubble monolayers. We can see that we start with around 10^4 bubbles for each sample, and the number then decreases over time as a power law with different exponents. In fact, we can see that $\langle A \rangle$ grows in time as a power law itself with an exponent ranging between 1 and 2/3. Indeed, the mean bubble area is given by definition by $\langle A \rangle = \sum A_i / N = A_{\text{tot}}/N$, where A_{tot} is the total cell area, which is constant. Thus, if $\langle A \rangle \sim t^{2\beta}$, the total number of bubbles, given by the ratio $N = A_{\text{tot}}/\langle A \rangle$, is expected to scale as $N \sim t^{-2\beta}$. The sublinear growth of the average area translates into power law growths $\langle R \rangle \sim t^{\beta}$ for the average bubble radius, with exponents β between the predictions 1/2 and 1/3 for the dry and wet case respectively.

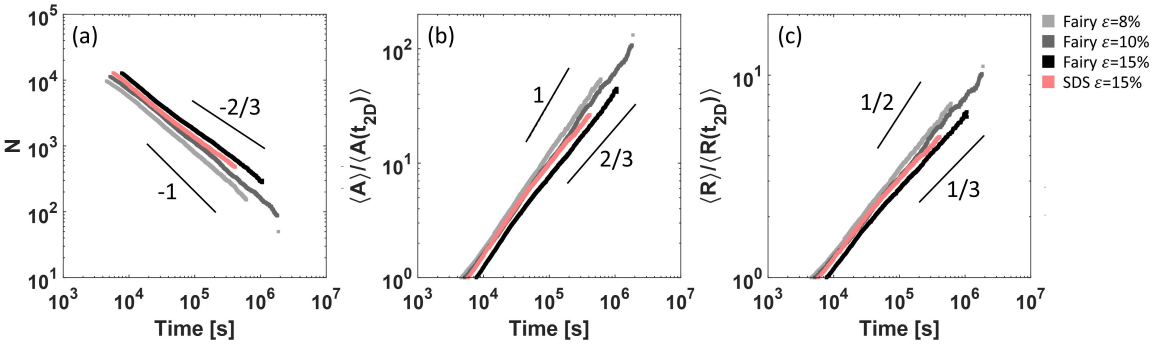

Figure 6.16 – **Coarsening evolution at different initial liquid fractions.** Time evolution of (a) the total number of bubbles $N(t)$, (b) the normalised mean area $A(t)/A(t_{2D})$, and (c) the normalised mean radius $R(t)/R(t_{2D})$.

Despite the impressive robustness of these power laws over many decades, we remark that there is no theoretical reason why we could expect *a priori* a power law growth with different exponents, especially in quasi-2D foams: the effective diffusion coefficient D_{eff} is indeed not constant over time in our systems because of the gradual change in the foam structure. In fact, as seen in section §3.3.3, a gradual increase of the bubble size at constant liquid fraction and plate separation, makes the Plateau borders inflate over time, resulting in a gradual decrease of the total vertical film area. Moreover, as soon as the surface Plateau borders reach the critical size $r_{\text{PB}} = d/2$, adjacent bubbles are separated by films of zero height. We thus would expect to observe, within the same sample, a transition between a regime in which the gas diffusion occurs mainly through the thin films, and a regime in which the diffusion occurs only through the liquid bulk as the films have all vanished.

Clearly, this transition cannot be sharp because of the polydispersity of the bubbles, which makes r_{PB} uneven in the sample, as it is set by the bubble capillary pressure, so the bubbles will not lose their films all at the same instant.

Not-so-constant liquid fraction

The rubber joint which sets the cell thickness prevents the foam liquid from leaking and causing a drastic loss of liquid fraction. However, since the experiments now span several decades in time, even if the cell looks perfectly sealed, water evaporation could be no longer negligible.

To check whether and how the liquid fraction varies over time during the experiment, we can look at the evolution of the surface liquid fraction ε_s. This is expected to decrease over time as the average bubble size grows, since as long as we are within the conditions for the decoration lemma, one can write the scaling relation:

$$\varepsilon_s \sim \frac{r_{\text{PB}} R}{R^2} \sim \frac{r_{\text{PB}}}{R} \tag{6.14}$$

The Plateau border size also grows in time, but if the volume liquid fraction is constant, we can see from equation (6.7) that r_{PB} grows as $\sqrt{R}$, thus ε_s is expected to decrease over time as $1/\sqrt{R}$. We thus measure the surface liquid fraction ε_s from our foam pictures and we plot its time evolution in figure 6.17 (a), where we can see that the curves initially follow the predicted scaling, but at some point they start to deviate.

Since we want to check if the volume liquid fraction is constant over time, we can rewrite equation (6.7) in terms of the surface liquid fraction as:

$$\varepsilon \sim \frac{r_{\text{PB}}^2 R}{R^2 d} \sim \varepsilon_s^2 \cdot \frac{R}{d} \tag{6.15}$$

We thus plot in figure 6.17 the evolution of $\varepsilon_s^2 \cdot \langle R \rangle / d$ over time for each sample. We can see that, after a time of approximately 24 hours, the 3D liquid fraction starts decreasing over time. The apparent increase exhibited by the two samples at $\varepsilon = 15\%$ could be due to their higher wetness, so that the scaling of equation (6.15) no longer holds properly as one should account also for the vertical Plateau borders.

The strikingly straight power laws observed in figure 6.16 over many decades in time are thus misleading, as they are the result of the combination of coarsening plus evaporation.

We remark that evaporation does not in any case invalidate the characterisation of the SSGR done in section §6.3.1. Indeed, as long as there are only triangular vertical

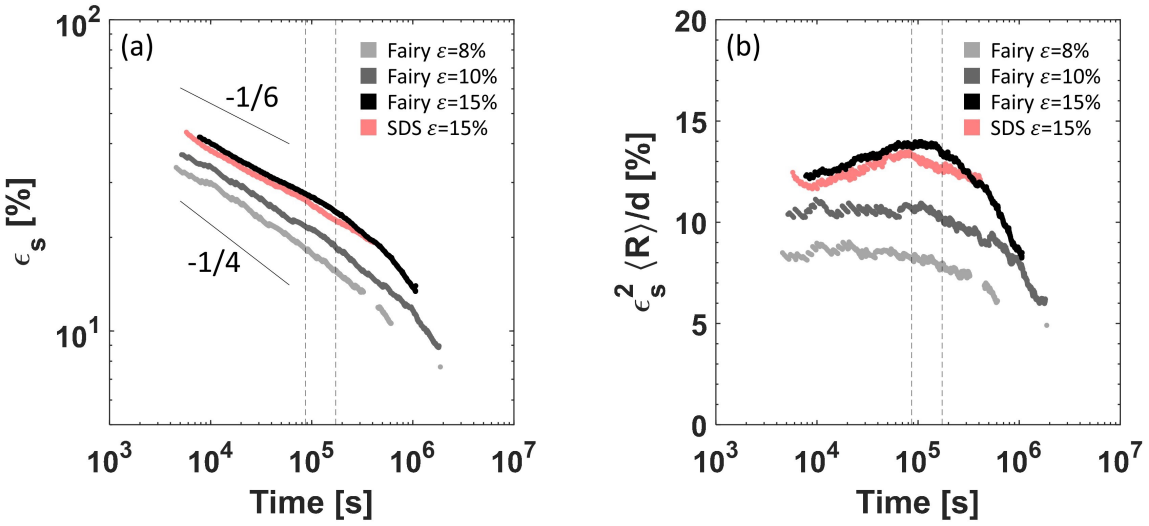

Figure 6.17 – **Liquid fraction evolution.** (a) Time evolution of the surface liquid fraction ε_s. The two vertical dashed lines correspond to a time of 24 and 48 hours respectively. The surface liquid fraction is expected to evolve as $\varepsilon_s \sim r_{\mathrm{PB}}/R$, but if the volume liquid fraction is constant the Plateau borders grow as $r_{\mathrm{PB}} \sim \sqrt{R}$. The two power laws correspond to a mean radius growth as $\langle R \rangle \sim t^{1/3}$ and $\langle R \rangle \sim t^{1/2}$. (b) Time evolution of the scaling $\varepsilon \sim \varepsilon_s^2 \langle R \rangle / d$. We can see that for the two drier samples the curves are flat up to 24 hours, but remain in good approximation constant up to 48 hours. For the wetter samples, the curves show an increasing trend before dropping, probably due to the gradual loss of films which makes the scaling of ε no longer valid.

Plateau borders (that is the case for each of our samples if we stop at N=1000), the geometrical and topological distributions are the same as the undecorated ideal foam, and it has been shown experimentally that they do not depend on the foam liquid content [97]. The same consideration also holds for the initial time interval when evaporation is negligible and thus the foam is gradually getting wetter: this is why the statistical dimensionless distributions are stationary as long as the foam does not contain n-sided Plateau borders with $n > 3$. Things change as soon as the foam starts having a non-negligible number of many-sided Plateau borders: the foam topology for example is expected to evolve, as the mean coordination number should decrease from 6 to 4 at the unjamming point [4]. Evaporation however prevents the exploration of the unjamming point in our experiments as it partially counteracts the fattening of the Plateau borders.

Different attempts to stop evaporation have been carried out, from sealing the cell contour with oil or silicone, to putting a bath of liquid all around the cell to locally increase the humidity. However, one should really work in a saturated environment to completely stop the evaporation process, which would require putting the cell inside a chamber at 100% humidity. Beyond the difficulty of an effective humidity control, vapor condensation on the glass plates would decrease the image quality.

On the other hand, one could intuitively think to reach the unjamming point faster by increasing the initial volume liquid fraction of the foam. However, we observed that values of ε larger than 15% make the foam very sensitive to tiny cell thickness gradients, which would result in an undesired uneven distribution of liquid among the bubbles, as the latter

tends to accumulate where the cell gap is thinner.

Even though the liquid fraction is observed to be decreasing over time, we can try to extract useful information from these samples by looking at the local coarsening rate, namely its value over infinitesimal time intervals in which the liquid fraction can be considered constant.

Local coarsening rate

At constant liquid fraction, the Plateau borders grow over time and, as soon as their size extends to half of the gap, the area of thin vertical films is expected to vanish. We remark that this effect is due to the foam confinement, and thus specific to quasi-2D foams: it does not occur in 3D foams as long as their cell size is much larger than the typical bubble size so that it can be approximately considered as infinite. In this case, the constant liquid fraction sets the ratio between the size of the Plateau borders and the bubble radius, which thus remains constant as the foam coarsens. However, something similar could in principle happen once there are only a few bubbles left, so that confinement effects start to be significant.

In our quasi-2D foam experiments, this transition is delayed by evaporation, which slowly removes part of the liquid between the bubbles counteracting the Plateau border growth and thus maintaining the foam drier than expected.

The fact that the liquid fraction is changing over time does not allow comparisons of the global evolution of the mean bubble size over time. However, what we can do is to consider the local coarsening rate at a given time, as there exists a time interval over which the liquid fraction can be considered constant.

Once the foam approaches the critical point of zero film height, it is not possible to overlook the gas transfer through the bulk liquid, thus we cannot use a border-blocking model. The only model accounting for the gas diffusion through the Plateau borders currently existing in the literature has been developed by Schimming and Durian [104]. This border-crossing model turns Von Neumann's relation for a single bubble into a more complicated expression for the rate of bubble volume variation, which includes the contribution to gas transfer of all the bulk liquid elements around the bubble, thus surface and vertical Plateau borders but also surface vertices.

If vertical Plateau borders and nodes can be neglected, and if the bubbles are not too small so that their volume can be approximated with $V = Ad$, they derived the following approximate equation for the single bubble area growth [104]:

$$\frac{\mathrm{d}A}{\mathrm{d}t} = K_0\left(1 - \frac{2r_{\mathrm{PB}}}{d} + \frac{\pi\sqrt{r_{\mathrm{PB}}l}}{d}\right)\left[(n-6) + \frac{6Cnr_{\mathrm{PB}}}{\sqrt{3\pi A}}\right] \tag{6.16}$$

where l is the film thickness and $K_0 = \gamma D_f He/l$ is the parameter enclosing the foam physical chemistry.

We can see that we have several additional terms compared to the ideal Von Neumann's law. The negative term in the brackets, $-2r_{\mathrm{PB}}/d$, accounts for the reduction of the thin film height due to the two bottom and top surface Plateau borders (as in the border-blocking model), while the additional term $\pi\sqrt{r_{\mathrm{PB}}l}/d$ accounts for the diffusion through such Plateau borders, and thus reactivates coarsening when the limit of $r_{\mathrm{PB}} = d/2$ is reached. Moreover, we can see from the expression in the square brackets that we no longer have only the topological term $n - 6$, but now a second term appears accounting for the bubble shape,

through a circularity parameter C, and for the bubble size, through the presence of A under the square root.

Here we are interested in the overall growth rate rather than the one of single bubbles, as we cannot measure bubble shape parameters from our pictures to compare the latter. Calculating the rate of change of the average bubble area from the modified Von Neumann's law requires two assumptions: first the decoration lemma has to hold for each bubble in the sample, and second the foam has to be self-similar, so that the parameter $\langle A^2\rangle/\langle A\rangle^2$ is constant. The average area is given by definition by $\langle A\rangle = \sum A_i/N$. Then one can write the following identity:

$$\frac{\langle A^2\rangle}{\langle A\rangle^2}\langle A\rangle = \frac{\sum A_i^2}{A_{\mathrm{tot}}} \tag{6.17}$$

which can be differentiated and rearranged to obtain:

$$\frac{\mathrm{d}\langle A\rangle}{\mathrm{d}t} = 2\frac{\langle A\rangle^2}{\langle A^2\rangle}\sum \frac{A_i}{A_{\mathrm{tot}}}\frac{\mathrm{d}A_i}{\mathrm{d}t} \tag{6.18}$$

from which we can see that the growth rate of the average area is set by the area-weighted average of the individual area growth rates $\mathrm{d}A_i/\mathrm{d}t$. If we now insert equation (6.16), we can write:

$$\frac{\mathrm{d}\langle A\rangle}{\mathrm{d}t} = 2\frac{\langle A\rangle^2}{\langle A^2\rangle}\left\langle\!\!\left\langle K_0\left(1-\frac{2r_{\mathrm{PB}}}{d}+\frac{\pi\sqrt{r_{\mathrm{PB}}l}}{d}\right)\left[(n-6)+\frac{6Cnr_{\mathrm{PB}}}{\sqrt{3\pi A}}\right]\right\rangle\!\!\right\rangle \tag{6.19}$$

where $\langle\langle ...\rangle\rangle$ indicates area-weighted average. While performing the average, one should consider that the parameters n, C and A, but also r_{PB}, vary from bubble to bubble. However, by assuming that the foam is rather dry, so that r_{PB} is small compared to $\sqrt{A}$ and its variations could be neglected, one can average r_{PB} and $\sqrt{A}$ separately, and the relation (6.19) can be further simplified to get the following prediction for the average area growth rate [104]:

$$\frac{\mathrm{d}\langle A\rangle}{\mathrm{d}t} \approx \alpha_1 K_0\left(1-\frac{2r_{\mathrm{PB}}}{d}+\frac{\pi\sqrt{r_{\mathrm{PB}}l}}{d}\right)\left(1-\frac{\alpha_2 r_{\mathrm{PB}}}{\sqrt{\langle A\rangle}}\right) \tag{6.20}$$

where $\alpha_1 \simeq 0.62$ and $\alpha_2 \simeq 3.2$ are wetness-independent parameters [104]. We can see that in this relation the rate $\mathrm{d}\langle A\rangle/\mathrm{d}t$ still depends on both the Plateau border size r_{PB} and the mean bubble area $\langle A\rangle$, which are not independent from each other as they are linked by equation (6.7). To compare our results with this equation, we would need to quantify both the area and the average Plateau border radius in our samples, which we recall is polydisperse. However, it is not possible to accurately measure the Plateau border radii from our foam images as they are only a few pixels thick. Since we cannot measure r_{PB}, we could think to rewrite (6.20) using the scaling relation (6.7) to obtain $\mathrm{d}\langle A\rangle/\mathrm{d}t$ as a function of r_{PB} only. This yields:

$$\frac{\mathrm{d}\langle A\rangle}{\mathrm{d}t} \approx \alpha_1 K_0\left(1-\frac{2r_{\mathrm{PB}}}{d}+\frac{\pi\sqrt{r_{\mathrm{PB}}l}}{d}\right)\left(1-\frac{\alpha_2\varepsilon d}{\alpha' r_{\mathrm{PB}}}\right) \tag{6.21}$$

where α' is a geometrical prefactor that we estimated to be roughly 1.52 for a rather dry quasi-2D foam [42]. We can see that now $\mathrm{d}\langle A\rangle/\mathrm{d}t$ depends on r_{PB}, but also on the liquid fraction ε, which in our systems varies over time because of evaporation. We cannot vary

both independently, as r_{PB} and ε are also interdependent according to the scaling (6.7). However, we can first have a look at the behaviour of $\mathrm{d}\langle A\rangle/\mathrm{d}t$ predicted for a constant liquid fraction ε. We thus consider three different constant liquid fractions, namely 8%, 10% and 15%, and we generate a vector of different linearly-spaced r_{PB} values in a range reasonable for a gap d=1 mm, and we insert it in equation (6.21). We remark that for a given ε and d there is a minimum r_{PB} set by the minimum bubble size at which the foam can be quasi-2D: values smaller than this threshold would lead to unphysical negative coarsening rates. If we consider for simplicity the minimum R to be equal to half the gap size d, we obtain $r^2_{\mathrm{PB,min}} = \sqrt{\pi}\varepsilon d^2/2\alpha'$.

The results are shown in figure 6.18. We can see that this approximation leads to mean bubble growth rates which are unphysically increasing with r_{PB} at low values of the latter. This is probably because for low r_{PB} the corresponding bubble sizes are comparable to the size of the gap, so one of the first assumptions for this simplification fails.

Therefore, we cannot compare our results with this prediction, as we highlight that our samples do not fullfill many of the assumptions for equation (6.20): the latter indeed assumes to be in conditions of a rather dry foam with bubbles much larger than the gap. This is not true for our samples at early stage, which are also very wet so that the actual bubble shape plays a fundamental role in its evolution. Moreover, the high foam wetness can also affect the geometric prefactor α', as the latter is based on the assumption that vertical Plateau borders also have a curvature radius roughly equal to r_{PB}: this is not true if the foam is wet, as their cross section have a larger radius of curvature and one should account for this in the scaling relation (6.7) [42].

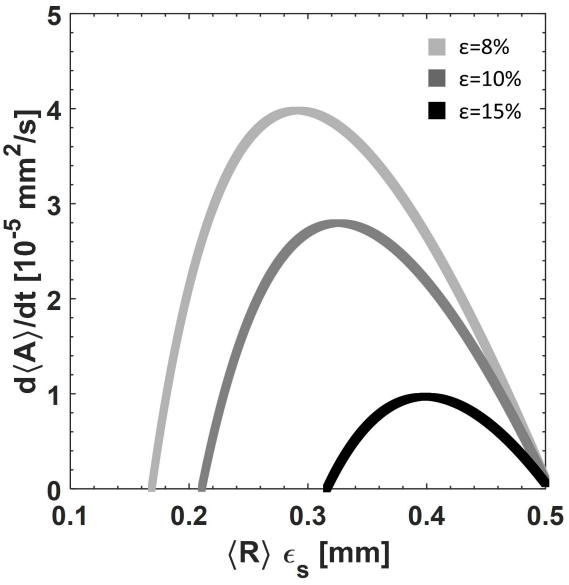

Figure 6.18 – **Coarsening rate.** Coarsening rate calculated from equation (6.21) for constant liquid fractions of 8%, 10% and 15%.

Even if we cannot compare our results to this theoretical prediction, we can try to compare the evolution of the local coarsening rate in our samples with the evolution of the Plateau border size. For evaluating the former, we can fit the mean bubble area growth over time with an exponential function of the type $\langle A\rangle = at^b + c$, that well fits the data

(coefficient of determination r^2>0.999), and which we then derive to quantify the global rate $\mathrm{d}\langle A\rangle/\mathrm{d}t$. The same is done also with the evolution of the mean bubble radius. To follow the evolution of the average r_{PB}, we use the approximate scaling relation (6.14) which links it to the surface liquid fraction ε_s and use the latter to compare the coarsening rate between the different samples.

In figure 6.19 we plot the evolution of $\mathrm{d}\langle A\rangle/\mathrm{d}t$ and $\mathrm{d}\langle R\rangle/\mathrm{d}t$ versus $\varepsilon_s\langle R\rangle$, which is in first approximation proportional to r_{PB}. We can see that the coarsening rate decreases as the surface Plateau borders inflate. We can also see that while the curves of the mean area growth rate in the different samples are separate from each other, the rates of the mean bubble radius show a good collapse.

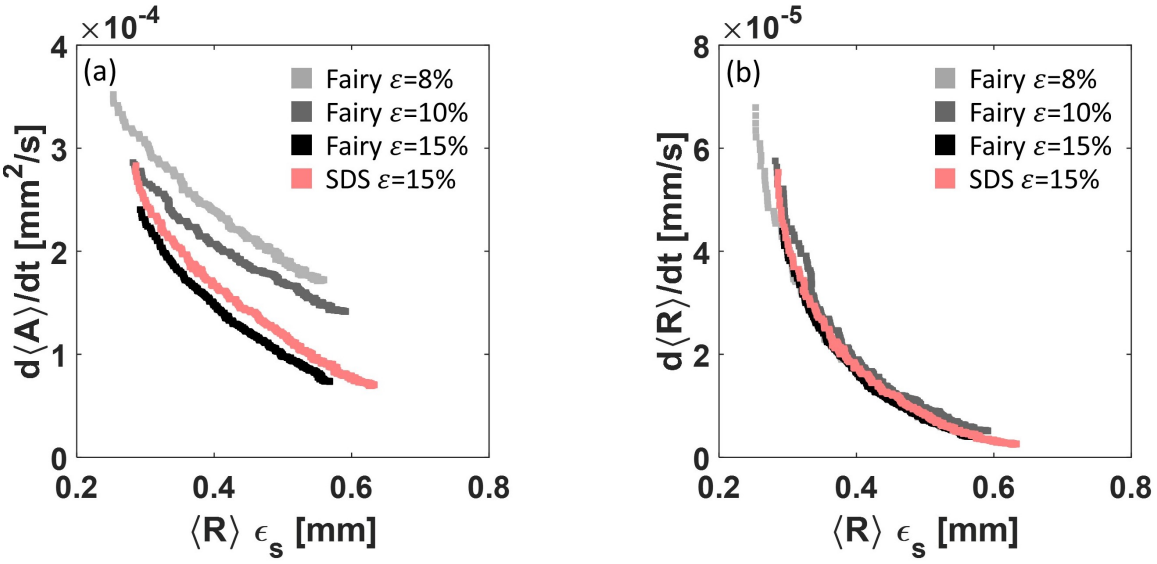

Figure 6.19 – **Coarsening rates vs Plateau border size.** Evolution of (a) $\mathrm{d}\langle A\rangle/\mathrm{d}t$ and (b) $\mathrm{d}\langle R\rangle/\mathrm{d}t$, plotted versus the product $\varepsilon_s\langle R\rangle$ which represents, in first approximation, the variation of the surface Plateau border size.

We highlight however that the scaling relation (6.14) is a strong simplification, as we are neglecting the enlargement of the vertical Plateau borders. Accounting for the contribution of the vertical Plateau borders would require a direct measurement of their average size, which is not possible to perform accurately from our pictures. Moreover, we remark that we are considering the surface liquid fraction measured from the bulk pictures, which in any case underestimates the real Plateau border size. Indeed, if the foam is dry, we expect roughly a factor 2 in the scaling between the Plateau border radius and the surface liquid fraction $\varepsilon_s\langle R\rangle \simeq 2r_{\mathrm{PB}}$, so that the curves in the graph would be shifted towards values smaller than $d/2$, even though our samples are losing the thin vertical films during their evolution.

In conclusion, one should accurately measure the average size of both surface and vertical Plateau borders from the picture for an in-depth characterisation of the coarsening process in this wet regime, by for example carrying out imaging experiments which probe the evolution both at the scale of the foam and at the local scale of a few bubbles to be able to retrieve accurate information on the bubble shapes.

6.4 Conclusions

In this first experimental chapter we focused on the impact of a constant liquid fraction on the coarsening of aqueous quasi-2D foams. We experimentally showed how the 3D structure of such systems strongly influences their coarsening process by gradually reducing the area of the vertical films between the bubbles. The progressive swelling of the surface Plateau borders partially screens the gas transfer between bubbles, as being several order of magnitude thicker than the films, the gas diffusion across them is much slower. We showed that a simplified model which neglects the contribution of the bulk liquid inside the borders is able to describe the reduced mean bubble growth as long as we are far away from the transition at which the thin films vanish and the portion of films between adjacent bubbles is still significantly large.

However, as soon as the Plateau borders reach a critical size equal to half the spacing between the plates, the vertical thin films reduce to lines of zero height. As we approach this critical point, the gas diffusion through the Plateau borders can no longer be neglected, in order to avoid predicting an unphysical arrest of coarsening.

The investigation of the bubble unjamming in our experiments was partially hindered by the onset of evaporation which, as it gradually removes liquid from the foam, partially counteracts the fattening of the Plateau borders. The combination of coarsening and evaporation gives rise to robust power laws which can be misleading, as there is no theoretical justification for a quasi-2D system at intermediate liquid fraction regime to evolve in time as a power law with an exponent depending on the liquid fraction. Despite evaporation, we showed that we can in any case extract interesting information from our systems by looking at the local coarsening rate. The comparison of our results with the existing prediction for the mean bubble area growth fails, as the assumptions done for getting the final average equation do not hold for our foams. Our results however show that the mean bubble growth rate for the different samples collapses onto a single master curve when plotted versus the size of the Plateau borders. As a perspective, experiments looking at both the scale of the foam and of the bubble should be carried out in parallel in order to extract information on the global coarsening rate and the local bubble shapes. Further modelling would be in any case needed to extend our understanding of foam behaviour in the proximity of the film vanishing transition.

It is worth highlighting that an increasing liquid fraction in our quasi-2D samples is not observed to reduce the coarsening rate below the prediction for bubbly liquids. In the next chapter, we will show that, to further slow down the coarsening process, one can play with the mechanical properties of the foam continuous phase, for example by using a viscoelastic fluid, whose elasticity can be exploited to tune not only the overall foam ripening but also the foam structure.

7 Quasi-2D foamed emulsions

7.1 Introduction

In the previous chapter we saw how the coarsening of aqueous foams in sealed quasi-2D configurations is influenced by the fattening of their Plateau borders over time, which gradually reduces the area of thin films available for direct gas transfer. However, we saw that even by increasing the initial liquid fraction, the coarsening rate was never below the prediction for dilute bubbly liquids. Enriched of these experimental observations in traditional systems, which we shall use as a reference, we now focus our attention on more complex foams.

In many applications, indeed, the foam liquid phase is often not a simple aqueous solution, but can be a fluid with non-Newtonian rheological properties. For instance, the introduction of bubbles in soft solids can be exploited to tune the overall mechanical response of the final product, depending on the gas fraction, bubble size and matrix elasticity [25, 26, 50]. Liquid foams can also be solidified to get solid cellular structures, in order to enlarge the range of physical properties achievable compared to dense solids. However solid foams inherit their structure from their liquid precursors, which can destabilise before solidification resulting in a nonuniform final composition. In many applications the necessary amount of liquid inside the foam is not negligible and thus gravitational drainage rapidly leads to an irregular distribution of the liquid phase and bubble size inside the sample. This process can be stopped if the continuous phase has a yield stress higher than the buoyancy force per unit area exerted on the bubble [58]. Coalescence of adjacent bubbles more likely occurs at very low liquid fractions, and it is thus negligible in rather wet foams when drainage has already been counteracted.

However, depending on the application, times required for product storage or foam solidification can be very long, and thus diffusive phase separation can start playing a crucial role in modifying the foam internal structure over time. Nevertheless, little is known about how foam coarsening is impacted when the aqueous phase is replaced with a complex fluid. This is why finding the link between the mechanical properties of the continuous phase and the overall foam stability is of great interest.

In this chapter, we shall experimentally probe the coarsening of foams in a viscoelastic liquid phase, given by concentrated O/W emulsions: the scale separation between drops and bubbles in our systems allows seeing the emulsion as a continuous viscoelastic medium among the bubbles. We will consider once again quasi-2D foam systems, as they simplify the monitoring and the characterisation of the bubble pattern evolution.

We saw in chapter §5 that the mechanical properties of concentrated emulsions mainly depend on their drop packing fraction [82, 81], meaning that we can tune their elasticity simply by varying the relative amount of dispersed oil. Moreover, their typical storage

moduli fall in a range in which we expect to see an effect of their elasticity on the coarsening process, as they are higher than the typical bubble capillary pressures in our quasi-2D foams. The combination of these two features makes foamed emulsions ideal systems for our purpose: we thus generate foams from emulsions having different oil fractions, and follow their evolution over time to characterise the ripening of such complex foams.

After giving a detailed overview of the experimental protocol, we will show how the coarsening process in foamed emulsions is indeed heavily affected by the continuous phase viscoelasticity. We shall study the effect of an increasing emulsion storage modulus on both coarsening rate and foam structure, showing how the two are interdependent, and proposing a mechanism for describing our experimental observations. We will finally probe the influence of a doubled foam liquid fraction as well as the impact of the foam confinement in such systems, giving interesting preliminary results which open up new questions for future experimental investigations.

7.2 Experimental approach

7.2.1 Emulsion generation

Concentrated O/W emulsions are generated by mechanically mixing the oil and the surfactant solution with the double-syringe technique, the same method already used in §6.2.2 to make aqueous foams, just replacing the gas phase with oil in figure 6.1.

This time, a syringe of total volume 60 mL (Codan Medical) is partially filled with a volume V_{oil} of rapeseed oil (from Brassica Rapa, Sigma Aldrich) or sunflower oil (from Helianthus Annuus, Sigma Aldrich) when specified, while a second one is partly filled with a volume V_{aq} of SDS solution at 30 g/L. The two oils have a similar density ρ_{oil} equal to 920 kg/m^3 at 20°C. The volumes of oil and aqueous phase are chosen according to the desired emulsion oil volume fraction given by $\phi = V_{\text{oil}}/(V_{\text{oil}} + V_{\text{aq}})$. The two syringes are then connected with a double luer lock and the syringe plungers are pushed 30 times back and forth. The syringe inlets, having an inner diameter of 2 mm, act as constrictions in the flow of the mixture, which break the oil phase into micrometric droplets giving rise to a homogeneous but polydisperse O/W emulsion.

Since we want to work with elastic emulsions, the oil fractions investigated are all above the close packing fraction and range from 65% to 85%. The high SDS concentration in the aqueous phase ensures complete surface coverage of the drops at these oil fractions, with free surfactant left after emulsification which enhances the foamability of the emulsion.

After emulsion generation, the drop size distribution is measured with laser diffraction granulometry, a standard technique which will be extensively used in chapter §9 and for which a detailed explanation is thus given in section §9.2.3.

7.2.2 Emulsion rheology

The mechanical properties of concentrated emulsions are probed by performing oscillatory strain sweep tests with a compact rheometer (Physica MCR 301 by Anton Paar) in a cylindrical Couette geometry (CC27) with a gap of 1.1 mm, like the one sketched in figure 7.1.

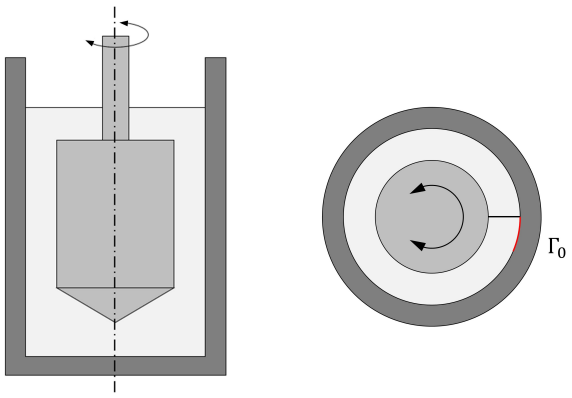

Figure 7.1 – **Cylindrical Couette geometry.** Vertical (left) and horizontal (right) section of the cylindrical Couette geometry used for emulsion rheology measurements. The rotating inner cylinder applies a sinusoidal strain with increasing amplitude Γ_0 to the emulsion inside the stationary cup.

Oscillatory measurements are often used in the literature to probe the rheological response of a material as they allow to study the linear response but also detect the onset of yielding [82, 81, 100]. Actually, one could perform two different kinds of oscillatory experiments: amplitude sweep tests at fixed frequency or frequency sweep tests at fixed amplitude. We choose amplitude instead of frequency sweeps, as experimental results of the latter in the literature revealed a large range of frequencies where the elastic response of emulsions is constant, even though their viscous dissipation is more frequency-dependent [82].

Strain sweep tests allow obtaining the storage and loss moduli of the emulsion by imposing an oscillatory shear strain and measuring the resulting stress. A sinusoidal strain $\Gamma(t) = \Gamma_0 \sin(\omega t)$ with increasing amplitude Γ_0 is applied to the emulsion inside the stationary cup by rotating the inner cylinder at a constant angular frequency ω equal to 1 rad/s, which is chosen as in [82]. The surface of the inner cylinder has been sand blasted in order to avoid emulsion slippage. As long as the strain amplitude is sufficiently small, the resulting stress $\tau(t)$ will also be sinusoidal with an amplitude proportional to the applied strain Γ_0, but with a phase lag δ due to dissipation. One can thus write the following equation:

$$\tau(t) = \tau_0 \sin(\omega t + \delta) = \Gamma_0 [G'(\omega) \sin(\omega t) + G''(\omega) \cos(\omega t)] \tag{7.1}$$

where the first term is in phase with the strain Γ and proportional to the storage modulus G' while the second term is in phase with the strain rate $\dot{\Gamma}$ and is proportional to the loss modulus G''. The ratio $G''/G' = \tan\delta$ is often called loss or damping factor.

The strain amplitude is swept over 30 logarithmically spaced values from 0.001% to 100%, and the resulting shear stress is measured for 20 seconds at each point.

In addition to sweep tests, we use the same geometry to measure the flow curve of our emulsions in order to get a more accurate estimate of their yield stress. To do that, we apply a constant shear rate $\dot{\Gamma}$ for 10 seconds at 30 logarithmically spaced values starting from 1000 s^{-1} to 0.1 s^{-1} and we measure the resulting shear stress τ.

All measurements are performed at a temperature (20.3±0.1)°C close to the room temperature at which all the foam coarsening experiments are carried out.

7.2.3 Foam generation

In order to obtain a foamed emulsion, air bubbles need to be incorporated inside our concentrated O/W emulsions. The most efficient way to aerate viscous and viscoelastic materials is to use a planetary mixer. Such kinds of mixers are indeed widely employed within the food and pharmaceutical industry to reliably mix and aerate solid-liquid systems [62, 12, 92], in the same way as in our kitchens they are typically used to first mix the ingredients and then aerate the batter to make a cake.

Planetary mixers are characterised by a double opposing rotation of the whisk, from which they take their name in analogy to the Earth's motion revolving around the Sun and around its own axis: the whisk shaft rotates anticlockwise about the centre of the vessel, while the whisk itself simultaneously rotates clockwise about its shaft, as illustrated in figure 7.2 (a).

The planetary motion, combined with the variation of the whisk radius with height, results in a range of motion patterns and position-dependent velocities inside the bowl as shown in figure 7.2 (b,c), which will clearly determine the final product structure. However,

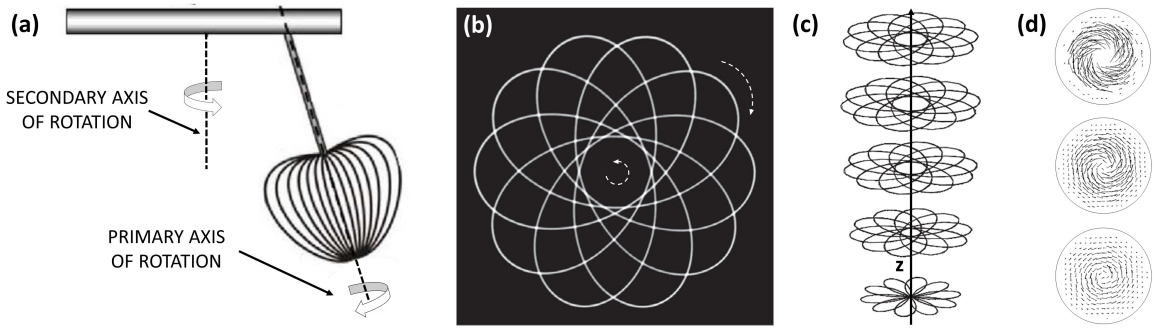

Figure 7.2 – **Planetary motion and flow patterns.** (a) The whisk rotates clockwise around its own axis, which in turns rotates anticlockwise about the axis of the vessel. (b) Trajectory of a small LED attached to the whisk perimeter obtained with a time-lapse photograph. Picture from [13]. (c) Trajectories of five points on the whisk perimeter for a Kenwood mixer at different heights. Picture from [13]. (d) Angular velocity fields recorded on horizontal planes at different heights inside the mixer. The magnitude is minimum close to the wall and maximum at the centre. Picture adapted from [62].

linking the structure development to the flow pattern during mixing is not trivial as for many applications the mixed materials are often soft solids characterised by a complex rheological behaviour [12].

The flow of material inside a planetary mixer has been investigated with positron emission particle tracking on dry and wet powders [62], showing that the characteristic motion pattern imposed by the mixing tool does not depend on its speed or on the level of fill, whereas the magnitude of radial, angular and vertical speed varies with height and depends mainly on the frequency of whisk passages. Two main flow regions have been essentially observed, as shown in figure 7.2 (d): a well-mixed central zone characterised by rapid motion, and a quasi-stagnant wall layer receiving only periodic vertical shunts by the passage of the whisk blades. Indeed, the whisk tip moves with the lowest angular velocity when closest to the wall as it directly encounters the orbital motion, while it has its highest velocity when at the centre of the vessel as the two speeds sum up [62].

The shear rate experienced by a fluid during the mixing is also not uniform inside the bowl being dependent on the whisk speed and gap dimensions, which both vary with height, and it has been shown that it is exactly at the wall that the shear rate is maximum, namely where the gap between the whisk and the vessel is minimum [13].

The aeration process in planetary mixers has been studied for different surfactant solutions, showing that this specific foaming mechanism makes the final outcome strongly dependent on the bulk viscosity of the solution [92].

The mechanism of air entrapment is depicted in figure 7.3. The rotation of the mixer tool generates waves first on the solution surface and then, as some bubbles start forming, on the bubbly surface. The formation of a large cavity on the foam surface is eventually covered by a foam layer entrained by the metal rods of the tool, leading to the formation of a big air pocket. These large air pockets are then gradually broken down into smaller bubbles under the action of the shear stress inside the mixed foam. These two processes of air entrapment and bubble breakage occur simultaneously, leading to an increase of the air volume fraction in the foam, and a concurrent reduction of the average bubble size in the sheared foam. As a result, the viscoelastic response of the foam also increases. Thus,

at a certain critical value of the foam shear stress, the power of mixing becomes unable to generate waves of sufficiently large amplitude on the foam surface: the rotating tool can still create ripples but with an amplitude too low to be able to entrap air [92].

As a consequence, the foam volume eventually reaches a maximum value and then remains constant upon further mixing. It has been shown that the amplitude of the waves on the foam surface is controlled by the foam dimensionless shear stress, defined as $\tilde{\tau} = \tau R_{32}/\gamma$, where τ is the foam shear stress, R_{32} is the surface-weighted mean bubble radius and γ is the solution surface tension. The key parameter which determines the final air volume fraction and bubble size in the foam is this dimensionless shear stress, and experimental results showed that the process of air entrapment stops when a critical value $\tilde{\tau}^* \sim 0.25$ is reached.

Depending on the bulk and surface properties of the surfactant solutions, this critical stress is achieved for foams with different air volume fractions and mean bubble sizes. For example, in solutions with higher bulk viscosity, $\tilde{\tau}^*$ is reached at lower air fractions and with smaller bubbles, due to the faster bubble breakage as compared to air entrapment. That is why, both the final volume of trapped air and the bubble size decrease upon increase of solution viscosity.

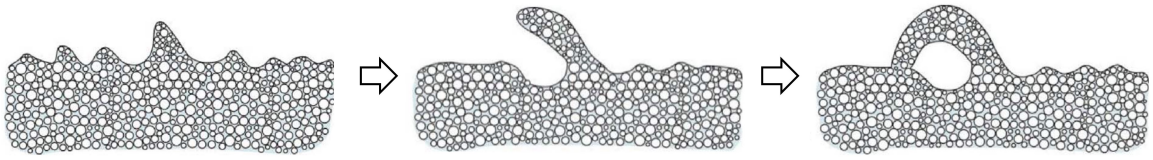

Figure 7.3 – **Mechanism of air entrapment.** The waves generated by the rotating whisk on the foam surface can form cavities, which are then covered with a layer of foam creating an air pocket. The large air pockets are gradually reduced into smaller bubbles by shear. Pictures from [92].

In this study we use a Kenwood MultiOne mixer (1000W) with a standard wire whisk provided by the producer, both shown in figure 7.4 (a,b). This device has six different mixing speed levels, labelled as *min*, 2, 3, 4, 5, *max*. We pour 240 mL of freshly-generated emulsion in the vessel and we start operating the mixer at speed level 2 for 1 minute. We then gradually increase the speed to level 3 for 2 minutes, to level 4 for 3 minutes, to level 5 for 7 minutes, and then we keep mixing at the maximum speed level for 10 minutes. We consider the instant at which the mixer is stopped to be the t_0 of our foamed emulsions, their age being therefore taken as the difference $t - t_0$.

The same mixing protocol is followed for each oil fraction ϕ, as it allows getting rather dry foamed emulsions, with final liquid fractions around 11% slightly varying with ϕ. The liquid fraction is measured by weight, namely a glass container of known volume V_{foam}=133 mL is filled with the freshly-made foamed emulsion and then weighed, as shown in figure 7.4 (c). By considering the density of air to be zero, what we measure is the mass of the foam liquid content, thus of the emulsion, m_{em}. If we assume the density of the emulsion to be given by the weighted sum of its two component densities, $\rho_{\text{em}} \simeq \phi\rho_{\text{oil}} + (1-\phi)\rho_{\text{water}}$, we retrieve the volume of emulsion inside our foam as $V_{\text{em}} = m_{\text{em}}/\rho_{\text{em}}$, so that the foam liquid fraction is then given by $\varepsilon = V_{\text{em}}/V_{\text{foam}}$.

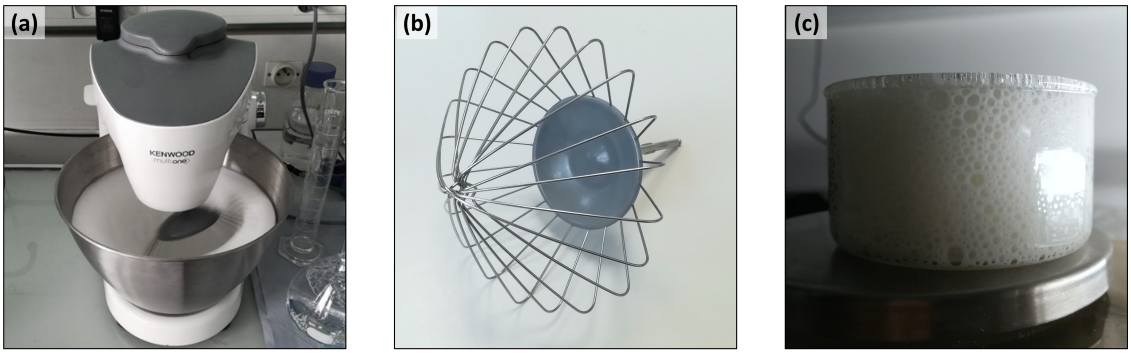

Figure 7.4 – **Foamed emulsion generation.** (a) Kenwood planetary mixer with (b) its wire whisk mixing tool. (c) The liquid fraction is measured by weighing a known volume of freshly generated foam. The picture has been taken a couple of hours after foam generation, which explains the millimetric bubbles visible at the glass surface.

7.2.4 Imaging

Set-up

The set-up used for foamed emulsion imaging is similar to the one used for quasi-2D aqueous foams described in section §6.2.3. After switching off the planetary mixer, the freshly-made 3D foamed emulsion is sandwiched between two glass plates (24 cm x 24 cm), separated by a rubber joint of thickness 1 mm. Only in section §7.3.7 we shall use also larger gaps of 2 mm and 3 mm. The cell is placed on a black tissue to enhance the image contrast between the bubbles and the liquid phase. A square of LED lights provides rather uniform illumination from above, while a camera (Basler acA3800-14um, resolution 3840x2748 pixels) equipped with a lens (Tamron, 16mm F/1.4) is installed above the cell and used to take pictures of the sample at fixed time intervals equal to 180 seconds at early stage and to 1800 seconds at late stage. Once again, since after generation the bubbles are smaller than the gap between the plates, the foamed emulsion is initially three dimensional. Therefore, we wait for the foamed emulsion to coarsen until we get a single layer of bubbles, namely a quasi-2D foamed emulsion. The time t_{2D} increases with the emulsion oil fraction and is of the order of a few hours.

Image treatment

Different custom-made MATLAB scripts are used for processing the foamed emulsion images. A first script performs the image pre-treatment, which consists in cropping the raw frames around a region of interest, adjusting the contrast and get the so-called foamed emulsion skeleton. The original pictures already show a good contrast, as the emulsion is naturally white and the air bubbles black. However, at high oil fractions the appearance of an atypical foam structure, with much thinner Plateau borders between large bubbles, makes a direct thresholding of the picture not optimal for tiny bubbles, which would disappear from the skeleton too early, as shown in figure 7.6 (a). To overcome this problem, an intermediate step is added, as shown in figure 7.5. We first detect the Plateau border edges based on the image intensity gradients. We then fill the connected holes, which correspond to the bubbles, and subtract the resulting image to the original one so that the bubbles will

be perfectly black. The resulting image is then thresholded and a watershed algorithm is used to get the foam skeleton. As shown in figure 7.6 (b), this way the small bubbles are correctly detected. A second script is then used to retrieve the area, the perimeter, and the centroid of each cell of the foam skeleton, using the built-in MATLAB function *regionprops*. A third script is finally used to calculate the foam features like the mean bubble size or the bubble size distributions for each frame.

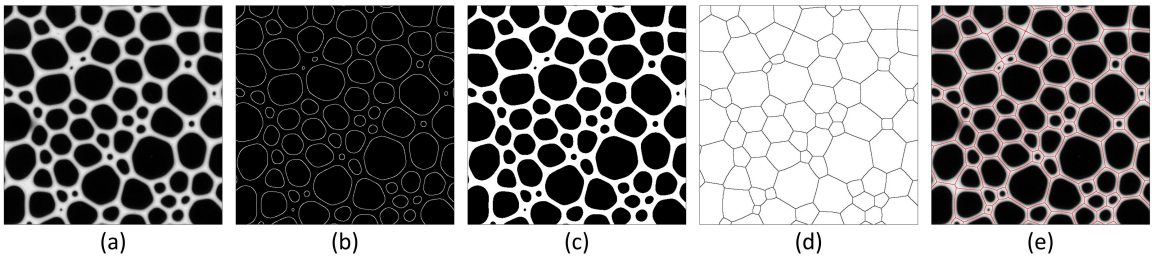

Figure 7.5 – **Image treatment steps.** (a) Small portion of an original foam picture at $\phi = 70\%$ after adjusting the contrast. (b) Edge intensity gradients for the same picture. (c) Binarised picture after thresholding. (d) Inverted foam skeleton obtained with a watershed algorithm. (e) Overlay between the foam picture and its skeleton in red. The edge length of the frames is 35 mm.

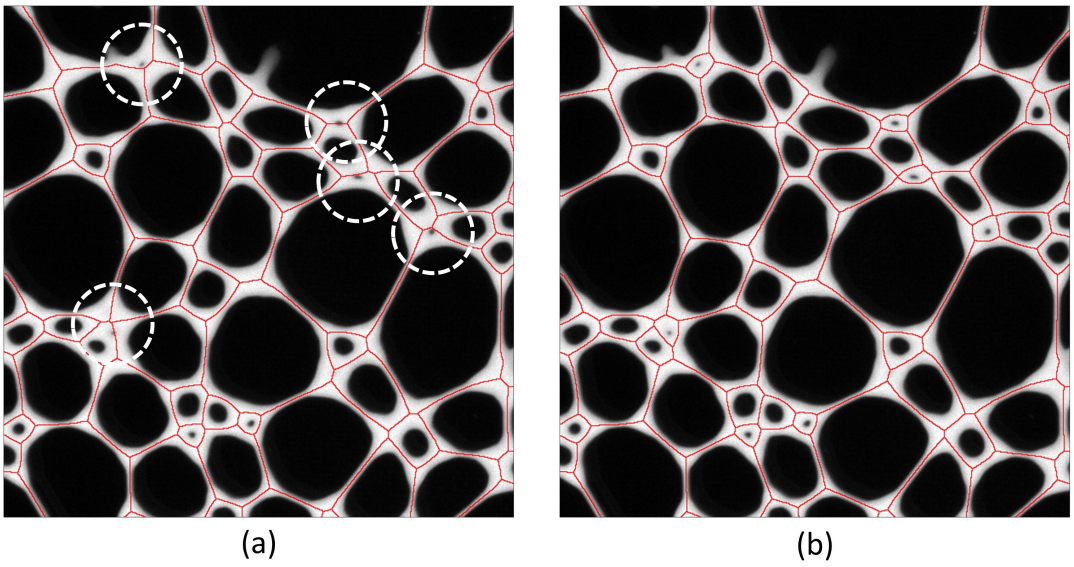

Figure 7.6 – **Comparison with direct thresholding.** (a) Foam skeleton obtained by directly applying an adaptive threshold on the contrast-adjusted picture. The dashed circles highlight some small bubbles which are not detected. (b) Foam skeleton obtained by adding the intermediate step described in the text. The small bubbles are now present in the skeleton. The edge length of both frames is 35 mm.

7.3 Results

7.3.1 Emulsion properties

Droplet size distributions and stability

The double-syringe technique allows generating O/W emulsions with droplets of a few micrometers in size. We measure the drop size distribution using laser diffraction granulometry, and an example of the volume-weighted drop size distributions obtained with this technique is shown in figure 7.7 (a) for a set of samples at the oil fractions of interest. One can see that the population of droplets generated with the double-syringe method is rather polydisperse, but always peaked around a single diameter value which slightly decreases with increasing oil fraction ϕ. Moreover, we can also observe that the increase of the oil fraction makes the drop size distributions narrower. The observed drop size dependency on ϕ is consistent with results in the literature for emulsification in turbulent flow [116].

To better visualise this variation in our emulsions, how the average droplet diameter varies with the oil fraction is shown in figure 7.7 (b), where we plot the results obtained for all the samples generated along the PhD thesis. The drop diameter is reported as the moment mean D_{43}, which corresponds to a volume-weighted average being defined as $D_{43} = \sum D_i^4 / \sum D_i^3$. However, since we are mainly interested in the rheological properties of these emulsions, we also report the surface-weighted average diameter defined as $D_{32} = \sum D_i^3 / \sum D_i^2$. We can see that both decrease upon increase of ϕ.

To quantify the change in the polydispersity, we can look at the distribution width by defining the span as:

$$\text{span} = \frac{D(90\%) - D(10\%)}{D(50\%)} \tag{7.2}$$

where the $D(50\%)$ is the median of the volume size distribution, and the $D(10\%)$ and $D(90\%)$ its corresponding percentiles. We can see in figure 7.7 (c) that the span decreases as the emulsion oil fraction ϕ is increased.

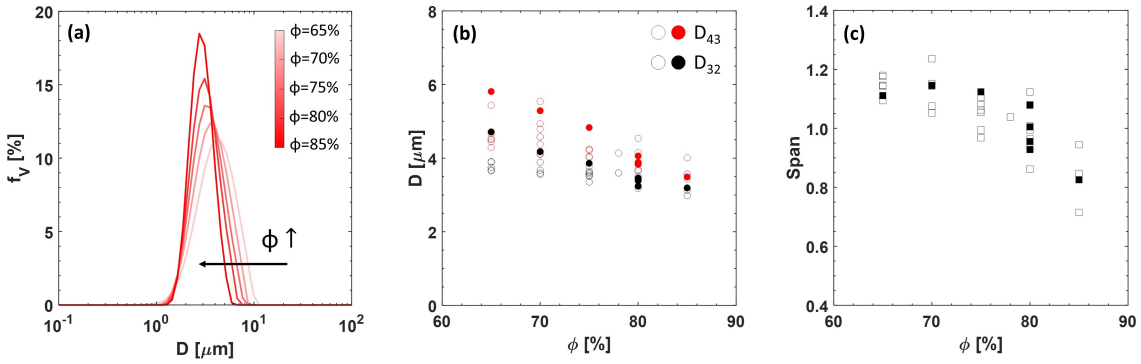

Figure 7.7 – **Emulsion drop size.** (a) Example of drop size distribution for emulsions made with rapeseed oil at different oil fractions. (b) Volume-weighted D_{43} and surface-weighted D_{32} diameter at different oil fractions. We can see that they both slightly decrease with increasing ϕ. (c) The span of the drop size distribution also slightly decreases, meaning that the higher ϕ the narrower the distribution. Solid markers refer to samples made with sunflower oil, empty markers to rapeseed oil samples.

Let us briefly comment on the stability of these concentrated emulsions. We first point out that, despite the shearing undergone inside the mixer, the drop size distribution is not affected by the foaming process, the energy input of the mixer being probably not high enough to modify it significantly. Sometimes a slight refinement of the oil drop size distribution can be observed, as the one shown for example in figure 7.8 (a), which is however negligible at these levels of polydispersity. The fact that emulsions do not change their structure during the foaming step allows to assume that their mechanical properties are essentially the same as the ones measured for freshly generated samples.

Furthermore, despite the high drop packing fractions, these emulsions are very stable over time. The drop size distribution can be measured at the end of a foam coarsening experiment by taking some emulsion from the foam inside the cell after opening. The drop size distribution for an emulsion at ϕ=80% after 19 days is shown as example in figure 7.8 (b) compared with the one measured right after foaming: the two curves basically overlap. A perfect overlap has been observed also in an emulsion at 75% of rapeseed oil after 33 days, corresponding to the longest experimental time. This means that our emulsions are stable over weeks at least, and ageing effects are negligible over the long time scales of our foam coarsening experiments.

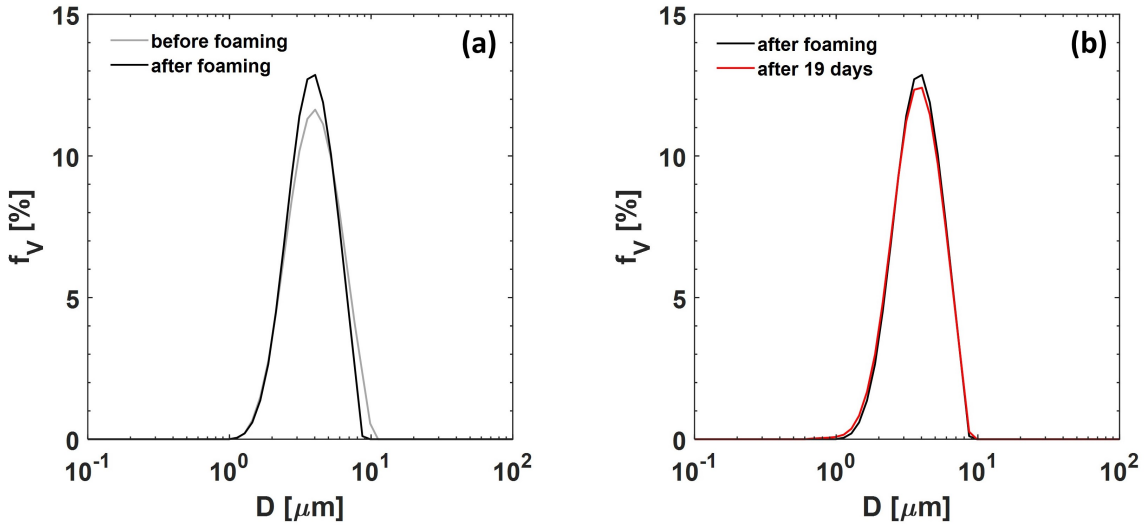

Figure 7.8 – **Emulsion stability.** (a) Drop size distribution before and after foaming for an emulsion at 80% of rapeseed oil. The distribution after foaming appears slightly narrower, however this is the largest discrepancy experimentally observed. (b) Drop size distribution for the same emulsion after foaming and after 19 days of experiment. The difference between the two is negligible, the emulsion is highly stable.

Mechanical properties

Let us start by looking at the results of the oscillatory strain sweep tests. By applying an oscillatory strain with increasing amplitude Γ and measuring the resulting shear stress τ, we can get the storage and loss moduli as a function of the strain amplitude for each emulsion. The typical resulting curves are reported in figure 7.9 for emulsions made with rapeseed oil. Let us first consider a single oil fraction ϕ as in figure 7.9 (a). We can see that at small strain values the storage modulus G' is constant: in this range of strain amplitude

the emulsion is in its linear viscoelastic regime (LVE), namely the regime in which the stress τ varies linearly with the strain Γ, the storage modulus G'_{LVE} being the coefficient of proportionality between the two. In this regime G'_{LVE} is greater than the loss modulus G''_{LVE}, reflecting the elastic nature of the emulsion. As we increase the strain amplitude, we can observe a gradual drop in the storage modulus, while the corresponding loss modulus G'' begins to rise, mirroring the approach to the nonlinear yielding behaviour and plastic flow. Beyond the characteristic point at $G' = G''$, typically called flow point, the apparent G'' overcomes G', reflecting the dominance of the energy loss due to the nonlinear flow.

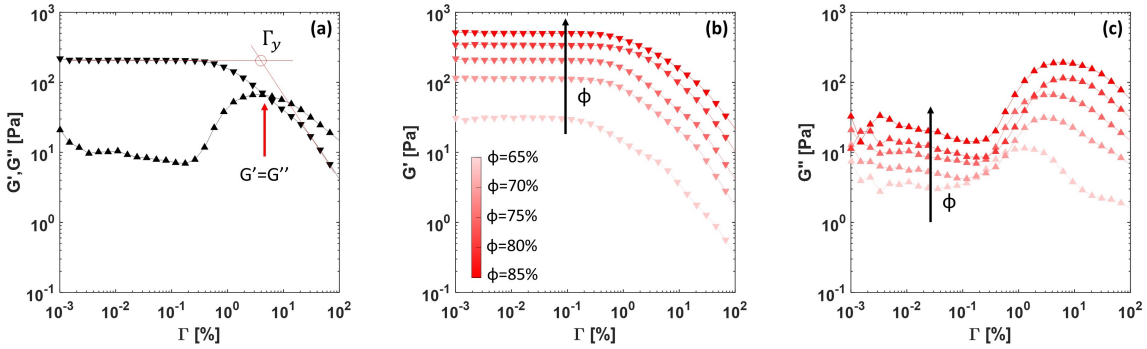

Figure 7.9 – **Emulsion viscoelasticity.** (a) Storage modulus G' and loss modulus G'' at different strain amplitude Γ for an emulsion at ϕ=75%. The point Γ_y indicates the yield strain, while the flow point $G' = G''$ occurs at a higher strain value. (b) G' and (c) G'' for the different oil fractions. Both increase with ϕ.

Figure 7.9 (b) and (c) report the curves for each oil fraction, from which we can see that G'_{LVE} strongly increases as we increase the emulsion oil fraction ϕ, reflecting an enhancement of its elasticity. The loss modulus G''_{LVE} is also observed to increase with ϕ meaning that the emulsion becomes also more viscous. As seen in section §5.2.2, the storage modulus G' of a concentrated emulsion is expected to scale with the oil volume fraction ϕ as $G'/(\gamma/r) \sim \phi(\phi - \phi^*)$ [82], where ϕ^* is the critical oil fraction 64% for monodisperse drops. Although predicted for monodisperse emulsions, this scaling is not expected to vary for polydisperse emulsions as long as the spread of the drop size distribution is moderate and centred around a single value [100], as in our case. Figure 7.11 (a) shows the variation of G'_{LVE} with ϕ for emulsions made with either rapeseed or sunflower oil, showing a good agreement with the predicted scaling. A summary of the storage and loss moduli in the linear viscoelastic regime at different ϕ is reported in table 7.1.

From the sweep test data we can roughly estimate the yield stress [23]. In figure 7.10 (a) we plot the measured shear stress τ versus the amplitude of the applied shear strain Γ. We fit the shear stress curve both in the linear viscoelastic regime (the slope of this fit corresponding to the emulsion storage modulus G'_{LVE}) and in the part of the curve above yielding: the ordinate of the intersection between the two lines gives the yield stress.

However, in order to get a more accurate estimate of the yield stress, in addition to sweep tests we also measure the flow curve of our emulsions. The results are shown in figure 7.10 (b) for emulsions made with rapeseed oil at different oil fractions ϕ. To obtain the yield stress τ_y, we can traditionally fit the flow curve with the empirical Herschel–Bulkley (HB) equation $\tau = \tau_y^{\mathrm{HB}} + K\dot{\Gamma}^n$ or with a recently proposed three component (TC) model

described by the equation $\tau = \tau_y^{\mathrm{TC}} + \tau_y^{\mathrm{TC}}(\dot{\Gamma}/\dot{\Gamma}_c) + \eta_{bg}\dot{\Gamma}$ [8]. However, we can see that the flow curves of our emulsions show a decay with decreasing shear rate $\dot{\Gamma}$ for $\dot{\Gamma} < 1\ \mathrm{s}^{-1}$ which could be due to emulsion slip, as pointed out also in [8]. These data points are thereby not considered in the fit. We fit the reliable data range with both models and the resulting yield stress values are summarised in table 7.1, which also contains the values τ_y^{sw} estimated from the sweep test data. We know that the emulsion yield stress is also expected to scale with the oil fraction ϕ as $\tau_y \sim (\phi - \phi^*)^2$ [81]. We thus plot all the results obtained with the different methods in figure 7.11 (b), where we can see that the data are globally in good agreement with the predicted trend, even though their absolute values result vertically shifted, with the HB fit giving the largest values, and the lowest ones given by the strain sweep tests.

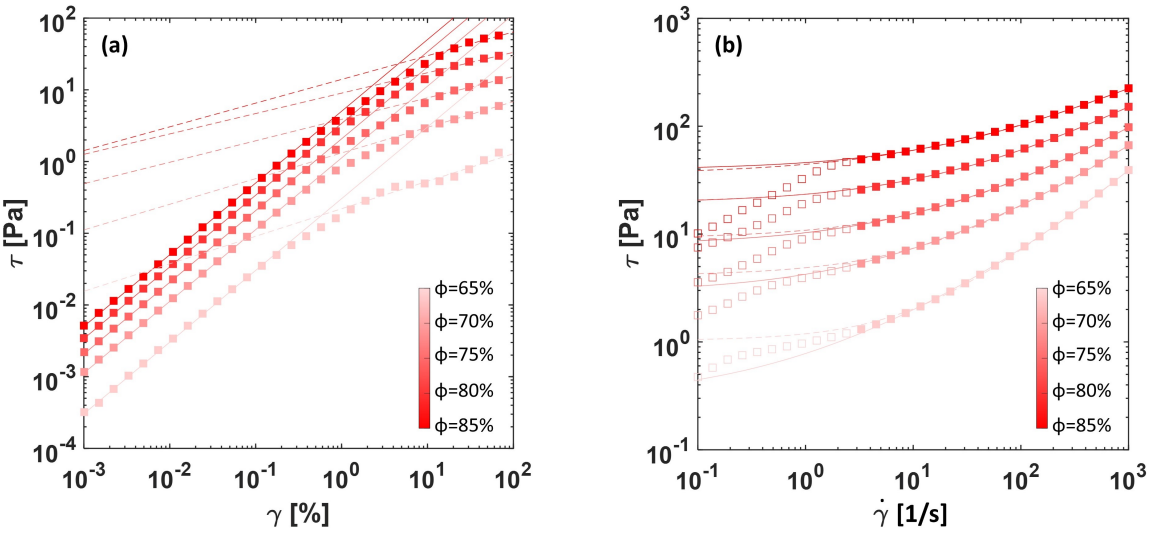

Figure 7.10 – **Emulsion yield stress determination.** (a) Sweep tests: shear stress vs shear strain. The yield stress can be estimated from the intersection of the two solid and dashed lines interpolating respectively the linear and the high strain regime. (b) Flow curves: shear stress vs shear rate. The yield stress is calculated by fitting each curve with a Herschel-Bulkley (dashed lines) or a three component equation (solid lines). The solid symbols indicate the fitted data range, while the open square data points are excluded because of emulsion slip.

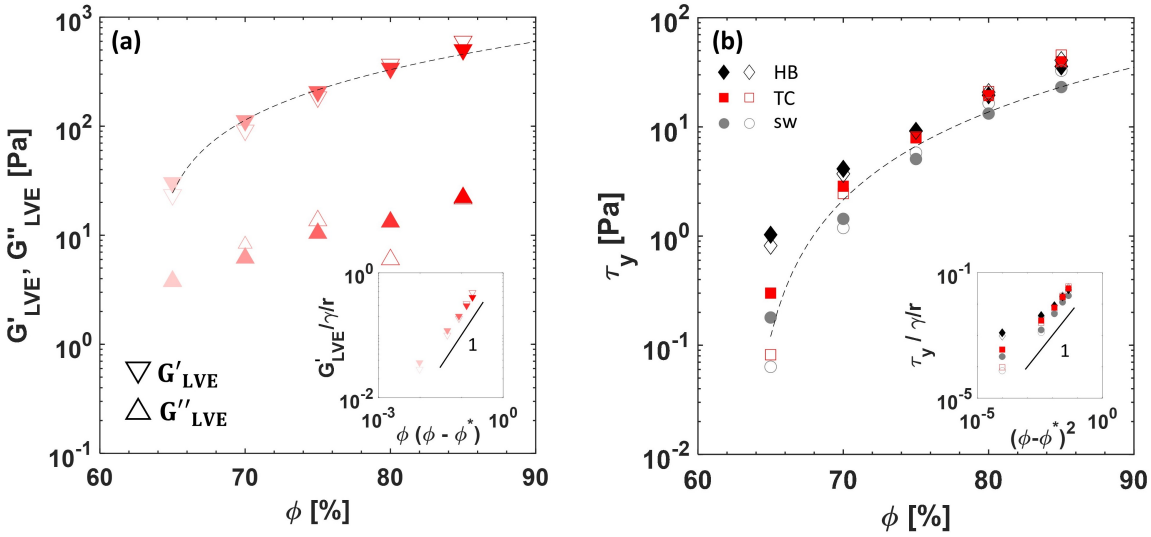

Figure 7.11 – **Emulsion mechanical properties vs oil fraction.** (a) Storage and loss moduli in the linear viscoelastic regime (G'_{LVE}, G''_{LVE}) as a function of emulsion oil fraction ϕ. The dashed line represents the expected scaling $G' \sim \phi(\phi - \phi^*)$. The inset shows the scaling of G'_{LVE} normalised by the Laplace pressure of the drops γ/r where $\gamma = 2$ mN/m and r is the surface-weighted radius of the droplets. (b) Yield stress τ_y obtained with different methods. The dashed line represents the expected scaling $\tau_y \sim (\phi - \phi^*)^2$. The inset shows the scaling $\tau_y/\gamma/r \sim (\phi - \phi^*)^2$. In both graphs (a) and (b), the solid symbols refer to emulsions made with rapeseed oil, while the empty symbols to the ones made with sunflower oil.

	ϕ [%]	G'_{LVE} [Pa]	G''_{LVE} [Pa]	τ_y^{sw} [Pa]	τ_y^{HB} [Pa]	τ_y^{TC} [Pa]
Rapeseed oil	65	31	4	0.2	1	0.4
	70	114	7	1.4	4.1	2.9
	75	209	11	5.1	9.1	7.9
	80	342	14	13.3	19.5	19.4
	85	506	24	23.2	35.8	39.5
Sunflower oil	65	24	4	0.06	0.8	0.08
	70	95	9	1.2	3.7	2.5
	75	191	15	5.8	9.2	8.1
	80	370	7	16.5	20.8	21.0
	85	604	25	32.8	40.8	45.4

Table 7.1 – **Emulsion rheological properties.** Values of the storage and loss moduli in the linear viscoelastic regime, and the yield stress obtained with different methods, for each emulsion oil fraction and oil type.

7.3.2 Mean bubble size evolution

In chapter §6 we saw that, in our set-up, aqueous foams can reach a self-similar growth regime within a few hours. We learnt how the evolution of the bubble size in such systems

is influenced by the thickening of the Plateau borders over time which gradually reduces the thin film area available for gas transfer. We now aim to probe what happens to the overall coarsening process when the aqueous phase is replaced by a viscoelastic fluid.

With the Kenwood mixer, we thus prepare foams from concentrated emulsions having ϕ ranging from 65% to 85%. The foam liquid fraction is observed to vary a little with the emulsion oil fraction, with slightly wetter foams obtained at higher ϕ, as reported in figure 7.12. This is in agreement with literature expectations as an increase of ϕ reflects an increase of the emulsion bulk viscosity, meaning that the air entrapment stops at lower gas fractions [92].

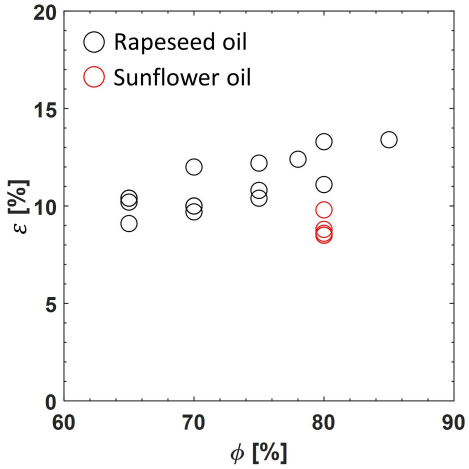

Figure 7.12 – **Foamed emulsion liquid fraction.** Foam liquid fractions for each foamed emulsion prepared along the thesis. For a given oil fraction $\phi = 80\%$, the use of sunflower oil is observed to give slightly drier foamed emulsions.

The freshly-generated foamed emulsion is then sandwiched between two glass plates with a spacing of 1 mm in order to monitor its coarsening evolution. In this case, we observe that the high oil drop concentration makes evaporation negligible, probably for two reasons: first, when closing the cell the foamed emulsion destroyed at the borders quickly creates a layer of free oil all around the joint perimeter, which helps sealing the cell from the external environment; second, the area available for water evaporation is strongly reduced, as in foamed emulsions the cross-section of a foam Plateau border is mainly made of oil, with the aqueous phase confined in the network of emulsion Plateau borders which are much thinner. Moreover, to extract water from the emulsion one needs to overcome a higher osmotic pressure than in an aqueous foam.

We characterise the coarsening of such systems starting from the time t_{2D} when they become monolayers of bubbles. In figure 7.13 (a) we plot the time evolution of the total number of bubbles in the foam. We can see that for each sample the initial total number of bubbles at $t = t_{2D}$ is of the order of 10^4, which then gradually decreases over time but always remains above 700.

For the same samples, we now plot in figure 7.13 (b) the growth of the average bubble radius $\langle R \rangle$ normalised by its value $\langle R(t_{2D}) \rangle$ when the foam has just become a monolayer. We can see that, while the foam having $\phi = 65\%$ in the continuous phase evolves in good approximation as $t^{1/3}$, at higher ϕ values the samples no longer show a power law evolution and the coarsening rate decreases with increasing ϕ. We remark that in foamed emulsions

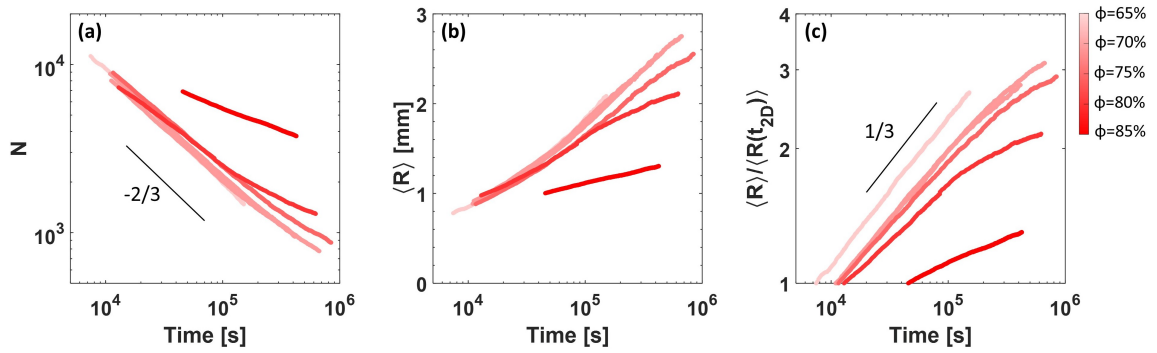

Figure 7.13 – **Number and mean bubble size evolution.** (a) Evolution of the total number of bubbles over time for the different foamed emulsion samples. (b) Growth of the average bubble size at different emulsion oil fraction ϕ. (c) Time evolution of the mean bubble size normalised by its initial value when the foam has just become 2D. The time shown in the graphs is the time elapsed after the foam generation.

the average bubble size is observed to grow in time with a rate lower than the diffusion-limited prediction for bubbly liquids, even though in our foams we always observe thin films between the bubbles. In fact, since emulsions are completely white, from a side view of the sample we can clearly distinguish the films between adjacent bubbles from the surface Plateau borders, as shown in figure 7.14 (a,b) for two different oil fractions. This is a first signature of a change in the foam structure, and especially in the shape of the surface Plateau borders which is clearly not traditional, as in light of what discussed in chapter §6 we would expect the thin film area to vanish during the experiments.

We also notice that the samples at lower ϕ showed a higher number of coalescence events which is the reason why the experiments are stopped earlier. This can be seen in figure 7.14, where we compare the final appearance of the foam sample having $\phi = 65\%$ in the continuous phase (c) with the one of the sample at $\phi = 80\%$ (d) at the same foam age.

From a close inspection of the samples we can already see that the overall foam structure is strongly affected by the increase of the emulsion viscoelasticity, and while at $\phi = 65\%$ we can still recognise a foam pattern made of polygonal bubbles, as we increase ϕ up to 80% the bubble pattern no longer resembles the one of an aqueous quasi-2D foam: the bubbles are not at all relaxed and the emulsion appears unevenly distributed inside the sample. We shall return on a more detailed description of the foam structure later in section §7.3.5, while in the next section we start by looking at the bubble size distributions to see whether they give some insights on the foam structure evolution.

7.3.3 Bubble size distributions

From the characterisation of quasi-2D aqueous foams in chapter §6, we saw that the distribution of the normalised radii is in general more informative than the one of the normalised areas. Therefore, we start by comparing the initial size distribution in our foamed emulsions at different ϕ, when the samples have just become a bubble monolayer, to see whether strong differences are already present since the beginning of the image acquisition. Figure 7.15 shows no significant variations with the oil fraction ϕ, meaning that each sample starts in good approximation from the same bubble size distribution.

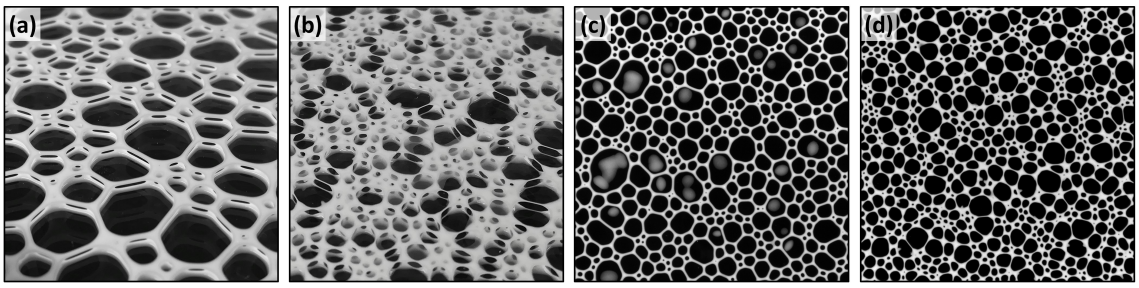

Figure 7.14 – **Films and coalescence.** (a) Perspective view of the sample at ϕ=70% at the end of the acquisition. We can recognise the films between adjacent bubbles. (b) Perspective view of the sample at ϕ=85%, where we can see that the Plateau borders have atypical shapes. (c) Appearance of the sample at ϕ=65% at the end of the image acquisition. We can recognise where coalescence events have occurred from the patches of emulsion left by the surface Plateau borders. Edge size 12 cm. (d) Appearance of the sample at ϕ=80% at the same time, from which we can see that less coalescence events have occurred, and that the bubbles start assuming stretched shapes. Edge size 12 cm.

Let us now look at how these distributions evolve over time. This is plotted in figure 7.16 for each sample, with the curve grey scale becoming darker as the foam ages. We can see that the evolution is qualitatively different from the one observed in section §6.3.1 for aqueous foams. While the sample at the lowest ϕ shows a distribution which resembles the one of an aqueous foam in its self-similar regime, the shape of the dimensionless size distribution in samples at higher oil fractions changes over time. The non-stationary behaviour is reflected by the time evolution of the polydispersity p and the second moment of the distribution μ_2^R reported in figure 7.16, where we can see that both increase over time, indicating a general broadening of the distribution. More precisely, we can see that the distributions at higher oil fractions clearly exhibit a time-increasing positive skewness. The distribution asymmetry can be quantified by looking at the time evolution of its third moment μ_3^R, defined as:

$$\mu_3^R = \left\langle \left(\frac{R}{\langle R \rangle} - 1 \right)^3 \right\rangle \tag{7.3}$$

Its time evolution is also reported in figure 7.16, where we can see that, after an initial constant plateau, μ_3^R steeply increases for each sample. As a first remark, we can see that these foamed emulsions are obviously not self-similar, which is not at all surprising given the numerous conditions which should be satisfied for that, but what is worth highlighting is that this cannot be only a transient effect, as it evolves further away from a SSGR distribution.

This increase of the skewness over time, which shifts the distribution peak towards smaller bubbles, geometrically reflects an accumulation of small bubbles which does not occur in aqueous foams. This means that there must be an overall dynamic asymmetry in the evolution of bubbles of different sizes: either big bubbles grow faster or small bubbles shrink more slowly than expected. The first scenario can be readily discarded as the overall mean size evolution would then be faster than an aqueous foam of equivalent liquid fraction, whereas the opposite is observed. The slight increase of μ_3^R registered for the sample at 65% of oil, associated with no evident change in the distribution shape, can be reasonably

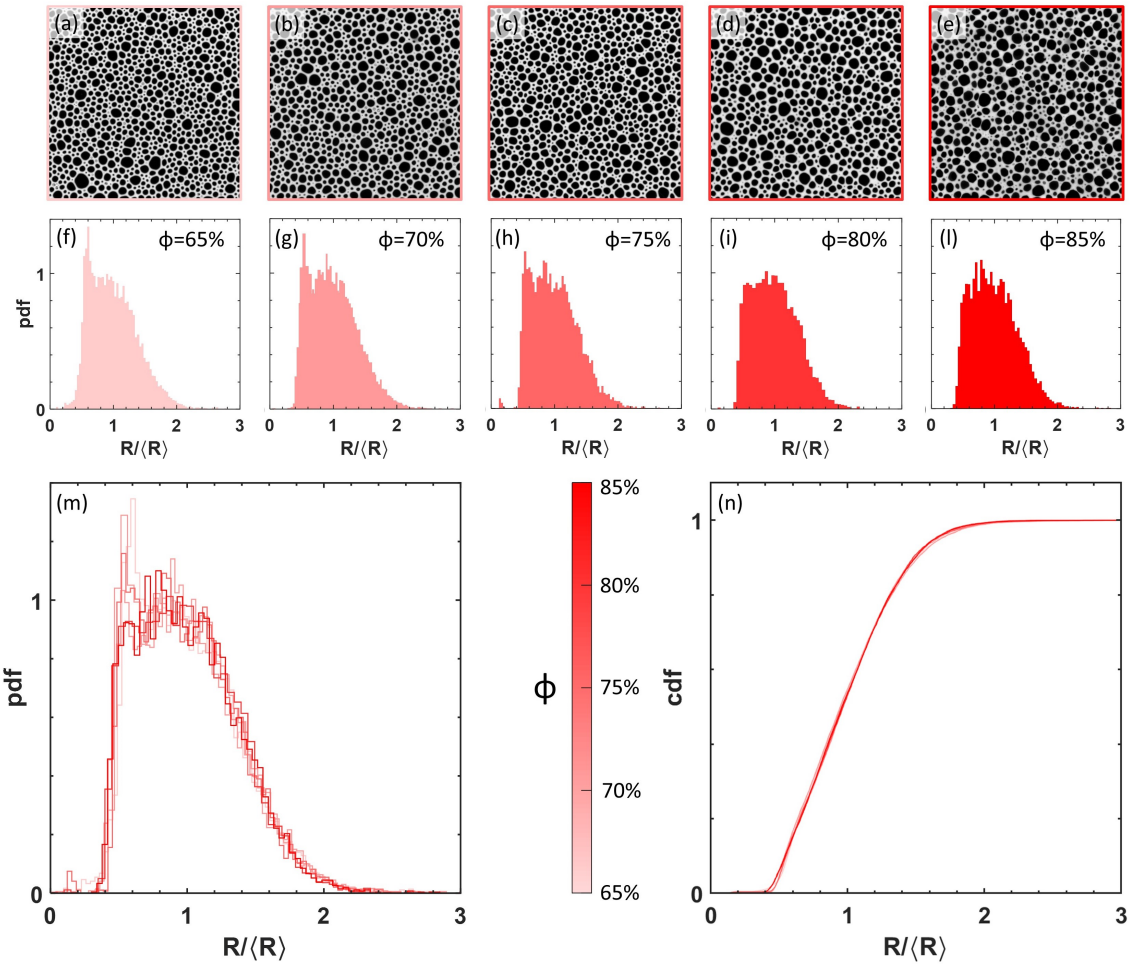

Figure 7.15 – **Initial bubble size distributions.** (a-e) Foamed emulsions at time t_{2D} at ϕ=65%, 70%, 75%, 80% and 85% from left to right. Edge size 5 cm. (f-l) Corresponding dimensionless bubble size distributions at time t_{2D}. (m) Comparison of the distributions shown in (f-l). (n) Comparison of the corresponding cumulative distributions.

ascribed to the occurrence of bubble coalescence events. However, the steep increase of μ_3^R observed in all other samples is more likely due to a delay in the disappearance of small bubbles, with their slower shrinkage in agreement with the globally reduced coarsening rate.

To confirm that the coarsening rate is limited by the delayed vanishing of small bubbles, we can compare the evolution of the average bubble size with the evolution of other moment means of the bubble radius. In figure 7.17 we plot different moment means $R_{mn} = \sum_i R_i^m / \sum R_i^n$: in (a) we report the usual normalised number-weighted average bubble size $R_{10} = \langle R \rangle$, in (b) we plot the normalised R_{21} which corresponds to a perimeter-weighted bubble radius and in (c) the surface-weighted mean bubble size R_{32}, which in this quasi-2D configuration clearly means weighing by the bubble area, and thus it would be the equivalent of the volume-weighted bubble size in three dimensions. At each instant, the latter two moment means weigh more the larger bubbles when computing the average, and we can clearly see that their evolution curves are straighter compared to the one of the number average R_{10}, meaning that larger bubbles keep growing: the low growth rates

observed for R_{10} are thus limited by the slower shrinkage of small bubbles and their delayed disappearance. We remark that in an aqueous foam attaining its SSGR all the moment means would have different absolute values but are expected to grow in the same way, as all the length scales in the foam are magnified by the same factor. We can see that this is approximately true for the sample at $\phi = 65\%$, where all the moment means evolve approximately as $t^{1/3}$, exhibiting however a faster increase in the late stage that can be ascribed to the onset of bubble coalescence.

The delay in the disapperance of small bubbles is markedly enhanced at increasing oil fractions, which suggests that the local coarsening dynamics is linked to the change in the mechanical properties of the emulsion and thus of the foamed emulsion itself. In the next section we shall propose a mechanical explanation of why such small bubbles shrink more slowly than expected.

3D bubbles

Before discussing the origin of the delayed disappearance of small bubbles, we briefly comment on the absence of the instability undergone by shrinking bubbles at oil fractions ϕ higher than 65%. Indeed, we saw in section §4.5 that shrinking bubbles at some point can detach from the bottom plate and become 3D. In foamed emulsions, when small bubbles reach a bubble size small enough so that this instability is expected to happen, they are completely surrounded by the emulsion, whose yield stress hinders their rising upwards.

Indeed, if the buoyancy force per unit area exerted on the bubble $\sim \rho_{\mathrm{em}} gR/3$ does not overcome the emulsion yield stress τ_y, the bubble is not able to rise. ρ_{em} is the emulsion density, which depends on the oil fraction ϕ, and if we calculate it as $\rho_{\mathrm{em}} = \phi\rho_{\mathrm{oil}} + (1 - \phi)\rho_{\mathrm{water}}$, where $\rho_{\mathrm{oil}} = 910$ kg/m^3 $< \rho_{\mathrm{water}}$, the heaviest emulsion will then be the one at ϕ=65%, as it contains more water, with a global density of 941.5 kg/m^3. If we consider a shrinking bubble reaching a radius R=0.5 mm, we then get $\rho_{\mathrm{em}} gR/3$ ∼1.5 Pa, which is slightly larger than $\tau_y(\phi = 65\%)$ but smaller than all the other emulsion yield stresses measured at higher oil fractions. This is why we do not observe any 3D bubble at $\phi > 65\%$.

This means that the complete disappearance of the small bubbles occurs while suspended in the middle of the cell gap, not on the top. Moreover, the thickening of the foam surface Plateau borders, together with their turbid white appearance, makes them disappear from the picture before they actually disappear in the foam, so that no size threshold is needed when processing the pictures to get the bubble size distributions.

7.3.4 Coarsening mechanism

In this section we shall describe in more detail the coarsening mechanism observed in our foamed emulsions. We have seen in section §7.3.3 that an increase of the emulsion oil fraction causes a delay in the disappearance of small bubbles, as confirmed by the increase of the lopsidedness of the bubble size distribution over time, and that this delay is at the origin of the reduced global coarsening rates registered in section §7.3.2. However, the increase of the third moment μ_R^3 does not say anything on the spatial distribution of such small bubbles, which could be evenly spread all over the foam sample.

In fact, an attentive visual inspection of the coarsening movies reveals that this is not the case, and that the delay of the small bubble disappearance is not the only effect observed. An increase of the emulsion oil fraction also results in heterogeneous bubble growth, which eventually creates a pattern made of growing bubbles arranged in chains and regions of

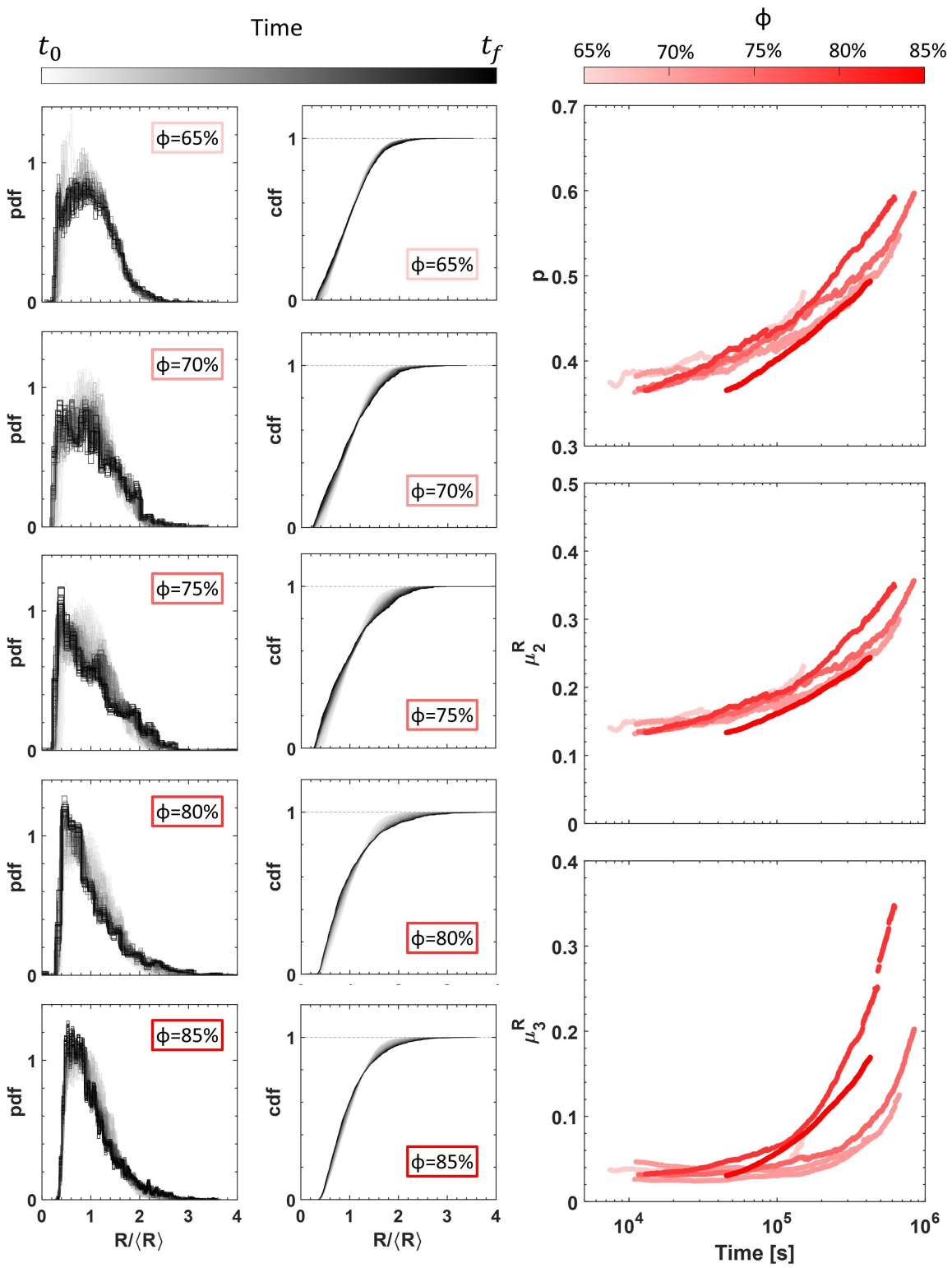

Figure 7.16 – **Bubble size distributions over time.** First column: time evolution of the dimensionless $R/\langle R\rangle$ distribution for the samples at different ϕ. Second column: time evolution of the corresponding cumulative distribution. Third column, from top to bottom: time evolution of the polydispersity, second moment μ_2^R, and third moment μ_3^R for the different samples.

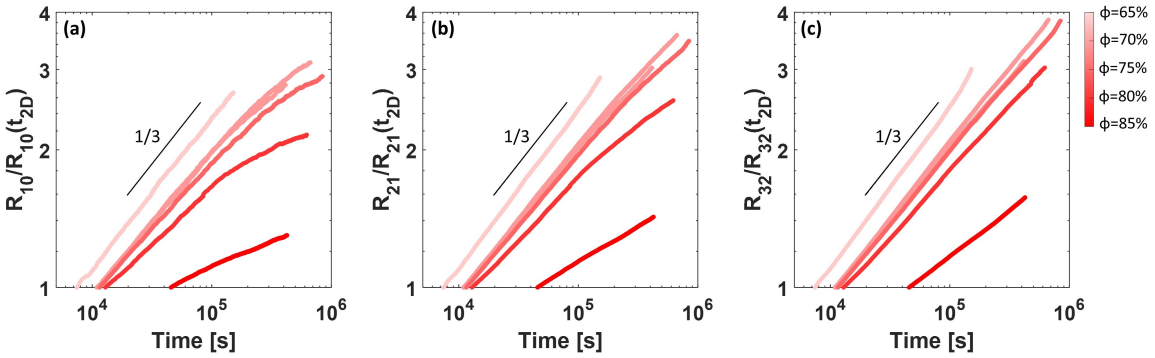

Figure 7.17 – **Time evolution of different R moment means.** (a) Time evolution of the normalised number-weighted average bubble radius $R_{10} = \langle R \rangle$ at different oil fractions. (b) Time evolution of the normalised perimeter-weighted average R_{21}, and (c) area-weighted average R_{32} at different ϕ.

smaller bubbles grouped together. The time evolution of the two samples at $\phi = 70\%$ and $\phi = 80\%$ is reported in figure 7.18 as example: the pictures clearly show the different foam structure with the irregular bubble pattern eventually developed by the foamed emulsion at higher ϕ.

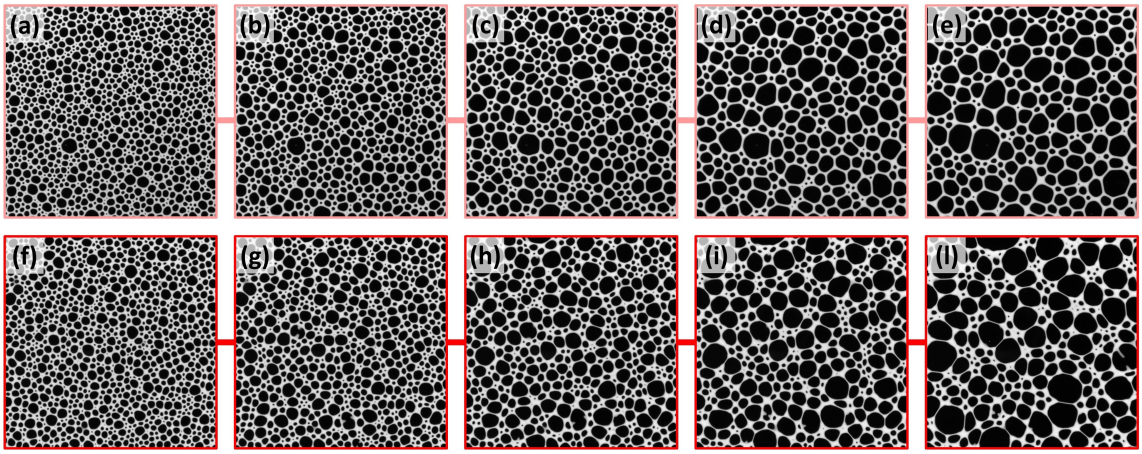

Figure 7.18 – **Time evolution of two samples at different ϕ.** (a-e) Evolution of the sample at $\phi = 70\%$ after 6, 12, 24, 48 and 96 hours. (f-l) Evolution of the sample at $\phi = 80\%$ at the same times. The edge size of each photo is 7 cm.

It is not possible to state *a priori* whether and how these two distinctive features of foamed emulsion coarsening are correlated. Nevertheless, we attempt to interpret our qualitative observations by starting from the latter effect.

Since their generation, our foamed emulsions are polydisperse. This means that at any time we have both small and stiff bubbles coexisting with larger and more easily deformable ones, all of them surrounded by a certain amount of emulsion, which is viscoelastic. Whether the bubble is stiff or weak with respect to the emulsion matrix is quantified by the elastocapillary number defined in section §5.3.2, that we recall to be the ratio between the emulsion storage modulus G_0 and the bubble capillary pressure γ/R, namely:

$$Ca_{\mathrm{el}} = \frac{G_0}{\gamma/R} \tag{7.4}$$

A Ca_{el} higher than one means that the bubble is more easily deformable than the emulsion, while on the contrary a Ca_{el} lower than one means that it is easier to stretch the emulsion than the bubble, as the latter is stiffer. We can thus estimate a size threshold at which a bubble is supposed to switch from stiffer to weaker than the emulsion as $R_{\mathrm{el}} = \gamma/G_0$. By considering a surface tension $\gamma \simeq$30 mN/m and the emulsion storage moduli G_0 reported in table 7.1, we find that this critical radius varies from 0.98 mm for the foamed emulsion at 65% to 60 μm for the sample at 85%, as reported in table 7.2. We can thus see that for the highest oil fraction, R_{el} is much smaller than the typical bubble size in our quasi-2D systems. Therefore the bubbles are always easier to deform in the latter.

However, since the bubbles are not isolated and completely surrounded by the emulsion, we should better think in terms of local foamed emulsion rheology: we can consider the volume encapsulating a single bubble as a small portion of foamed emulsion, which can be more or less rigid. Indeed, for a given emulsion, we saw in section §5.3.2 that the storage modulus of a 3D foamed emulsion G_{FE} depends on the liquid fraction ε, as well as on the bubble size R [50]. Indeed, we recall that G_{FE} has been found to be well described by the sum of the two contributions coming from the elastic deformation of the bubbles, G_{F}, and of the continuous phase, G_{E}, namely we can write:

$$G_{\mathrm{FE}} = G_{\mathrm{F}} + G_{\mathrm{E}} = 1.6\frac{\gamma}{R}(1-\varepsilon)(0.36-\varepsilon) + \varepsilon^2 G_0 \tag{7.5}$$

For simplicity, we shall not consider here the coupling term ψ between the two, as the proposed expression was empirical [50] and it could be dependent on the system: in our case we are not even in a 3D system but in a quasi-2D foam configuration. We shall use this expression as a scaling relation to describe the behaviour of our foamed emulsions.

If we assume that the liquid fraction is homogeneous, then we can infer from equation (7.5) that a cell containing a small bubble will be stiffer than a cell containing a larger one. The fact that our foamed emulsions are polydisperse, means that we have local "one-bubble" regions that are more or less elastic. The Laplace pressure difference between two adjacent bubbles of different size will make the gas want to diffuse from the smaller bubble to the larger one, and for the latter to grow, it needs to strain the neighbouring bubbles. Since the environment around smaller bubbles is locally stiffer, the growing bubble will end up yielding the material where it is weaker, thus it will grow towards its larger neighbours. This can qualitatively be at the origin of the heterogeneous growth that we observe at high ϕ even well before the appearance of stretched bubble shapes.

However, this heterogeneous growth has a key consequence in the foam evolution: it eventually segregates the small bubbles in regions separated by chains of larger ones, as better shown in figure 7.19 (a). This idea is also supported by the shape of the Plateau border edges that can be seen from the enlargement in figure 7.19 (b): where the thin Plateau borders between two adjacent large bubbles adjoin the vertices, their curvature often assumes the shape of a hour-glass. This inversion of curvature suggests that the larger bubbles are actually pushing towards each other as if they wanted to kiss, which is confirmed also by the video of the image acquisitions.

Once this segregation occurs, we can extend our reasoning to larger but still local regions of a few bubbles: since the bubble sizes are no longer homogeneously distributed as in a

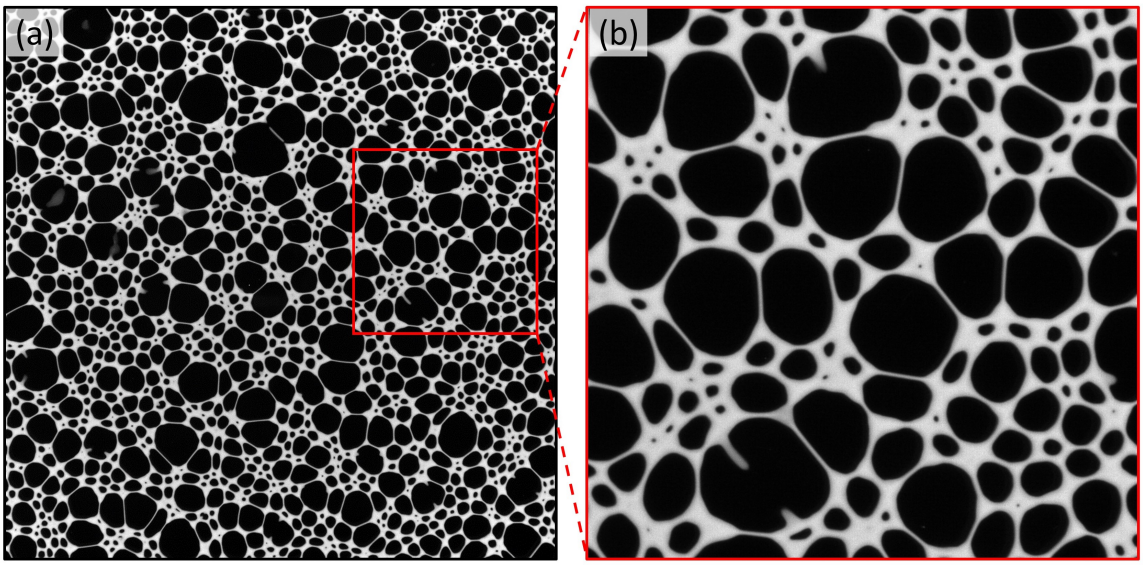

Figure 7.19 – **Late-stage bubble pattern at high ϕ.** (a) Bubble pattern at late stage for the sample ϕ=80%. One can recognise the chains of large bubbles impinging on each other and the wetter regions of small bubbles grouped together. Edge length 15 cm. (b) Enlargement of the same picture. One can notice the hour-glass shape of the thin Plateau borders between large bubbles. On the bottom left one can also see the emulsion relaxation after a coalescence event. Edge length 5 cm.

traditional foam, the local regions containing smaller bubbles will be stiffer than the regions of adjacent larger bubbles. Thus, coarsening will more likely occur in the weaker regions of the foam, as it is easier for the bubbles to vary their size: if we take a single bubble inside a region of small bubbles, this will see a more elastic environment around itself compared to the one seen by larger bubbles, which offers a higher elastic resistance to its size variations. It will thus be harder for such bubbles to shrink than for the ones impinging on the large bubble chains. This can explain why the shrinkage and subsequent disappearance of small bubbles is delayed in such systems: the heterogeneity of the local foam rheology hinders the shrinkage of small bubbles while the big bubbles continue to coarsen by taking gas from the adjacent small gas cells and expanding against other large bubbles.

Since the mean bubble size in our systems grows over time because of coarsening, we can try to estimate the bubble size at which we expect to see bubble coarsening to be hindered by the foamed emulsion elasticity, by introducing a new elastocapillary number, now comparing the stiffness of the foamed emulsion with the Laplace pressure of the bubbles:

$$Ca_{\mathrm{el}}^{\mathrm{FE}} = \frac{G_{\mathrm{FE}}}{\gamma/R} \tag{7.6}$$

from which we can calculate a critical bubble size R_{FE} given by:

$$R_{\mathrm{FE}} = \frac{(1 - 1.6(1-\varepsilon)(0.36-\varepsilon))\gamma}{\varepsilon^2 G_0} \tag{7.7}$$

which corresponds to the point at which $Ca_{\mathrm{el}}^{\mathrm{FE}}$=1. We calculate R_{FE} for each foamed emulsion sample and we report the results in table 7.2.

On the other hand, the average bubble size at which we start observing an anomalous accumulation of bubbles smaller than the average can be estimated from the third moment of the normalised bubble radii distribution. Figure 7.20 (a) reports the evolution of μ_3^R now as a function of the average bubble size $\langle R \rangle$ for the different samples. We can see that at small bubble sizes all samples have a μ_3^R which is in first approximation constant and centred around a value ~ 0.035. As the foam coarsens the mean bubble size increases, and at some point μ_3^R steeply diverges to high values. This divergence is not sharp, but we can still define a critical bubble size at which we observe a departure of μ_3^R from the initial plateau, and we call this size R_{sk}. To do that we consider a common average value of the initial plateau for all samples. For each sample we calculate the average of μ_3^R for $\langle R \rangle < 1.1$ mm, and then we average these values to obtain a common value $\mu_3^{R,i} = 0.0355$ corresponding to the solid line in figure 7.20 (a). To get R_{sk}, we consider the bubble size at which μ_3^R crosses a threshold value equal to 150% its initial plateau $\mu_3^{R,i}$, as indicated by the dashed line in the same plot. The early but slight increase of μ_3^R for the sample at $\phi = 65\%$ is more likely due to the observed coalescence events, so we shall not consider it, as even at the end of the acquisition the size distribution shape is still in good approximation close to the one of a self-similar aqueous foam. The values of R_{sk} obtained for the different samples are also reported in table 7.2.

If we now compare in figure 7.20 (c) the values of R_{sk} with the ones calculated for R_{FE}, we can see that, although there is a correlation between the two, the latter are much larger than the former, but also larger than the maximum bubble size attained during our experiments. This means that we observe a delay in the small bubble shrinkage earlier than expected for the foamed emulsion local elasticity to hinder the coarsening according to this line of reasoning.

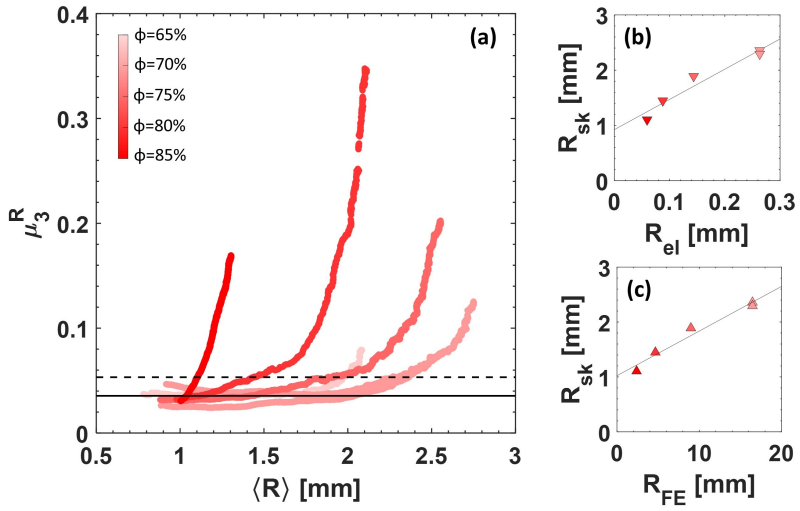

Figure 7.20 – **Evolution of the distribution skewness.** (a) Third moment of the bubble radii distribution vs average bubble size for each sample. The solid line indicates the initial average plateau, the dashed line corresponds to 150% its value. R_{sk} is found by the intersection between the curves and the dashed line. (b) Correlation between R_{sk} and the critical R_{el}. The latter is too small to explain the observed deviation of μ_3^R. (c) Correlation between R_{sk} and the critical R_{FE}. The latter is now too large to explain the observed deviation of μ_3^R.

However, we stress that so far we have considered the foam liquid fraction to be homogeneous inside the sample, but this is not true, especially at high oil fractions. Indeed, from the coarsening movies, we observe a lack of emulsion redistribution inside the sample after T2 events, which in the long run results in an uneven distribution of emulsion around the bubbles in the system.

This has a larger impact on small bubbles, as even in an aqueous foam the latter are surrounded in proportion by more liquid than their larger neighbours. Moreover, as seen in chapter §6, coarsening at constant ε in a quasi-2D configuration makes the Plateau borders thicken over time, further increasing the local liquid fraction around the bubbles along time.

If we now remember that in these systems the bubbles themselves are not evenly distributed, as smaller bubbles are grouped together, we can see that the regions of small bubbles can be stiffer not only because the mean bubble size is locally smaller but also because they are locally wetter than the regions of larger bubbles. Thus, the local rheology difference between regions of small and large bubbles depends also on the change in the local liquid fraction.

Whether an increase of liquid fraction further strengthens the foamed emulsion depends on the emulsion G_0 and on the bubble size R. Indeed, in figure 7.21 (a), we now show how the storage modulus of a foamed emulsion changes with the liquid fraction for different emulsion oil fractions, namely for different G_0. We can see that for a fixed bubble size $R = 1$ mm, around $\varepsilon \simeq 10\%$ the foamed emulsion at the lowest ϕ shows a G_{FE} which decreases with increasing ε, whereas the sample at the highest ϕ becomes more elastic if the liquid fraction is increased. This means that while in the former the G_{FE} is governed by the first term G_{F} linked to the rheology of an equivalent aqueous foam, in the latter the overall elasticity is governed by the contribution of the emulsion matrix G_{E}. In the sample at ϕ=85%, a local increase of ε in regions of bubbles having $R = 1$ mm translates into a more elastic medium, as the addition of emulsion among the bubbles strengthens the material.

However, for a given ϕ, G_{FE} also depends on the bubble size, and in our foamed emulsions $\langle R \rangle$ is not constant over time but increases because of coarsening. As it can be inferred from equation (7.5), an increase of $\langle R \rangle$ would gradually make the contribution of the term G_{F} less and less important: we could then expect for each sample to have a ϕ-dependent critical bubble size at which the contribution of the emulsion becomes predominant and thus the trend of $G_{\mathrm{FE}}(\varepsilon)$ around $\varepsilon \simeq 10\%$ inverts from decreasing to increasing.

Let us then look at how $G_{\mathrm{FE}}(\varepsilon)$ varies as we increase the bubble size $\langle R \rangle$ at a fixed emulsion oil fraction ϕ. In figure 7.21 (b-f), we plot for each oil fraction considered, the evolution of G_{FE} with ε at different $\langle R \rangle$. We can see that, in each graph, as $\langle R \rangle$ is increased we observe a local change in the slope of G_{FE} around their liquid fraction value ε, which we recall is not very different as it ranges between 9% and 13%. We can estimate the critical bubble radius R^* at which this happens by deriving equation (7.5) with respect to the liquid fraction ε. We report in the insets of figure 7.21 (b-f), the evolution of $\mathrm{d}G_{\mathrm{FE}}/\mathrm{d}\varepsilon$, evaluated at the sample ε, as a function of $\langle R \rangle$ for each sample, and we can see that indeed it crosses the line zero at a critical mean bubble radius that we shall call R^*.

This means that in each sample, at some point we reach a mean bubble size at which a local increase of the liquid fraction would translate into a local higher elasticity. Since the beginning smaller bubbles are wetter than larger bubbles, and as the foam coarsens the local liquid fraction further increases, and so does the average bubble size. When a critical mean bubble size is reached, smaller bubbles in the wetter regions are thus surrounded

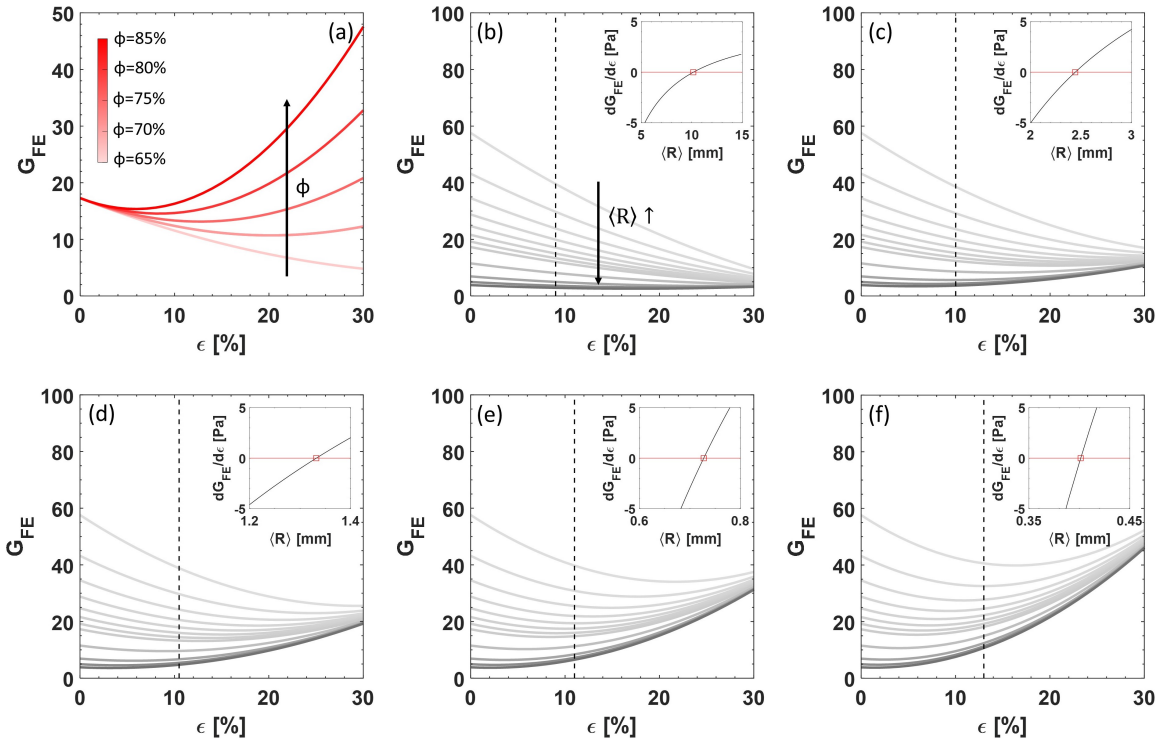

Figure 7.21 – **Foamed emulsion elasticity**. (a) Dependency of G_{FE} on the liquid fraction for foamed emulsions having a fixed average bubble size $\langle R\rangle = 1$ mm and different emulsion storage modulus (different ϕ). By comparing the curves, we can see that around ε=10% an increase of liquid fraction would weaken the foamed emulsion at ϕ=65%, while it would strengthen the sample at ϕ=85%. The behaviour however depends also on the bubble size. (b-f) Dependency of G_{FE} on ε for different average bubble sizes at a fixed emulsion storage modulus, corresponding to the samples ϕ=65% (b), 70% (c), 75% (d), 80% (e) and 85% (f). The vertical dashed lines indicate the liquid fraction for each sample. The insets show the critical size R^* at which we expect an inversion of G_{FE} behaviour with increasing ε, around the ε value of each sample, mirrored by $\mathrm{d}G_{\mathrm{FE}}/\mathrm{d}\varepsilon$=0.

by a more elastic medium which hinders their shrinkage, whereas the bigger bubbles are surrounded by a locally less elastic medium and thus it is easier for them to keep growing.

Now that we have computed the critical radius R^* for each sample, we can compare it with R_{sk}, which we recall corresponds to the onset of the steep increase of the skewness in the bubble size distribution. In figure 7.22 we plot R_{sk} versus R^* where we can see that there is a rather good correlation between the mean bubble size at which we start observing an accumulation of small bubbles, due to a delay in their shrinkage, and the mean bubble size at which we expect a difference in the local liquid fraction to result in a stiffening of wetter regions. Moreover, we see that the two critical values are now of the same order of magnitude.

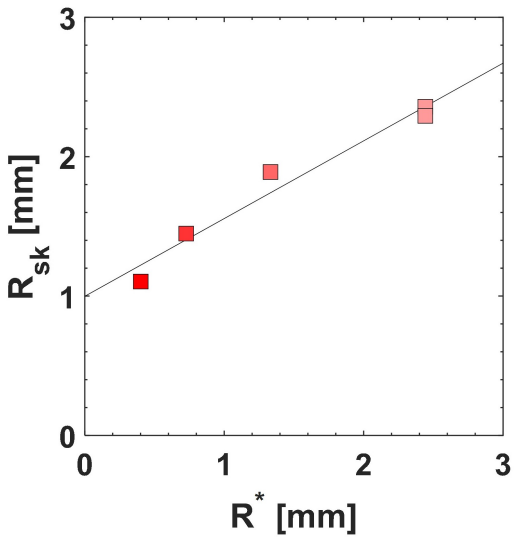

Figure 7.22 – **Correlation between R_{sk} and R^*.** The graph shows the correlation between the mean bubble size R_{sk} at which we start observing an accumulation of small bubbles and the critical mean bubble size R^* at which we expect, according to the scaling relation of G_{FE}, a stiffening of the foamed emulsion upon increase of the liquid fraction.

ϕ [%]	R_{el} [mm]	R_{FE} [mm]	R^* [mm]	R_{sk} [mm]
65	0.97	73.05	10.23	-
70	0.26	16.50	2.45	2.36
70	0.26	16.50	2.45	2.29
75	0.14	8.98	1.33	1.89
80	0.09	4.66	0.73	1.45
85	0.06	2.39	0.40	1.10

Table 7.2 – **Summary of the critical mean bubble sizes.** Critical bubble radius R_{el} coming from the condition Ca_{el}=1, R_{FE} coming from the condition Ca_{el}^{FE}=1, R^* coming from the condition $dG_{FE}/d\varepsilon$=0 around the sample liquid fraction, and R_{sk} obtained from the evolution of μ_3^R.

We remark that we did a big approximation in modelling the elastic response of these quasi-2D foamed emulsions, as equation (7.5) comes from 3D foamed emulsion rheology. When using this scaling relation we are not considering any prefactors which could be dependent on the system configuration, and for example change with the level of foam confinement. The strong foam confinement can play a non-negligible role in the mechanical behaviour of the foamed emulsions and thus change their elastic response, as we shall see in section §7.3.7. However, the correlation observed between R_{sk} and R^* suggests that, for a given level of confinement, the scaling relation used for G_{FE} qualitatively describes the behaviour of our systems, and that the local elastic response of the foam plays a crucial role in the evolution of the bubble pattern, affecting the overall coarsening process.

7.3.5 Bubble pattern

In this section, we go back to the atypical foam structure observed in quasi-2D foamed emulsions at high oil concentrations in their continuous phase. As seen in figure 7.19 (a) for the sample at $\phi = 80\%$, the bubble pattern shows some peculiar features: regions of smaller and wetter bubbles appear all together, separated by chains of larger and drier bubbles sharing thin elongated surface Plateau borders.

Quantifying the change in the bubble shapes is not a trivial task, as one should find the right parameter which highlights the difference between these stretched patterns and a traditional foam structure. To do that, one could define the elongation e of a bubble as:

$$e = \frac{2p}{\sqrt{A}} \tag{7.8}$$

where $2p$ is the bubble perimeter and A is the bubble area, so that e is a dimensionless parameter. For regular n-sided bubbles with curved edges, the elongation value slightly decreases with n, being $e \simeq 3.72$ for a regular hexagon [55].

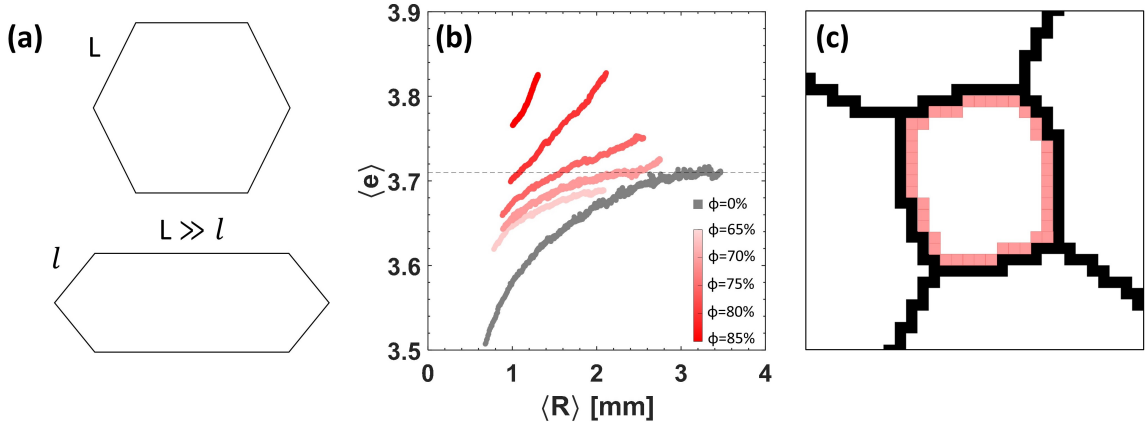

Figure 7.23 – **Bubble elongation.** (a) Qualitative difference between a regular hexagonal bubble and the elongated bubble shape that we observe at high oil fractions. (b) Average bubble elongation versus the average bubble size in the sample. The systematic error due to the underestimation of the bubble perimeter gives unphysical elongation values below the expected minimum 3.71. (c) Example of small skeletonised bubble for which the underestimation of the perimeter, calculated as the distance between the pink pixels, is not negligible and gives a too low elongation.

The ground state of a 2D foam corresponds to the bubble configuration having minimum total perimeter, in order to minimise the global surface energy. It has been shown that a relaxed foam is expected to have an average elongation $\langle e \rangle$ close to 3.72, as for an array of regular hexagons [55]. Since we saw that the bubble pattern of our foamed emulsions becomes unrelaxed over time, we could think about calculating the average elongation for each sample to see if we can pinpoint the onset of the bubble stretched shapes from its time evolution. Indeed, in our pictures we observe that larger bubbles often share an edge much longer than the other sides, as roughly schematised in figure 7.23 (a). We thus expect to see an increase of the average bubble elongation over time compared to a foam in its relaxed state.

However, in our experiments, the high resolution of the camera is fully exploited to achieve the highest accessible bubble statistics. Thus, in our frames, each bubble is represented by a sufficient number of pixels to robustly calculate its area (from which its equivalent radius is derived) but not to reliably estimate its perimeter. An accurate evaluation of bubble elongations, which rely on a precise measurement of the perimeter, is therefore not possible from our pictures. Indeed, if we calculate the average bubble elongation and plot it against the average bubble size in figure 7.23 (b), we can see that unphysical values of $\langle e \rangle$ below 3.71 are obtained, while elongations of polygonal bubbles cannot be below 3.71 [55], and neither can their average. This is due a systematic error in the detection of the bubble perimeter coming from the MATLAB function *regionprops*, that computes the perimeter by calculating the distance between each adjoining pair of pixels around the border of the bubble region, as depicted in figure 7.23 (c). While this method works well above a certain bubble size, where bubbles contain a large number of pixels and thus the systematic error becomes negligible, it fails for bubbles having a small area as it underestimates the real perimeter. Indeed, as we can see from the curve obtained for the aqueous foam in figure 7.23 (b), as the average bubble size increases because of coarsening, the elongation slowly approaches the minimum value 3.71, but from below and not from above as one would expect. However, since our foams are polydisperse and we always have small shrinking bubbles of a few pixels in our pictures, we cannot simply consider the data above a certain size threshold, as in each picture there will be small bubbles for which the perimeter is badly assessed, thus the results are not reliable. However, we can see how, despite the underestimated e for the smaller bubbles, for a given mean bubble size the average elongation of the samples at high ϕ is larger than the one calculated in the aqueous foam, marking the presence of highly elongated bubbles in the pattern. We cannot use these data for further quantitative relative comparisons, as the number fraction of small bubbles also changes between the samples, as seen in section §7.3.3. Future work aiming to investigate the local coarsening dynamics at a scale of a few bubbles will possibly give further insights on the individual bubble shapes by exploiting the camera resolution in this sense.

Viscoelastic phase separation

The peculiar emulsion distribution and bubble shapes observed in our foamed emulsions are reminiscent of the aspect of polymer mixtures undergoing what is called in the literature *viscoelastic phase separation* [110].

In his work [112, 113], Tanaka has pointed out that systems in which components have a strong dynamical asymmetry, phase separation can lead to the formation of a sponge-like continuous network of the slower component (even if this is the minority phase), like the one shown in figure 7.24 (a). In polymer mixtures, this kind of transition can be induced by deeply quenching the system in order to initiate a glass transition of one of the two components [110]. It has been shown that this leads to the nucleation of domains rich in the fast component, while the phase rich in the slow component starts shrinking over time transforming into an intermediate sponge-like morphology and preventing any self-similarity of the pattern evolution.

Even though a general model to describe viscoelastic phase separation has been proposed [111], the resulting effects and the pattern formation have been mainly discussed on qualitative grounds. It has however been stated that such behaviour is universal and common to any phase-separating fluid mixture presenting a strong dynamical asymmetry

between its phases, independently of the physical origin of this asymmetry [110, 114].

The resemblance between the sponge-like pattern observed in polymer mixtures and the emulsion distribution in our high-ϕ foams is striking, as it can be seen from figure 7.24 (b). It would thus be tempting to see foamed emulsions as a macroscopic example of viscoelastic phase separation, where the emulsion would represent the slower component and the gas the faster one. However, although sharing qualitatively many characteristics in the pattern evolution, the phase separation process in the two cases has two main differences. First, the bubbles are not spontaneously nucleated in our systems, but they are mechanically incorporated inside the emulsion with the mixer before starting to coarsen. Second, in polymer mixtures there is a volume shrinkage of the slow component, which does not occur in our systems: the emulsion is only apparently shrinking in our pictures, as the surface liquid fraction decreases as the average bubble size grows, but its volume is conserved. However, what actually decreases in our foamed emulsions is the total amount of interfaces, whose minimisation is at the origin of the phase separation. Finding a quantitative parallel between the two systems is not easy, but it would be of great interest as it would link two mechanisms at two different length scales.

Finally, we remark that bubble patterns similar to ours have been encountered in the work by Webster and Cates [127] already discussed in section §5.4. In that work, a configuration in which large bubbles impinging on each other were decorated by shrunken and osmotically stabilised bubbles at their vertices, for which we refer to figure 5.5 (c), was postulated at large excess of soluble gas. In our foamed emulsions the small bubbles do not contain any insoluble gas species which could osmotically stabilise them, but they accumulate in the system as their shrinkage is delayed by the higher local foam elasticity.

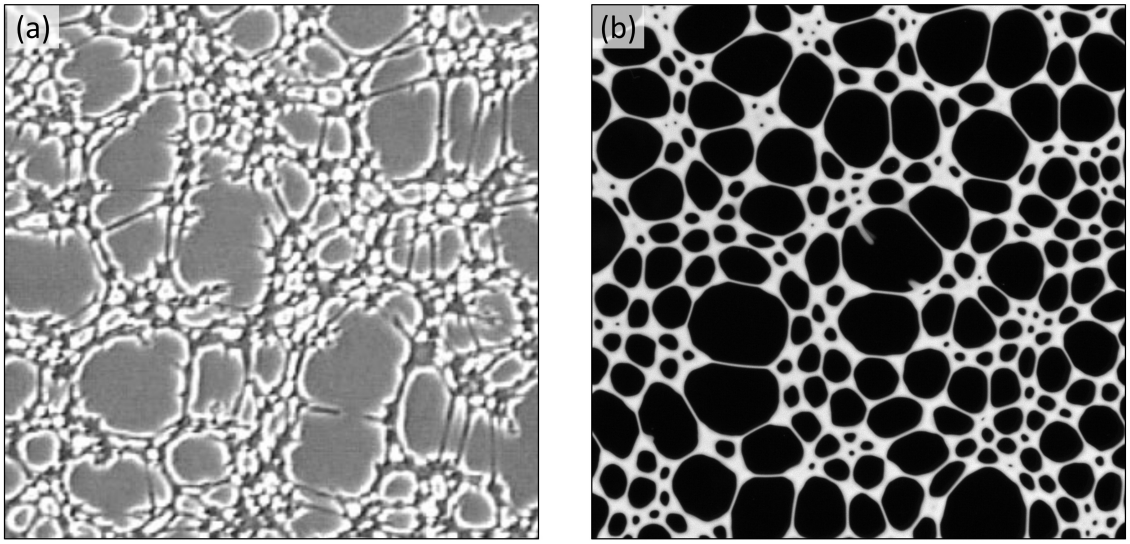

Figure 7.24 – **Morphology comparison.** (a) Mixture of polystyrene and diethyl malonate undergoing viscoelastic phase separation after thermal quenching, seen under a phase-contrast microscope. The edge size is 556 μm. Picture taken from [115]. (b) Emulsion distribution at late stage of coarsening in a foamed emulsion at $\phi = 80\%$. The edge length is 7 cm. The resemblance with the phase-separating polymer mixture is remarkable.

7.3.6 Effect of the liquid fraction

In the previous sections, we focused on rather dry foamed emulsions, with liquid fractions ε between 9% and 13% depending on the emulsion oil fraction ϕ. In this section we want to probe how the coarsening of such systems is affected by an increase of the global liquid fraction. To do that, we generate two emulsions at $\phi = 75\%$ and $\phi = 80\%$ with rapeseed oil and we slightly modify the foaming step. We pour 120 mL of emulsion in a beaker and we then foam it with a commercial milk frother (Fkant) at its maximum speed until a final foam volume of 475 mL is reached, as shown in figure 7.25. The foaming mechanism is very similar to the one occurring in a planetary mixer: a small balloon whisk rotates anticlockwise around its shaft, while a second clockwise rotation is manually imposed to the mixing tool. The surface waves generated by the whisk allow to gradually incorporate air inside the emulsion while the shear simultaneously reduces the size of the bubbles. However, the milk frother being less powerful than the Kenwood mixer, the air entrapment saturates at lower gas fractions. Indeed, the final liquid fraction obtained for these two samples is equal to $(25 \pm 1)\%$ for both $\phi = 75\%$ and $\phi = 80\%$. The liquid fraction is now measured by dividing the initial volume of emulsion by the final foam volume, and we highlight that we are more than doubling the liquid fraction considered in the previous sections.

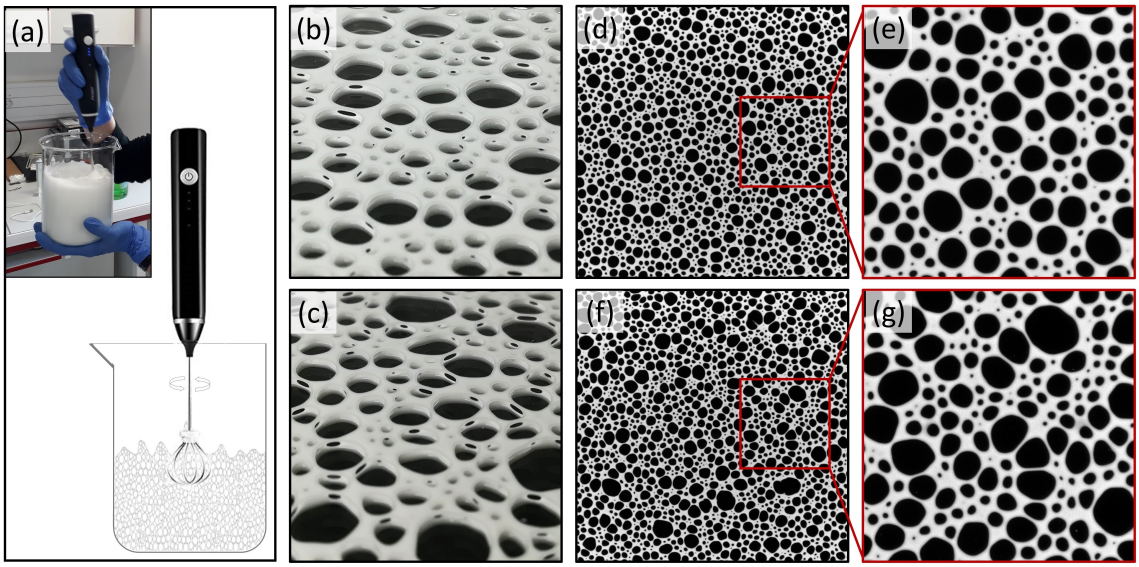

Figure 7.25 – **Wet foamed emulsion samples.** (a) Foaming with a manual milk frother. (b-c) Perspective view of the samples at (b) ϕ=75% after 13 days and (c) ϕ=80% after 15 days. Thin films between adjacent bubbles are still visible despite the high liquid fraction ε=25%. (d) Sample at ϕ=75% at the end of the acquisition (t=33 days). Edge size 12 cm. (e) Enlargement of the same picture. Edge size 4 cm. (f) Sample at ϕ=80% at the end of the acquisition (t=19 days). Edge size 12 cm. (g) Enlargement of the same picture. Edge size 4 cm.

We then follow the same experimental protocol for studying their coarsening in a quasi-2D configuration. In figure 7.26 (a) we plot the time evolution of the number of bubbles for both wetter samples, and we compare them with the corresponding curves obtained from

the coarsening of the drier samples at the same oil fractions. We can see that the initial number of bubbles is roughly the same, as it is dictated mainly by the gap and the cell size, but the curves start at later times, which indicates that it takes longer for the foam to become quasi-2D at higher liquid fractions. Moreover, the number of bubbles decreases over time with a different rate: the decrease is slower in the wet samples than in the dry ones. This is mirrored by their slower mean bubble growth shown in figure 7.26 (b) and (c), where in the latter it has been renormalised by its initial value at $t = t_{2D}$ as usual to better appreciate the difference between the samples.

We can see that for both samples the maximum mean bubble size at the end of the image acquisition is roughly $\langle R \rangle \simeq 1.6$ mm. We remind that, if the foam was monodisperse, at a liquid fraction ε=25% the films are expected to vanish when the ratio between the gap and the bubble size is around 0.7 [18]. At the end of our experiments, this ratio is 0.63, which means that we should have lost most of the thin films between the bubbles. However, as shown in figure 7.25 (b-c), after two weeks many films are still present in our samples, mainly between large bubbles. This is not only due to the polydispersity of the system, but also to the heterogeneous growth that gradually leads to the appearance of the characteristic foam structure already discussed for the drier samples.

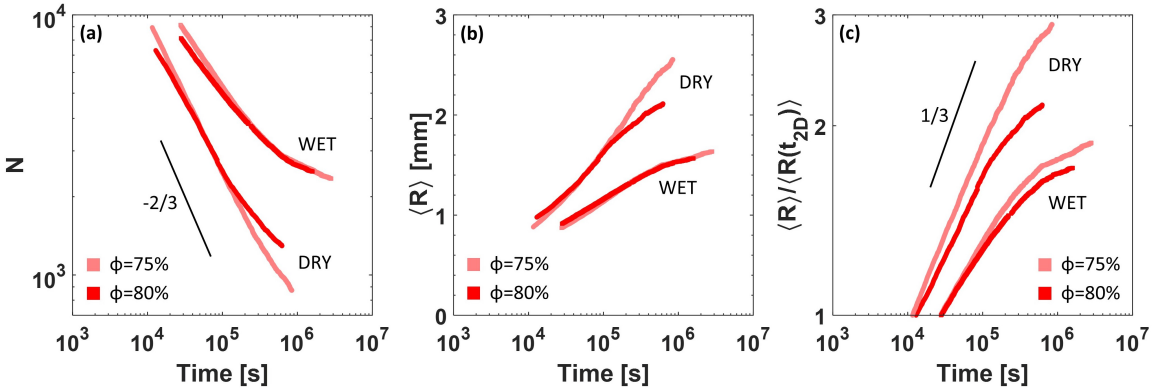

Figure 7.26 – **Wet foamed emulsion evolution.** (a) Time evolution of the total number of bubbles for the two wet samples, compared with the respective drier foamed emulsions. (b) Mean bubble size growth for the wet samples compared with their dry equivalents. (c) Mean bubble size evolution after normalisation with $\langle R(t_{2D}) \rangle$.

Indeed these wetter samples present the major structural features of the drier ones, as it can be seen from figure 7.25, which shows how the two foamed emulsions look like at the end of the experiment, namely after 33 days (d,e) for the sample at $\phi = 75\%$, and after 19 days (f,g) for the sample at $\phi = 80\%$. One can start recognising the segregation of small wetter bubbles from the drier large bubble chains.

In fact, let us look at the normalised bubble size distributions. We report the distributions of the adimensional radius $R/\langle R \rangle$ in figure 7.27 (a-d) for both oil fractions at different times, from which we can see that both samples gradually enhance their skewness over time. However, the effect is less evident than in the dry samples, as the coarsening is slower so probably one should wait longer and have a larger bubble size variation to reach the same skewed distribution shapes.

In the same spirit of section §7.3.4, we plot in figure 7.27 (e) the third moment of these distributions μ_3^R as a function of the average bubble size $\langle R \rangle$. We can see that the initial

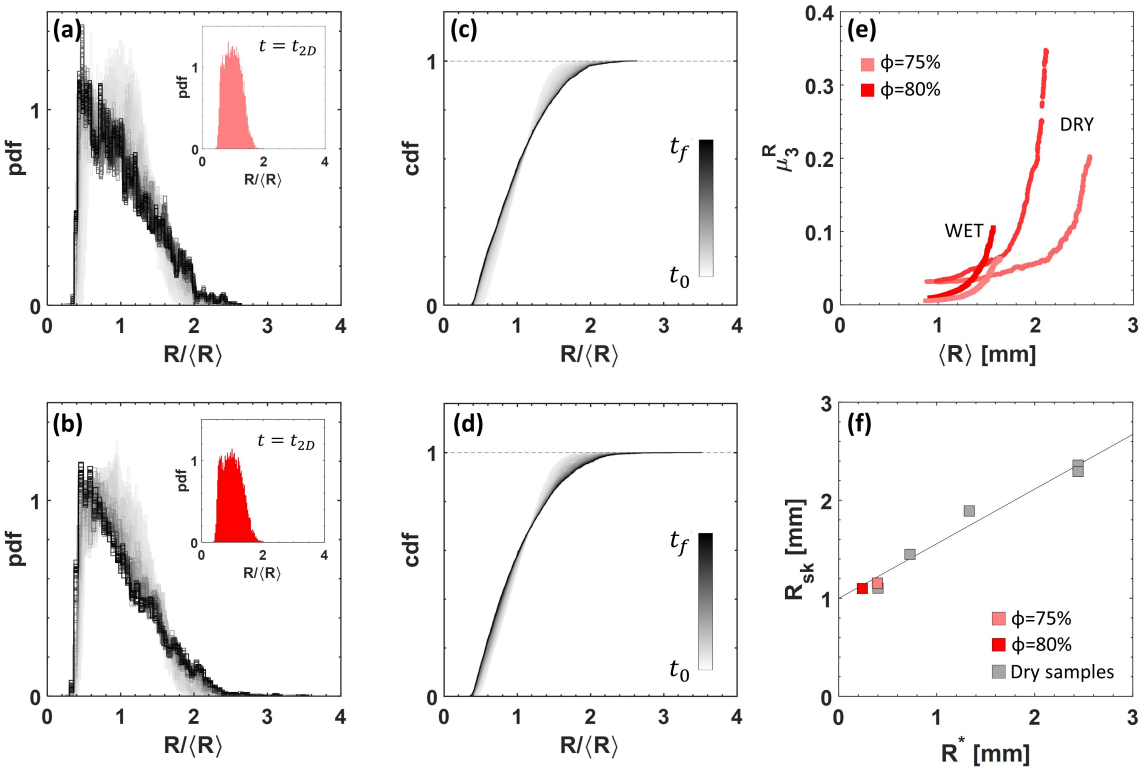

Figure 7.27 – **Bubble size distributions at higher liquid fraction.** (a,b) Frequency normalised bubble size distributions for the wet samples at (a) $\phi = 75\%$ and (b) $\phi = 80\%$. The insets show the corresponding initial distribution at time $t = t_{2D}$. (c,d) Corresponding cumulative distributions for the two wet samples at (c) $\phi = 75\%$ and (d) $\phi = 80\%$ which better shows the shape variation. (e) Third moment μ_3^R versus the average bubble radius for wet and dry samples. (f) R_{sk} versus R^* for the wet samples, compared with the correlation obtained at lower liquid fractions.

value of μ_3^R is almost the same for the two wet samples, even though it is lower than the initial plateau registered for the drier foamed emulsions. Discrepancies may come from the definition of bubble size due to the image segmentation at such high liquid fractions: since the foam is wet, not all the bubbles share thin films, and as the emulsion is white we cannot accurately pinpoint the presence of many-sided Plateau borders. Thus, in this case, the cells obtained with image segmentation actually reflect the free space available for each bubble rather than its real size. However, we can see that both curves start diverging after reaching a critical bubble size, being smaller for the larger oil fraction. As done in section §7.3.4, we can estimate this critical bubble size R_{sk} in which the skewness departs from its initial plateau as the point at which μ_3^R becomes 1.5 times its initial value. At the same time, we can calculate the critical R^* linked to the foamed emulsion rheology expected at such high liquid fraction, and see how these two additional points of R_{sk} and R^* compare with the ones obtained for the drier samples. This is shown in 7.27 (f), where we can see that the results are in good agreement with the previous data points, suggesting that liquid fraction plays a fundamental role in the structural evolution of these systems.

7.3.7 Effect of confinement

All the foamed emulsion samples investigated so far were confined within a 1 mm gap. We now aim to check whether and how the appearance of stretched bubble shapes observed at high oil fractions is influenced by the foam confinement. To do that, we prepare dry foamed emulsions with sunflower oil at a fixed oil fraction $\phi = 80\%$ for each sample and we sandwich them between two glass plates with different spacing varying from 1 mm to 3 mm. As shown in the plot of figure 7.12 in section §7.3.2, these foams are slightly drier, with a liquid fraction ε around 8%. For these samples, pictures are taken at higher frame rates, as the same image sequences are also used in chapter §8 to study their coarsening dynamics.

As usual, we start characterising their evolution when the foam becomes a bubble monolayer. This clearly means that the larger the gap the longer the time it takes for the foam to become quasi-2D, as bubbles need to reach a larger size to touch both top and bottom glass surfaces. Moreover, since the total area of the foam cell is the same for each sample, the larger the gap the lower the total number of bubbles at time t_{2D}. This can be seen in figure 7.28 (a) where we plot the evolution of the total number of bubbles over time. In the same figure, we also plot the mean bubble size growth before (b) and after (c) normalisation with its initial value at $t = t_{2D}$.

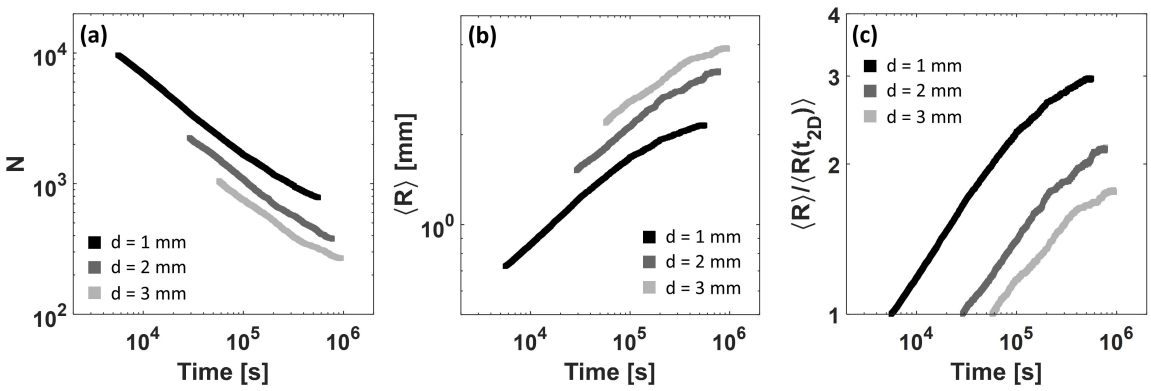

Figure 7.28 – **Foamed emulsion coarsening at different levels of confinement.** (a) Temporal evolution of the total number of bubbles for the samples at $\phi = 80\%$ confined in different gaps d equal to 1, 2 and 3 mm. (b,c) Time evolution of the average bubble radius before and after normalisation.

We can see that as the cell gap is enlarged, the curves start at later times and at a higher bubble size $\langle R(t_{2D})\rangle$, but we can also notice that the curves appear to have a similar shape, just vertically and horizontally shifted: after an initial power law growth, each curve starts bending. We saw in section §7.3.3 that the reduction of the coarsening rate is due to the accumulation of smaller bubbles, whose disappearance is delayed due to their higher local liquid fraction which translates into a higher elastic resistance to size variations. This accumulation is mirrored by a gradual enhancement of the asymmetry of the adimensional radii distributions, which we quantified with their third moment μ_3^R. Let us then check how the third moment of the distribution evolves as the average bubble size grows in these samples. This is plotted in figure 7.29 (a), where we can notice how in each sample, after an initial plateau, we observe a steep increase of μ_3^R which however occurs at different

mean bubble sizes. More precisely, we can see that the critical $\langle R \rangle$ at which this happens increases with the size of the gap: the more confined the foam, the sooner this deviation occurs, meaning that the shrinkage of small bubbles starts to be delayed earlier.

This can be tentatively explained by the combination of two effects. The first concerns the foam rheology, namely we observe an increased foam rigidity when the latter is confined within a narrow gap. The equation used for G_{FE} discussed in section §7.3.4 is indeed intended only as a scaling relation, we do not consider any prefactor which can be system-dependent and thus depend on the foam confinement. This could explain why we observe a different behaviour between samples having the same liquid and oil volume fraction but coarsening in a different confinement. However, we would in principle expect, for a given larger gap, to still observe a correlation between R_{sk} and R^* at different oil fractions.

The second argument concerns the local liquid fraction around the smaller bubbles. Indeed, we know that for a given volume liquid fraction and a given bubble size, we can have a different foam wetness depending on the gap [18]. This means that when we enlarge the gap, small bubbles need to have a larger size on average to have the same local liquid fraction of small bubbles in a more confined foam. Thus, the effect of the delay in their shrinkage occurs at larger mean bubble sizes. Indeed, we can see in figure 7.29 (b,c,d) that, although the samples show the same global structure, the typical bubble size of the wetter small bubble regions increases with the gap d.

It is not possible at this stage to state which is the main mechanism between the two, as both of them can contribute to the onset of the observed heterogeneous structures. Nevertheless, these preliminary results show that a future systematic study of quasi-2D foamed emulsion coarsening at different levels of confinement, and at different oil fractions, could possibly give more insights on the underlying coarsening mechanism.

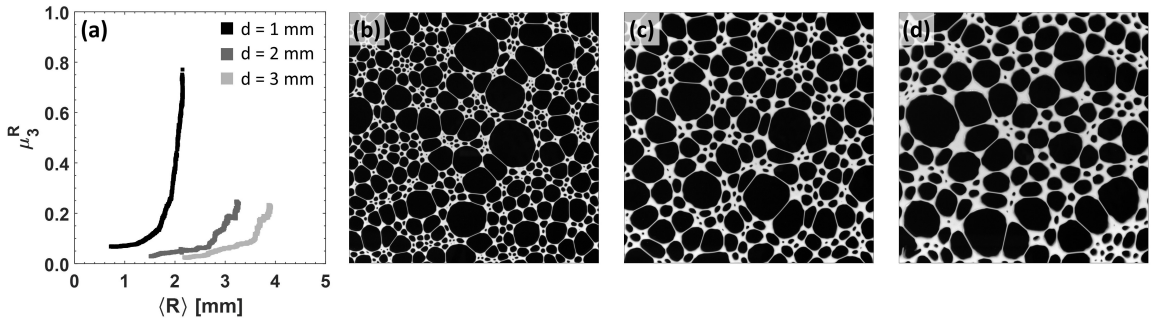

Figure 7.29 – **Bubble pattern at different cell spacing.** (a) Third moment of the radii distribution μ_3^R vs the average bubble size $\langle R \rangle$. The larger the gap d, the larger the critical bubble size at which μ_3^R steeply increases, reflecting the onset of the delayed disappearance of small bubbles. (b,c,d) Photos at the end of the image acquisition at gap equal to 1, 2, and 3 mm respectively. The edge size of the pictures is 12 cm.

7.4 Conclusions

In this chapter, we studied how a viscoelastic continuous phase can impact the foam coarsening process, by carrying out experiments on foamed concentrated emulsions in quasi-2D configurations. Our results showed that the increase of the oil droplet fraction, and thus of the emulsion elasticity, effectively reduces the coarsening rate, due to a delay in the shrinkage and consequent disappearance of small bubbles.

The initial polydispersity of the system results in heterogeneous bubble growth which eventually leads to a segregation of smaller bubbles into regions wrapped by chains of interconnected large bubbles. Moreover, we observed a lack of emulsion redistribution after the vanishing of small bubbles which leads to an uneven liquid fraction inside the foam.

The onset of this heterogeneous foam structure further contributes to hamper the coarsening process as the accumulation of small bubbles in these wetter regions translates into regions of different local foam elasticity which opposes to bubble size variations. Indeed, we observed a correlation between the average bubble size at which we start having an anomalous accumulation of small bubbles in the system and the mean bubble size at which we expect a local increase of the liquid fraction to stiffen the material according to our tentative explanation.

Preliminary experiments on foamed emulsions at a higher liquid fraction showed a further delay of the overall coarsening process, but that the evolution of the foam structure still presents the hallmarks observed in the drier samples. This suggests that the liquid fraction indeed plays a fundamental role in the evolution of such systems, which would be an interesting aspect to probe systematically in future investigations.

At high oil fractions the foam gradually develops a pattern in which the bubble shapes are not at all relaxed and in which the Plateau borders no longer follow Plateau's laws. Large bubbles often share a thin elongated Plateau border which presents a bulge at the two extremities like an hour glass, as a result of the heterogeneous bubble growth. Around small bubbles the Plateau borders are instead thicker, reflecting the uneven emulsion distribution inside the sample, but their cross section does not have a traditional shape, as a small area of thin film between adjacent bubbles is often present even though the Plateau border width from the top is larger than the gap. A closer look at the bubble shapes, which was not possible from our pictures, could help understanding the local behaviour of bubbles in these systems. However, we noticed a striking resemblance between the global bubble pattern evolution at high oil fraction and the sponge-like pattern developed by polymer solutions undergoing viscoelastic phase separation, even though the link between the two phenomena is not straight forward.

Finally, we have probed the effect of foam confinement by changing the cell gap: preliminary results show that the evolution of the foam structure is qualitatively similar, but that the coarsening rate and the average bubble size at which we observe the appearance of unrelaxed bubble patterns is influenced by the level of confinement. The larger the cell thickness the larger the mean bubble size at which small bubbles start accumulating in the system. Whether this is due to wall effects or to the local liquid fraction around the small bubbles, or a combination of these two aspects, requires further investigations.

In the next chapter, we shall study how the presence of the emulsion affects the bubble dynamics during coarsening and see whether and how this depends on the wall confinement.

8 Coarsening dynamics in foamed emulsions

8.1 Introduction

In the previous chapter, we saw how the viscoelasticity of the foam continuous phase dramatically affects the foam structure, inducing heterogeneous bubble growth which translates into reduced overall coarsening rates. Moreover, we saw that the onset of a change in the foam structure depends on the level of confinement, with unrelaxed bubble shapes appearing earlier in more confined foams. However, from the visualisation of the coarsening movies, we can observe another qualitative feature, namely that the bubble dynamics also changes as we increase the emulsion elasticity: at high oil fractions the bubble displacements and rearrangements seem hindered, so that the bubbles appear to grow or shrink without moving substantially from their initial position.

To probe this behaviour, in this chapter we shall start by investigating the foam coarsening dynamics in 3D foamed emulsions at different oil fractions. The yield stress of the emulsion among the bubbles allows delaying the gravitational drainage in such systems, so that we have a time range in which the liquid fraction and the bubble size distribution can be considered homogeneous inside the samples and we can probe their coarsening.

While the mean bubble size growth will be measured with image segmentation, the bubble dynamics will be investigated with a technique called Differential Dynamic Microscopy (DDM) [11]. This technique is able to give insights on the dynamics of a sample by looking at Fourier domain correlations between frames separated by increasing time intervals, and it has been recently applied to probe the dynamics of coarsening traditional foams [45]. We shall analyse our pictures by applying a protocol similar to the one in the literature and we will highlight the main differences observed between our foamed emulsions and a standard shaving foam.

After studying 3D systems, where the foam is confined between two plates with a spacing much larger than the typical bubble size, we shall examine what happens in a more confined environment. We shall thus use the same technique to probe the coarsening during the transition from a 3D to a quasi-2D foam system. In fact, the quasi-2D foams considered in the previous chapter were obtained by letting the initially 3D foamed emulsions coarsen within a narrow gap, until the bubble size was large enough to be touching both plates and the foamed emulsion could be considered a bubble monolayer. To check whether this approach has an impact on the foam behaviour, we shall then use the same technique to probe the coarsening dynamics during the transition from a 3D to a quasi-2D foam system at different levels of confinement.

Finally, we shall go back to quasi-2D configurations to quantify the rate of bubble rearrangements in the real space at different emulsion oil fractions and we shall compare the coarsening dynamics of a concentrated foamed emulsion with the one of an aqueous foam at the same level of confinement.

The experimental results presented in this chapter are the outcome of two collaborations: a first one with Fabio Giavazzi (University of Milan, Italy) and Roberto Cerbino (University of Vienna, Austria) for the characterisation of the coarsening dynamics with DDM analysis in the reciprocal space, and a second one with Antti Puisto and Jonatan Mac Intyre (Aalto University, Espoo, Finland) for the automatic quantification of bubble rearrangements in quasi-2D foams from images in the real space.

8.2 Experimental approach

8.2.1 Sample preparation and imaging

Emulsions and their foams are prepared with the same procedure explained in the previous chapter, using either rapeseed or sunflower oil as described in the text, while the reference aqueous foam considered in section §8.3.3 is generated with the double-syringe technique as explained in section §6.2.2. The imaging set-up used is also the same used in the previous chapter, the only variation is the gap between the two plates of the foam cell that we now vary from 1 mm to 10 mm for 3D samples by changing the rubber joint thickness.

The frame rate during image acquisition is higher compared to the previous chapter to ensure a suitable time resolution for image correlation analysis: for 3D samples we acquire images at fixed time intervals of 5 or 15 seconds for the entire duration of the experiment, whereas for more confined foamed emulsions, for which the total experimental time is much longer, the time interval is 5 seconds at early stage and is then increased up to 10, 60 or 600 seconds accordingly to the coarsening rate. The idea is that between two successive pictures the bubble size variation is imperceptible and only a few rearrangements are occasionally observed, so that we can probe the coarsening dynamics by looking at image correlations in the reciprocal space, as we shall explain in section §8.2.4.

8.2.2 Real space image treatment

Using the same steps for image treatment explained in section §7.2.4, it is possible to segment the pictures of 3D samples and get the skeleton of the surface bubble layer, in order to assess the average bubble size in the foam. Clearly, while for quasi-2D foams the bubble detection is accurate, in 3D foams the different layers of bubbles below the surface are visible in the picture and can lead to possible misdetection of bubbles, as shown in figure 8.1, where an example of 3D foamed emulsion image with the surface skeleton superimposed is reported. However, given the high statistics available in the samples, the treatment is still able to give a robust estimate of the bubble size evolution over time.

8.2.3 Correlation maps

For a visual inspection of the bubble motion in the different foamed emulsions, we can calculate a correlation map between pictures taken at different times as done in [15] with a home-made MATLAB script. We consider two pictures separated by a time delay Δt, and we call $\mathbf{S}$ the source image taken at time t and $\mathbf{T}$ the target image taken at time $t + \Delta t$. Before looking at their correlation, we perform a median filtering of the images with a filter window large 10 pixels, in order to reduce the noise. As shown in figure 8.2 (a), we plot the intensity correlation between the pixels of the two frames (b) and (c) and we fit it with a linear regression. The correlation map is obtained by plotting for each pixel of the source image its distance from the linear regression with a suitable color map, as shown in the example of figure 8.2 (d). If nothing happens between the source and the target image, the correlation map will exhibit only noise fluctuations. By contrast, if the bubbles have slightly moved during the time Δt, as in figure 8.2 (f,g), we can see that the intensity correlation shown in (e) spreads and the corresponding correlation map in (h) allows to pinpoint where the bubble movement occurred, even if it is almost imperceptible when we look at the original pictures.

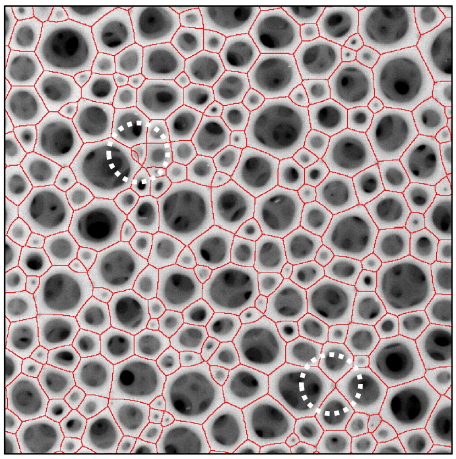

Figure 8.1 – **3D image treatment.** Example of image segmentation for the sample at ϕ=70% after 4 hours. The dashed circles show two examples of bubble mis-detection, more precisely the detection of a fake bubble and the missed detection of a real one. By playing with the script parameters to detect the intensity gradients it is possible to reduce the occurrence of these events, which however, given the high statistics of correctly detected bubbles available, represent a negligible contribution to the mean bubble growth. The edge size of the frame is 3 cm.

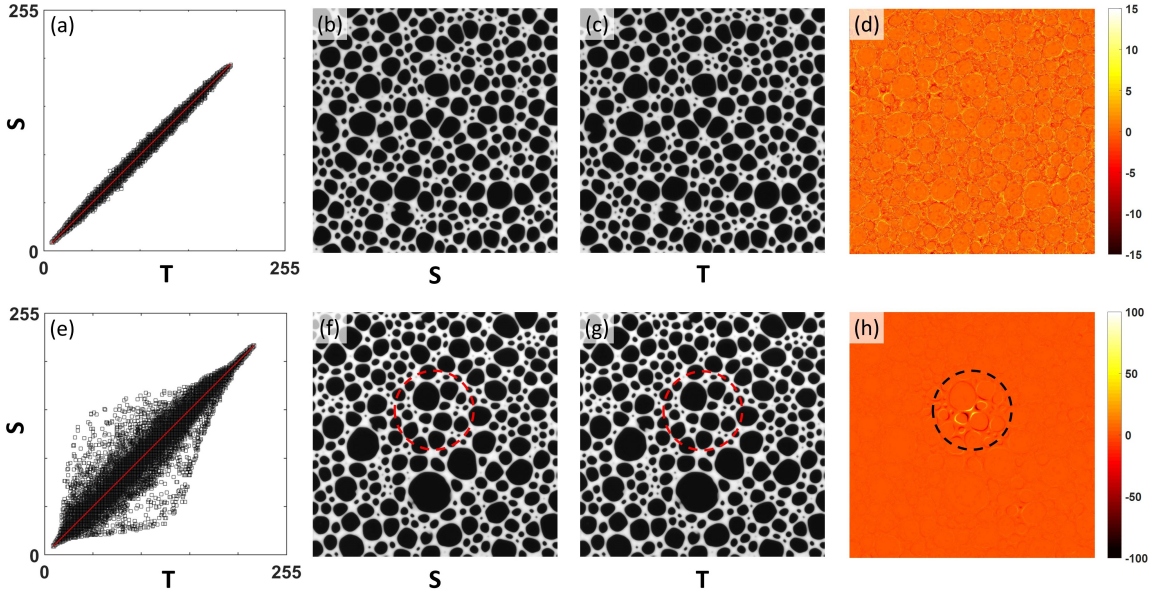

Figure 8.2 – **Correlation maps.** (a) Intensity correlation between image (b), taken at time t, and image (c), taken at time $t+\Delta t$. Since the bubbles have not moved significantly, the correlation map (d) shows only noise fluctuations although the outline of the bubbles can be recognised due to their slight growth or shrinkage. (e) Intensity correlation between the images (f) and (g), in which four bubbles are now slowly rearranging, as it can be seen from the spread of the points in (e). The corresponding correlation map (h) highlights the region in which the images are decorrelated due to the bubble movement.

8.2.4 Differential Dynamic Microscopy

To probe the coarsening dynamics in foamed emulsions we shall move to the reciprocal space, using an experimental imaging technique which probes the correlations between real space images separated by increasing time delays in the Fourier domain.

In this section, we shall first briefly describe the basic idea behind this technique, which is called differential dynamic microscopy [11]. Then, before explaining the protocol followed for investigating our samples, we shall see how this technique has been recently applied for studying the coarsening dynamics of a traditional (shaving) foam [45], highlighting the main results which will be used as a reference to compare with our foamed concentrated emulsions.

The concept

Differential Dynamic Microscopy (DDM) is a powerful technique which allows to perform light scattering experiments with traditional imaging methods [11]. DDM is part of a wider family of techniques called Digital Fourier Microscopy (DFM) which share the underlying general idea that the sample correlation properties can be characterised in the reciprocal space via spatial Fourier analysis of images collected in the real space [43].

The principle of DDM, and of DFM in general, is that, by collecting a stack of images of a certain sample, the analysis of the correlation properties of such images in the reciprocal space, obtained by a temporal analysis of their spatial Fourier transforms, allows extracting information about the sample equivalent to the one obtainable in light scattering experiments [43]. The main advantage of this technique is that it does not require the objects of interest to be clearly visible in the picture, so it allows studying the dynamics of objects having a size below the camera resolution [11]. Moreover, and more important for our purpose, it is a tracking-free analysis: this is particularly relevant for turbid media like 3D foams where it is usually tricky to track the surface bubbles as the bubbles underneath are also visible.

A typical DDM experiment therefore consists in the acquisition of a stack of images, usually at fixed time intervals Δt_0. Then the correlation properties of the sample are analysed in the reciprocal space for images separated by increasing time delays. Figure 8.3 graphically illustrates the steps typically performed for this kind of analysis. Two pictures separated by a time delay $\Delta t = k\Delta t_0$, with $k \in \mathbb{N}$, are subtracted, then a fast 2D Fourier transform algorithm is applied to the pixel matrix representing their difference and the squared amplitude of the result is calculated. If the statistical properties of the investigated dynamics do not change in time, this operation is repeated for all the pairs of images separated by the same Δt, but at different reference time t. After calculating the spatial Fourier transform and its square modulus for each of these differences, these are averaged to get the so-called image structure function as $d(\mathbf{q}, \Delta t) = \langle |\hat{d}(\mathbf{x}, \Delta t)|^2 \rangle$, where the notation $\hat{\cdot}$ indicates the Fourier transform. If however the sample evolves over time, this procedure must be limited on sequences of images in which the system dynamics can be studied in quasi-stationary conditions. The image structure function is linked to the intermediate scattering function $f(\mathbf{q}, \Delta t)$ through the relation [43]:

$$d(\mathbf{q}, \Delta t) = 2A(\mathbf{q})[1 - f(\mathbf{q}, \Delta t)] + 2B(\mathbf{q}) \tag{8.1}$$

where the term $A(\mathbf{q})$ is the static amplitude, which depends on the distribution and shape

of the objects in the picture, and the term $B(\mathbf{q})$ describes the detection noise coming from the camera [43]. From this relation one can thus estimate $f(\mathbf{q}, \Delta t)$, whose decay encloses the information on the sample dynamics at different length scales. This correlation function indeed will tend to 1 for lag times Δt tending to 0, as the images will be maximally correlated, while for Δt tending to infinity $f(\mathbf{q}, \Delta t)$ will tend to 0, as the correlation between the pictures is lost. The dynamics of the sample under study, and thus the physical origin of this decorrelation, lies in the dependency of $f(\mathbf{q}, \Delta t)$ on $\mathbf{q}$ and Δt. Depending on the sample under study and on its expected dynamics, $f(\mathbf{q}, \Delta t)$ is thus fitted with a suitable model function to obtain the relevant dynamic parameters.

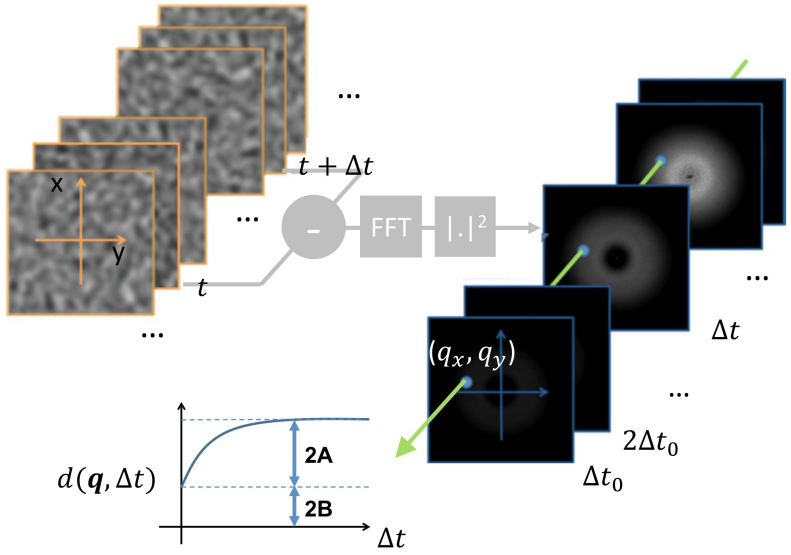

Figure 8.3 – **Differential dynamic microscopy.** Schematic illustration of typical DDM analysis steps, adapted from [43]. Images separated by a different Δt are first subtracted, then the 2D Fourier transform of the difference, and its square modulus, is calculated. The procedure is repeated for different Δt in order to obtain the image structure function $d(\mathbf{q}, \Delta t)$.

DDM applied to shaving foam

The DDM technique, combined with bubble tracking, has been recently used to probe the coarsening dynamics of a standard shaving foam (Gillette Foamy regular) [45]. The dynamics in coarsening foams is due to the bubble growth which continuously modifies the stress configuration in the system, where local stress imbalances eventually cause the bubbles to rearrange. We shall now have a look in detail at the results found for the coarsening Gillette foam, and their interpretation, as we shall use them as a reference for comparing our 3D foamed emulsion results.

It has been shown that the coarsening dynamics in Gillette foam is governed by intermittent bubble displacements with a persistent direction up to a critical length scale, which is identified as the bubble diameter [45]. These bubble displacements are caused by the strain fields generated by the growth and shrinkage of bubbles inside the coarsening foam. The DDM analysis showed that the intermediate scattering functions $f(q, \Delta t)$ (obtained

from the azimuthally averaged image structure functions) at different foam ages are well described by a compressed exponential function of the kind:

$$f(q, \Delta t) = \exp[-(\Gamma(q)\Delta t)^{\alpha}] \tag{8.2}$$

where the compressing exponent α is found to be constant around 1.2 and $\Gamma(q)$ is the q-dependent relaxation rate, which quantifies the time scale for the decorrelation of the length scale corresponding to q.

This $\Gamma(q)$ is found to exhibit two distinct dynamical regimes, separated by a crossover scattering vector q_c, which gradually decreases as the foam ages, as shown in figure 8.4. By renormalising the q axis with the average bubble radius R, and the relaxation rate $\Gamma(q)$ with the coarsening rate $\dot{R}/R$, all the data collapse into a single master curve, showing that the foam dynamics is entirely determined by a single length scale, the bubble size, and a single time scale, set by the coarsening rate.

As it can be seen from figure 8.4, at high q values, above the crossover point q_c, the relaxation rate shows a linear dependence on q, $\Gamma(q) \sim q$, with a prefactor becoming smaller over time. This linear dependency is associated to a ballistic-like regime representing the bubble movements with directional persistence: the stress inhomogeneities can induce strain fields which make the bubbles move slowly and consistently in one direction. This linear dependency is lost at $q = q_c$, which marks the crossover between the two different dynamical regimes. At q values below q_c, a stronger dependency of the kind $\Gamma(q) \sim q^{\delta}$ is found, where the scaling exponent δ is calculated to be 1.6±0.2. The value q_c, which marks the loss of linearity of $\Gamma(q)$ in the reciprocal space, mirrors the cutoff distance in the real space at which the persistence of the bubble motion is lost. This can be explained by the occurrence of bubble rearrangements implying a change of neighbours: a bubble feeling the strain field caused by coarsening will move in one direction until the direction of the motion is suddenly changed by a rearrangement that modifies the stress configuration, and then the force exerted on the bubble, so that the latter starts moving again but in a different direction. The low q regime thus reflects the dynamics of bubble rearrangements occurring in the foam.

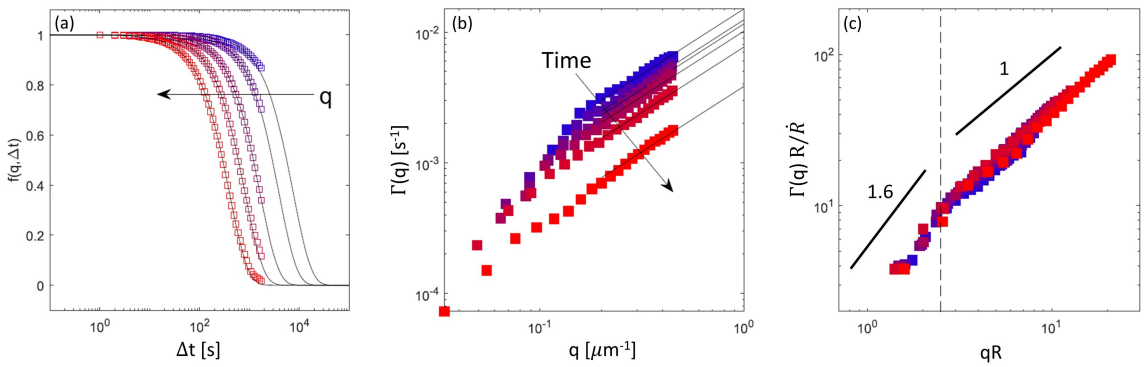

Figure 8.4 – **DDM results for Gillette foam.** (a) Intermediate scattering functions for different q at a given foam age. (b) Relaxation rate $\Gamma(q)$ obtained from the fit of $f(q, \Delta t)$ with a compressed exponential function. (c) Rescaling $\Gamma(q)$ with the coarsening rate and q with the mean bubble size makes the data collapse into a single master curve. Graphs adapted from [45].

DDM applied to foamed emulsions

To probe the dynamics of foamed emulsions we use a protocol very similar to the one used for the Gillette foam [45]. Since our samples are illuminated from the top with a square of LED lights all around the sample, the image borders appear brighter than the centre. In the 3D samples, the intensity of the pixels corresponding to Plateau borders is saturated close to the image edges, which means that we are not measuring the real intensity of those pixels and we are no longer within the linear imaging conditions [43]. However, this should not influence the characterisation of the dynamics of our samples, as we are interested in the movements of the Plateau borders and these are not affected if their intensity is constant. The raw frames are thus first cropped around a square region of interest (ROI) in which the illumination is rather uniform and the saturated pixels are a only a small portion of the total ROI. Even though the DDM analysis is not expected to particularly benefit from it [43], we correct for the residual uneven illumination by dividing each frame by a background image as done in [45]. This background image is obtained by averaging the first 100 foam pictures in which the bubbles are still small, and by applying a gaussian filter having a standard deviation of 15 mm to this average image. The width of the gaussian filter is chosen to be much larger than the typical bubble size but at the same time smaller than the extension of the intensity gradient due to the uneven illumination.

To determine the foam dynamics at different foam ages, we select image sub-sequences S_n centred at different times t_n among the entire set of images. Since the foam is evolving over time, it is not possible to completely decouple the dynamics from the evolution of the sample. However, if we choose each sub-sequence to cover a time interval $[t_n - t_n/8; t_n + t_n/8]$, of total duration equal to $t_n/4$, this ensures that, for our bubble growth rates, the mean bubble size in each sub-sequence grows less than 15% and thus we can assume to study the foam dynamics in quasi-stationary conditions. Each sub-sequence S_n is then analysed separately with a customised MATLAB script, developed by Fabio Giavazzi [45], which works as follows.

Within each S_n, it first calculates the difference between two background-corrected frames acquired at times t and $t + \Delta t$, namely $d(\mathbf{x}, t, \Delta t) = I(\mathbf{x}, t + \Delta t) - I(\mathbf{x}, t)$, for different log-spaced Δt going from the minimum time interval between two consecutive frames (Δt_0) to half the total time interval covered by the sub-sequence. A 2D fast Fourier transform algorithm is then applied to $d(\mathbf{x}, t, \Delta t)$, and the spatial Fourier power spectra obtained for the same lag time Δt but different reference times t inside the sequence are then averaged, given the quasi-stationarity of the sample within the sub-sequence. This way we obtain the image structure function $d(\mathbf{q}, \Delta t) = \langle |\hat{d}(\mathbf{x}, t, \Delta t)|^2 \rangle$, which captures the sample dynamics as a function of the 2D scattering wavevector $\mathbf{q}$ and of the lag time Δt. We then exploit the circular symmetry of the sample to calculate the azimuthal average of $d(\mathbf{q}, \Delta t)$, which provides $d(q, \Delta t)$ as a function of the radial wavewector $q = \sqrt{q_x^2 + q_y^2}$.

Finally, the intermediate scattering function (ISF) $f(q, \Delta t)$ is retrieved from the image structure function knowing that the two are linked by the relation $d(q, \Delta t) = 2A(q)[1 - f(q, \Delta t)] + 2B(q)$. The ISF is then fitted with a compressed exponential function $f(q, \Delta t) = \exp[-(\Gamma(q)\Delta t)^\alpha]$ to determine the rate $\Gamma(q)$ and the exponent α for each sub-sequence, thus at each foam age t_n. The same protocol is followed for foamed emulsion samples either at different oil fraction or different foam confinement, the latter set by the thickness of the cell housing the sample. The q-dependency of the rate of decay $\Gamma(q)$ and the exponent α will then be compared between the samples coarsening under the different conditions.

8.3 Results

8.3.1 3D foamed emulsions

We start by studying the evolution and dynamics of foamed emulsions confined within a gap of 10 mm, thus much larger than the initial bubble size ($R \sim 50$ μm), so that the foam samples can be safely considered 3D. For this set of experiments, foamed emulsions are prepared with rapeseed oil as explained in section §7.2.3. Thanks to the yield stress of the emulsion, gravitational drainage is delayed, namely the liquid fraction can be considered homogeneous up to a critical bubble size at which the bubble buoyancy force per unit area overcomes the emulsion yield stress, namely until $\rho g R/3 < \tau_y$. Since the yield stress depends on the emulsion oil fraction, this size threshold R_d is not the same for each foamed emulsion investigated, but it decreases with ϕ, as shown in table 8.1.

ϕ [%]	R_d [mm]
65	0.1
70	0.9
75	2.6
80	6.3

Table 8.1 – **Critical size for bubble buoyancy.**

The bubble polydispersity makes this transition not sharp, as larger bubbles will rise upwards before the average bubble size reaches the critical threshold. This is indeed observed in our coarsening movies. Clearly, the slow rise of these large bubbles from the bulk to the top of the sample can result in an average bubble growth on the top surface apparently faster than the actual bubble growth in the bulk, due to the vertical bubble size segregation.

Before looking at the dynamics of these samples, we measure their mean bubble size evolution to see whether and how the coarsening rate in 3D systems is affected by an increasing continuous phase viscoelasticity.

Bubble size evolution

The image treatment performed in the real space consists in the segmentation of the top foam surface in order to get the foam skeleton, from which we estimate the typical bubble size in the sample. The evolution of the average bubble size at different oil fraction ϕ is reported in figure 8.5 (a). We can see that the samples do not show a significant difference in their evolution, and in addition they all evolve in time in first approximation as power laws. This can be better appreciated from the plot in figure 8.5 (b), where the curves have been renormalised by the mean bubble size at the beginning of the image acquisition.

Here we can see that while the sample at ϕ=80% shows a power law growth as $R \sim t^{1/3}$, the growth of the samples at lower oil fractions appears to be faster, with the sample at ϕ=65% showing a gradual change in the slope from 1/3 to 1/2. This behaviour can be due to the gravity-driven bubble segregation inside the sample mentioned in the previous section, as the foam is polydisperse since its generation and some millimetric bubbles can already be present inside the foam samples.

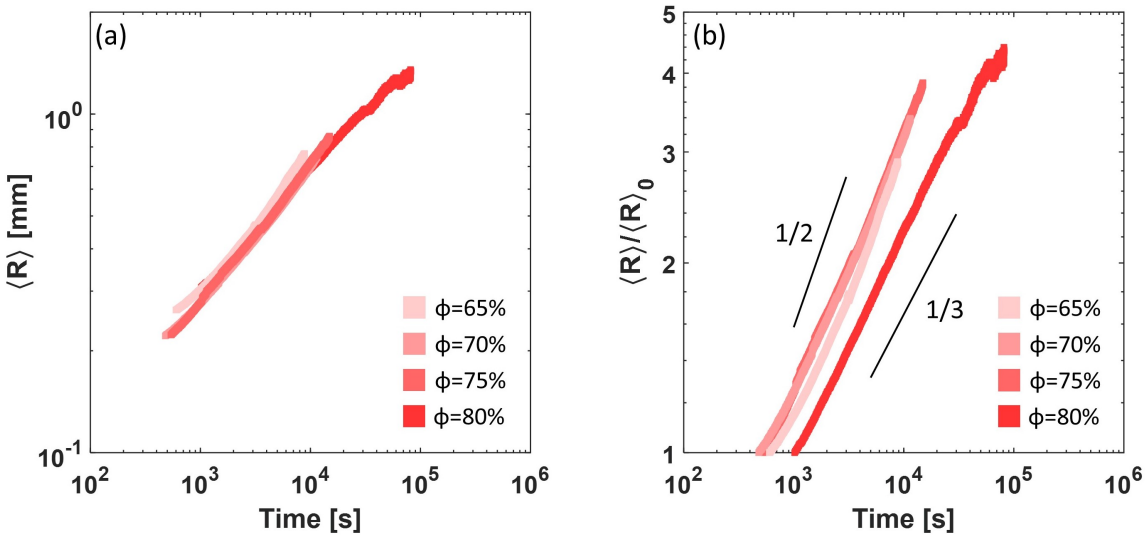

Figure 8.5 – **3D foamed emulsion at different ϕ.** Time evolution of the mean bubble size before (a) and after (b) normalisation with its value at the beginning of the image acquisition.

The effect of gravitational drainage is shown in figure 8.6, where the appearance of the top and the bottom of the two samples at ϕ=65% and ϕ=80% is compared at the end of the image acquisition. As one can see, for the sample at ϕ=65% the bubbles on the top appear slightly larger and drier than the ones at the bottom. The sample at ϕ=80% shows even a larger effect of drainage as the image acquisition was stopped much later compared to the other samples, just to qualitatively check its structure evolution. Indeed, we can see from the top that the sample exhibits a stretched bubble pattern similar to the ones observed in quasi-2D configurations, with thin Plateau borders between larger bubbles and smaller bubbles grouped together. However its coarsening rate at late stage is highly influenced by this bubble sorting, as we can see that most of the small bubbles remained at the bottom, which is why we do not observe a gradual flattening of the $\langle R(t) \rangle$ curve. In the following, we shall not consider the last part of the curve, but we restrict to times up to five hours, comparable with the other samples.

The fact that we do not observe a large difference in the coarsening rate unlike in their quasi-2D counterparts, can be explained by the smaller typical bubble size that we are considering. In quasi-2D systems, all the bubbles were roughly millimetric at the beginning of the experimental curves. By contrast, in these experiments we are following the mean bubble growth since the beginning of the image acquisition, so that we start at much smaller bubble sizes of the order of 200 μm, and we stop it when the average bubble size approaches 1 mm due to the onset of non negligible gravitational drainage. The typical bubble capillary pressure is thus higher than the one considered in quasi-2D foams, which means that we are now at lower elasto-capillary numbers: indeed, if we consider an initial bubble size of 200 μm and a surface tension of roughly 30 mN/m, the elasto-capillary number ranges from 0.2 for the sample at ϕ=65% to 2.2 for the sample at ϕ=80%.

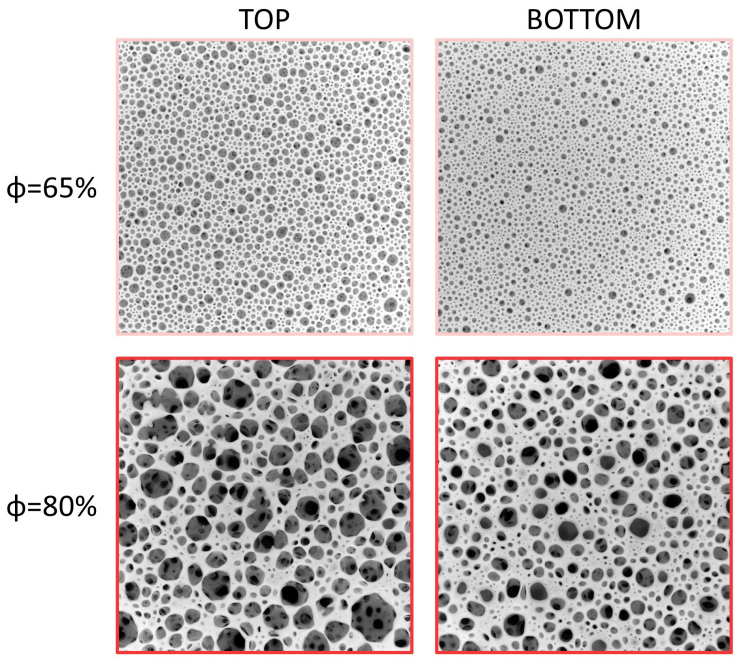

Figure 8.6 – **Gravitational drainage and bubble size sorting.** The top row shows the appearance of the top and the bottom surface of the foamed emulsion sample at ϕ=65% at the end of the image acquisition, namely after roughly 2.5 hours. We can see that the top surface appears slightly drier than the bottom and with larger bubble size on average. The bottom row shows the appearance of the sample at ϕ=80% at the end of the image acquisition, which in this case corresponds to 23 hours. We can see the appearance of the unrelaxed bubble patterns, with however most of the smallest bubbles remained at the bottom due to the buoyancy of the largest ones. The edge size of each photo is 85 mm.

Coarsening dynamics

The same image stacks are used to perform DDM analysis for each 3D sample. The aim of this approach is to extract information on the dynamics of the sample without needing to track the bubbles. This can be done by first calculating the ISF $f(q, \Delta t)$ and then fitting it with a suitable model function. We remark that no model is available *a priori* for the dynamics of foamed emulsions, as this is the first time in which this technique is applied to foams having a viscoelastic continuous phase. However, DDM has been recently applied to shaving foam [45], we shall then use the same protocol and the same fitting function in order to point out possible dynamical differences between our samples and the standard Gillette reference.

Figure 8.7 reports a few examples of ISF measured for the two samples at the extreme oil fractions ϕ=65% and ϕ=80%, one hour after their generation. We can see that in both cases, $f(q, \Delta t)$ decorrelates earlier for larger q, which corresponds to smaller length scales. On the other hand, at small q we cannot capture the full decay as it decorrelates at times much larger than the total length of the image sub-sequence: we recall that since we are working with evolving systems, we need to restrict the total time window for a given foam age in order to perform the analysis in quasi-stationary conditions.

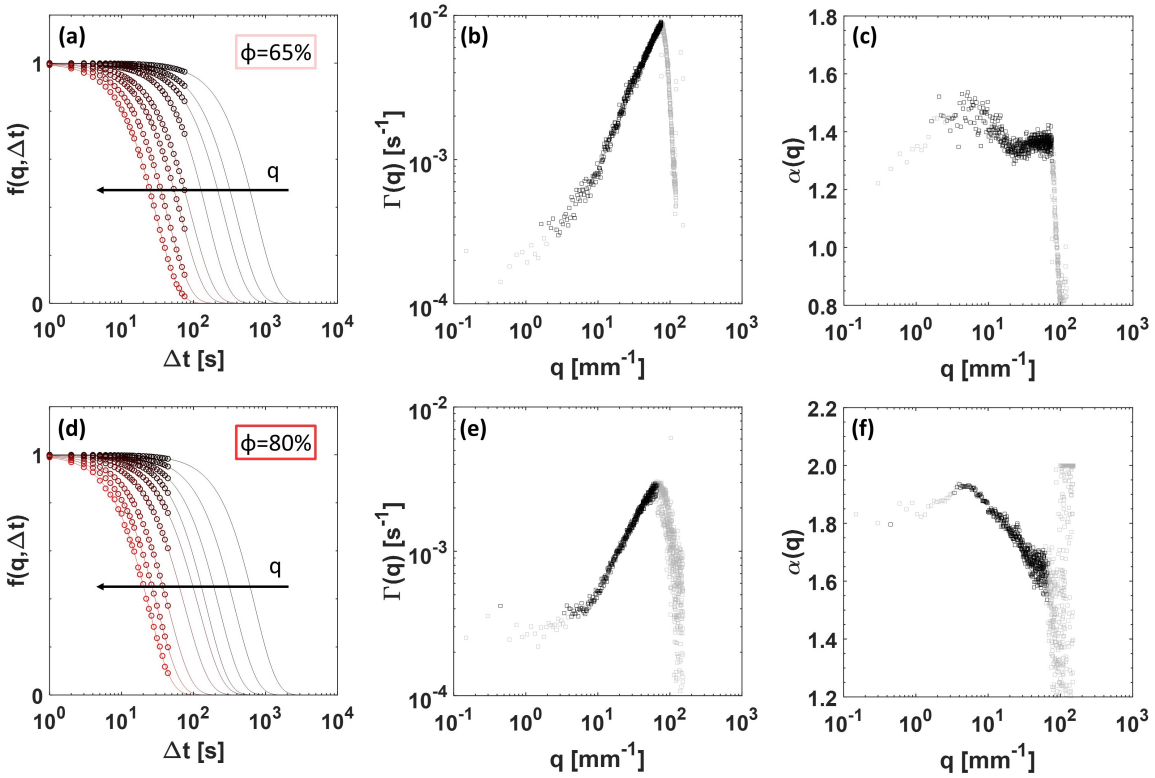

Figure 8.7 – **Intermediate scattering function.** (a) A few examples of ISF $f(q, \Delta t)$ for the sample at ϕ=65% for the time window centred around t=1 hour. We can see that the curves shift towards smaller Δt with increasing q, meaning that the larger the length scale considered (the smaller the q) the larger the decorrelation time. The curves are fitted with a compressed exponential function having equation $f(q, \Delta t) = \exp[-(\Gamma(q)\Delta t)^{\alpha}]$. (b) Fit results for the relaxation rate Γ for the full range of accessible q (grey) and for the selected range of reliable q (black). (c) Compressing exponent α for the same sample. We can see that it is close to the one found in Gillette foam [45]. (d,e,f) Example of ISF and corresponding fit parameters for the sample at ϕ=80% at the same foam age. We can see in (f) that the exponent is larger than the sample at ϕ=65% and it shows a more pronounced dependency on q.

For each q, we fit $f(q, \Delta t)$ with a compressed exponential function, and the corresponding relaxation rate $\Gamma(q)$ and compressing exponent $\alpha(q)$ are also shown in figure 8.7 for the two different samples. However, $f(q, \Delta t)$ can not be reliably fitted for all q, thus limits on the range of accessible q are imposed as follows. In principle, the lowest q that could be investigated is dictated by the image size L, namely $q_{\min} = 2\pi/L$. However, at such small q the system is very slow and it is not possible to observe a complete decorrelation, preventing an accurate determination of the dynamics. We restrict our q range at low q by imposing a threshold on the lowest Γ to be $1/\Gamma = 5\Delta t_n$ where $\Delta t_n = t_n/4$ is the total duration of each image sub-sequence. This choice, which is arbitrary, means that for the lowest q considered, $f(q, \Delta t)$ will completely decorrelate only after a time which is five times larger than the time window of the sub-sequence, and we try to predict its behaviour by observing only the initial 1/5 of its decay.

On the other hand, the upper limit at high q is mainly dictated by the sampling time Δt_0 between consecutive pictures, which determines the shortest correlation time that can be reliably measured. For the two samples in figure 8.7, Δt_0 is equal to 5 seconds for ϕ=65% and to 15 seconds for ϕ=80%, corresponding to $\Gamma = 1/\Delta t_0$ approximately 0.2 s^{-1} and 0.07 s^{-1} respectively. However, we can see from figure 8.7 (b,e) that the rate Γ at high q, after increasing, suddenly drops towards very small values. This decrease is an artifact due to the movement of the bubbles crossing the image borders that reduces the actual range of high q accessible, which could be recovered by applying a spatial window filter to smooth out the intensity gradients at the edges [44]. However, we shall not do this for our image analysis, as we are more interested in the behaviour at low q and spatial windowing, beyond a general intensity loss, could affect the results in that range. To cut out the spurious results at high q, we select the q values by imposing a threshold on the static amplitude $A(q)$ to be larger than 1/3 of the average noise level in that range, and a further restriction is imposed on the ISF fit quality by putting a threshold for the r^2 to be larger than 0.999.

The values of Γ and α in the selected q range are highlighted in black in figure 8.7 (b-f). By comparing the results for these two samples, a first difference can already be noticed by looking at the compressing exponent: a weakly varying $\alpha(q)$ between 1.4 and 1.5 is found for the sample ϕ=65%, close to the 1.2 value found for the Gillette foam, whereas higher values around 1.8 with a stronger dependency on q are found for the sample ϕ=80%, meaning that the exponential functions are more compressed. Given the change of α with q, and with ϕ, in order to compare the relaxation rates Γ we consider its average value so that it is less dependent on the specific shape of the decay. The values of Γ obtained from the fit are thus corrected to compensate for the variations of the compressing exponent by considering the general following relation for the average characteristic time of decay:

$$\langle \tau \rangle = \int_0^\infty dt e^{-(t/\tau)^\alpha} = \frac{\tau}{\alpha} \mathbb{\Gamma}\left(\frac{1}{\alpha}\right) \tag{8.3}$$

where $\mathbb{\Gamma}(1/\alpha)$ is Euler's gamma function. The average $\Gamma(q)$ is thus calculated as:

$$\Gamma = \frac{\Gamma_{\text{fit}} \alpha}{\mathbb{\Gamma}(1/\alpha)} \tag{8.4}$$

All the values of $\Gamma(q)$ shown in the different figures are thus accounting for this correction.

This treatment is repeated over time windows at different foam ages for each 3D foamed emulsion sample. The results of the relaxation rates $\Gamma(q)$ obtained for the different oil fractions are reported in figure 8.8.

As a general comment, from the first column of graphs we can see that the rates vertically shift towards lower values as the foam ages, consistently with the reduction of the coarsening rate. If we now look at the first sample ϕ=65% we can recognise two different slopes in the curves, with a crossover point that horizontally shifts towards smaller q over time, consistently with an increase of the average typical length in the system induced by the coarsening process. In the same spirit of [45], we can rescale the curves by renormalising $\Gamma(q)$ with the coarsening rate $\dot{R}/R$, and by multiplying q by the average bubble size R. The coarsening rate and the average bubble size at time t is obtained by fitting the $R(t)$ curves reported in figure 8.5 with a power law function $R(t) = a \cdot t^b + c$ which is then derived in time. As we can see in the second column of plots in figure 8.8, the rescaling works rather well, with a good collapse of the curves onto a master curve, with the only exception of the

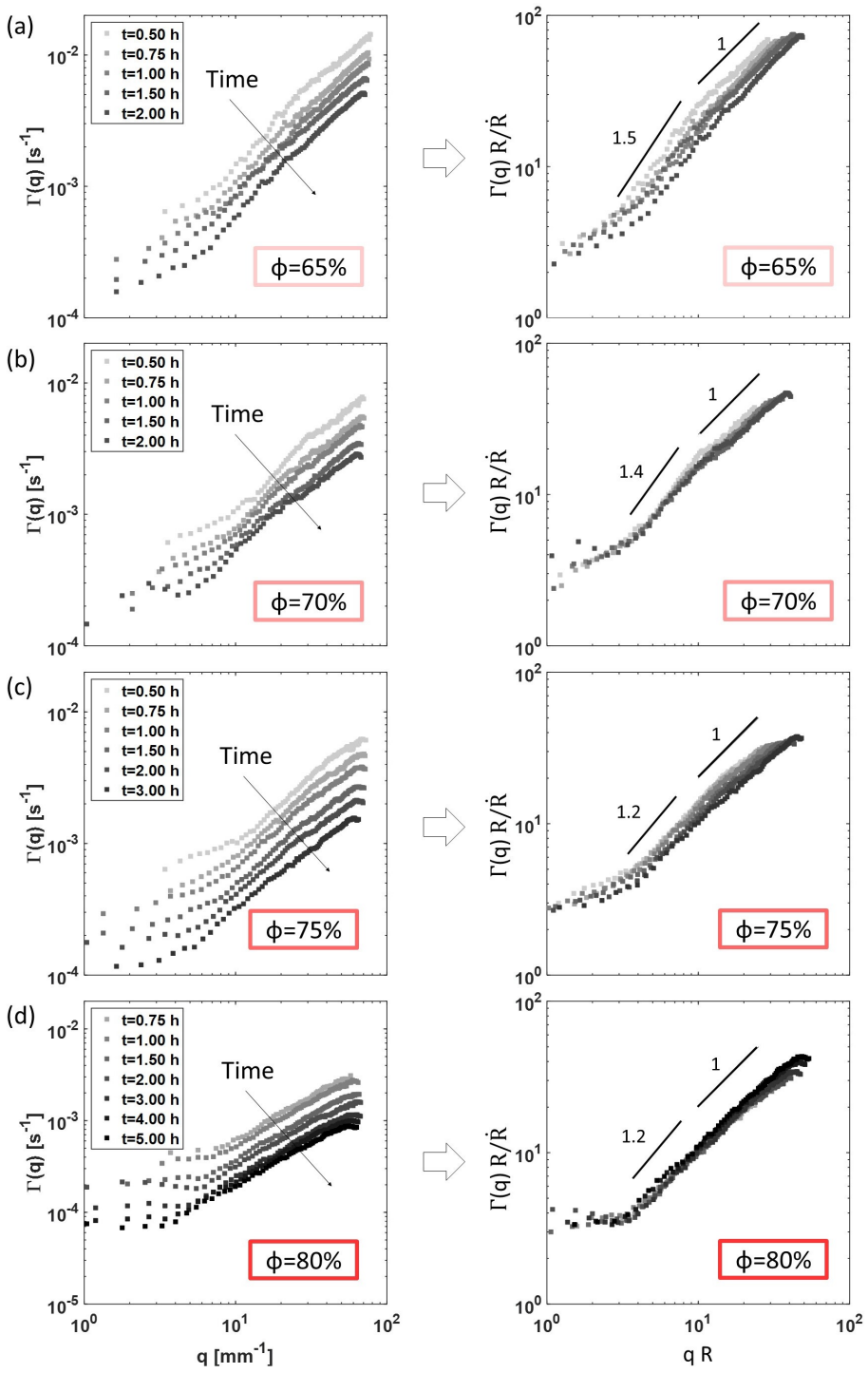

Figure 8.8 – **Coarsening dynamics in 3D.** Relaxation rates obtained from the ISF fit for each sample as indicated in the graph. The left column shows the raw $\Gamma(q)$ calculated at different foam ages, while the right column show the collapse of the data after rescaling $\Gamma(q)$ with the coarsening rate and q with the average bubble size R.

sample ϕ=65% which presents the widest spread of the curves after normalisation among all the samples. This could be due to the gradual change in the top surface liquid fraction due to drainage, as we can see that the curves appear only horizontally shifted, suggesting a change in q, since R is measured from the skeleton and is thus independent of the liquid fraction.

Let us now have a look in more detail at the two dynamical regimes observed for the sample at ϕ=65%. At high q the curves show a linear dependency of $\Gamma(q)$ in analogy to Gillette foam. This ballistic-like regime has been ascribed to the strain field developed inside the coarsening foam, which makes the bubbles move constantly in one direction until a rearrangement occurs and suddenly modifies their trajectories [45]. The occurrence of bubble rearrangements involving a change of neighbours sets a cutoff length for this persistent motion which is identified with the bubble diameter: the crossover q_cR was found to be around 2.4 for Gillette foam [45]. In our foamed emulsion the crossover appears at a larger value of $q_cR \sim$10. This could be in part due to the different bubble size definition that we use for estimating R compared to [45]: for Gillette foam, indeed, the bubble size is measured from the mean gas surface area of the bubbles as $R = \sqrt{\langle A_{\mathrm{gas}} \rangle / \pi}$, as shown in figure 8.9. By contrast, in our case we use the foam skeleton to estimate the equivalent radius from the bubble area, thus our estimate of R is larger and expected to be closer to the actual bubble size. Indeed, by taking the gas surface area A_{gas}, one underestimates the real bubble size, and in the case of Gillette this effect could be further enhanced by a higher surface liquid fraction due to some drainage occurring during the acquisition, as the pictures are taken in reflection from the bottom of the sample [45]. In order to quantify this difference, we compare the two definitions in figure 8.9 for a Gillette foam picture: we find that our definition of R obtained from the skeleton is larger of a factor 1.6, thus it cannot completely explain the horizontal shift of the crossover q_cR. This means that, while the crossover between the two regimes in Gillette foams occurs at roughly the bubble size even with a more accurate definition of R, in our case it actually occurs at a length scale which is only a fraction of the bubble size, thus the bubbles move much less before changing direction.

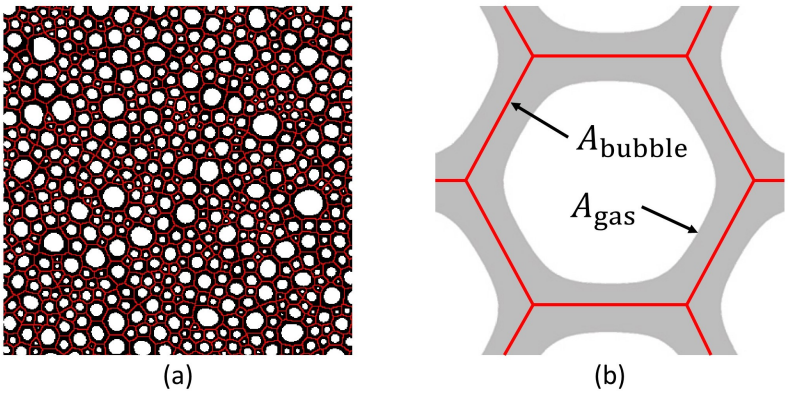

Figure 8.9 – **Comparison between bubble size definitions.** (a) Example of binarised Gillette foam picture with its skeleton superimposed. (b) Illustration of the bubble area measured from the skeleton, A_{bubble}, and from the gas surface, A_{gas}.

Despite this, the slope observed below q_c is in good approximation equal to 1.5, namely in agreement with the 1.6±0.2 found for Gillette [45]. The shape of $\Gamma(q)$ at low ϕ is thus approximately the same as for Gillette foam, just horizontally shifted.

If we now compare the normalised plots for the different samples, we can see that the two slopes are gradually lost as the oil fraction is increased, with only the ballistic regime at high q surviving in each sample. At ϕ=80%, the power law 1.5 observed for ϕ=65% reduces to 1.2, so that the curves appear almost flat, as if only one dynamical regime was present.

From the graphs, we can also distinguish the existence of a third regime: for qR<3 the normalised relaxation rates exhibit a plateau where their value is q-independent. We do not have a physical interpretation for this regime, but we highlight that for these low wavevectors the intermediate scattering function decays over times much longer than the duration of the image sub-sequence considered. Since the sample is evolving, it is more likely that such long characteristic times become comparable to the time at which the foam structure has evolved because of coarsening. Thus, at such low q it becomes hard to decouple the coarsening dynamics from the kinetics, as the two blend together.

The difference between the samples can be better appreciated in figure 8.10 where we first compare in (a) the different samples at the same foam age and then we plot all the rescaled curves together in (b).

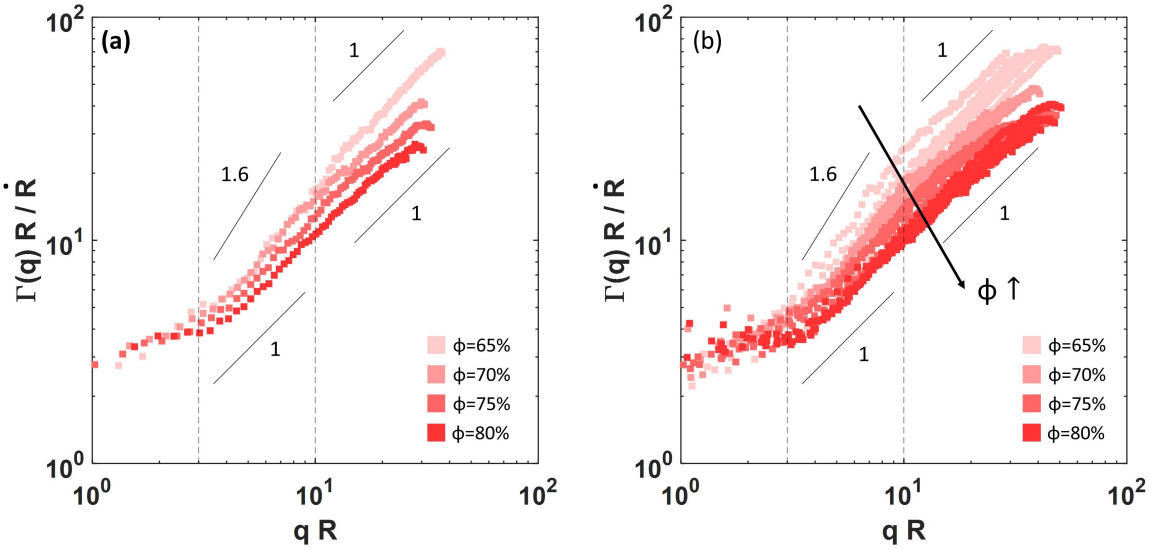

Figure 8.10 – **3D foamed emulsions at different ϕ.** (a) Normalised rates versus qR for each sample at foam age equal to 1 hour. (b) All the curves together for each sample and each foam age. We can see that while the high-q regime remains in good approximation ballistic for each ϕ, an increase of the oil fraction modifies the power law at intermediate q regime.

We can see that the regime at high q is roughly the same for each sample, whereas an increase of ϕ results in a gradual reduction of the slope at the intermediate q regime. If we now recall that this intermediate regime has been associated with the onset of bubble rearrangements, we can see that increasing emulsion viscoelasticity suppresses the dynamics of bubble rearrangements in the foam sample. This result is particularly interesting given

that no significant change in the coarsening rate is observed between the samples, except for the gravity-induced effect of bubble size sorting inside the sample which makes the average bubble size grow apparently faster at lower ϕ.

The different dynamics of bubble rearrangements is confirmed by a visual observation of the foam coarsening videos: while at low ϕ we can still observe bubbles to rearrange and change their neighbours, as ϕ is increased the bubbles appear less and less mobile. Small bubbles shrink and disappear while larger bubbles grow without moving substantially from their initial position. Therefore, at high ϕ, the linear dependency of Γ on q is more likely caused by the movement of the Plateau borders during the bubble growth or shrinkage, rather than a persistent motion of bubbles.

In figure 8.11 we graphically compare the correlation maps between two pictures taken at a time interval of one minute at the same foam age for the samples at different ϕ. We can see that in all the samples bubble rearrangements have occured, but while for example in the sample at ϕ=65% a single bubble rearrangement causes the motion of several bubbles around, as we increase ϕ the bubbles affected are less and less. We shall see in section §8.3.3 that the same behaviour is observed also in quasi-2D systems, thus the higher bubble mobility observed at lower ϕ is not due to the enhanced bubble rising.

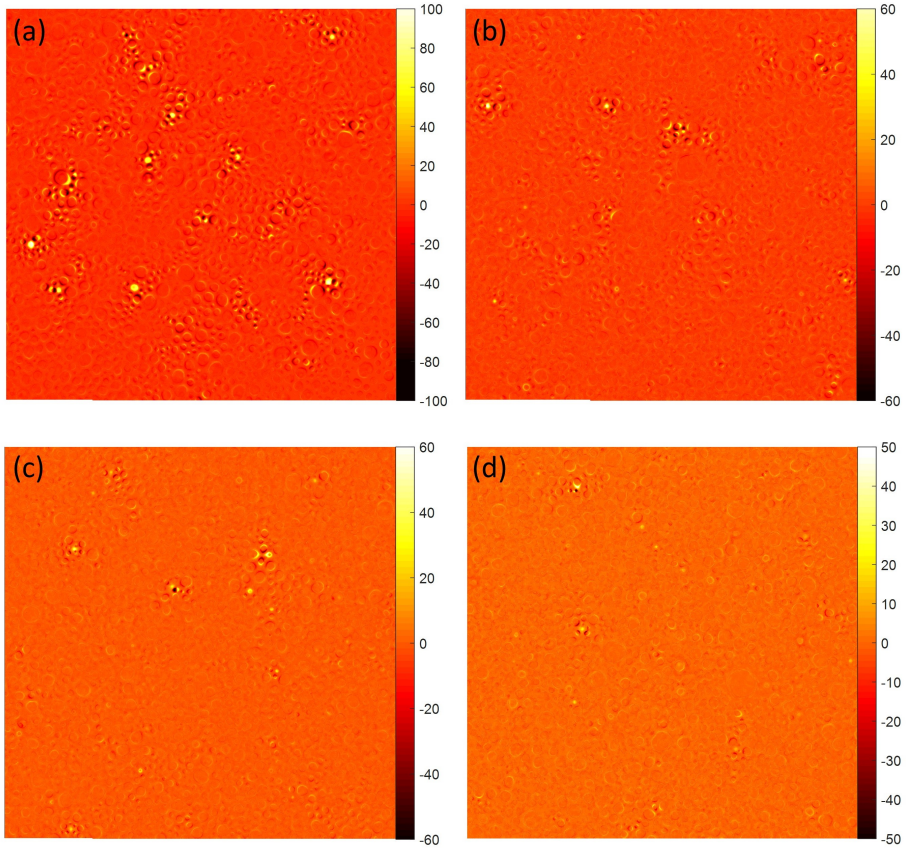

Figure 8.11 – **Bubble rearrangements in 3D foamed emulsions.** Correlation between two pictures separated by 1 minute at the same foam age of 1 hour for the different samples: (a) ϕ=65% (b) ϕ=70% (c) ϕ=75% and (d) ϕ=80%. The edge size of each picture is 5 cm.

8.3.2 3D/2D transition

To probe the effect of foam confinement, we monitor three foamed emulsion samples having the same oil fraction ϕ=80% but sandwiched between two glass plates with a different spacing equal to 1, 2 and 3 mm. As we can see in figure 8.12, the foamed emulsion is initially 3D, as the typical bubble size is much smaller than the gap between the two plates. As the foam coarsens and the bubbles grow, their diameter will eventually equal the gap between the two plates, so that they start touching both top and bottom glass surfaces and become 2D bubbles. This does not occur simultaneously for each bubble in the sample, as only the larger bubbles are initially involved, meaning that we go through an intermediate regime in which both 3D and 2D bubbles coexist and coarsen inside the sample. In the long run, however, the average bubble size will become much larger than the gap so that the sample can be considered a bubble monolayer and thus a quasi-2D foam. In principle, this eventually happens for any cell gap. However, we restrict our study to rather small cell thicknesses in order to reduce the time needed for the foam to fully overstep the intermediate 3D/2D regime. Moreover, larger gaps would be affected by gravity, which creates a vertical liquid fraction gradient, that in quasi-2D systems translates into larger surface Plateau borders at the bottom and thinner ones at the top.

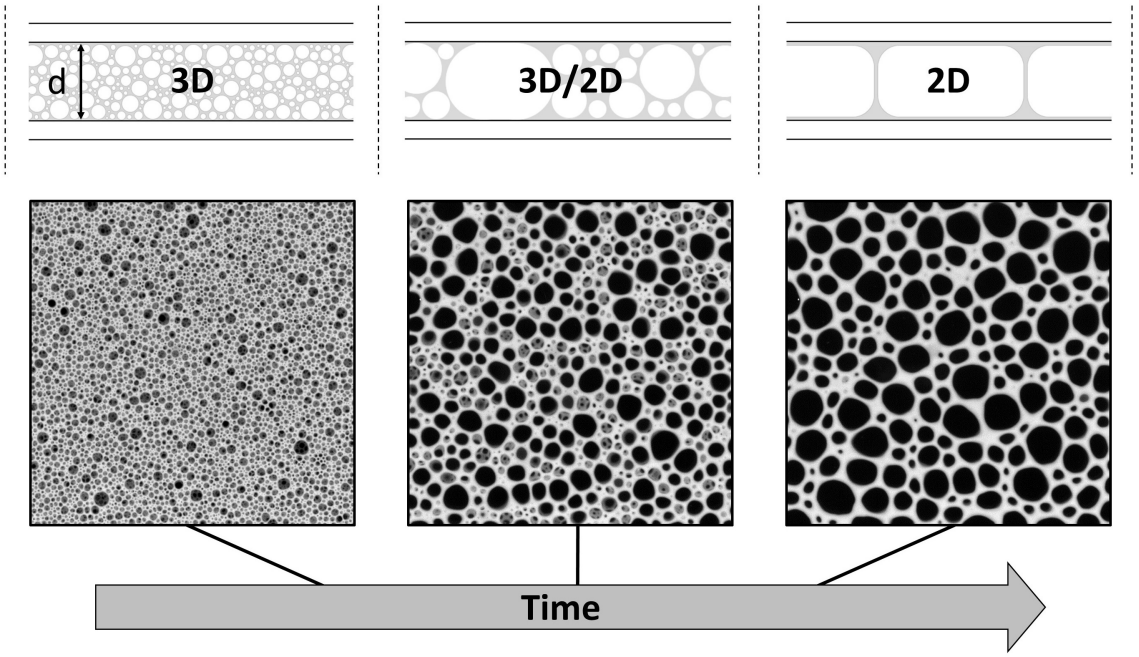

Figure 8.12 – **From 3D to quasi-2D.** Transition from a 3D to a quasi-2D sample for a foamed emulsion at ϕ=80% and cell gap of 2 mm. We can see that the foam crosses a regime in which both 3D and 2D bubbles coexist, which makes the measure of the average bubble size ambiguous. Photo edge length 40 mm.

To probe the coarsening of these confined samples, once again we start from the real space and we measure the average bubble size from the skeleton of the surface foam layer, in order to monitor its evolution over time. The time evolution of the total number of bubbles, together with the mean bubble growth, for the three samples at different cell thicknesses is reported in figure 8.13.

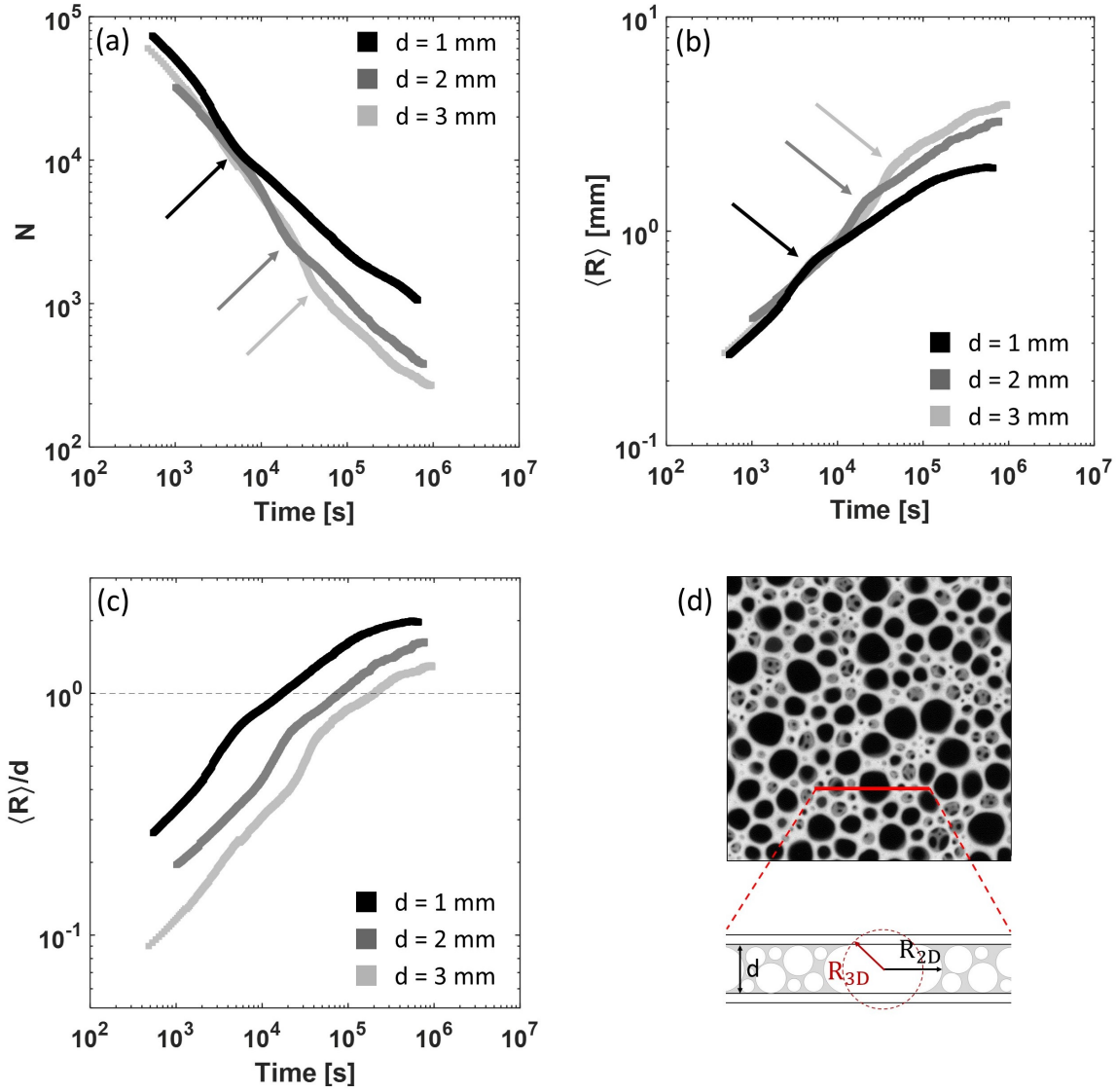

Figure 8.13 – **Coarsening during the 3D/2D transition.** Time evolution of the number of bubbles (a) and average bubble radius (b) for the samples in different cell gaps. The arrows indicate the bumps in the curves, which are more visible in (c) where the mean bubble size is normalised by the cell thickness. The bump is due to the change in the definition of R during the transition from 3D to quasi-2D as sketched in (d).

We can see that in all samples, the average bubble size grows in time showing a bump when it approaches the gap size. This is due to the change in the definition of equivalent bubble radius as we switch from 3D to quasi-2D systems.

Indeed, what we measure is the area of each cell in the surface foam skeleton, which can now represent either a 3D or a 2D bubble. We might think about converting the measured area in the equivalent bubble volume, but in order to do that we need to know which bubbles are 3D and which are 2D, thus one should in principle apply a size threshold to discriminate between the two. However, we stress that this size threshold is not unique, as it changes

between the early stage (3D) and the late stage (2D) of coarsening. On one hand, when the foam is 3D, the growing bubbles will gradually approach the gap size and they start assuming a pancake shape only once their radius is equal to half the cell thickness. On the other hand, when the foam is in good approximation a bubble monolayer, the shrinking bubbles can deform before detaching from the bottom plate and become 3D, so that they can exhibit a radius smaller than half the spacing between the plates but still be 2D. In the transition between 3D and 2D both mechanisms occur simultaneously as the samples are highly polydisperse. Moreover, the conversion from the measured area and the actual volume of the sample would require an approximation on the shape of the 3D bubbles as they are not simply spherical, first because the foamed emulsion is rather dry and second because they are pressed against the glass surface.

The most robust and size independent parameter is the total number of bubbles. However, as we can see from figure 8.13 (a), the time evolution of the latter also shows a change in the rate during the transition from 3D to 2D. This is because it measures the number of bubbles appearing on the top surface, and while as long as the foam is 3D or completely quasi-2D this reflects the total number of bubbles present in the sample (proportional in the first case, exact in the second), this is no longer true when we have both 3D and 2D bubbles.

For these reasons, which prevent a correct estimation of the average bubble size at each time, characterising the bubble growth rate during the transition is tricky and we shall not consider it further. The apparent faster coarsening rate during the transition would inevitably affect the normalisation of the $\Gamma(q)$ curves once studying the dynamics with DDM, preventing their collapse. However, we can still look at the shape of $\Gamma(q)$ over time, which are reported in figure 8.14, to check if they present the same q-dependence observed in 3D.

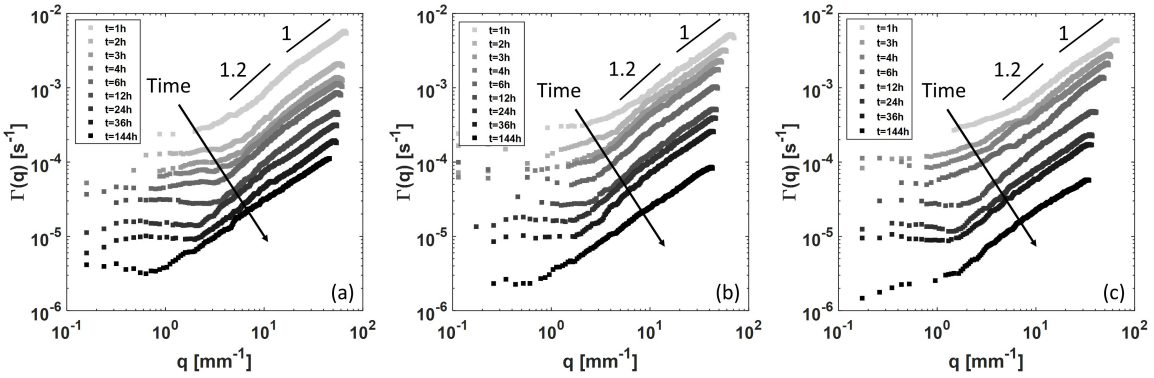

Figure 8.14 – **3D/2D transition.** Time evolution of the relaxation rates $\Gamma(q)$ for a foamed emulsion at ϕ=80% coarsening at different levels of confinement. The cell thickness is 1 mm in (a), 2 mm in (b), and 3 mm in (c). We can see that it is harder to distinguish two different dynamical regimes as the exponent values are really close. We can see that in (a) and (b) the curve shape becomes completely flat at t=144 h: at this stage the foam is completely 2D and has developed the typical unrelaxed bubble pattern observed in chapter §7. The strong change in the foam structure could thus affect the results.

We can see that they present a shape very similar to the $\Gamma(q)$ measured in 3D, where it is harder to distinguish two different power laws as clearly as in the 3D sample at ϕ=65%. Thus, despite the confinement, the dynamics is qualitatively the same for the samples at 80% at each cell thickness, with a reduced slope of the dynamic regime at intermediate wavevectors q. It thus seems that the bubble dynamics in foamed emulsions is not affected by the foam confinement, which means that we can now go back to quasi-2D foam configurations to study the coarsening dynamics of such complex systems.

8.3.3 Coarsening dynamics in quasi-2D foams

Since we saw that the global shape of the relaxation rates $\Gamma(q)$ does not change with the foam confinement, we can safely go back to quasi-2D foam configurations which are easier to treat and they are not affected by gravitational drainage. In this section we shall first probe the coarsening of bubble monolayers with DDM, starting from an aqueous foam which we then compare to a highly concentrated foamed emulsion. We shall then go back to the real space to quantify the rate of bubble rearrangements inside the samples at different emulsion oil fractions.

Aqueous foam

Since there are no DDM experimental results in the literature for quasi-2D foams, we start by probing the dynamics of an aqueous foam made with the same SDS solution used for foamed emulsions but with no oil in the continuous phase. With the double-syringe method, we generate a foam at a liquid fraction ε=10% and we sandwich it within a gap of 1 mm. A stack of images is taken at constant time intervals Δt_0 of 5 seconds, on which we then perform DDM analysis to evaluate the intermediate scattering function $f(q, \Delta t)$. By fitting $f(q, \Delta t)$ with a compressed exponential function we obtain the relaxation rates $\Gamma(q)$ reported in figure 8.15, where we show the $\Gamma(q)$ curves obtained at different foam ages before and after rescaling with the coarsening rate and the mean bubble size. The latter are evaluated from a power law fit of the mean bubble size evolution shown in the inset, as done in section §8.3.1

We can see that the rescaling makes the curves collapse, showing a crossover between two different dynamical regimes around $q_c R$=10. The first regime at high q presents a slope slightly higher than the linear regime found in 3D foams. Indeed, by fitting the curves with a power law $y = ax^b$ in the qR interval [25;90] we find an average exponent equal to 1.20±0.02. By contrast, similar fits at lower qR between 4 and 12 give an average slope of 1.51±0.05 which is fully coherent with the value 1.6±0.2 observed in the 3D Gillette foam. The physical interpretation is thus expected to be the same as in 3D: the 2D bubbles move persistently in one direction driven by the coarsening-induced strain field, until the occurrence of bubble rearrangements changes the stress configuration and modify their trajectories. However, the ballistic bubble motion is interrupted at length scales below the bubble diameter, thus the bubbles move less than in Gillette foam, even though the continuous phase is only an aqueous surfactant solution. This could be due to the fact that we are in a quasi-2D foam geometry, where the bubbles can rearrange only on the horizontal plane, they thus have one degree of freedom less than in 3D foams. Nevertheless, we remark that even when the foam is 3D, DDM probes the dynamics mainly of the surface bubble layer, where the bubble motion is in any case more restricted than in the bulk.

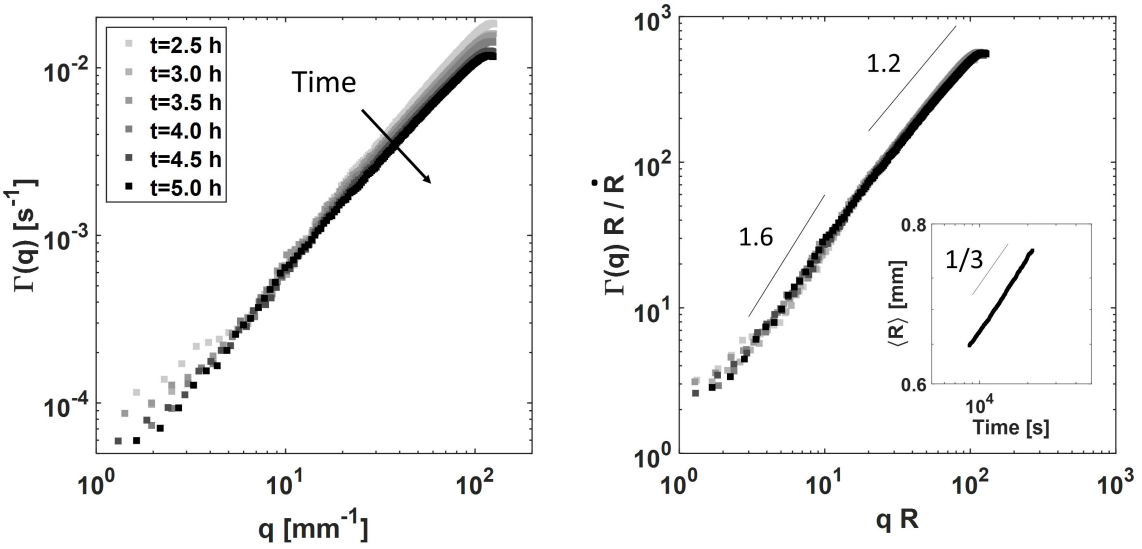

Figure 8.15 – **Quasi-2D aqueous foam.** Evolution of the relaxation rate $\Gamma(q)$ over time, before (left) and after (right) rescaling with the coarsening rate and the bubble size. Inset: time evolution of the mean bubble size.

Foamed concentrated emulsion

We now want to see what happens when the aqueous phase is replaced by a highly viscoelastic emulsion. We thus perform the same experiment on a foamed emulsion at ϕ=80% made with sunflower oil. The DDM results and the mean bubble size evolution obtained from the real space are reported in figure 8.16.

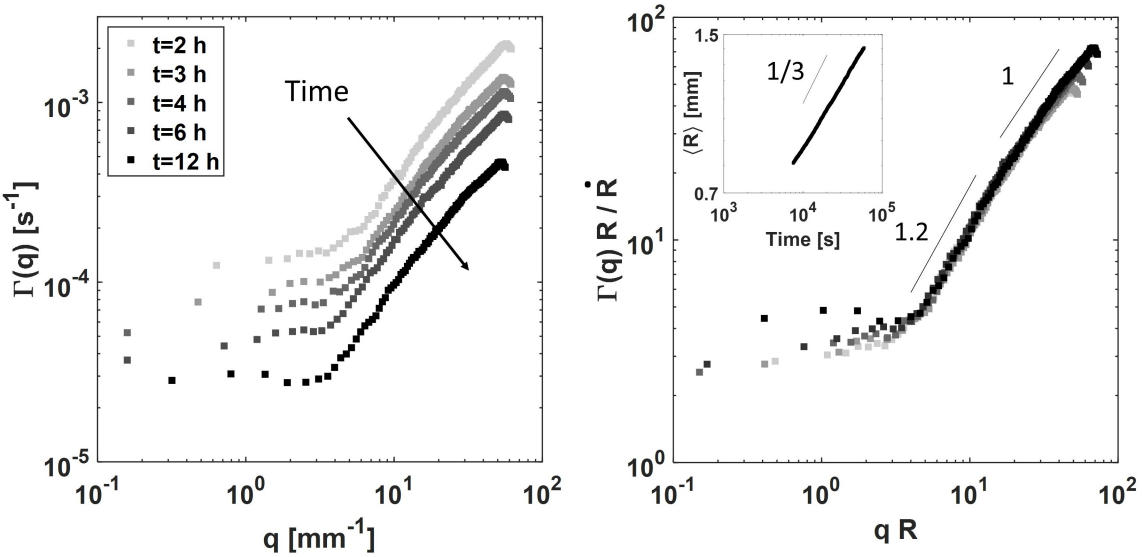

Figure 8.16 – **Quasi-2D foamed emulsion.** Evolution of the relaxation rate $\Gamma(q)$ over time, before (left) and after (right) rescaling with the coarsening rate and the bubble size. Inset: time evolution of the mean bubble size.

We can see that the collapse of the normalised relaxation rates is still very good, with a crossover between two power laws at $qR \simeq 10$, which however have now changed the slope values. We can see that at high q we recover the linearity of $\Gamma(q)$, with an average exponent value 0.95±0.05 obtained by exponential fitting, but now the intermediate q regime has an average exponent of 1.19±0.02, which is thus reduced compared to the aqueous foam. For a better visual comparison, we plot the normalised curves for the two samples in the same graph in figure 8.17, where we can see how the q-dependency of Γ is different between the samples. Thus, also in quasi-2D systems we see an effect of the continuous phase viscoelasticity on the bubble rearrangements.

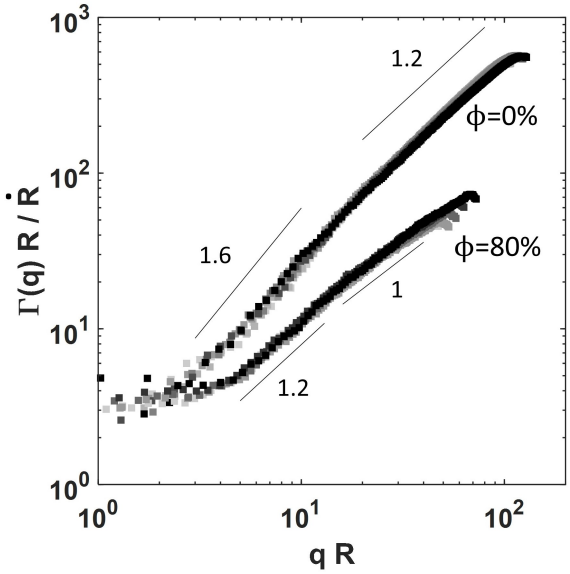

Figure 8.17 – **Quasi-2D foam comparison.** Normalised relaxation rate $\Gamma(q)R/\dot{R}$ at different foam ages for an aqueous foam (ϕ=0%) and a foamed emulsion (ϕ=80%).

More precisely, we highlight that the change in the slope reflects a change in the effect of the bubble rearrangements on the motion of the bubbles in the sample. As we shall see in the next section, a visual inspection of the correlation maps between successive pictures at different ϕ reveals that at higher oil fractions the occurrence of a rearrangement causes surrounding bubbles to move only in the region close to the event location, without affecting bubbles further away.

We conclude by noticing that the mean bubble size evolution in the two samples show a different coarsening rate, which is lower in the foamed emulsion than in the aqueous foam. The observation of a slower coarsening in presence of hindered bubble rearrangements naturally raises the question of whether and how the two observations are correlated, as in 3D samples it seems that a lack of rearrangements does not affect significantly the coarsening rate of the foam. In the next section we shall try to quantify the rate of bubble rearrangements to partially answer this question.

Rate of bubble rearrangements

Our DDM results reveal a lower bubble mobility as we increase the emulsion oil fraction and thus the viscoelasticity of the foam continuous phase. Now we shall quantify the number of

bubble rearrangements occurring between two pictures separated by a time interval Δt. We remark that, while in the previous section we actually looked at the motion of the bubbles until rearrangements occur to modify the stress configuration in the system, we are now addressing the question of whether an increasing ϕ also reduces the rate of these events, with the final goal of exploring the correlation between the rate of bubble rearrangements and the overall foam coarsening rate.

To quantify the rate of bubble rearrangements involving a change of neighbours in our samples, we go back to the real space. We exploit the same data sets of quasi-2D foamed emulsions considered for the study of their evolution in chapter §7. We remark that the temporal resolution of those image stacks is not high enough for a DDM analysis, which is why here we only consider the real space. By contrast, the quasi-2D configuration allows to easily track the bubbles to pinpoint the occurrence of neighbour switching events. The quantification of bubble rearrangements from the skeletonised pictures is carried out by Jonatan Mac Intyre, who developed a MATLAB script to track the bubbles over time and automatically pinpoint the ones that are changing neighbours. This script is applied to both the aqueous foam discussed at the beginning of this section and to the foamed emulsions at different ϕ. In the graphs we shall indicate the bubble rearrangements with the name T1s for the sake of simplicity, to highlight the topological change of neighbours between bubbles, even though we stress that we are considering foams that are not very dry and thus the neighbour switching is not an instantaneous process.

The raw output of this treatment is shown in figure 8.18 (a), where we plot the time evolution of the number of rearrangements registered between two consecutive frames for the different samples. In this plot we compare only the portion of data in which the Δt between the pictures is the same and equal to 180 s for each sample. We can see that the number of bubble rearrangements decreases over time, as expected for a coarsening foam, but we can already glimpse the effect of the increase of ϕ: at early times the samples having a highly elastic continuous phase present up to 10 times less events than the aqueous foam. However, since foamed emulsion are not self-similar, their evolution can be history-dependent, which makes comparisons over time not very significant. In the inset we thus compare the number of rearrangements versus the mean bubble size, where we can see that for a given average bubble radius the number of bubble rearrangements also decreases with increasing ϕ.

However, for a proper comparison between the samples, it is necessary to normalise this raw counting by the time interval Δt between the pictures and by the total number of bubbles N inside the sample, in order to get the number of bubble rearrangements occurring per second and per bubble. This is done in figure 8.18 (b), where we plot the rate of bubble rearrangements for each sample and for the entire image acquisition. By comparing the curves, we can notice that, for a given mean bubble size, the rate of bubble rearrangements strongly decreases as the emulsion ϕ is increased. From the graph we can also see that at late stage (larger bubble size) the number of events is often zero, even if the Δt is enlarged to 1800 s. This can be better appreciated from the inset, where the same data are plotted in logarithmic scale and we can see that the data split on discrete curves due to the zero counting of rearrangement events. In the following we shall not consider the latter part, where the statistics for these rearrangements become too low to be reliable, and the sample at ϕ=85%, as it exhibits a negligible number of events since the beginning, resulting in just a noisy cloud of points. Moreover, we stress that once the foamed emulsions start assuming heterogeneous bubble shapes, with uneven distribution of emulsion among the bubbles, the

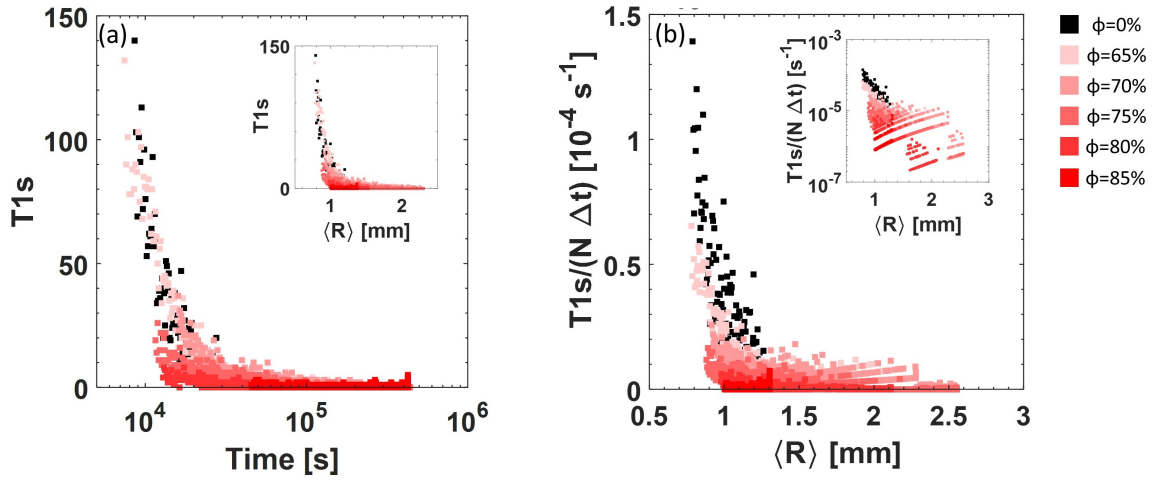

Figure 8.18 – **Bubble rearrangements in quasi-2D foams and foamed emulsions.** (a) Raw data obtained from the counting of the number of bubble rearrangements occurring between two consecutive pictures, separated by the same Δt=180 s, for samples having no oil or an increasing oil fraction in the continuous phase. For each sample, the number of events decreases over time, as expected for a coarsening foam. The inset shows the same data plotted against the average bubble radius, where we can see that increasing ϕ dramatically reduces the number of rearrangements for a given mean bubble size. (b) Rate of bubble rearrangements, namely their number normalised by the time interval Δt between the frames and the total number of bubbles N. We can see that as the bubble size grows, we often count no events between frames even if the Δt is increased up to 1800 s. This can be better appreciated from the inset, where the plot is in logarithmic scale: the discretisation results in data split on separated lines.

counting can become unreliable. The number of bubble rearrangements is indeed counted from the foam skeleton retrieved from image treatment, which can only guess which bubbles are actually touching in the wetter regions, as given the white appearance of the emulsion we cannot see from the top where the actual contacts between bubbles are. We shall then restrict our analysis to the initial part of the foam evolution, namely for mean bubble sizes $\langle R \rangle < 1.2$ mm, where the foam skeleton well approximates the actual foam topology and the statistics of rearrangement events is high enough to allow comparisons between the data. In this size range, the time evolution of the mean bubble size can be fitted with a power law function $R = at^b + c$, which we then derive to determine the coarsening rate $\dot{R}$, as we now want to probe the link between the rate of the bubble rearrangements and the global coarsening rate of the foam.

In figure 8.19 we plot the normalised coarsening rate $\dot{R}/R$ versus the rate of bubble rearrangements in linear (a) and in logarithmic (b) scale. In the graphs we plot both the raw noisy data and the average trend obtained by applying a moving average filter over larger time intervals. We can see that the curves corresponding to the different samples do not collapse onto a single master curve, but they seem shifted. This is really interesting as it suggests that we could observe the same coarsening rate even though the rate of bubble rearrangements is different.

From these graphs we can see that as we increase the emulsion viscoelasticity we reduce the occurrence of bubble rearrangements, without affecting too much the coarsening rate.

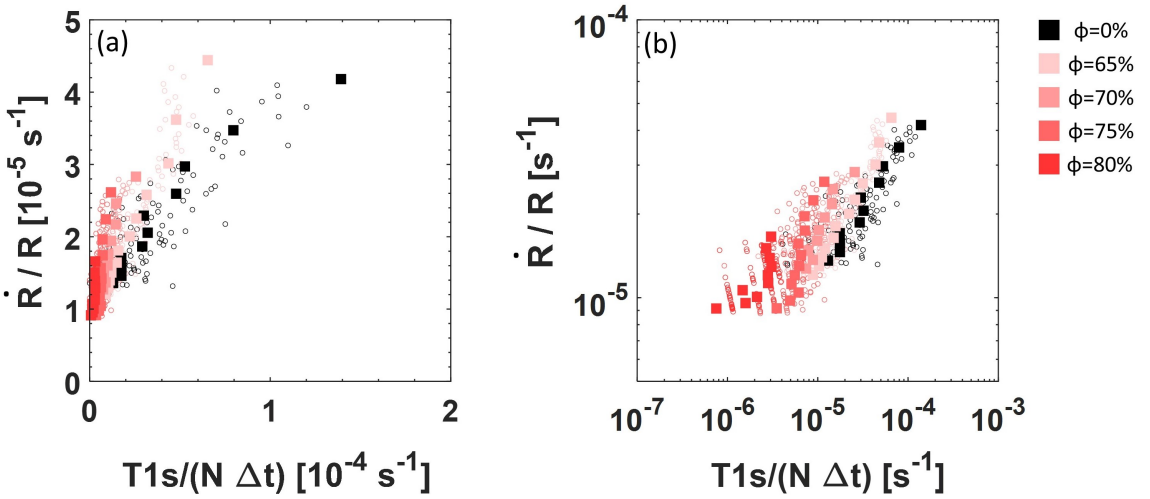

Figure 8.19 – **Link between coarsening rate and bubble rearrangements.** (a) Coarsening rate $\dot{R}/R$ versus the rate of bubble rearrangements. The empty circles correspond to the raw data, while the solid squares correspond to a binning of the T1s data over larger time intervals. We can see that the data do not perfectly collapse. (b) Same plot but in logarithmic scale. We can see that, beyond the scatter in the data, the curves at different ϕ appear slightly shifted on average, and in the right order: the higher ϕ the lower the rate of bubble rearrangements.

However, we remark that these data consider only the absolute number of topological events in which the bubbles have changed their neighbours, but do not say anything on the motion of the surrounding bubbles when these events occur.

For a direct visualisation of what happens in the different samples, once again we can compare the image correlation maps. In figure 8.20 we report the correlation maps between two frames separated by a delay of 3 minutes at the same foam age of 5 hours for each sample. We can see that while in the sample at lower ϕ we can recognise several bubble rearrangements which make the surrounding bubbles move, as ϕ is increased up to 80% the movement induced by bubble rearrangements, which are less in number, involve smaller regions of bubbles, while the rest of the foam remains basically static. Thus an increase of the emulsion viscoelasticity among the bubbles has a double effect: it reduces not only the rate of rearrangements but also the effect of the latter on the bubbles around, whose movement appears hindered.

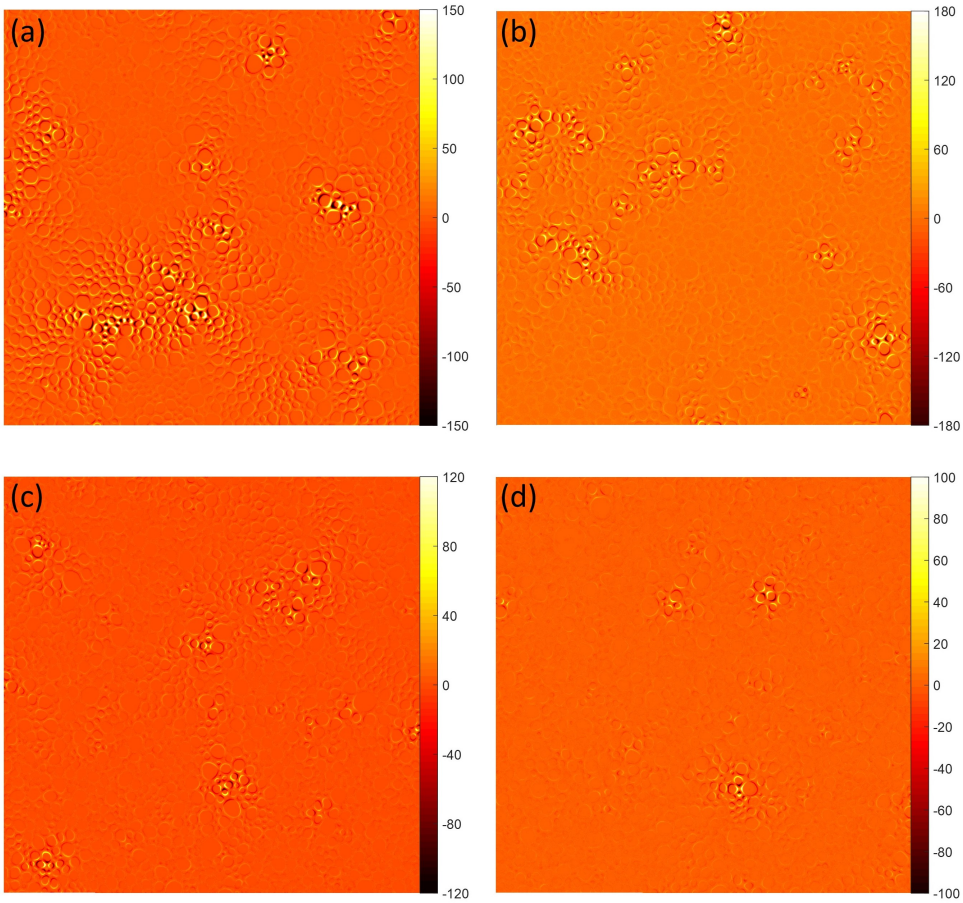

Figure 8.20 – **Bubble rearrangements in quasi-2D foamed emulsions.** Correlation between two pictures separated by 3 minutes at the same foam age of 5 hours for the different samples: (a) ϕ=65% (b) ϕ=70% (c) ϕ=75% and (d) ϕ=80%. We can see that, while in (a) a bubble rearrangement makes the bubbles around move substantially from their position, in (d) only the bubbles involved in the rearrangements and the first neighbouring ones move, while the rest of the bubble pattern remains stuck in its place. The edge size of each picture is 9 cm.

8.4 Conclusions

In this chapter we probed the coarsening dynamics of foams made of viscoelastic emulsions in both 3D and quasi-2D configurations, giving also a glance at what happens when the system transits between these two regimes.

It is well known that the coarsening process keeps altering the stress configuration inside the foam, giving rise to strain fields that make the bubbles move persistently until they eventually rearrange. The dynamics of foamed emulsions was investigated with a tracking-free technique called differential dynamic microscopy, which examines the Fourier domain correlations between pictures at different time delays. The analysis carried out on 3D coarsening foamed emulsions has revealed that the bubble movements are hindered, with the persistent motion up to a length scale which is only a fraction of the bubble size, thus smaller than the one observed in a 3D shaving foam [45].

This effect is mirrored by the gradual loss of two well-defined dynamical regimes in the relaxation rates $\Gamma(q)$ as the emulsion oil fraction is increased. This behaviour in the Fourier domain is confirmed by visual observations in the real space: at high ϕ the bubbles do not move significantly from their initial positions as they coarsen, and the linear ballistic regime observed for $\Gamma(q)$ is thus more likely to come from the movement of the Plateau borders as the bubbles shrink or grow. We remark that the suppression of the bubble motions is evident already at low elasto-capillary numbers, thus well before the appearance of the unrelaxed bubble shapes observed at late stage for quasi-2D coarsening foamed emulsions in the previous chapter.

The experiments carried out in more confined cell geometries do not show a significant difference in the overall dynamical behaviour of the bubbles at high ϕ, which is qualitatively the same both in 3D and in quasi-2D systems, and also during the transition between the two configurations, even though the impossibility to define a univocal bubble size in this situation prevents the rescaling of the results. This observation is important as it allows to study the coarsening dynamics in quasi-2D systems, which are intrinsically more controlled as at least gravitational drainage is negligible. Moreover, the choice of bubble monolayers allows a direct comparison between the reciprocal and the real space. For example we showed that we could quantify the rate of bubble rearrangements occurring in the samples at different ϕ. The comparison of the latter with the global coarsening rate does not collapse on a single master curve, suggesting a possible decorrelation between the coarsening rate and the bubble mobility.

We also observed that the long relaxation times of wavevectors q corresponding to length scales above the bubble size prevents the study of their dynamics, as the latter starts unavoidably mixing with the coarsening kinetics: over the time at which they decorrelate, the foam structure has evolved because of coarsening, making difficult any reliable assessment from the DDM analysis, which gives a constant plateau in the q-dependency of the relaxation rates.

The physical interpretation of the power laws that we observe in the relaxation rates is still an ongoing discussion. Further analysis can be carried out in the real space with bubble tracking looking at the mean square displacements of the bubbles during coarsening. We remark that even in 3D samples, DDM probes the dynamics of the surfacial bubble layer, which could feel the effect of the glass wall. Future experimental investigation exploiting a different technique, like diffusing-wave spectroscopy, could thus reveal useful to compare and further understand the coarsening dynamics in the bulk of such systems.

9 One-step generation of aerated emulsions

9.1 Introduction

As already mentioned several times, aerated emulsions are widely encountered in different fields. Knowing the composition of such systems is fundamental to predict their behaviour: the amount of incorporated gas and the structure of the emulsion around the bubbles strongly affect their properties. Thus, parameters like the gas and oil fraction, as well as the bubble and drop size, are crucial for their characterisation. Moreover, the desired properties of such systems change depending on the final application and one has to choose a generation method able to create a product which fulfills all the requirements.

These complex systems are typically generated in two steps: either the emulsion is generated first and then aerated [68, 51, 101], as done for instance in chapters §7 and §8, or an emulsion and a foam are generated separately and then mixed [26, 50]. This is because free oil can be an effective antifoam [22], while once the oil is dispersed into well stabilised droplets, the latter can even help stabilising the overall foam [68].

In the previous chapters we have focused on foamed concentrated emulsions, to investigate the effect of the viscoelasticity of the foam liquid phase on the coarsening behaviour of such systems. We exploited the scale separation between the bubble and drop size to treat the emulsion as a continuous viscoelastic medium, thus using a "foam" approach that neglected in a sense the discrete nature of the emulsion.

We shall now have a more general attitude, privileging a description of aerated emulsions for what they actually are: double dispersions of gas bubbles and oil drops in a continuous aqueous medium. Even though we shall refer to *bubbly* and *foamed* emulsions, as if we still considered the gas to be the favoured dispersed phase, we shall use a different definition of oil fraction, equivalent to the one of gas fraction, highlighting the presence of two dispersed phases with no preference between them.

In fact, in this chapter we shall explore a new one-step generation of bubbles and drops with the double-syringe technique, the same method already used in chapters §6 and §7-8 to make aqueous foams and emulsions respectively. This time, however, the gas, oil and aqueous phases are simultaneously mixed to generate aerated emulsions in a single step. We shall probe the bubble and drop sizes resulting from this generation process at different gas and oil fractions.

While a variety of techniques to characterise emulsions and foams exist, the characterisation of composite dispersions is usually more tricky. In this chapter, we will show how laser diffraction granulometry, traditionally used for measuring the size distribution of oil

drops or gas bubbles alone, can be used to assess the typical bubble size also in double dispersions. Given the novelty in the use of this standard particle sizing technology for measuring composite systems, we will also do an in-depth characterisation of the method exploring the limits of this approach.

Part of the data presented in this chapter come from experiments carried out by Ning Jiang, visiting PhD student, during her stay in the MMOI group. The main results of this work have been published in Colloids and Surfaces A: Physicochemical and Engineering Aspects [57].

9.2 Experimental approach

In this section we report the materials and discuss the methods used for this experimental investigation. Seen the extensive use of laser diffraction granulometry in this project, in section §9.2.3 we shall first give a general overview of the technique before going into the details of the experimental protocol.

9.2.1 Materials

For this project, we use n-dodecane (99% pure, ACROS Organics) for the oil phase of aerated emulsions, while the gas phase is made of air containing traces of perfluorohexane (C_6F_{14}, Sigma-Aldrich) to slow down the coarsening thanks to its low solubility in water.

Drops and bubbles are dispersed in an aqueous matrix given by a solution of sodium dodecyl sulfate (SDS, Sigma Aldrich) dissolved in deionised water (Purelab, 18.2 MΩ) at a concentration of 20 or 10 g/L as specified further on. Such values, much higher than the critical micellar concentration of SDS, (which is 8.2 mM, roughly 2.4 g/L), provide stability to both oil/water and gas/water interfaces after their generation. All SDS solutions are freshly prepared and used within one day to avoid surfactant hydrolysis.

9.2.2 Sample generation

All samples are generated with the double-syringe technique, the same method already used for the generation of foams and emulsions as explained in sections §6.2.2 and §7.2.1 respectively. The novelty is that three fluids are now mixed all together in one step to directly generate an aerated emulsion, as depicted in figure 9.1. A syringe of total volume 10 mL (Braun, Inkjet) is partially filled with the two liquids, dodecane and SDS solution, while a second one is partly filled with the gas mixture, in proportions corresponding to the desired oil and gas volume fractions. Since the perfluorohexane is liquid at room temperature, the air was slowly bubbled through it while filling the syringe to include traces inside the gas phase. The two syringe inlets are connected and the three fluids are manually pushed back and forth through the constriction until the whole body of the syringe looks completely filled with a homogeneous mixture, typically 100 times. It has been shown that the presence of traces of C_6F_{14} allows generating aqueous foams having bubbles of 40 μm in diameter [40]. Bigger syringes of total volume 20 mL (Braun, Inkjet) are used for generating samples of which we follow the evolution over time in section §9.3.5.

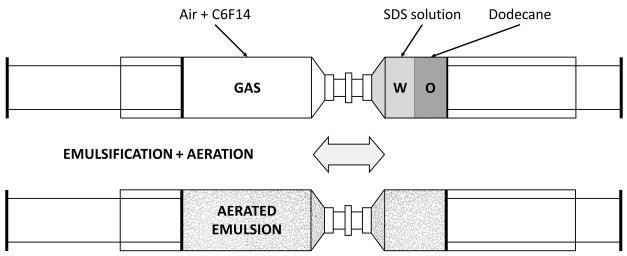

Figure 9.1 – **One-step generation.** Double-syringe method for one-step generation of aerated emulsions: the three phases are simultaneously mixed together.

9.2.3 Laser diffraction granulometry

Laser diffraction is a technique which basically measures the scattering pattern of a monochromatic laser beam by an ensemble of dispersed particles, and then converts the pattern to a particle size distribution using a model-based matrix [84]. In this section, we start by giving some insights on the technique and then explain how we apply it to measure both bubble and drop size in our aerated emulsions.

The concept

Laser diffraction is based on the measurement of the light scattered by a collection of particles to retrieve their size distribution. Before delving into a more technical description of this particle sizing method, let us briefly recall how the light interacts with a single particle.

It is well known that we can distinguish four types of interaction between light and a particle, as sketched in figure 9.2 (a):

- diffraction of light at the contour of the particle (Fraunhofer);
- reflection of light at the particle surface, both inside and outside;
- refraction of light at the interface between the particle and the dispersion medium;
- absorption of light inside the particle.

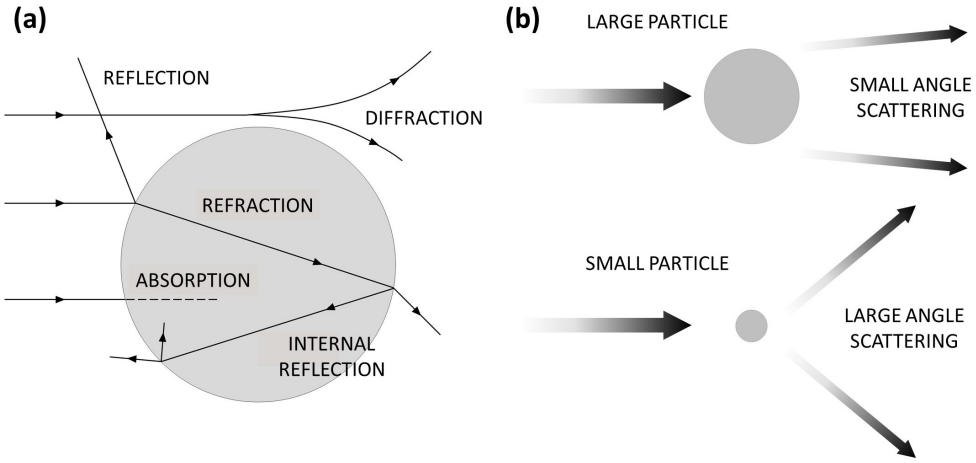

Figure 9.2 – **Light interaction with a single particle.** (a) Types of light-particle interactions. (b) Small particles scatter more light at larger angles than big particles.

The interference between these interactions gives rise to a characteristic scattering pattern in the far field, where the scattered light intensities at different angles will depend on the size, shape, and optical properties of the particle. Typically, the pattern will exhibit characteristic alternating maximum and minimum intensities, with high intensity in the forward direction and much lower intensities at larger scattering angles. The pattern will also present a certain degree of symmetry reflecting the symmetry of the original particle, that is for example circular for spherical particles.

Generally, small particles will scatter light at wider angles than big particles, as sketched in figure 9.2 (b). The dependency of the scattering pattern on the particle size is the basis for the application of the laser diffraction technique for particle sizing. The scattering pattern of an ensemble of particles is given by the sum of the patterns of each individual particle, if we can assume that multiple scattering is absent and that there is no interference between the radiation scattered by different particles. The latter condition is fulfilled if the particles move randomly with respect to each other and if the global scattering pattern is averaged over many measurements [84].

In general, the scattering intensity of unpolarized light by a single spherical particle can be written as:

$$I(\theta) = \frac{I_0 \lambda^2}{8\pi^2 a^2} \{[S_1(\theta)]^2 + [S_2(\theta)]^2\} \tag{9.1}$$

where $I(\theta)$ is the total scattered intensity at the angle θ with respect to the forward direction, I_0 is the intensity of the incident light, λ is its wavelength, a is the distance between the scatterer and the detector, and the terms $S_1(\theta)$ and $S_2(\theta)$ are dimensionless complex functions describing the change of amplitude as a function of angle and particle diameter.

Two main theories have been developed to describe and predict the angular scattering patterns. Fraunhofer theory was the first optical model used for particle size measurement. It is an approximation based on the assumption that particles can be considered as circular two-dimensional opaque disks. Moreover, it considers only the interaction of light at the edge of the particle and only the light scattered at small angles θ, which means that is suitable only for rather big particles. In such a case one could write:

$$[S_1(\theta)]^2 = [S_2(\theta)]^2 = \alpha^4 \left[\frac{J_1(\alpha \sin\theta)}{\alpha \sin\theta} \right]^2 \tag{9.2}$$

which therefore simplifies equation (9.1), yielding to:

$$I(\theta) = \frac{I_0 \lambda^2}{4\pi^2 a^2} \alpha^4 \left[\frac{J_1(\alpha \sin\theta)}{\alpha \sin\theta} \right]^2 \tag{9.3}$$

where $\alpha = \pi D/\lambda$ is a dimensionless parameter, with D the particle diameter, and J_1 is a Bessel function of the first kind of the order unity.

Despite its simplicity, Fraunhofer theory is no longer commonly used in modern instruments as it gives biased results for small transparent particles. The particle size is currently computed using Mie theory.

This model is a rigorous solution for light scattering by homogeneous spheres which takes into account all four types of light interaction. For doing so, it requires the knowledge of the optical properties of both particle and dispersing medium, in terms of a complex refractive index n^* defined as:

$$n^* = \frac{n_p - i k_p}{n_m} \tag{9.4}$$

where n_m is the refractive index of the medium, n_p is the real part of the particle refractive index, and k_p is its imaginary counterpart which basically quantifies the absorption of light from the particle.

Then, for calculating the particle size distribution, single scattering is assumed and the particles are considered to be spherical, which means that non-spherical particles would

result in a distribution of equivalent diameters depending on the particle orientation. Under these assumptions a model matrix is calculated, based on Mie theory, which provides the scattered light intensities of the different detector elements per unit of volume of a given set of particle size classes. Such scattering matrix M has the following general form:

$$M = \underbrace{\begin{pmatrix} M_{1,1} & \cdot & \cdot & \cdot & \cdot & M_{1,m} \\ \cdot & \backslash & \cdot & \cdot & \cdot & \cdot \\ \cdot & \cdot & \backslash & \cdot & \cdot & \cdot \\ \cdot & \cdot & \cdot & \backslash & \cdot & \cdot \\ \cdot & \cdot & \cdot & \cdot & \backslash & \cdot \\ M_{n,1} & \cdot & \cdot & \cdot & \cdot & M_{n,m} \end{pmatrix}}_{\#\text{ size classes}} \Bigg\} \#\text{ detectors} \tag{9.5}$$

where n is the total number of detectors, m is the total number of size classes, and $M_{i,j}$ is the calculated light intensity or signal of detector i per unit volume of spherical particles in the size class j.

Thus, for a given sample, the signal intensities L that will hit the set of detectors are given by multiplying the scattering matrix M and the size distribution Q, whose elements are the normalised volumes of material in each size class:

$$L = MQ \tag{9.6}$$

However, in particle sizing L is what the instrument actually measures and Q is the unknown quantity that one wants to estimate. Thus, the particle size distribution Q is obtained from the measured detector signals L by inverting the previous equation:

$$Q = M^{-1}L \tag{9.7}$$

where M^{-1} is the inverse of the model matrix M.

It is worth stressing that the fact that the matrix elements $M_{i,j}$ describe the signal intensity per unit of volume is the reason why laser diffraction is typically referred to as a volume-based technique although interfaces are at play. This justifies the choice of considering volume-weighted size distributions and corresponding moment means in the following.

The instrument

All laser diffraction measurements in this thesis are carried out with a Mastersizer 3000E equipped with a small volume Hydro SM wet dispersion unit (Malvern Panalytical). This device can probe particles of diameter ranging from 0.1 to 1000 μm. However, according to the producer, the Hydro SM dispersion unit further limits the maximum particle size to 600 μm, depending on the sample density.

The internal structure is shown in figure 9.3. A red light (wavelength 632.8 nm) from a He-Ne laser hits the particle dispersion flowing inside the measuring cell and a log-spaced array of detectors measures the scattering pattern in the far field at an angle up to 60° with respect to the forward direction. The central detector is used to calculate the obscuration, which quantifies the amount of laser light blocked by the sample and is used as a real-time guide to the particle concentration in the measuring cell.

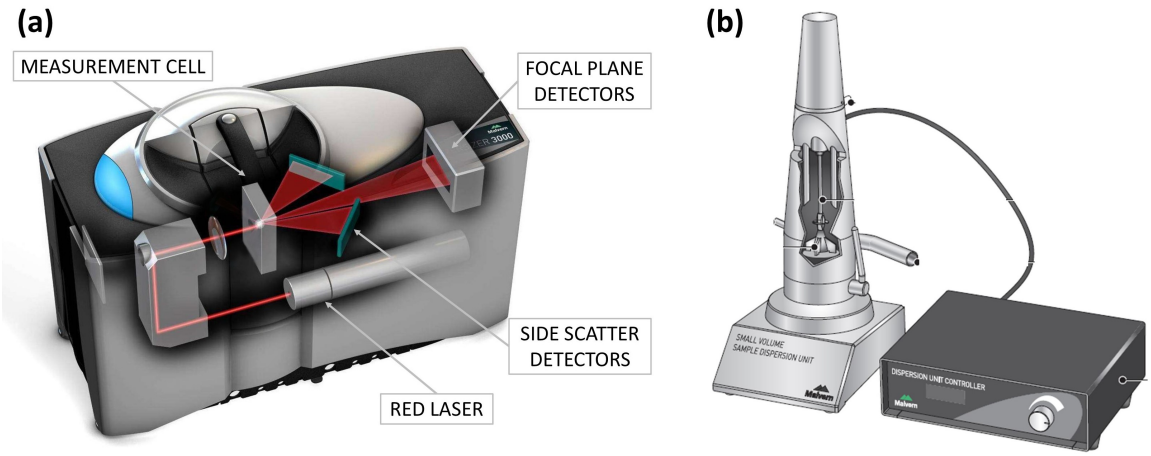

Figure 9.3 – **Mastersizer 3000E.** (a) Internal structure of the Mastersizer 3000E. Picture adapted from Malvern training class slides. (b) Scheme of the Hydro SM dispersion unit with its flow speed controller. Picture adapted from Mastersizer 3000E user guide.

The natural particle size distribution given by the instrument is intrinsically volume-weighted [84]. However, the Malvern software can provide also the surface-weighted and number-weighted distributions, but one should be careful in using them, as they are calculated from the volume-based distribution and conversions can yield to biased results. Thus, in general it is not recommended to consider other kinds of distributions when using laser diffraction unless the main features of the particle ensemble under analysis are well known a priori or cross-checked with another more traceable technique, like microscopy.

Measuring bubbles and drops

While laser diffraction has been widely used for measuring drops and bubbles alone, it has not been used so far for characterising double dispersions of different fluids. Our aerated emulsions are dispersions of both bubbles and drops, and while we can easily get rid of bubbles for measuring the drops alone, to measure the bubble size we can not avoid the simultaneous presence of drops during the measurement.

In order to measure the bubble size, the dispersion unit is filled with SDS solution at a concentration higher than the cmc to enhance bubble stability during the flow. The stirrer speed is gradually increased from 0 to 1100 rpm to limit the unavoidable generation of millimetric bubbles inside the dispersion unit, which however burst quickly. The absence of residual undesired bubbles flowing inside the Mastersizer is checked by looking at the stability of the background signal before proceeding with the measurements.

After generation, a small amount of sample is directly dispersed inside the dispersion unit with a spatula and a sequence of 5-second measurements is started immediately. Five consecutive distribution curves, corresponding to the highest signal-to-noise ratio in the raw intensity data, are considered and averaged to get the final size distribution.

During these measurements, the light is scattered from both oil drops and gas bubbles. The Mastersizer will therefore detect the overall scattering pattern and convert it into a size distribution, which will exhibit two different peaks corresponding to the two different scatterers, as it will be clarified in section §9.3.2.

By contrast, for a proper measure of the drop size distribution, part of the sample is

first prediluted in pure water. This allows getting rid of the bubbles as they are lighter and quickly rise to the surface and burst. A few drops of the diluted mixture are then gradually added to the dispersion unit, this time filled with pure water, until an appropriate obscuration level is reached. Then a sequence of five 10-second measurements is started immediately and averaged to get the final size distribution.

The size distribution in both cases is calculated by the software with Mie theory, which requires the input of the complex refractive index of both dispersed and dispersant fluids. Thus, in the first case, we use the refractive index of air, which is 1: indeed, despite the simultaneous presence of drops, we use those measurements for assessing only the bubble size. By contrast, for the independent measurements of the drop size distribution we use the refractive index of dodecane, which is 1.42. The absorption parameter of the dispersed phase is set to 0.001 in both cases, as normally suggested for liquid dispersions. The refractive index of the dispersant is kept equal to 1.33 like pure water, we thus neglect the presence of surfactant in the first case.

9.2.4 Optical microscopy

Optical microscopy is traditionally used whenever a direct visualisation of the sample is required. However, aerated emulsions are highly turbid when looked at under the microscope, due to the multiple light scattering from bubble and drop interfaces. For this reason, an accurate measurement of drops and bubbles in three dimensional samples via imaging is usually a hard task.

Concerning the drops, the small difference between the refractive index of water and oil makes optical microscopy not ideal to measure the drop size distribution as, although visible, the lack of contrast makes it difficult to automatically detect the contour of the drops in a reliable way during image processing. Thus, since we can easily get rid of bubbles by pre-diluting the sample in pure water, the drop size distributions will be measured only with laser diffraction granulometry.

By contrast, we use optical microscopy to measure the bubble size in a few samples, in order to compare with the results obtained from light scattering. Since in our samples bubbles and drops are tightly packed together, their shape is deformed. For this reason, to measure the bubble size with microscopy, aerated emulsions, and foams in general, need to be diluted [39]. A small amount of sample is put on a microscope slide immediately after generation and quickly diluted by pouring a few drops of SDS solution on top. The dilution must ensure a good separation between the bubbles, which thereby appear perfectly round. The diluted bubbles are then sandwiched using two glass coverslips of thickness $2h = 150$ μm as spacers and a third one on top to cover. The glass slide is put under the microscope (Keyence VHX-2000) equipped with a digital camera and a lens with adjustable magnification between 50x and 500x.

Pictures of several thousands of bubbles are then taken in light transmission configuration. The bubbles in our samples are indeed polydisperse, thus a high number of bubbles needs to be measured in order to plot a size distribution with good statistics.

Such high polydispersity also influences the choice of the lens magnification. Indeed, a high magnification is in principle needed to ensure the detection of the smallest bubbles. However, the higher the magnification the lower the depth of field (which is about 10 μm at 100x [84]), which can limit the possibility of getting sharp images of both small and big bubbles at a single magnification, as their horizontal great circles, which give the bubble

contours on the image, do not lay on the same plane and some of them might be out of focus.

Moreover, when dealing with wide size distributions it is not easy to make a true monolayer of bubbles, as tiny bubbles tend to partially overlap larger ones, further complicating their detection. A compromise is thus necessary to choose a magnification that provides an image quality good enough for an automatic detection of bubbles without losing too many tiny ones.

The bubble size is obtained by processing the pictures with Circle Finder [105], a MATLAB application based on circular Hough transform. This simple script allows detecting bubbles as circular objects from their edge intensity gradients. An example of processed picture is shown in figure 9.4 (a), where detected bubbles are outlined with red circles.

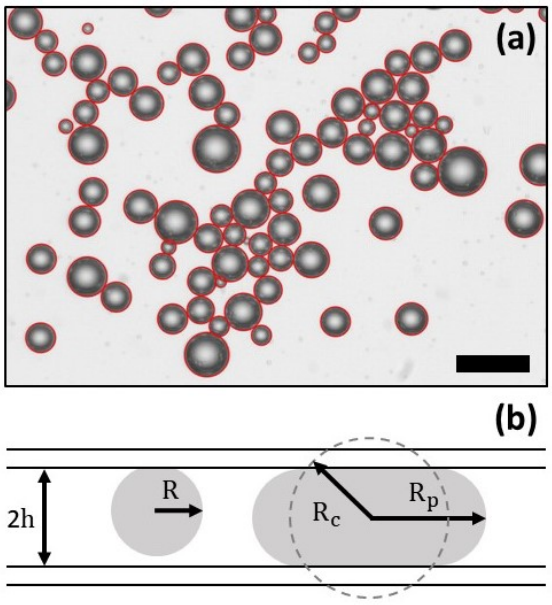

Figure 9.4 – **Optical microscopy.** (a) Example of image treatment with Circle Finder. Scale bar 100 μm. (b) Sketch of bubbles seen from a vertical section of the glass slide.

If the bubble diameter is smaller than the spacing between the glass surfaces, the diameter of the detected circle directly corresponds to the size of the bubble.

The effect of gravity at the bubble sizes considered can be neglected. In fact, it has been shown that the bubble shape is well approximated by a capped sphere as long as the bubble radius is smaller than the capillary length [39], defined as:

$$l_c = \sqrt{\frac{\gamma}{\Delta\rho g}} \tag{9.8}$$

where γ is the surface tension of the foaming solution, $\Delta\rho$ is the density difference and g is the standard gravity. With γ typically of the order of 30 mN/m and a $\Delta\rho$ equal to 1 g/cm^3, l_c is roughly 1.7 mm: thus a bubble as large as the spacing between the glass surfaces, namely 150 μm, is still much smaller than l_c and gravitational deformation is thereby negligible. Moreover, the size of the truncated part is small compared to the overall volume, thus we can assume that the radius of the capped sphere is the same as the

undisturbed and perfectly spherical bubble.

By contrast, when bubbles are bigger than the gap ($2R > 2h$), they touch both upper and lower plates and thus take a pancake shape, as the one depicted in figure 9.4 (b). The radius R_p of the circle visible in the picture and measured by the script must then be corrected as follows to recover the actual bubble size, that is given by the radius of the equivalent sphere R_c [39]:

$$R_c = \left(\left(\frac{3}{4\pi}\right)\left(2h\pi(R_p - h)^2 + \pi^2 h^2 (R_p - h) + \frac{4}{3}\pi h^3\right)\right)^{\frac{1}{3}} \tag{9.9}$$

Even though microscopy offers the advantage of a direct visualisation of the sample, it is easy to imagine how this technique is time consuming. Moreover, the time needed to prepare the glass slide and take the pictures can be a limit to the estimation of the bubble size at a given time as the sample can age during the measurement. This is why in this chapter we use this technique only for a few samples to validate the results obtained with laser diffraction, whereas the latter is then extensively used to assess the bubble size as we vary the composition of our samples.

9.2.5 Surface tension measurements

The interfacial tensions are measured with a drop/bubble shape tensiometer (Tracker® from Teclis). All measurements reported in the present thesis are carried out by Laura Wallon, assistant engineer in the MMOI research group.

Let us briefly describe how the tensiometer works. Two different configurations can be used in the Tracker: the pendant drop and the rising bubble. A sketch of both is reported in figure 9.5.

The pendant drop allows measuring the surface tension of liquids in air. A drop of liquid is formed in air with a needle and allowed to stabilise. Since gravity tends to elongate the drop whereas surface tension tends to make it spherical, the equilibrium value for the surface tension γ can be obtained by fitting the drop outline with the Laplace theoretical profile for gravity-deformed drops:

$$\gamma\left(\frac{1}{R_1} + \frac{1}{R_2}\right) = \Delta P_0 + \Delta\rho g z \tag{9.10}$$

where R_1 and R_2 are the two principal curvature radii, ΔP_0 is the pressure difference between the liquid and the gas at the bubble apex, $\Delta\rho$ is the density difference between the two phases, g is the gravitational acceleration and z is the vertical coordinate of point at the drop surface counted from the drop apex along the center line of the drop.

An analogous description holds for the rising bubble configuration as well, where a bubble of gas is generated at the tip of a U-shaped needle immersed in the liquid. The latter configuration is used also to measure the interfacial tension between two liquids, with the drop of the less dense liquid generated inside a bath of the heavier one. This geometry usually allows more stable measurements as it is not affected by evaporation.

For this project we are interested in the tensions of the interfaces between the three different phases: we call γ_{ow} the one between oil and water, γ_{gw} the one between water and air and γ_{og} the one between oil and air. All measurements are carried out at 20°C. The results are shown in figure 9.6.

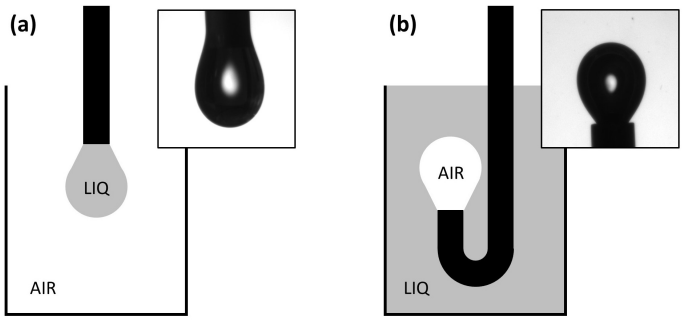

Figure 9.5 – **Interfacial tension measurements.** Scheme of the pendant drop (a) and the rising bubble (b) configurations for interfacial tension measurements. A photo of a dodecane drop in air (a) and an air bubble inside a bath of SDS solution (b) are shown as example in the squares.

The surface tension of dodecane is measured with a pendant drop configuration: a drop of oil is formed in air and allowed to stabilise for 15 minutes. At equilibrium we obtain a surface tension γ_{og} of 25.8 mN/m.

The surface tension of the SDS solution is instead measured in a rising bubble configuration. The equilibrium value measured using just air inside the bubble is equal to 33.4 mN/m. The measurement has been repeated also with a bubble of air containing traces of C_6F_{14} and a slightly lower value equal to 32.1 mN/m is registered in this case. This is because of the formation of a mixed layer of SDS and C_6F_{14} at the air/water interface [32]. Since in our samples we have traces of C_6F_{14} inside the bubbles, we consider the latter value for γ_{gw}.

The same configuration is used also for measuring the interfacial tension γ_{ow} between the oil and the aqueous phase. Since the density of dodecane is lower than the one of water, a drop of dodecane is generated inside the SDS solution. After 15 minutes, the value of γ_{ow} stabilises around 5.6 mN/m.

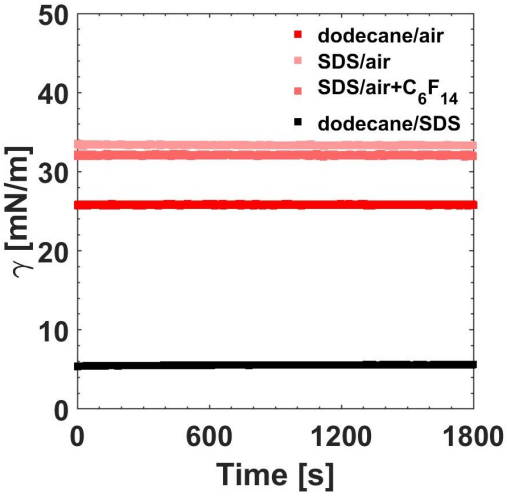

Figure 9.6 – **Interfacial tension.** Values of γ registered for the different oil/gas, oil/water and water/gas interfaces.

9.3 Results

9.3.1 Bubbly and foamed emulsions

By varying the proportion of gas and oil, we can strongly modify the structure and the properties of the final mixture. As seen in section §5.3, as we increase the gas fraction, that we recall is defined as $\phi_{gas} = V_{gas}/V_{sample}$, we gradually switch from *bubbly* emulsions at low ϕ_{gas}, to *foamed* emulsions at ϕ_{gas} above close packing. An example of a bubbly and a foamed emulsion are shown in figure 9.7 (b) and (c) respectively.

Similarly, as we vary the oil volume fraction, here defined as $\phi_{oil} = V_{oil}/V_{sample}$, we can modify the structure of the emulsion between the bubbles. More precisely, in order to know whether the emulsion around the bubbles is diluted or highly concentrated, we define the concentration of oil drops inside the emulsion matrix as $\phi_{oil}^{cp} = \phi_{oil}(1 - \phi_{gas})^{-1}$. Note that this definition of ϕ_{oil}^{cp} corresponds to the definition of emulsion oil fraction ϕ used in chapters §7 and §8.

The internal structure of the two samples shown in figure 9.7 is very different not only because of the different amount of gas but also because of the different oil concentration in the liquid phase. The bubbly sample has $\phi_{oil} = \phi_{gas}$=40%, thus the oil fraction in the emulsion matrix is ϕ_{oil}^{cp}=67% which means that the droplets are jammed. By contrast, the foamy sample has ϕ_{gas}=90% and ϕ_{oil}=1%, corresponding to a ϕ_{oil}^{cp}=10%, which means that in this case the emulsion matrix is diluted.

In this project, we consider only systems having high total internal phase fraction, defined as $\phi_{tot} = \phi_{gas} + \phi_{oil}$, namely higher than 70%. The graph reported in 9.7 (a) shows the region of ϕ_{oil} and ϕ_{gas} investigated. The solid black line corresponds to $\phi_{tot} = 100\%$, which represents the upper bound that obviously can not be crossed by experimental data. Moreover we can see that at ϕ_{gas}=90% the maximum ϕ_{oil} is 5%, as in attempts at higher ϕ_{oil} we did not manage to incorporate all the gas. We are thus not able to produce with this method dry foamed emulsions with a ϕ_{oil}^{cp} as high as the ones in chapters §7 and §8.

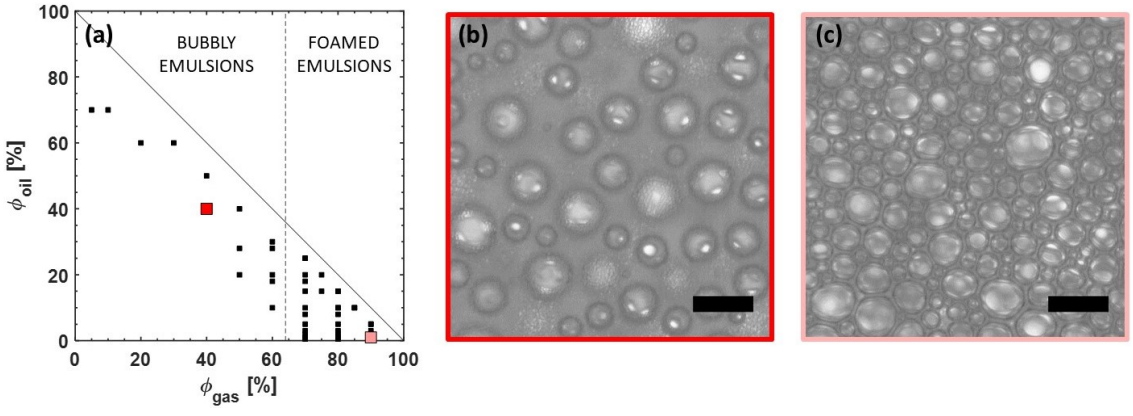

Figure 9.7 – **Bubbly and foamed emulsions.** (a) Diagram of ϕ_{oil} vs ϕ_{gas} for the samples investigated. (b) Bubbly emulsion having $\phi_{oil} = \phi_{gas}$=40% , and (c) foamed emulsion having ϕ_{gas}=90% and ϕ_{oil}=1%. Scale bars 100 μm.

9.3.2 Comparison with microscopy

We start by showing that laser diffraction allows measuring the bubble size in composite dispersions with a precision sufficient for most applications. In this section, we thus compare the bubble size distribution obtained from light scattering with the one obtained with a standard technique for measuring bubble sizes in foams: optical microscopy. We do that for three aerated emulsions having very different internal composition.

In optical microscopy, one naturally calculates the size of each single bubble, thus retrieving a size distribution in which each bubble has the same weight, namely a number-based distribution. On the other hand, we saw in section §9.2.3 that laser diffraction is volume-based.

Therefore, in order to compare the results from the two different techniques, we need to convert the number frequency distribution obtained from image processing into a volume-weighted size distribution. This can be done simply as follows. For every size class of the histogram representing the number distribution, the bin count is multiplied by the cube of the diameter corresponding to the midpoint of the respective size class. In the continuous case, this translates into:

$$\frac{\mathrm{d}V}{\mathrm{d}D} \propto \frac{\mathrm{d}N}{\mathrm{d}D} D^3 \tag{9.11}$$

where $\mathrm{d}V/\mathrm{d}D$ is the differential volume distribution f_V, $\mathrm{d}N/\mathrm{d}D$ is the differential number distribution f_N, and D^3 is the weight representing the bubble volume.

An example of different representation as number and volume size distribution for the same bubble population, measured with microscopy, is reported in figure 9.8.

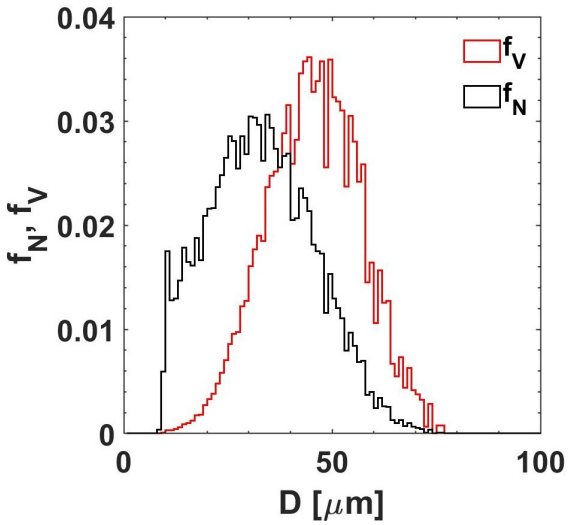

Figure 9.8 – **Frequency size distributions.** Number (black) and volume (red) distribution for the same population of 11000 bubbles measured with microscopy. One can visually see how bigger bubbles have a higher weight in f_V, as to get the latter the bin counts of f_N have been multiplied by D^3 for each size class before renormalisation.

Let us now go back to aerated emulsions. As a first sample, we consider a bubbly concentrated emulsion, containing 40% of oil and 40% of gas in volume. The global size distribution obtained from light scattering is reported as a black line in figure 9.9 (a).

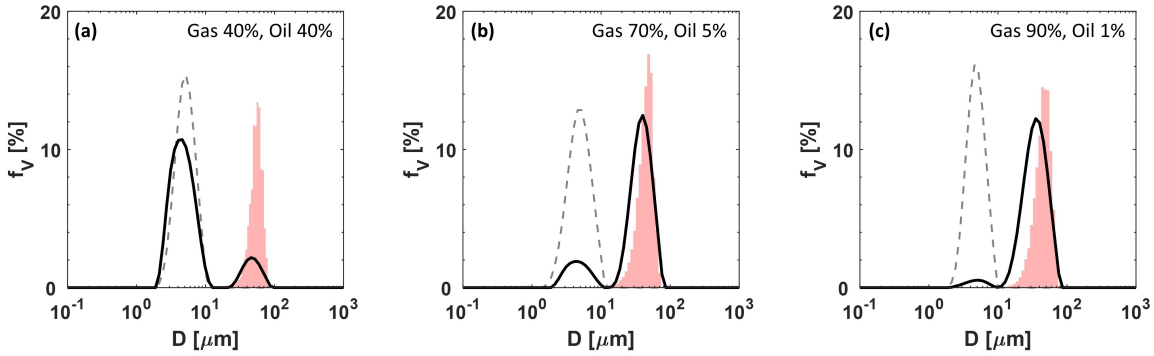

Figure 9.9 – **Comparison between light scattering and microscopy.** (a) Bubbly emulsion having $\phi_{oil} = \phi_{gas}$=40% , (b) wet foamed emulsion having ϕ_{gas}=70% and ϕ_{oil}=5% and (c) dry foamed emulsion having ϕ_{gas}=90% and ϕ_{oil}=1%. In each graph, the solid black line represents the global volume size distribution measured with light scattering for bubbles and drops together. The dashed grey line represents the drop size distribution measured independently. The pink-shaded histogram represents the bubble size distribution obtained from microscopy.

The graph shows that the Mastersizer recovers a bimodal distribution from the detected scattering pattern. Indeed, the laser beam is scattered by both gas bubbles and oil drops. The first peak appearing at around 5 μm corresponds to the size distribution of the population of oil drops. This can be seen by comparing the position of the peak with the drop size distribution measured separately, which is reported in the same graph as a grey dashed line. We can see that the two peaks are in the same position. However, to assess the average drop size in our samples we always consider the distribution measured for drops alone, in absence of bubbles, as the latter is obtained by setting the correct refractive index of dodecane.

The size distribution generated by the Mastersizer shows then a second peak at around 50 μm, which corresponds to the gas bubbles of our sample. In fact, since the drop size distribution measured independently clearly shows only one peak, we can exclude the presence of droplet aggregates which could cause a second peak at such larger size. Moreover, to ensure that the second peak is indeed caused by the scattering of bubbles, we now compare it with the volume-weighted bubble size distribution obtained with microscopy, which is plotted in the same graph as a pink-shaded histogram. We can see that once again the two peaks are in the same position.

Similar bimodal distributions are obtained also for other two samples having very different composition. The distribution for a sample containing 5% of oil and 70% of gas, that is a wet foam with a diluted emulsion as liquid phase, is reported in figure 9.9 (b), whereas the same figure in (c) shows the distribution obtained for a dry foamed emulsion having 90% of gas and just 1% of oil.

The change in the relative height of the two peaks of the bimodal distributions reflects the change in the global volumes of gas and oil inside the sample, as better explained later in section §9.3.4.

Once again, we observe an excellent agreement between the position of the first peak and the independently measured drop size distribution. A good match is observed also when comparing the bubble peaks obtained with the two different techniques, although a

small shift is observed between the two, with microscopy returning slightly bigger bubble sizes.

Let us now compare the mean bubble size obtained with the two methods. Being number-based, the natural bubble size given by microscopy measurements is the number average diameter D_{10}. But since in this case we are considering the volume distribution, we calculate the De Brouckere diameter D_{43}, defined as $D_{43} = \sum_i D_i^4 / \sum_i D_i^3$, which corresponds to a volume-weighted average. On the other hand, when performing laser diffraction, moment means like the D_{43}, as well as percentiles and mode values, are automatically provided by the Mastersizer software. However, in our bimodal size distributions, the D_{43} given by the software is no longer representative of the average bubble size in the sample, as it accounts also for the drop peak. We thus choose the mode value of the bubble peak, D_{mode}, as representative of the typical bubble size in our samples. We plot the results in figure 9.10 for the three samples.

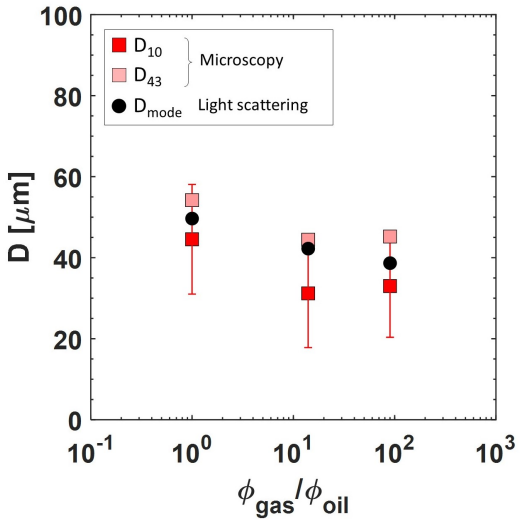

Figure 9.10 – **Mean bubble diameters.** Comparison between the typical bubble diameters obtained with the two methods for the three samples considered. We compare the number average D_{10} and the volume-weighted average D_{43} obtained from microscopy (squares), with the mode of the bubble peak measured with light scattering D_{mode} (circles). The error bar on D_{10} corresponds to the standard deviation and is reported to give an idea of the number-based distribution width.

We can see that the mode value D_{mode} resulting from laser diffraction always lays between the number average D_{10} and the volume-weighted average D_{43} obtained from image treatment, and can thus be considered a good estimate of the typical bubble size. Although very close, D_{mode} is always slightly smaller than the D_{43} measured with microscopy. We remark that the choice of D_{mode} actually underestimates the real D_{43} of the bubbles in the Mastersizer, that is the centroid of the bubble peak, as the latter has a positive skewness (see next subsection). Moreover, the bubbles measured with optical microscopy can coarsen during the sample preparation and thus the resulting size would be a bit larger.

However, the discrepancy between the bubble size measured with the two techniques, D_{43} and D_{mode}, is within the experimental error coming from the reproducibility of the samples made by hand (as for each choice of ϕ_{gas} and ϕ_{oil} two different samples must be

generated to be measured with the two methods), and the image treatment. Thus, our results show that laser diffraction allows a fast estimate of the bubble size in such complex systems, with sufficient accuracy for many applications.

The case of aqueous foams

Laser diffraction has already been used to measure bubbles alone, comparing the results with another indirect measurement of the bubble size from their rising speed in a liquid [17]. Here we now use the same light scattering protocol for measuring bubbles in aqueous foams with no oil drops in the liquid phase, and we compare the results with a more direct and well-established technique as optical microscopy.

We generate two aqueous foam samples having both $\phi_{\text{gas}} = 90\%$ using the gas mixture of air and C_6F_{14} and pushing the syringe plunger back and forth 100 times. We then measure the bubble size right after generation using light scattering for one sample and optical microscopy for the other. The volume-weighted bubble size distributions obtained with the two techniques are displayed in figure 9.11 (a), showing a good agreement.

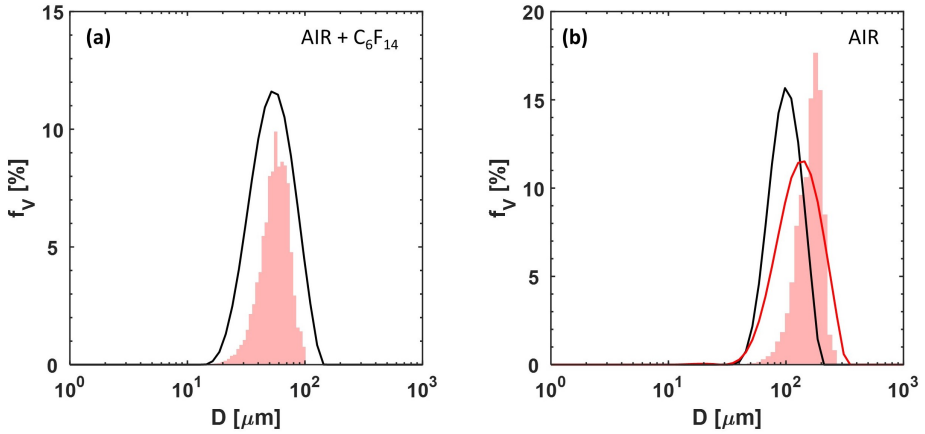

Figure 9.11 – **Bubble size distribution for aqueous foams.** (a) Bubbles containing traces of C_6F_{14}. Comparison between the bubble size distribution obtained with light scattering (black solid line) and with optical microscopy (pink-shaded histogram). 5052 bubbles have been measured under the microscope, with a resulting volume-weighted average diameter D_{43}=56.7 μm, whereas the Mastersizer gives D_{43}=60.1 μm and D_{mode}=57.7 μm. (b) Air bubbles. The size distribution obtained with microscopy (pink-shaded histogram, 6687 bubbles, D_{43}=161.3 μm) appears bigger than the one obtained from light scattering right after generation (black solid line, D_{mode}=105.6 μm and D_{43}=107.4 μm. However, the size distribution measured with light scattering one minute after foam generation (red solid line, D_{mode}=145.4 μm and D_{43}=147.8 μm) is shifted towards larger bubbles, suggesting that the shift between microscopy and light scattering results is due to foam coarsening.

Since in this case there is only a single peak, the D_{43} of the bubble size distribution is automatically given by the Mastersizer software, and is slightly higher than the mode value D_{mode}, as the distribution is positively skewed. The shape of the bubble size distribution is similar to the ones observed in foamed emulsions, which can partially explain why the bubble D_{mode} of the samples in figure 9.10 is smaller than the D_{43} measured with microscopy.

We then repeat the same experiment using only air as the gas phase of the foam. The comparison between the resulting distributions is shown in figure 9.11 (b). First, we note that the typical size of the bubbles is bigger, around 100 μm, compared to the size obtained when traces of C_6F_{14} are present. Thus, in the microscopy sample, the bubbles larger than the gap between the glass slides have a pancake shape, and their size has therefore been corrected in order to get the equivalent sphere radius [39]. We can see that this time the size distribution obtained with the Mastersizer after foam generation is smaller than the one obtained with optical microscopy. This could be due to foam coarsening occurring during the preparation of the microscopy sample, which is faster when bubbles contain only air. To check this, we prepare a second sample and this time we wait for one minute before measuring the bubble size distribution with light scattering, displayed in (b) as a red solid line. The substantial increase of the bubble size in just one minute suggests that the shift observed between microscopy and light scattering after generation is due to the faster foam coarsening occurring during the glass slide preparation, which can reasonably take one minute. Moreover, bubbles can slightly grow also after dilution as taking pictures of thousands of bubbles usually takes several minutes.

9.3.3 Bubble and drop size

Since during sample generation the three phases are mixed together in one step, emulsification and aeration are performed simultaneously. We thus probe whether and how the typical size of the so-generated drops and bubbles depends on the amounts of gas, oil and water we are mixing.

We generate many samples at different ϕ_{gas} and ϕ_{oil}, as already shown in figure 9.7, using an SDS solution at 20 g/L, and we measure the drop and bubble size with the Mastersizer for each sample. The resulting sizes are shown in figure 9.12 (a). We plot the typical bubble diameter in pink and the drop diameter in red as a function of the total internal phase fraction $\phi_{\text{tot}} = \phi_{\text{gas}} + \phi_{\text{oil}}$.

Since for the bubble size we have to consider the mode value of the corresponding peak, here called D_b, for comparison we consider the mode value, D_d, also for the oil drops, but evaluated from the drop size distribution measured independently.

As shown in the graph, this one-step generation method allows creating bubbles and drops well separated in size, with the former in a range between 30 and 60 μm, and the latter in a range between 4 and 7 μm. A calculation of the total area of interfaces per unit volume shows that the SDS concentration used ensures a complete coverage of all the oil/water and gas/water interfaces for each gas and oil volume fraction considered, thus the size of the dispersed phase in our samples is not limited by a lack of surfactant.

From figure 9.12 (a), we can see that both drop and bubble diameters globally decrease as we increase the total internal fraction ϕ_{tot}. Furthermore, when plotted in log-log scale the typical diameter decreases with approximately the same slope for drops and bubbles. Indeed, if we consider the ratio between the bubble and the drop size D_b/D_d for each sample, as shown in figure 9.12 (b), we can see that it is constant in first approximation as we vary ϕ_{tot}. Moreover, we can see that the average value is very close to the ratio between the interfacial tension γ_{gw} of the SDS/air interface, and γ_{ow} of the interface SDS/dodecane. This suggests that in this particular system and generation method, the relative size of drops and bubbles is fixed by the interfacial tension between the dispersed and the continuous phases [24].

However the vertical scatter observed for the bubble and drop diameters at a given ϕ_{tot} is still present when we consider their ratio. This fluctuation suggests that there might be an underlying dependency on the relative volume fraction of oil and gas. Indeed, for a fixed ϕ_{tot} both ϕ_{gas} and ϕ_{oil} are varied in our samples.

A detailed characterisation of the bubble and drop size variation to probe this dependency would require a finer control of the generation process, for instance by controlling the speed of the syringe plunger while mixing. However, the data show that even by hand it is possible to generate double dispersions of oil and gas by mixing all together in one step, avoiding the two traditional steps of emulsification and foaming. Moreover, the samples generated in this way exhibit a good, and in first approximation constant, size separation between the two species over a wide range of gas and oil fractions.

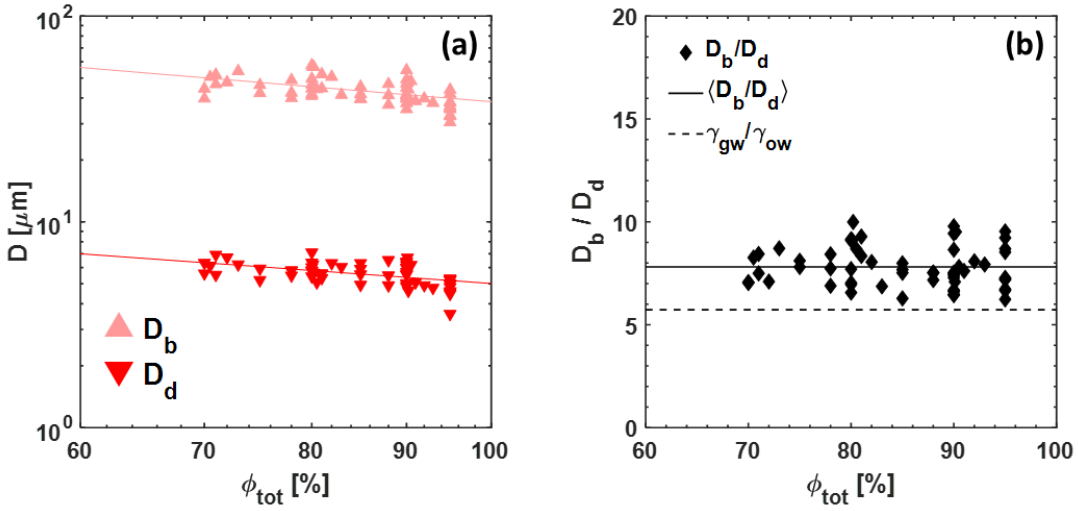

Figure 9.12 – **Bubble and drop sizes.** (a) Bubble and drop size vs ϕ_{tot}: both bubble (pink) and drop (red) diameters, taken as the mode, decrease as we increase the total internal phase fraction, and with the same slope $\simeq -0.7$ in log-log scale indicated in the graph by the two solid lines. (b) Bubble to drop size ratio. The ratio D_b/D_d is in good approximation constant and close to the ratio between the interfacial tensions γ_{gw}/γ_{ow}, where γ_{gw} corresponds to the interface between the aqueous SDS solution and air with traces of C_6F_{14}, whereas γ_{ow} to the one between the SDS solution and dodecane. The vertical scatter of the data points for a given ϕ_{tot} remains after taking the size ratio and suggests an underlying dependency of D_b/D_d on the relative proportion of gas and oil.

On the choice of the mode value

In order to compare the drop and the bubble size generated in one step, we considered the mode value of their respective size distribution. The mode value is not an average value, but for bubbles this choice was dictated by the impossibility to choose another mean diameter definition as from light scattering we obtain a bimodal distribution.

However, we saw in figure 9.11 for the case of aqueous foams, that if the size distribution is not strongly skewed, the mode value D_{mode} is not very far from the centroid of the peak given by the volume-weighted diameter D_{43}, with the mode value being slightly smaller in general due to the positive skewness.

When measuring the drop size independently, the size distribution is unimodal, thus the Mastersizer software directly provides also the De Brouckere diameter D_{43} which is the natural average to consider for a volume-weighted distribution. We can thus check if the mode value actually provides a good estimate of the actual average drop size.

In figure 9.13 we plot the correlation between the mode value D_{mode} and the D_{43} for each sample considered. We can see that D_{mode} is in general slightly smaller than the D_{43} as the drop size distributions are positively skewed. The good linear correlation between the two quantities justifies the choice of the mode value as a representative estimate of the typical drop size in our work.

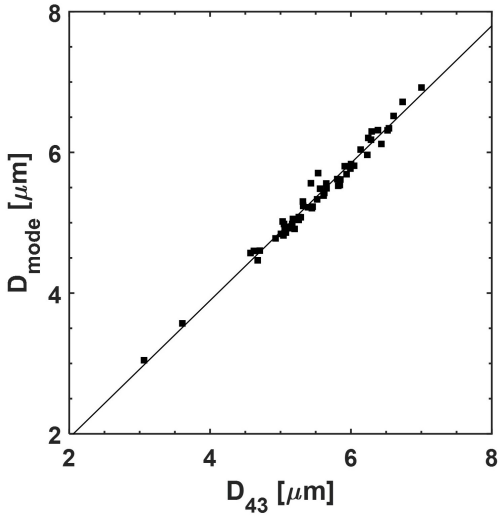

Figure 9.13 – **Typical droplet size.** Correlation between the mode value D_{mode} and the volume-weighted average D_{43} for the oil drops. The solid line corresponds to a linear fit of equation $D_{\text{mode}} = 0.976 * D_{43} - 0.008$, coefficient of determination $r^2 = 0.98$.

Bubble and drop stability during the flow

The two different scatterers in our samples present a different stability when flowing inside the Mastersizer. Indeed, despite the presence of surfactants in the dispersing solution, bubbles are more prone to coalesce during the flow. This instability causes the bubble peak to gradually shift towards bigger diameters over time and has already been observed for bubbles [17]. On the other hand, oil droplets are observed to be much more stable during the measurements.

To visualise the different stability, we compare the evolution of the distribution percentiles for bubbles and drops flowing inside the Mastersizer, as reported in figure 9.14. In particle sizing the percentiles traditionally considered are the median D(50%), the D(10%) which is sensitive to small particles, and the D(90%) which is more sensitive to large ones.

To check the stability of bubbles we consider an aqueous foam, having $\phi_{\text{gas}} = 90\%$ and $\phi_{\text{oil}} = 0\%$, to avoid the co-presence of oil drops. After generation, we disperse the sample and start a sequence of 60 short measurements of 5 seconds each, and follow the evolution of the percentiles over time. One can see in figure 9.14 (a) that the bubble size distribution is unstable: the percentiles are not constant, both D(50%) and D(90%) grow over time,

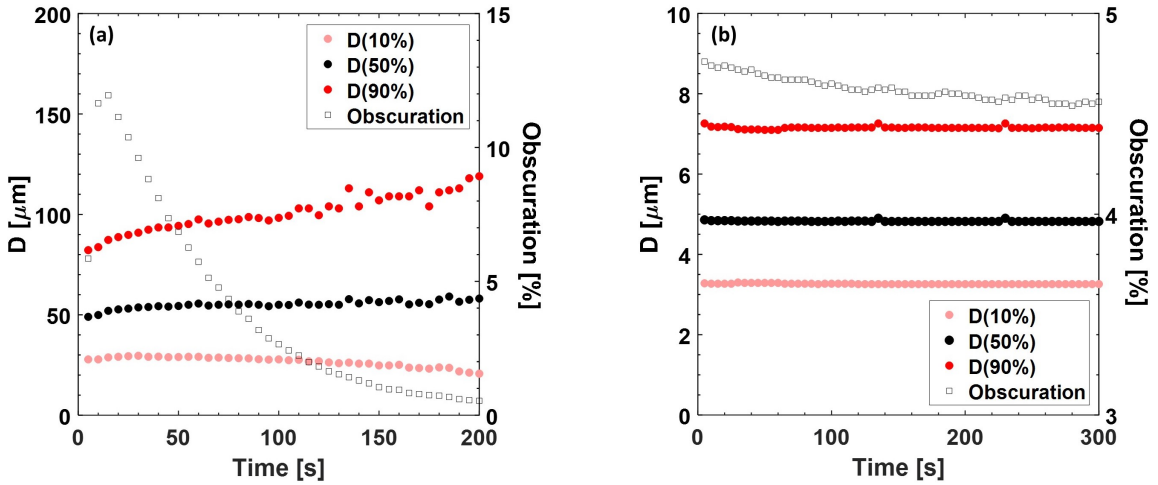

Figure 9.14 – **Bubble and drop stability during the measurement.** Percentile evolution over time for gas bubbles (a) and oil droplets (b) flowing inside the Mastersizer. The decrease of the obscuration is also reported in both cases. The graphs clearly show the higher stability of droplets.

with the former showing a 10% increase over one minute. By contrast, the value of D(10%), which considers the smaller bubbles, is initially stable and then decreases.

The increase of the average bubble size is mirrored by a simultaneous fast decrease of the obscuration, as bigger bubbles scatter less light and more light is thus able to reach the detector in the forward direction. Moreover, as the bubbles coalesce and get larger, they will tend to rise and float inside the dispersion unit, no longer carried by the flow inside the measuring cell and thus no longer detected, further reducing the obscuration. A decrease of the obscuration means a decrease of the signal-to-noise ratio in the raw intensity data which becomes too poor for a reliable measure after 100 seconds. This is why all bubble size distributions in this work have been assessed by considering only five consecutive acquisitions of 5 seconds, corresponding to the maximum signal-to-noise ratio observed at the beginning of the measurement.

For comparison, we check the drop stability over time considering a bubbly emulsion having $\phi_{\text{gas}} = \phi_{\text{oil}} = 40\%$. We measure the drop size in the same way but we first pre-dilute part of the sample in pure water before adding it to the dispersion unit, in order to get rid of the bubbles. We can see in figure 9.14 (b) that this time the three different percentiles remain constant within 1% for at least 5 minutes. Dodecane droplets are thus highly stable during the measurement despite the dilution and flow in pure water.

9.3.4 Detected volume fractions

Laser diffraction is traditionally used to measure drops or bubbles separately, but for the first time we employ it for measuring the size of dispersions of two different fluids, with different refractive indices. It is therefore natural to address the question of what are the limits of this approach. In this section we will show that this method is robust over a wide range of gas and oil volume fractions.

We saw in section §9.3.2 that, when measuring aerated emulsions with the Mastersizer, the co-presence of oil drops and gas bubbles results in bimodal size distributions, the two peaks corresponding to the population of drops and bubbles respectively. In figure 9.9 we could also notice that the height of the two peaks changes as we vary the relative oil and gas fractions of the samples. We now look at this variation in more detail.

Let us consider samples having the same ϕ_{tot}, but different ϕ_{gas} and ϕ_{oil}. In figure 9.15, for example, we plot the size distributions for different samples having all $\phi_{\text{tot}} = 90\%$.

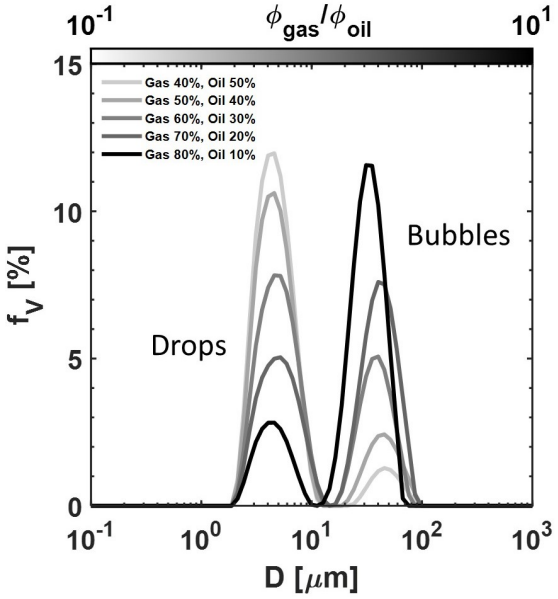

Figure 9.15 – **Relative height of the peaks.** Bimodal distributions for samples at different ϕ_{gas} and ϕ_{oil}, but constant $\phi_{\text{tot}} = 90\%$. The height of the bubble peak increases as we increase $\phi_{\text{gas}}/\phi_{\text{oil}}$, reflecting the increase of the total volume of gas at the expense of oil in our sample.

Since the bubble and drop diameters are approximately the same for each sample, as we vary the relative amounts of oil and gas we change the relative heights of the corresponding peaks without changing their positions. For instance, we can see that the sample having $\phi_{\text{gas}} = 40\%$ and $\phi_{\text{oil}} = 50\%$, plotted in pale grey, has the drop peak higher than the bubble peak. But as we gradually increase the amount of gas in our sample, at the expense of oil, we see that the height of the bubble peak increases, until it surpasses the one of oil drops. To understand this, we need to remember that these frequency distributions are volume-weighted. This means that, if we integrate the area below the curve from 0 to a certain size D_x (namely obtaining the cumulative volume distribution $F_V(D_x)$ as $f_V(D) = dF_V(D)/dD$ by definition), the result will represent the fraction of the total sample volume that has a size below D_x.

We thus expect the area below each peak to be representative of the total volume of oil and gas inside the sample. Let us define A_1 and A_2 as the areas below the drop and the bubble peaks respectively in our bimodal distributions, as depicted in figure 9.16 (a).

If the sample is well dispersed inside the Mastersizer during the measurement, we expect the ratio between the peak areas A_2/A_1 to be related to the ratio between the total volume of gas and oil inside the sample, which is known *a priori* and is given by $V_{\text{gas}}/V_{\text{oil}} = \phi_{\text{gas}}/\phi_{\text{oil}}$.

To quantify A_2/A_1 we consider the cumulative volume distribution F_V. Since the frequency distribution f_V is bimodal, F_V exhibits an intermediate plateau. The height of the inflection point h gives in our case the total volume of drops with respect to the total volume of the dispersed phase, namely $V_{\text{oil}}/(V_{\text{oil}} + V_{\text{gas}})$, whereas its complementary value $100\% - h$ gives the analogous fraction of gas. Thus the ratio A_2/A_1 is equal to the ratio $(100\% - h)/h$.

We use the data collected for the samples in section §9.3.3, which span a wide range of $\phi_{\text{gas}}/\phi_{\text{oil}}$, and measure A_2/A_1 from each bimodal size distribution. We remind that those distributions were obtained using the refractive index of air, as it is not possible to input two different refractive indexes for bubbles and drops, and what we wanted to estimate was the bubble size, so it is not the right value for the dodecane droplets.

Despite this, we show in figure 9.16 (b) that we find a robust linear correlation between the two ratios over several decades of $\phi_{\text{gas}}/\phi_{\text{oil}}$, even though the experimental data lie below the black solid line corresponding to $A_2/A_1 = \phi_{\text{gas}}/\phi_{\text{oil}}$. The systematic downward shift of the data reflects the detection of a fraction of oil drops higher than expected. This is possibly due to the use of air refractive index to measure them or the fact that their smaller size makes them easier to disperse inside the dispersion unit.

However, the observed agreement between the bubble size distributions measured with light scattering and with microscopy, shown in figure 9.9 for samples at very different $\phi_{\text{gas}}/\phi_{\text{oil}}$, proves that we still perform the measurement on a representative set of bubbles.

In samples having $\phi_{\text{gas}}/\phi_{\text{oil}}$ lower than shown, the relative amount of gas is too low and we do not observe the second peak corresponding to the bubbles. This gives us a rough limit on the minimum $\phi_{\text{gas}}/\phi_{\text{oil}}$, around 0.3, for which we can detect the bubbles in a double dispersion with the Mastersizer at these drop and bubble sizes.

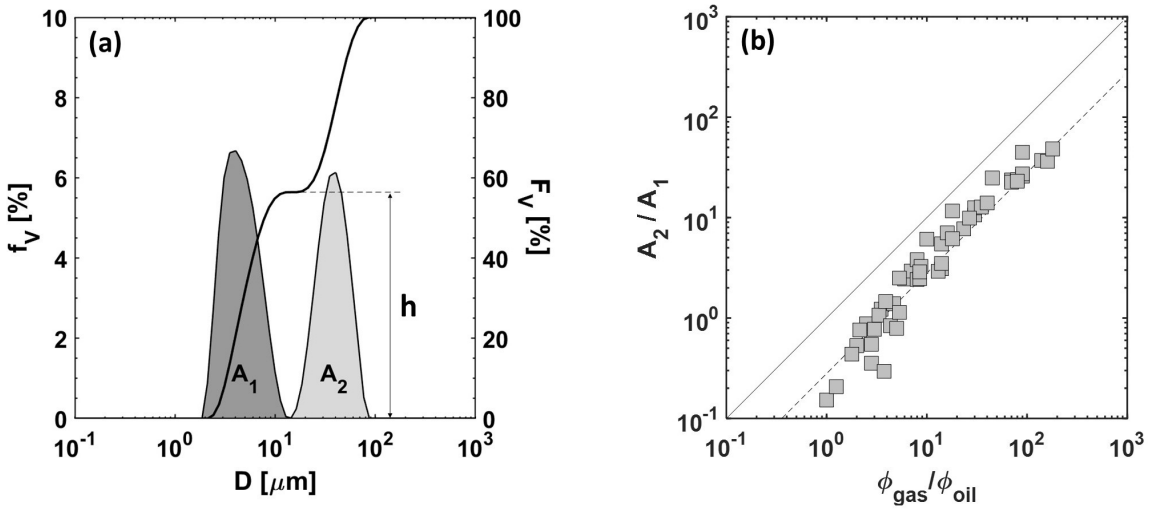

Figure 9.16 – **Detected volume fractions.** (a) Differential f_V and cumulative F_V volume distribution for a sample having $\phi_{\text{gas}} = 60\%$ and $\phi_{\text{oil}} = 20\%$. The ratio between the areas below the bubble and drop peaks is calculated as $A_2/A_1 = (100\% - h)/h$, where h is the height of the plateau in the cumulative volume distribution. (b) Correlation between the experimental ratio A_2/A_1 and the nominal ratio $\phi_{\text{gas}}/\phi_{\text{oil}}$. The solid line corresponds to the equation $A_2/A_1 = \phi_{\text{gas}}/\phi_{\text{oil}}$. The experimental points exhibit a robust linear correlation over several decades of $\phi_{\text{gas}}/\phi_{\text{oil}}$. The dashed line corresponds to $A_2/A_1 = 0.28 \cdot \phi_{\text{gas}}/\phi_{\text{oil}}$.

9.3.5 Limit on the bubble size

We have seen in §9.3.3 that the one-step generation of aerated emulsions ensures an approximately constant size ratio between bubbles and drops, with a slight decrease of both sizes with increasing ϕ_{tot}. This means that so far we have considered only bubbles within a rather narrow range of diameters, with mode values between 30 and 60 μm.

However, as we increase the bubble size we expect at some point the bigger bubbles to rise to the top surface of the dispersing solution and float without being carried by the water flow inside the measuring cell. This would clearly lead to an underestimation of the actual bubble size in the sample.

In this section, we thus explore this limit, in order to understand what is the maximum bubble size at which the measurement reliably reflects the real population of bubbles inside the sample. To this end, we exploit the coarsening process undergone by the samples to gradually increase the bubble size without varying either the drop size distribution (as the emulsion droplets are stable against coalescence and coarsening within the time scale of the experiments) or the total gas volume fraction ϕ_{gas}.

We can estimate the dispersed gas fraction as the ratio between the area below the bubble peak and the total area below the distribution, that is $\phi^A_{\text{gas}} = A_2/(A_1 + A_2) = 100\% - h$, to check if the gas fraction detected by the Mastersizer is constant. We saw in the previous paragraph that A_2/A_1 does not exactly match the nominal value $\phi_{\text{gas}}/\phi_{\text{oil}}$, and it is slightly lower. For the same reason, ϕ^A_{gas} will also be different from its nominal value given by $V_{\text{gas}}/(V_{\text{oil}} + V_{\text{gas}})$. However, here we want to check that ϕ^A_{gas} remains constant over time, independently of its initial absolute value. As the sample coarsens, the gas diffusion from smaller bubbles to larger ones makes the small bubbles shrink until they disappear, with a consequent reduction of the total number of bubbles over time and an increase of the average size of the bubbles left. But the total volume of gas and oil inside the sample is conserved, and so is their ratio. Thus, a decrease in the measured ϕ^A_{gas} could occur because of incomplete dispersion during the measurement.

We generate three foamed emulsions having all the same gas fraction $\phi_{\text{gas}} = 90\%$ but different oil fractions $\phi_{\text{oil}} = 1\%, 3\%, 5\%$. This means that we are changing only the composition of the emulsion around the bubbles by varying $\phi^{\text{cp}}_{\text{oil}} = \phi_{\text{oil}}(1 - \phi_{\text{gas}})^{-1}$ from 10% to 50%. Their different structures are shown in figure 9.18 (d, e, f). We can see that the foam liquid phase gradually becomes more turbid as we increase ϕ_{oil}, because of the presence of more oil drops in the foam Plateau borders. The SDS concentration used for these samples is 10 g/L, which is enough to ensure complete surface coverage of bubbles and drops at such dispersed volume fractions.

Thanks to their low solubility in water, the C_6F_{14} molecules inside the bubbles significantly slow down the coarsening process. However, the choice of rather dry foam samples ensures significant variations of the bubble size over the experimental time [6], whereas the presence of C_6F_{14} allows remaining within the size range explorable with the Mastersizer for at least one day.

After mixing, the samples are kept inside the syringes, which are closed and kept horizontally between the measurements to limit the effects of gravitational drainage.

For each sample, we then measure the evolution of the size distribution with the Mastersizer. The results are reported in figure 9.17 (a, b, c). The size distributions are plotted with a grey level proportional to the time elapsed after foam generation, thus the curves get darker as the foam ages. As we can see, all samples show a peak corresponding to the oil

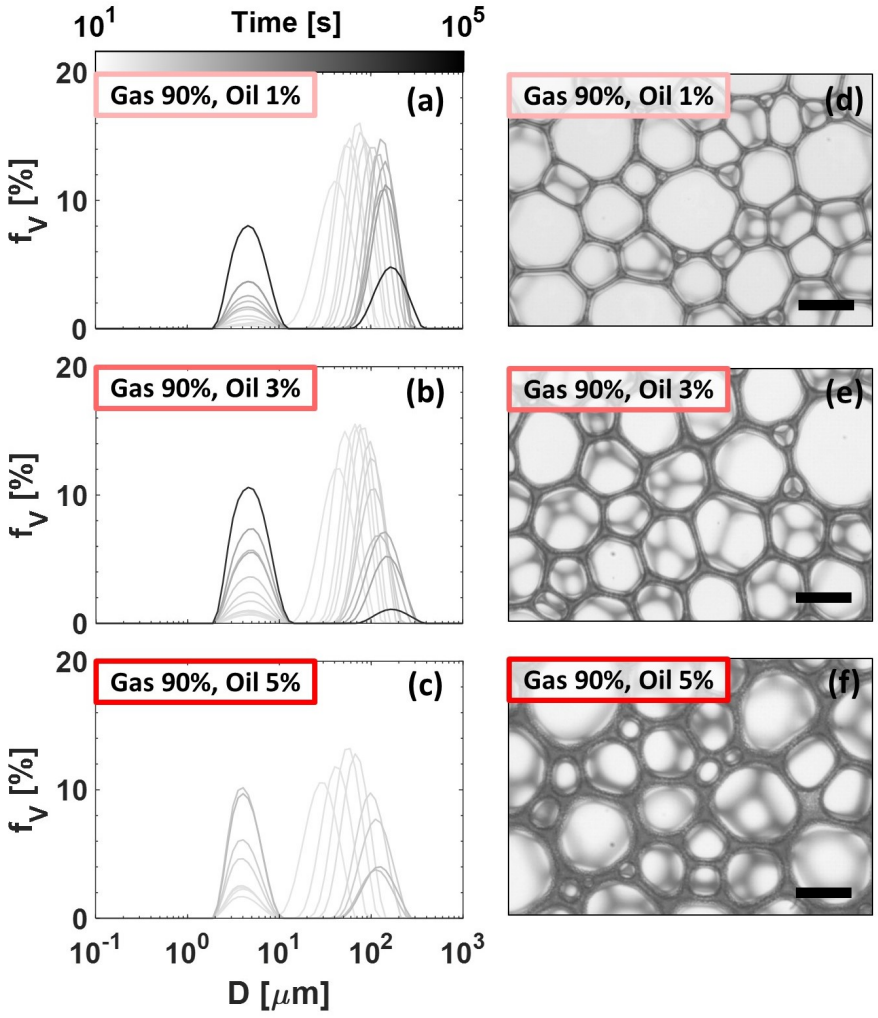

Figure 9.17 – **Coarsening samples.** (a, b, c) Bimodal distributions for different coarsening foam samples. We can see that the peak on the left corresponding to the oil drops does not move over time, as the emulsion is stable, while the bubble peak gradually move towards bigger sizes because of coarsening. (d, e, f) Pictures of the foam samples seen under the microscope two hours after generation. We can see the change of the liquid phase aspect as we gradually replace part of the aqueous phase with more oil drops. Scale bars 100 μm.

drops around 5 μm, which remains stuck in its place as the emulsion drops are stable. By contrast, the peak corresponding to the gas bubbles gradually moves towards bigger sizes over time, reflecting the bubble growth due to the coarsening process.

From each of these curves we now calculate ϕ^A_{gas} to check how it evolves as the foam coarsens. In figure 9.18 (a), we plot the evolution of ϕ^A_{gas}, normalised by its initial value $\phi^{A,i}_{\text{gas}}$, versus the bubble diameter D.

We can see that as the mean bubble size grows because of coarsening, the ratio $\phi^A_{\text{gas}}/\phi^{A,i}_{\text{gas}}$ initially remains constant, until it drops once a critical mean bubble size is reached, roughly around 100 μm. The decrease of $\phi^A_{\text{gas}}/\phi^{A,i}_{\text{gas}}$ can reflect an incomplete dispersion of the gas

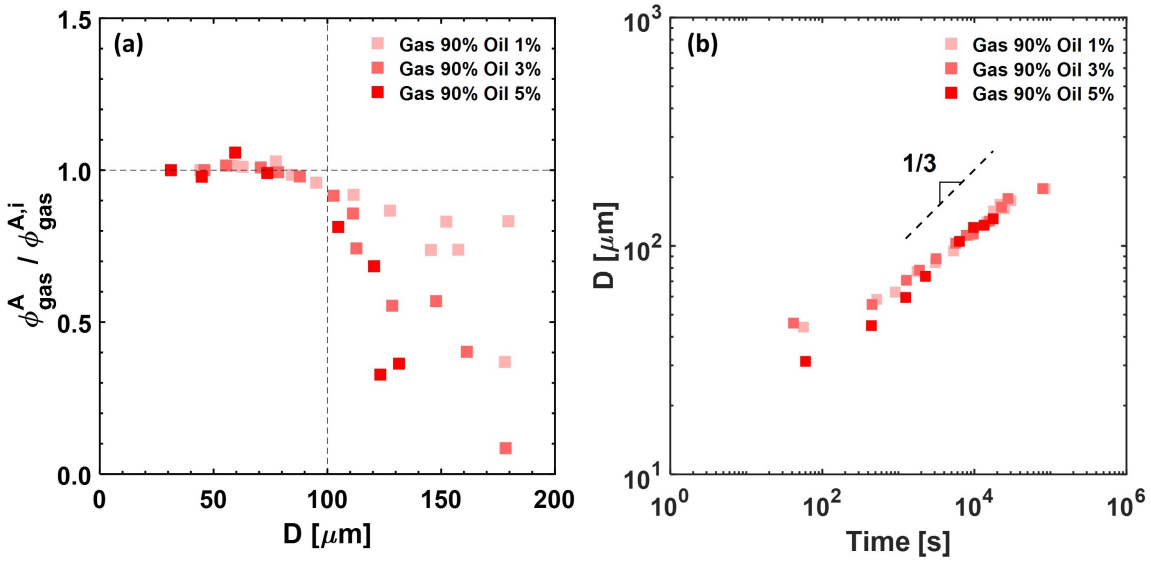

Figure 9.18 – **Limit on the bubble size.** (a) Evolution of the gas fraction as measured from the cumulative distributions. We can see that for each sample $\phi^A_{\text{gas}}/\phi^{A,i}_{\text{gas}}$ is constant and then drops as the bubble size reaches a value around 100 μm. (b) Evolution of the bubble size over time due to coarsening.

phase inside the Mastersizer: the bigger bubbles tend to rise to the surface of the dispersion unit, preventing many of them from entering the measuring cell and being detected. This means that the measured distribution might no longer be representative of the total bubble population inside the sample, and the mean bubble size taken as the mode can thus be underestimated. However, it can mirror also another effect: as the foam coarsens the total number of drops inside the sample remains constant, because they are stable, but the number of bubbles decreases over time. This means that even if we keep the ratio $V_{\text{oil}}/V_{\text{gas}}$ constant inside the sample, the ratio $N_{\text{drops}}/N_{\text{bubbles}}$ increases over time. Thus, when diluting the sample inside the dispersion unit, we increase the relative number of drops, that are more likely to enter the measuring cell as seen in the previous section.

Our results show that this method is anyway robust for bubbles up to at least 100 μm in diameter. It thus provides an efficient tool for assessing the bubble size of such systems in a range of interest for most applications.

From the coarsening measurements we can also look at the evolution of the bubble diameter over time for the three samples, which is plotted in figure 9.18 (b). No significant difference in the coarsening rate is observed between the three foam samples, despite the different composition of their liquid phase. In fact, we remind that by increasing the oil fraction ϕ_{oil} from 1% to 5%, we are actually increasing $\phi^{\text{cp}}_{\text{oil}}$ from 10% up to 50%, which means that in the latter case half of the foam liquid phase is made of oil. This suggests that, despite the solubility of air being higher in oil than in water, the presence of emulsion does not affect the coarsening process at such oil and gas fractions. The oil drops are expelled from the thin films between neighbouring bubbles and accumulate into the Plateau borders [68, 101], so that the foam coarsening is still governed by the gas diffusion through the aqueous phase. Moreover, the highest $\phi^{\text{cp}}_{\text{oil}}$ considered here is 50%, which is too low to see effects of emulsion elasticity on the coarsening process with such small bubble sizes.

The presence of poorly soluble C_6F_{14} molecules generates an osmotic pressure which opposes to the Laplace pressure differences between bubbles of different size, thus delaying the overall coarsening process [127]. In fact, we register a bubble growth slower than the power law $t^{1/2}$ predicted for dry foam coarsening, and even slower than the predicted $t^{1/3}$ for dilute bubbly liquids. Note, however, that these measurements do not allow assessing whether the samples actually attain a self-similar growth regime for which this growth law has been predicted. In fact, even if we follow the bubble size distribution over time, we have no information at all on the topology, and the presence of insoluble species can strongly affect the topological properties of the bubbles inside the foam [124, 127]. Nevertheless, similar slow coarsening in presence of C_6F_{14} has already been experimentally observed in slightly wetter foams using microscopy [85].

9.4 Conclusions

In this chapter we have seen that double dispersions of gas and oil in water can be generated by simultaneously mixing the three phases in one step. The double-syringe method allows generating gas bubbles and dodecane drops with a good size separation, without the need of pre-emulsifying and subsequently aerating the emulsion. We have shown that, for the system under study, the ratio between the bubble and drop size is constant in first approximation, although scatter in the data suggests a dependency on ϕ_{gas} and ϕ_{oil}, that would be interesting to investigate further with an automatic device to push the syringes in a more controlled way.

However, the limit in the amount of gas that can be incorporated with this method at relatively high oil fractions is one of the reasons why in chapters §7 and §8 we stuck to a two-step generation to make dry foams from highly concentrated emulsions. The other reason being the smaller size of oil droplets attainable with double-syringe emulsification in absence of air, which translates into higher emulsion elasticity for a given $\phi_{\mathrm{oil}}^{\mathrm{cp}}$.

We then used a well-established and traceable technique as optical microscopy to show that laser diffraction works very well for measuring gas bubbles, offering the advantage of being faster without reducing the accuracy. Moreover, we have shown that laser diffraction allows estimating the bubble size also in the presence of a second dispersed phase sufficiently separated in size and having a different refractive index.

In the latter case, the simultaneous light scattering of drops and bubbles results in two well-resolved peaks in the volume-weighted size distribution, which correspond to the two different populations of scatterers. Again we tested the accuracy of the light scattering results by comparing them with microscopy, finding a remarkable agreement between the volume-weighted bubble size distributions obtained from the two methods.

Furthermore, we have investigated the limits of this approach and shown that laser diffraction is robust over a wide range of volume fractions ϕ_{gas} and ϕ_{oil}. The main limit to the measurement accuracy comes from an incomplete sample dispersion inside the Mastersizer due to the rapid separation of bubbles of several hundreds of microns on top of the dispersion unit, which can lead to an underestimation of the real average bubble size of the sample.

Nevertheless, our measurements show that this method is suitable for measuring bubbles with mean diameter at least up to 100 μm, which includes the size range of interest in many common applications, like food and cosmetic products. Laser diffraction is thus an efficient tool to assess the bubble size with good precision in a few seconds both in aqueous foams and in aerated emulsions.

General conclusions

In the present thesis we experimentally investigated the pressure-driven ripening of foams in both aqueous surfactant solutions and dense viscoelastic emulsions.

In the first place, we started by probing the impact of a constant liquid fraction on the coarsening rate of quasi-2D aqueous foams, in which both gravitational drainage and coalescence are negligible. In chapter §6, after checking that the foams attained their self-similar growth regime, we experimentally showed how the progressive swelling of the surface Plateau borders, which gradually reduces the area of the vertical thin films between the bubbles, results in a slowing down of the coarsening rate over time. We showed that as long as we are far away from the transition at which the thin films vanish, the growth of the mean bubble area can be described with a simplified border-blocking model which neglects the gas transfer through the Plateau borders. As we approach the critical point at which the vertical films reduce to lines of zero height, the bubble shapes start playing a fundamental role in the overall evolution. This research work can be extended by performing imaging experiments to probe the foam structure at the scale of a few bubbles, in order to extract reliable quantities on their shape. Further modelling is however necessary to describe the behaviour of such foams close to the unjamming point, as when going from a single bubble to the global foam evolution, the predictions in the literature assume hypothesis which hold only for rather dry foams and thus fail for very wet ones [104].

After that, we probed how a viscoelastic medium between the bubbles impacts the foam coarsening process. To this end, in chapter §7 we used the same quasi-2D configuration to monitor the evolution of foamed concentrated O/W emulsions. By varying the emulsion mechanical properties via their oil volume fraction, we showed that an increase of the continuous phase elasticity causes a dramatic reduction of the foam coarsening rate. The time evolution of the bubble size distributions reveals that the slow mean bubble growth is due to a delay in the shrinkage and consequent disappearance of small bubbles.

The observation of such a slow coarsening process indeed comes together with a deep change in the foam structure. The initial foam polydispersity results in heterogeneous bubble growth which eventually leads to a segregation of smaller bubbles into regions wrapped by chains of larger ones. The onset of this heterogeneous foam structure is at the origin of the hindered coarsening process, as the accumulation of small bubbles translates into regions of different local foam elasticity which oppose to bubble size variations. This effect is enhanced by the liquid fraction inhomogeneity, as the clusters of small bubbles are wetter, which further increases the differences in the local foam rheology. Preliminary results on wetter foamed emulsions suggest that the liquid fraction plays indeed an important role in the evolution of such systems: future experiments in which the liquid fraction is systematically varied could thus reveal enlightening to further understand its role on the structure evolution.

At high oil fractions, the bubble pattern gradually developed by the foam exhibits bubbles which appear highly unrelaxed, with atypical Plateau border shapes. A characterisation of the bubble and Plateau border structures could provide a better understanding of the local foam behaviour, and it can be carried out with imaging experiments at the scale of a few bubbles. This could be better accomplished by changing the emulsion composition in order to make them transparent: index-matched emulsions would allow to see what happens between the bubbles and to pinpoint the real bubble contacts, which was here prevented by the typical white turbidity of the emulsion inside the Plateau borders.

Experiments performed at high oil fractions at different cell thicknesses showed that the foam structure evolution is qualitatively the same, but that the mean bubble size at which we start observing an anomalous accumulation of small bubbles depends on the level of confinement. This is interesting as, by contrast, the bubble dynamics does not seem to be substantially influenced by a different confinement.

Indeed, in chapter §8 we studied the coarsening dynamics in foamed emulsions both in 3D and in quasi-2D systems. The dynamics of 3D foamed emulsions was investigated with a tracking-free technique which examines the correlation between pictures at different time delays in the reciprocal space. The analysis revealed that the bubble movements in coarsening foamed emulsions are hindered, and as the oil fraction is increased, the bubbles just shrink or grow without moving significantly from their initial positions. We noticed that this suppression of the bubble movements at high oil fractions, which is mirrored by the gradual loss of two well-defined dynamical regimes in the measured relaxation rates, occurs both in 3D and quasi-2D systems well before the appearance of the unrelaxed bubble shapes typically observed at late coarsening stage.

The comparison between the rate of bubble rearrangements quantified in quasi-2D samples at different oil fractions and their overall coarsening rate, suggests a possible decorrelation between the latter and the bubble mobility. Since bubble monolayers offer the advantage of a direct comparison between the reciprocal and the real space, further analysis can be carried out in such systems by tracking the bubbles and look at their mean square displacement during coarsening, to help in the interpretation of the power laws observed in the relaxation rates.

We remark that in both 3D and quasi-2D samples, we probed the dynamics of a bubble layer in contact with one or two solid walls. To check the influence of this solid wall on the bubble motion, it would thus be interesting to compare these results with the coarsening dynamics in the bulk. To probe the latter, one can overcome the natural turbidity of these systems by using diffusing-wave spectroscopy [91, 90, 128], a photon-correlation technique that exploits the multiple light scattering to extract information not only on the bubble rearrangements but also on the bubble size evolution [30, 29, 118]. This technique however works under the assumption that the propagation of light through the sample can be described as a diffusion process: each photon must be scattered many times before exiting the sample and being detected. This requires the cell thickness to be much larger than the photon mean free path, which is known to be inversely proportional to the mean bubble size [118]. In our systems the latter becomes very quickly millimetric, which means that centimetric cell thickness should be used to fullfil the diffusive hypothesis. Moreover, one should also consider that the presence of oil droplets in the liquid phase of foamed emulsions, and their rearrangements, also contributes to the light scattering and temporal fluctuations. The use of transparent emulsions can thus prove useful also in this case to isolate the rearrangements of the bubbles from the ones of the oil droplets. Finally, we re-

mark that the slow dynamics observed in foamed emulsions at high oil fractions makes such systems non-ergodic, requiring the use of either a multi-speckle configuration [96, 16, 3, 119] or another solution to randomise the photon paths before their detection [103, 129, 130, 94].

In the final part of the thesis, we investigated a new way to generate aerated emulsions. In chapter §9 we showed that, despite the potential antifoam activity of free oil, aerated emulsions can be generated by simultaneously mixing the aqueous, oil and gas phases in one step. The double-syringe method allows generating these systems over a wide range of oil and gas fractions, providing a good separation between drop and bubble size in the final product. The ratio between their sizes, which is in first approximation constant, clearly exhibits a spread for a given total dispersed phase fraction that suggests an underlying dependency on the relative amounts of oil and gas. It would thus be interesting to systematically explore this effect further, by using an automatic device to push the syringe plungers with a controlled speed. We also showed how, under certain conditions, one can extend the use of laser diffraction for measuring gas bubbles in these composite dispersions, with the relevant advantage of having a fast measurement without any loss in the accuracy, as shown by the remarkable agreement of light scattering results with the ones obtained with a commonly used direct technique as optical microscopy. Laser diffraction thus shows to be an efficient time-saving tool to assess the typical bubble size in the system with good precision.

Appendices

A Résumé de la thèse

Les mousses sont des dispersions de bulles de gaz dans un milieu continu. Leur structure cellulaire typique leur confère une légèreté et des propriétés mécaniques particulières qui sont exploitées dans de nombreuses applications industrielles.

Leurs propriétés mécaniques et leur stabilité dépendent principalement de la taille et de la densité de ces poches de gaz, mais un rôle crucial peut également être joué par la nature du milieu continu. En effet, la matrice parmi les bulles peut être liquide, mais aussi solide ou encore un matériau composite caractérisé par une rhéologie complexe.

Alors que les mousses solides, qui ont autant d'applications que leurs homologues liquides, sont clairement des systèmes statiques, les mousses liquides sont intrinsèquement instables. En effet, lorsque leur phase continue est liquide, ces systèmes éphémères subissent différents mécanismes qui tendent à modifier leur structure au cours du temps et conduisent finalement à une dégradation irréversible de la mousse.

Même si de nombreux travaux ont été menés au cours des dernières décennies pour comprendre la stabilité des mousses aqueuses, ce qu'il se passe lorsque la phase continue est un fluide complexe est une question plus récente qui n'est pas encore totalement comprise. Néanmoins, étudier comment contrôler la stabilité de la mousse dans des systèmes plus complexes peut être utile par exemple dans le stockage de nombreux produits alimentaires aérés ainsi que dans la conception de nouveaux matériaux alvéolaires solides à structure interne bien contrôlée.

Dans la première partie de la thèse, nous donnons un aperçu général de l'état de l'art concernant la stabilité des mousses dans des solutions aqueuses simples mais aussi dans des milieux plus complexes. Parmi les trois mécanismes différents qui peuvent déstabiliser ces systèmes multi-échelles, nous nous concentrons sur le processus de mûrissement induit par les différences de pression, qui fait lentement diffuser le gaz des petites bulles aux plus grosses, entraînant une augmentation de la taille moyenne des bulles au cours du temps.

Si les effets du mûrissement sont bien compris théoriquement et vérifiés expérimentalement dans les deux cas extrêmes que sont les dispersions de bulles très sèches et très humides, il manque encore une description unifiée de ce qu'il se passe pour les fractions liquides intermédiaires. Le mûrissement des mousses a été étudié depuis plusieurs années dans ce que l'on appelle des mousses quasi-2D, à savoir des monocouches de bulles pressées entre deux plaques en verre (voir figure A.1 (a,b)), car elles permettent d'éviter les effets du drainage gravitationnel et, en même temps, simplifient fortement la caractérisation de la mousse par imagerie, car chaque bulle dans l'échantillon est visible et facilement mesurable.

Quand ces systèmes sont très secs, leur mûrissement est bien décrit par la loi de Von Neumann, qui prédit le taux de variation de la taille d'une seule bulle en fonction de sa topologie : le nombre de ses voisins détermine si la bulle se rétracte ou grandit, tandis que l'amplitude du taux dépend également de la physico-chimie de la mousse. Cependant,

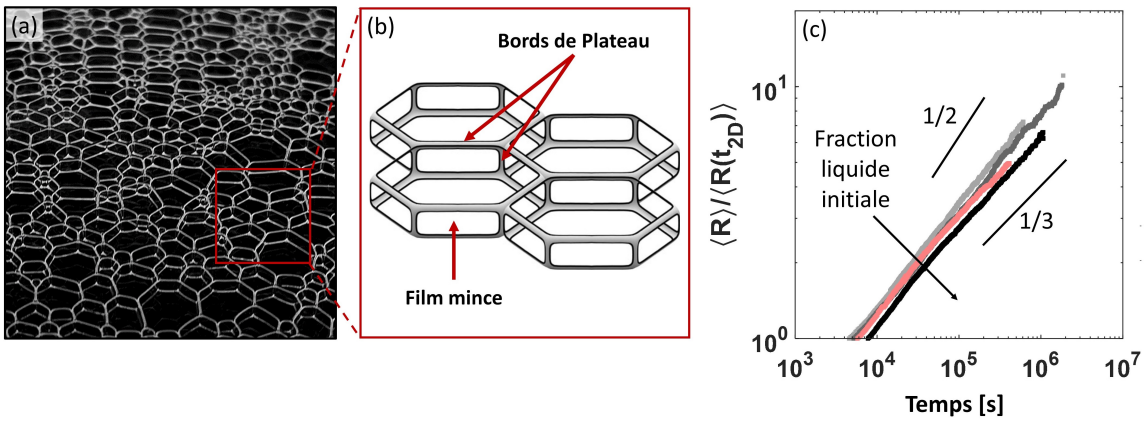

Figure A.1 – **Mousses aqueuses quasi-2D.** (a) Vue latérale d'une monocouche aqueuse de bulles. (b) Illustration de la structure 3D d'une mousse quasi-2D. Les bulles adjacentes sont séparées par de minces films verticaux, délimités par les bords de Plateau. (c) Évolution temporelle du rayon moyen des bulles (normalisé) pour différentes fractions initiales de liquide. La combinaison du mûrissement et de l'évaporation donne lieu à des lois de puissance robustes entre les deux limites prévues pour les mousses sèches (1/2) et les liquides bulleux (1/3).

dès que l'on ajoute du liquide à la mousse, des déviations de cette loi sont typiquement observées.

En effet, à des fractions liquides intermédiaires, leur structure tridimensionnelle joue un rôle crucial dans leur évolution, car les différentes teneurs en liquide déterminent la surface des films minces verticaux entre les bulles adjacentes. A notre connaissance, il n'existe pas dans la littérature d'expériences testant systématiquement l'effet d'une fraction volumique de liquide croissante, mais constante dans le temps, dans de tels systèmes.

Dans le chapitre §6, nous avons donc sondé expérimentalement le mûrissement de mousses aqueuses quasi-2D scellées. Après avoir vérifié que les mousses sont dans leur régime de croissance auto-similaire, nous avons montré expérimentalement que la réduction graduelle de la surface du film vertical mince au fil du temps entraîne un ralentissement du taux de mûrissement global au cours du temps. Nous avons montré qu'un modèle simplifié, qui néglige totalement le transfert de gaz à travers le bords de Plateau, est capable de décrire la croissance moyenne réduite des bulles tant que nous sommes loin de la transition à laquelle les films minces disparaissent.

Cependant, dès que l'on approche le point critique où les films minces se réduisent à des lignes de hauteur nulle, la diffusion de gaz à travers le volume de liquide ne peut plus être négligée, afin d'éviter de prédire un arrêt non physique du grossissement. L'étude du "unjamming" des bulles dans nos expériences a été en partie freinée par le début de l'évaporation qui élimine progressivement le liquide de la mousse, contrebalançant partiellement le gonflement des bords de Plateau. La combinaison du mûrissement et de l'évaporation donne lieu à des lois de puissance robustes pour la croissance des bulles qui peuvent être trompeuses (voir figure A.1 (c)), car il n'y a aucune justification théorique pour qu'un système quasi-2D à régime de fraction liquide intermédiaire évolue dans le temps comme une loi de puissance avec un exposant dépendant de la fraction liquide. Malgré l'évaporation, nos résultats montrent que le taux de croissance moyen des bulles pour les différents échantillons n'est dicté

que par la hauteur du film mince. Une modélisation plus approfondie est toutefois nécessaire pour décrire la croissance moyenne des bulles de ces mousses à proximité du jamming car les prédictions de la littérature concernant l'évolution globale de la mousse reposent sur des hypothèses qui ne sont valables que pour les mousses plutôt sèches et qui échouent donc pour les mousses très humides.

Nous avons ensuite étudié ce qu'il se passe lorsque nous modifions la rhéologie du fluide entre les bulles, afin de mettre en lumière le lien entre ses propriétés mécaniques et le mûrissement de ces monocouches de bulles. Dans de nombreuses applications, en effet, la phase liquide des mousses n'est pas une simple solution aqueuse, mais peut être elle-même un matériau complexe, caractérisé par un comportement rhéologique non-newtonien. Même si les mousses constituées de fluides complexes sont omniprésentes dans le vie quotidienne, les conditions de leur stabilité sont encore peu comprises. Cependant, les propriétés mécaniques du fluide entre les bulles peuvent jouer un rôle fondamental dans la stabilisation globale du système.

Afin d'étudier l'impact de la présence d'un milieu viscoélastique parmi les bulles sur le taux de grossissement de la mousse, nous avons utilisé des émulsions huile-dans-eau concentrées comme phase continue de nos mousses. Comme les mousses, les émulsions sont constituées de gouttelettes d'huile dispersées dans une solution aqueuse de tensioactifs, et si la fraction volumique des gouttelettes est supérieure à celle d'un compactage, ces dispersions biliquides denses sont viscoélastiques. Dans le chapitre §7, nous avons ainsi sondé l'évolution des émulsions denses moussées, en utilisant la même configuration quasi-2D que pour les mousses aqueuses du chapitre §6 : la séparation d'échelle entre les gouttes et les bulles dans nos systèmes permet de voir l'émulsion comme un milieu viscoélastique continu parmi les bulles. Les propriétés mécaniques des émulsions concentrées dépendent principalement de la fraction liquide des gouttes, ce qui signifie que nous pouvons régler leur élasticité en faisant simplement varier la quantité relative d'huile dispersée. De plus, leurs modules d'élasticité typiques se situent dans une plage dans laquelle nous nous attendons à voir un effet de leur élasticité sur le processus de grossissement, car ils sont plus élevés que les pressions capillaires typiques des bulles dans nos mousses quasi-2D.

Nos expériences ont montré que le mûrissement dans les mousse d'émulsions est fortement affecté par la viscoélasticité de la phase continue. L'augmentation de la fraction de gouttelettes d'huile, et donc de l'élasticité de l'émulsion, provoque une forte réduction du taux de grossissement de la mousse (voir figure A.2 (a)).

L'évolution dans le temps des distributions de taille des bulles révèle que la lente croissance moyenne des bulles est due à un retard dans le rétrécissement et la disparition consécutive des petites bulles. L'observation d'un tel processus de mûrissement lent s'accompagne en effet d'un changement profond dans la structure de la mousse : la polydispersité initiale de la mousse entraîne une croissance hétérogène des bulles qui conduit finalement à une ségrégation des petites bulles dans des régions enveloppées par des chaînes de grandes bulles interconnectées (voir figure A.2 (b,c)). L'apparition de cette structure hétérogène de la mousse contribue à empêcher le processus de grossissement, car l'accumulation de petites bulles se traduit par des régions d'élasticité locale différente de la mousse, ce qui s'oppose aux variations de taille des bulles. Cet effet est renforcé par l'inhomogénéité de la fraction liquide, car les clusters de petites bulles sont plus humides, ce qui augmente encore les différences dans la rhéologie locale de la mousse. À des fractions d'huile élevées, la mousse développe progressivement une structure dans lequel les formes des bulles ne sont pas du tout relaxées, ressemblant à la structure typiquement observée dans les solutions de

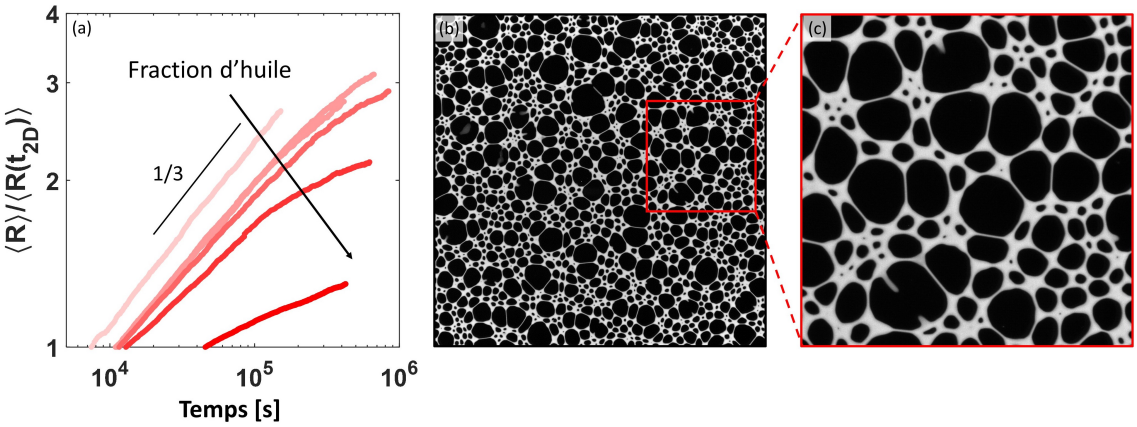

Figure A.2 – **Mousses des émulsions quasi-2D.** (a) Évolution temporelle du rayon moyen des bulles (normalisé) pour différentes fractions d'huile dans l'émulsion entre les bulles. L'élasticité de l'émulsion entraîne une croissance moyenne des bulles plus lente que la prédiction pour les liquides bulleux, même si des films minces entre les bulles sont toujours présents. (b) Structure de stade tardif de l'échantillon ayant une fraction d'huile égale à 80%. La structure hétérogène composée de régions plus humides de petites bulles séparées par des chaînes de bulles plus grosses se traduit par des régions d'élasticité locale différente de la mousse, ce qui est à l'origine du lent grossissement observé. Taille du bord de la photo 15 cm. (c) L'agrandissement de l'image montre les formes de bulles étirées. Taille du bord de la photo 5 cm.

polymères subissant une séparation de phase viscoélastique.

Après avoir caractérisé la croissance moyenne des bulles dans ces systèmes, nous avons porté notre attention sur leur dynamique de mûrissement. Il est bien connu que le processus de mûrissement modifie constamment la configuration des contraintes à l'intérieur de la mousse. En effet, les variations de taille des bulles donnent lieu à des champs de déformation qui font que les bulles se déplacent de manière persistante dans une direction, jusqu'à ce que des contraintes localement déséquilibrées à l'intérieur de la mousse finissent par les réarranger.

Dans le chapitre §8, nous avons donc étudié comment la présence d'une émulsion viscoélastique parmi les bulles affecte leur mouvement pendant le mûrissement. Nous avons sondé la dynamique de mûrissement des mousse d'émulsions dans des systèmes 3D, dans lesquels la taille des bulles est beaucoup plus petite que l'espace entre les cellules, et dans des configurations quasi-2D, en donnant également un aperçu de ce qu'il se passe lorsque le système transite entre ces deux régimes. La contrainte seuil de l'émulsion parmi les bulles permet de retarder le drainage gravitationnel dans ces systèmes, de sorte que nous disposons d'une plage de temps dans laquelle la fraction liquide et la distribution de la taille des bulles peuvent être considérées comme homogènes à l'intérieur des échantillons 3D et nous pouvons sonder leur mûrissement.

Si la croissance de la taille moyenne des bulles a été mesurée par segmentation d'images, la dynamique des bulles a été étudiée à l'aide d'une technique appelée microscopie dynamique différentielle (DDM), capable de donner un aperçu de la dynamique de l'échantillon en examinant les corrélations du domaine de Fourier entre les images séparées par des intervalles de temps croissants. Notre analyse a révélé que les mouvements des bulles dans

les émulsions moussées sont entravés, car le mouvement persistant des bulles s'arrête à une échelle de longueur qui n'est qu'une fraction de la taille des bulles, donc plus petite que celle observée dans une mousse à raser traditionnelle.

Cette suppression des mouvements des bulles à des fractions d'huile élevées, reflétée par la perte graduelle de deux régimes dynamiques bien définis dans la dépendance de q des taux de relaxation mesurés, se produit à la fois dans les systèmes 3D et quasi-2D, et également pendant la transition entre les deux configurations. Ce comportement dans le domaine de Fourier est confirmé par des observations visuelles dans l'espace réel : à des fractions d'huile élevées, les déplacements et les réarrangements des bulles semblent empêchés, et les bulles croissent ou rétrécissent simplement sans se déplacer de manière significative de leurs positions initiales (voir figure A.3 (a,b)).

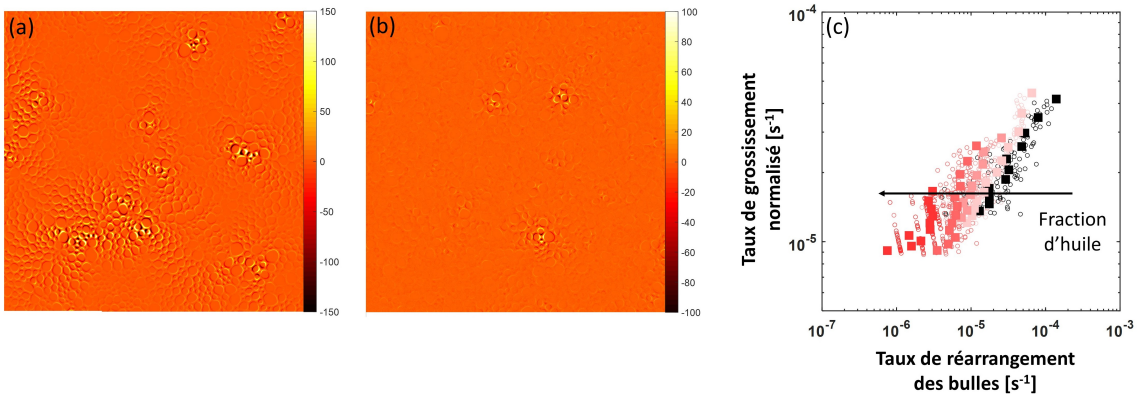

Figure A.3 – **Dinamique des bulles.** (a,b) Carte de corrélation pour deux images séparées par trois minutes, au même âge de mousse de cinq heures, pour les échantillons ayant une fraction d'huile de 65% (a) et 80% (b). Nous pouvons voir plus de réarrangements dans (a) que dans (b), mais aussi que si dans (a) ces réarrangements provoquent le déplacement de nombreuses bulles dans l'échantillon, dans (b) les bulles plus éloignées du lieu de réarrangement restent bloquées à leur place. (c) Comparaison de la vitesse de mûrissement et du taux de réarrangement des bulles dans des mousses d'émulsions quasi-2D à différentes fractions d'huile. Le glissement entre les courbes suggère une décorrélation entre les deux taux.

La comparaison entre le taux de réarrangement des bulles, quantifié dans les échantillons quasi-2D à différentes fractions d'huile, et le taux global de grossissement de la mousse, suggère une possible décorrélation intéressante entre les deux (voir figure A.3 (c)). L'interprétation physique des résultats de la DDM est toujours en cours de discussion, mais nous remarquons que même dans les échantillons 3D, la DDM sonde la dynamique de la couche superficielle de bulles : il serait donc intéressant d'étendre cette recherche pour sonder la dynamique de grossissement dans le volume de tels systèmes avec une technique différente.

Dans la dernière partie de la thèse, nous avons montré comment nous pouvons utiliser des méthodes bien établies d'une manière nouvelle pour générer et caractériser les émulsions aérées en une seule étape. En raison de l'activité antimousse potentielle de l'huile libre, les émulsions aérées sont généralement produites en deux étapes différentes, consistant soit à pré-émulsionner l'huile et puis à aérer l'émulsion, soit à préparer séparément une émulsion et une mousse qui sont ensuite mélangées.

Dans le chapitre §9, nous avons montré que des dispersions doubles de gaz et d'huile dans l'eau peuvent être générées en mélangeant simultanément les trois phases en une seule étape. La méthode de la double seringue permet de générer ces systèmes sur une large gamme de fractions volumiques d'huile et de gaz, en offrant une bonne séparation entre la taille des gouttes et celle des bulles dans le produit final. Le rapport entre leurs tailles, qui est en première approximation constant, présente clairement une dépendance en fraction d'huile pour une fraction totale de phase dispersée donnée, ce qui suggère une dépendance sous-jacente aux quantités relatives d'huile et de gaz qu'il serait intéressant d'étudier plus avant, en utilisant un dispositif automatique pour pousser les plongeurs de la seringue à une vitesse contrôlée.

Si les mousses sont généralement turbides, en raison de la diffusion de la lumière à leurs interfaces internes, dans les émulsions aérées cette turbidité est accentuée par la présence de gouttelettes parmi les bulles. Alors qu'il existe une variété de techniques pour caractériser les émulsions et les mousses, la caractérisation des dispersions composites est généralement plus compliquée. L'estimation de la taille des bulles dans ces systèmes, lorsque les gouttes et les bulles sont de l'ordre du micromètre, se fait traditionnellement par des techniques de microscopie, qui prennent cependant beaucoup de temps.

Dans le chapitre §9, nous avons également montré comment la granulométrie par diffraction laser, généralement utilisée pour mesurer la distribution de taille des gouttes d'huile ou des bulles de gaz séparément, peut être utilisée pour évaluer la taille typique des bulles également dans des dispersions doubles suffisamment séparées en taille et ayant un indice de réfraction différent. Dans ce dernier cas, la diffusion de la lumière des gouttes et des bulles donne lieu à deux pics bien résolus dans la distribution de taille pondérée en volume, qui correspondent aux deux populations différentes (voir figure A.4).

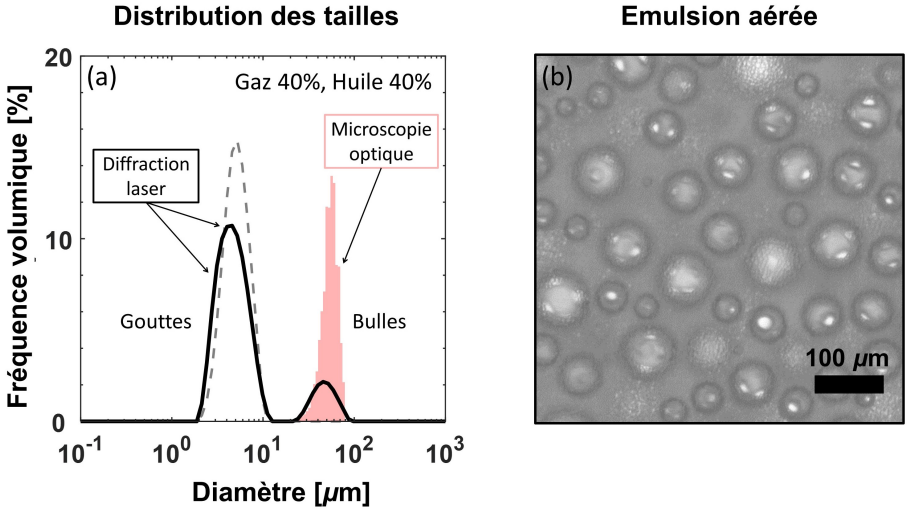

Figure A.4 – **Caractérisation des émulsions aérées.** (a) Comparaison entre la diffraction laser et la microscopie. La mesure d'une émulsion aérée par diffraction laser donne lieu à deux pics distincts correspondant à la diffusion des gouttes et des bulles. Le pic des bulles est remarquablement en accord avec celui mesuré par microscopie optique. (b) Exemple d'émulsion aérée contenant 40% d'huile et 40% de gaz, vue au microscope.

Nous avons testé la précision des résultats de la diffusion de la lumière en les comparant avec une technique bien établie et traçable comme la microscopie optique, et nous avons constaté un accord remarquable entre les distributions de taille des bulles pondérées en volume obtenues par les deux méthodes. De plus, nous avons étudié les limites de cette approche et montré que la diffraction laser est robuste sur une large gamme de fractions volumiques dispersées. La principale limite à la précision de la mesure provient d'une dispersion incomplète de l'échantillon à l'intérieur du Mastersizer en raison de la séparation rapide de bulles de plusieurs centaines de microns sur le dessus de l'unité de dispersion, ce qui peut conduire à une sous-estimation de la taille moyenne réelle des bulles de l'échantillon.

Néanmoins, nos mesures montrent que cette méthode est adaptée à la mesure de bulles de diamètre moyen au moins jusqu'à 100 μm, ce qui inclut la gamme de taille d'intérêt dans de nombreuses applications courantes, comme les produits alimentaires et cosmétiques. La diffraction laser s'avère donc être un outil efficace permettant de réduire le temps nécessaire pour évaluer la taille des bulles avec une bonne précision en quelques secondes, aussi bien dans les mousses aqueuses que dans les émulsions aérées.

Les résultats de cette thèse sur la génération et la séparation de phase des mousses d'émulsions fournissent de nouvelles perspectives sur leur mécanisme de déstabilisation qui peuvent aider à contrôler la stabilité de ces systèmes complexes pour la réalisation de nouveaux matériaux avec une morphologie cellulaire atypique.

Bibliography

[1] H. Bey, F. Wintzenrieth, O. Ronsin, R. Höhler, and S. Cohen-Addad. Stabilization of foams by the combined effects of an insoluble gas species and gelation. *Soft Matter*, 13(38):6816–6830, 2017.

[2] D. Bideau and J. P. Troadec. Compacity and mean coordination number of dense packings of hard discs. *Journal of Physics C: Solid State Physics*, 17(28):2–7, 1984.

[3] H. Bissig, S. Romer, L. Cipelletti, V. Trappea, and P. Schurtenberger. Intermittent dynamics and hyper-aging in dense colloidal gels. *PhysChemComm*, 6(5):21–23, 2003.

[4] F. Bolton and D. Weaire. Rigidity loss transition in a disordered 2D froth. *Physical Review Letters*, 65(27):3449–3451, 1990.

[5] F. Bolton and D. Weaire. The effects of Plateau borders in the two-dimensional soap froth. I. Decoration lemma and diffusion theorem. *Philosophical Magazine B: Physics of Condensed Matter; Statistical Mechanics, Electronic, Optical and Magnetic Properties*, 63(4):795–809, 1991.

[6] Z. Briceño-Ahumada and D. Langevin. On the influence of surfactant on the coarsening of aqueous foams. *Advances in Colloid and Interface Science*, 244:124–131, 2017.

[7] Z. Briceño-Ahumada, A. Soltero, A. Maldonado, J. Perez, D. Langevin, and M. Impéror-Clerc. On the use of shear rheology to formulate stable foams. example of a lyotropic lamellar phase. *Colloids and Surfaces A: Physicochemical and Engineering Aspects*, 507:110–117, 2016.

[8] M. Caggioni, V. Trappe, and P. T. Spicer. Variations of the Herschel–Bulkley exponent reflecting contributions of the viscous continuous phase to the shear rate-dependent stress of soft glassy materials. *Journal of Rheology*, 64(2):413–422, 2020.

[9] I. Cantat, S. Cohen-Addad, F. Elias, F. Graner, R. Hohler, O. Pitois, F. Rouyer, and A. Saint-Jalmes. *Foams. Structure and Dynamics.* Oxford University Press, New York, 2013.

[10] V. Carrier and A. Colin. Coalescence in draining foams. *Langmuir*, 19(11):4535–4538, 2003.

[11] R. Cerbino and V. Trappe. Differential dynamic microscopy: Probing wave vector dependent dynamics with a microscope. *Physical Review Letters*, 100(18):1–4, 2008.

[12] A. Chesterton, D. P. de Abreu, G. Moggridge, P. Sadd, and D. Wilson. Evolution of cake batter bubble structure and rheology during planetary mixing. *Food and Bioproducts Processing*, 91(3):192–206, 2013.

[13] A. Chesterton, G. Moggridge, P. Sadd, and D. Wilson. Modelling of shear rate distribution in two planetary mixtures for studying development of cake batter structure. *Journal of Food Engineering*, 105(2):343–350, 2011.

[14] A. T. Chieco and D. J. Durian. Experimentally testing a generalized coarsening model for individual bubbles in quasi-two-dimensional wet foams. *Phys. Rev. E*, 103:012610, Jan 2021.

[15] G. Chinga and K. Syverud. Quantification of paper mass distributions within local picking areas. *Nordic Pulp and Paper Research Journal*, 22(4):441–446, 2007.

[16] S. Cohen-Addad and R. Höhler. Bubble dynamics relaxation in aqueous foam probed by multispeckle diffusing-wave spectroscopy. *Physical Review Letters*, 86(20):4700–4703, 2001.

[17] H. J. Couto, D. G. Nunes, R. Neumann, and S. C. França. Micro-bubble size distribution measurements by laser diffraction technique. *Minerals Engineering*, (4):330–335.

[18] S. J. Cox and E. Janiaud. On the structure of quasi-two-dimensional foams. *Philosophical Magazine Letters*, 88(9-10):693–701, 2008.

[19] S. J. Cox, D. Weaire, and M. Fatima Vaz. The transition from two-dimensional to three-dimensional foam structures. *Eur. Phys. J. E*, 7:311–315, 2002.

[20] P.-G. de Gennes, F. Brochard-Wyart, and D. Quéré. *Capillarity and Wetting Phenomena: Drops, Bubbles, Pearls, Waves.* Springer Science, 2004.

[21] M. De Icaza, A. Jiménez-Ceniceros, and V. M. Castaño. Statistical distribution functions in 2D foams. *Journal of Applied Physics*, 76(11):7317–7321, 1994.

[22] N. D. Denkov. Mechanisms of foam destruction by oil-based antifoams. *Langmuir*, 20(22):9463–9505, 2004.

[23] M. Dinkgreve, J. Paredes, M. M. Denn, and D. Bonn. On different ways of measuring "the" yield stress. *Journal of Non-Newtonian Fluid Mechanics*, 238:233–241, 2016. Viscoplastic Fluids From Theory to Application 2015 (VPF6).

[24] W. Drenckhan and A. Saint-Jalmes. The science of foaming. *Advances in Colloid and Interface Science*, pages 228–259.

[25] L. Ducloué, O. Pitois, J. Goyon, X. Chateau, and G. Ovarlez. Coupling of elasticity to capillarity in soft aerated materials. *Soft Matter*, 10:5093–5098, 2014.

[26] L. Ducloué, O. Pitois, J. Goyon, X. Chateau, and G. Ovarlez. Rheological behaviour of suspensions of bubbles in yield stress fluids. *Journal of Non-Newtonian Fluid Mechanics*, 215:31–39, 2015.

[27] D. J. Durian. Foam mechanics at the bubble scale. *Phys. Rev. Lett.*, 75:4780–4783, Dec 1995.

[28] D. J. Durian. Bubble-scale model of foam mechanics: melting, nonlinear behavior, and avalanches. *Phys. Rev. E*, 55:1739–1751, Feb 1997.

[29] D. J. Durian, D. A. Weitz, and D. J. Pine. Multiple light-scattering probes of foam structure and dynamics. *Science*, 252:686–688, 1991.

[30] D. J. Durian, D. A. Weitz, and D. J. Pine. Scaling behavior in shaving cream. *Phys. Rev. A*, 44:R7902–R7905, Dec 1991.

[31] D. Eaves. *The Handbook of Polymer Foams.* Rapra Technology Limited, 2004.

[32] V. B. Fainerman, E. V. Aksenenko, and R. Miller. Influence of alkane and perfluorocarbon vapors on adsorbed surface layers and spread insoluble monolayers of surfactants, proteins and lipids. *Advances in Colloid and Interface Science*, pages 100–112.

[33] R. S. Farr and R. D. Groot. Close packing density of polydisperse hard spheres. *J. Chem. Phys.*, 131, 2009.

[34] E. Forel. Mûrissement et coalescence de mousses liquides. PhD thesis. Matériaux. Université Paris-Saclay, 2017. Français.

[35] E. Forel, B. Dollet, D. Langevin, and E. Rio. Coalescence in two-dimensional foams: A purely statistical process dependent on film area. *Phys. Rev. Lett.*, 122:088002, Feb 2019.

[36] E. Forel, E. Rio, M. Schneider, S. Beguin, D. Weaire, S. Hutzler, and W. Drenckhan. The surface tells it all: relationship between volume and surface fraction of liquid dispersions. *Soft Matter*, (38):8025–8029.

[37] I. Fortuna, G. L. Thomas, R. M. De Almeida, and F. Graner. Growth laws and self-similar growth regimes of coarsening two-dimensional foams: Transition from dry to wet limits. *Physical Review Letters*, 108(24), 2012.

[38] Y. Furuta, N. Oikawa, and R. Kurita. Close relationship between a dry-wet transition and a bubble rearrangement in two-dimensional foam. *Scientific Reports*, 6(October):1–8, 2016.

[39] T. Gaillard, C. Honorez, M. Jumeau, F. Elias, and W. Drenckhan. A simple technique for the automation of bubble size measurements. *Colloids and Surfaces A: Physicochemical and Engineering Aspects*, 473:68–74, 2015.

[40] T. Gaillard, M. Roché, C. Honorez, M. Jumeau, A. Balan, C. Jedrzejczyk, and W. Drenckhan. Controlled foam generation using cyclic diphasic flows through a constriction. *International Journal of Multiphase Flow*, 96:173–187, 2017.

[41] B. S. Gardiner, B. Z. Dlugogorski, and G. J. Jameson. Coarsening of two- and three-dimensional wet polydisperse foams. *Philosophical Magazine A*, 80(4):981–1000, 2000.

[42] C. Gay, P. Rognon, D. Reinelt, and F. Molino. Rapid Plateau border size variations expected in three simple experiments on 2D liquid foams. *European Physical Journal E*, 34(1), 2011.

[43] F. Giavazzi and R. Cerbino. Digital Fourier microscopy for soft matter dynamics. *Journal of Optics (United Kingdom)*, 16(8), 2014.

[44] F. Giavazzi, P. Edera, P. J. Lu, and R. Cerbino. Image windowing mitigates edge effects in Differential Dynamic Microscopy. *European Physical Journal E*, 40(11):1–9, 2017.

[45] F. Giavazzi, V. Trappe, and R. Cerbino. Multiple dynamic regimes in a coarsening foam. *Journal of Physics Condensed Matter*, 33(2):24002, 2021.

[46] J. A. Glazier, M. P. Anderson, and G. S. Grest. Coarsening in the two-dimensional soap froth and the large-q potts model: A detailed comparison. *Philosophical Magazine B*, 62(6):615–645, 1990.

[47] J. A. Glazier, S. P. Gross, and J. Stavans. Dynamics of two-dimensional soap froths. *Physical Review A.*, 36(1):306–312, 1987.

[48] J. A. Glazier and J. Stavans. Nonideal effects in the two-dimensional soap froth. *Phys. Rev. A*, 40:7398–7401, Dec 1989.

[49] J. A. Glazier and D. Weaire. The kinetics of cellular patterns. *Journal of Physics: Condensed Matter*, 4:1867, 1992.

[50] F. Gorlier, Y. Khidas, and O. Pitois. Coupled elasticity in soft solid foams. *Journal of Colloid and Interface Science*, 501:103–111, 2017.

[51] J. Goyon, F. Bertrand, O. Pitois, and G. Ovarlez. Shear Induced Drainage in Foamy Yield-Stress Fluids. *Physical Review Letters*, (12):128301.

[52] J. Goyon, A. Colin, and L. Bocquet. How does a soft glassy material flow: finite size effects, non local rheology, and flow cooperativity. *Soft Matter*, 6:2668–2678, 2010.

[53] J. Goyon, A. Colin, G. Ovarlez, A. Ajdari, and L. Bocquet. Spatial cooperativity in soft glassy flows. *Nature Letters*, 454, 2008.

[54] F. Graner, B. Dollet, C. Raufaste, and P. Marmottant. Discrete rearranging disordered patterns, part i: Robust statistical tools in two or three dimensions. *Eur. Phys. J. E*, 25:349–369, 2008.

[55] F. Graner, Y. Jiang, E. Janiaud, and C. Flament. Equilibrium states and ground state of two-dimensional fluid foams. *Physical Review E - Statistical, Nonlinear, and Soft Matter Physics*, 63(1 I):0114021–01140213, 2001.

[56] C. Guidolin. Controlling foam ageing in viscoelastic media. Master thesis. Università degli Studi di Padova, 2018.

[57] C. Guidolin, N. Jiang, D. Langevin, and A. Salonen. One-step generation and characterisation of aerated emulsions using laser diffraction. *Colloids and Surfaces A: Physicochemical and Engineering Aspects*, 641:128454, 2022.

[58] R. M. Guillermic, A. Salonen, J. Emile, and A. Saint-Jalmes. Surfactant foams doped with laponite: Unusual behaviors induced by aging and confinement. *Soft Matter*, 5(24):4975–4982, 2009.

[59] P. Hébraud, F. Lequeux, J. P. Munch, and D. J. Pine. Yielding and rearrangements in disordered emulsions. *Phys. Rev. Lett.*, 78:4657–4660, Jun 1997.

[60] W. H. Herschel and R. Bulkley. Measurement of consistency as applied to rubber-benzene solutions. *Proc. Am. Soc. Test. Mater.*, 26(2):621–633, 1926.

[61] S. Hilgenfeldt, A. M. Kraynik, S. A. Koehler, and H. A. Stone. An accurate von neumann's law for three-dimensional foams. *Phys. Rev. Lett.*, 86:2685–2688, Mar 2001.

[62] M. Hiseman, B. Laurent, J. Bridgwater, D. Wilson, D. Parker, N. North, and D. Merrifield. Granular flow in a planetary mixer. *Chemical Engineering Research and Design*, 80(5):432–440, 2002. Materials Processing.

[63] S. Hutzler and D. Weaire. Foam coarsening under forced drainage. *Philosophical Magazine Letters*, 80(6):419–425, 2000.

[64] N. Isert, G. Maret, and C. M. Aegerter. Coarsening dynamics of three-dimensional levitated foams: From wet to dry. *European Physical Journal E*, 36(10), 2013.

[65] K. Khakalo, K. Baumgarten, B. P. Tighe, and A. Puisto. Coarsening and mechanics in the bubble model for wet foams. *Phys. Rev. E*, 98:012607, Jul 2018.

[66] Y. Khidas, B. Haffner, and O. Pitois. Capture-induced transition in foamy suspensions. *Soft Matter*, 10(23):4137–4141, 2014.

[67] W. Kloek, T. Van Vliet, and M. Meinders. Effect of bulk and interfacial rheological properties on bubble dissolution. *Journal of Colloid and Interface Science*, 237(2):158–166, 2001.

[68] K. Koczo, L. A. Lobo, and D. T. Wasan. Effect of oil on foam stability - aqueous foams stabilised by emulsions. *Journal of Colloid and Interface Science*, 150(2):492–506, 1992.

[69] M. Kogan, L. Ducloué, J. Goyon, X. Chateau, O. Pitois, and G. Ovarlez. Mixtures of foam and paste: suspensions of bubbles in yield stress fluids. *Rheol Acta*, 52:237–253, 2013.

[70] R. Kurita, Y. Furuta, N. Yanagisawa, and N. Oikawa. Dynamical transition in a jammed state of a quasi-two-dimensional foam. *Physical Review E*, 95(6):1–6, 2017.

[71] M.-D. Lacasse, G. S. Grest, D. Levine, T. G. Mason, and D. A. Weitz. Model for the elasticity of compressed emulsions. *Phys. Rev. Lett.*, 76:3448–3451, Apr 1996.

[72] D. Langevin. Coalescence in foams and emulsions: Similarities and differences. *Current Opinion in Colloid and Interface Science*, 44:23–31, 2019.

[73] D. Langevin. *Emulsions, Microemulsions and Foams.* Springer Soft and Biological Matter, 2020.

[74] F. Leal-Calderon, V. Schmitt, and J. Bibette. *Emulsion Science. Basic Principles.* Springer, 2007.

[75] I. Lesov, S. Tcholakova, and N. Denkov. Factors controlling the formation and stability of foams used as precursors of porous materials. *Journal of Colloid and Interface Science*, 426:9–21, 2014.

[76] D. R. Lide. *CRC Handbook of Chemistry and Physics, Internet Version 2005.* CRC Press, Boca Raton, FL, 2005.

[77] I. Lifshitz and V. Slyozov. The kinetics of precipitation from supersaturated solid solutions. *Journal of Physics and Chemistry of Solids*, 19(1):35–50, 1961.

[78] M. Lundberg, K. Krishan, N. Xu, C. S. O'Hern, and M. Dennin. Reversible plastic events in amorphous materials. *Phys. Rev. E*, 77:041505, Apr 2008.

[79] C. W. Macosko. *Rheology. Principles, Measurements and Applications.* Wiley-VCH, 1994.

[80] A. Maestro, W. Drenckhan, E. Rio, and R. Höhler. Liquid dispersions under gravity: Volume fraction profile and osmotic pressure. *Soft Matter*, 9(8):2531–2540, 2013.

[81] T. Mason, J. Bibette, and D. Weitz. Yielding and flow of monodisperse emulsions. *Journal of Colloid and Interface Science*, 179(2):439–448, 1996.

[82] T. G. Mason, J. Bibette, and D. A. Weitz. Elasticity of compressed emulsions. *Physical review letters*, 75:2051–2054, 1995.

[83] D. J. McClements. *Food Emulsions. Principles, Practice and Techniques.* CRC Press LLC, 1999.

[84] H. G. Merkus. *Particle Size Measurements. Fundamentals, Practice, Quality.* Springer, 2009.

[85] A. Mikhailovskaya, V. Trappe, and A. Salonen. Colloidal gelation, a means to study elasto-capillarity effects in foam. *Soft Matter*, 16(9):2249–2255, 2020.

[86] W. Mullins. Estimation of the geometrical rate constant in idealized three dimensional grain growth. *Acta Metallurgica*, 37(11):2979–2984, 1989.

[87] W. W. Mullins. Two-dimensional motion of idealized grain boundaries. *Journal of Applied Physics*, 27:900, 1956.

[88] W. W. Mullins. The statistical self-similarity hypothesis in grain-growth and particle coarsening. *Journal of Applied Physics*, 59:1341–1349, 1986.

[89] M. Pasquet. Stabilité d'objets savonneux : mousses humides, bulles de surface et films géants. PhD thesis. Université Paris-Saclay, 2022. Français.

[90] D. Pine, D. Weitz, J. Zhu, and E. Herbolzheimer. Diffusing-wave spectroscopy: dynamic light scattering in the multiple scattering limit. *Journal de Physique*, 51(18):2101–2127, 1990.

[91] D. J. Pine, D. A. Weitz, P. M. Chaikin, and E. Herbolzheimer. Diffusing wave spectroscopy. *Physical Review Letters*, 60(12):1134–1137, 1988.

[92] N. Politova, S. Tcholakova, Z. Valkova, K. Golemanov, and N. D. Denkov. Self-regulation of foam volume and bubble size during foaming via shear mixing. *Colloids and Surfaces*, 539:18–28, 2018.

[93] H. Princen and A. Kiss. Rheology of foams and highly concentrated emulsions: Iii. static shear modulus. *Journal of Colloid and Interface Science*, 112(2):427–437, 1986.

[94] A. Raudsepp, A. J. Sutherland-Smith, and M. A. Williams. Rotating angled plate diffusing wave spectroscopy. *International Journal of Nanotechnology*, 11(5-8):573–582, 2014.

[95] E. Rio and A. L. Biance. Thermodynamic and mechanical timescales involved in foam film rupture and liquid foam coalescence. *ChemPhysChem*, 15(17):3692–3707, 2014.

[96] M. Rosenbluh, M. Hoshen, I. Freund, and M. Kaveh. Time evolution of universal optical fluctuations. *Physical Review Letters*, 58(26):2754–2757, 1987.

[97] A. E. Roth, C. D. Jones, and D. J. Durian. Bubble statistics and coarsening dynamics for quasi-two-dimensional foams with increasing liquid content. *Physical Review E - Statistical, Nonlinear, and Soft Matter Physics*, 87(4), 2013.

[98] A. Rust and M. Manga. Effects of bubble deformation on the viscosity of dilute suspensions. *Journal of Non-Newtonian Fluid Mechanics*, 104(1):53–63, 2002.

[99] A. Saint-Jalmes. Physical chemistry in foam drainage and coarsening. *Soft Matter*, 2(10):836–849, 2006.

[100] A. Saint-Jalmes and D. J. Durian. Vanishing elasticity for wet foams: Equivalence with emulsions and role of polydispersity. *Journal of Rheology*, 43(6):1411–1422, 1999.

[101] A. Salonen, R. Lhermerout, E. Rio, D. Langevin, and A. Saint-Jalmes. Dual gas and oil dispersions in water: Production and stability of foamulsion. *Soft Matter*, 8(3), 2012.

[102] R. Sander. Henry's law constants. *in NIST Chemistry WebBook, NIST Standard Reference Database*.

[103] F. Scheffold, S. E. Skipetrov, S. Romer, and P. Schurtenberger. Diffusing-wave spectroscopy of nonergodic media. *Physical Review E - Statistical, Nonlinear, and Soft Matter Physics*, 63(6 I):061404/1–061404/11, 2001.

[104] C. D. Schimming and D. J. Durian. Border-crossing model for the diffusive coarsening of two-dimensional and quasi-two-dimensional wet foams. *Phys. Rev. E*, 96:032805, Sep 2017.

[105] B. Schoelson. Circle finder. `https://www.mathworks.com/matlabcentral/fileexchange/34365-circle-finder`. ,MATLAB Central File Exchange. Retrieved May 12, 2021.

[106] O. Sonneville-Aubrun, V. Bergeron, T. Gulik-Krzywicki, H. Jönsson, B. Wennerström, P. Lindner, and B. Cabane. Surfactant films in biliquid foams. *Langmuir*, 16(4):1566–1579, 2000.

[107] J. Stavans. Temporal evolution of two-dimensional drained soap froths. *Phys. Rev. A*, 42:5049–5051, Oct 1990.

[108] J. Stavans and J. A. Glazier. Soap froth revisited: Dynamic scaling in the two-dimensional froth. *Phys. Rev. Lett.*, 62:1318–1321, Mar 1989.

[109] P. Stevenson. *Foam Engineering. Fundamentals and Applications.* John Wiley & Sons, Ltd, 2012.

[110] H. Tanaka. Universality of viscoelastic phase separation in dynamically asymmetric fluid mixtures. *Phys. Rev. Lett.*, 76:787–790, Jan 1996.

[111] H. Tanaka. Viscoelastic model of phase separation. *Physical Review E - Statistical Physics, Plasmas, Fluids, and Related Interdisciplinary Topics*, 56(4):4451–4462, 1997.

[112] H. Tanaka. Viscoelastic phase separation. *Journal of Physics Condensed Matter*, 12(15), 2000.

[113] H. Tanaka. Viscoelastic phase separation in soft matter and foods. *Faraday Discussions*, 158:371–406, 2012.

[114] H. Tanaka, T. Araki, T. Koyama, and Y. Nishikawa. Universality of viscoelastic phase separation in soft matter. *Journal of Physics Condensed Matter*, 17(45), 2005.

[115] H. Tanaka, T. Koyama, and T. Araki. Network formation in viscoelastic phase separation. *Journal of Physics Condensed Matter*, 15(1), 2003.

[116] S. Tcholakova, I. Lesov, K. Golemanov, N. D. Denkov, S. Judat, R. Engel, and T. Danner. Efficient emulsification of viscous oils at high drop volume fraction. *Langmuir*, 27(24):14783–14796, 2011.

[117] G. L. Thomas, R. M. C. de Almeida, and F. Graner. Coarsening of three-dimensional grains in crystals, or bubbles in dry foams, tends towards a universal, statistically scale-invariant regime. *Phys. Rev. E*, 74:021407, Aug 2006.

[118] M. U. Vera, A. Saint-Jalmes, and D. J. Durian. Scattering optics of foam. *Applied Optics*, 40(24):4210, 2001.

[119] V. Viasnoff, F. Lequeux, and D. J. Pine. Multispeckle diffusing-wave spectroscopy: A tool to study slow relaxation and time-dependent dynamics. *Review of Scientific Instruments*, 73(6):2336, 2002.

[120] J. Von Neumann. *Metal Interfaces.* American Society for Metals, Cleveland, 1952.

[121] C. Wagner. Theorie der alterung von niederschlägen durch umlösen (ostwald-reifung). *Zeitschrift für Elektrochemie, Berichte der Bunsengesellschaft für physikalische Chemie*, 65(7-8):581–591, 1961.

[122] D. Weaire. Counting constraints for hard disks. *Philosophical Magazine B*, 51(2):L19–L20, 1985.

[123] D. Weaire. Comment on "soap froth revisited: Dynamical scaling in the two-dimensional froth". *Phys. Rev. Lett.*, 64:3202–3202, Jun 1990.

[124] D. Weaire and V. Pageron. Frustrated froth: Evolution of foam inhibited by an insoluble gaseous component. *Philosophical Magazine Letters*, 62(6):417–421, 1990.

[125] D. Weaire and N. Rivier. Soap, cells and statistics—random patterns in two dimensions. *Contemporary Physics*, 25(1):59–99, 1984.

[126] D. L. Weaire and S. Hutzler. *The Physics of Foams.* Oxford University Press, 1999.

[127] A. J. Webster and M. E. Cates. Osmotic stabilization of concentrated emulsions and foams. *Langmuir*, 17(3):595–608, 2001.

[128] D. A. Weitz, H. Gang, D. J. Pine, J. X. Zhu, and D. J. Durian. Diffusing-wave spectroscopy: The technique and some applications. *Physica Scripta*, 1993(T49B):610–621, 1993.

[129] P. Zakharov, F. Cardinaux, and F. Scheffold. Accuracy preserving methods for faster measurements with dynamic light scattering and diffusing wave spectroscopy. 6164:61640K–61640K–8, 2006.

[130] P. Zakharov, F. Cardinaux, and F. Scheffold. Multispeckle diffusing-wave spectroscopy with a single-mode detection scheme. *Physical Review E - Statistical, Nonlinear, and Soft Matter Physics*, 73(1):1–5, 2006.